

Computations of Fully Nonlinear Three-dimensional Wave-Body Interactions

by

Hongmei Yan

Submitted to the Department of Mechanical Engineering
in partial fulfillment of the requirements for the degree of

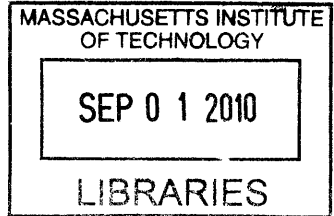
Doctor of Philosophy in Ocean Engineering

at the

MASSACHUSETTS INSTITUTE OF TECHNOLOGY


June 2010

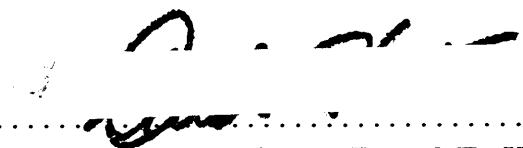
ARCHIVES



© Massachusetts Institute of Technology 2010. All rights reserved.

Author  5/16/2010
Department of Mechanical Engineering
May 16, 2010

Certified by  4/27/2010
Yuming Liu
Principal Research Scientist, Mechanical Engineering
Thesis Supervisor

Accepted by 
Professor David E. Hardt
Chairman, Department Committee on Graduate Students

Computations of Fully Nonlinear Three-dimensional Wave-Body Interactions

by

Hongmei Yan

Submitted to the Department of Mechanical Engineering
on May 16, 2010, in partial fulfillment of the
requirements for the degree of
Doctor of Philosophy in Ocean Engineering

Abstract

Nonlinear effects in hydrodynamics of wave-body interaction problems become critically important when large-amplitude body motions and/or extreme surface waves are involved. Accurate prediction and understanding of these fully nonlinear effects are still challenges in the design of surface ships and marine structures, owing to the complexity of the hydrodynamic problem itself and limited computational facilities. This research is focused on: (i) development of a highly efficient numerical scheme for the computation of fully-nonlinear three-dimensional wave-body interactions; and (ii) investigation of several highly nonlinear wave-body interaction problems for understanding associated key nonlinear effects.

A highly efficient high-order boundary element method is developed based on the framework of the quadratic boundary element method (QBEM) for the boundary integral equation and using the pre-corrected fast Fourier transform (PFFT) algorithm to accelerate the evaluation of far-field influences of source and/or normal dipole distributions on boundary elements. The resulting numerical scheme reduces the computational effort of solving the boundary-value problem from $O(N^{2-3})$ (with the traditional boundary element methods) to $O(N \ln N)$ where N represents the total number of boundary unknowns. Combining with the mixed-Eulerian-Lagrangian (MEL) approach for nonlinear free surface tracking, we develop an efficient and accurate initial boundary value problem (IBVP) solver, PFFT-QBEM, which allows for practical simulations of fully nonlinear three-dimensional wave-body interaction problems.

Three nonlinear wave-body interaction problems, which are of scientific interest and practical importance, are investigated in detail: water surface impact of three-dimensional objects, cavity dynamics in water entries, and coupled unstable motions of floating structures in waves. For the water impact problem, with the development of an adaptive jet flow treatment and an effective approach for accurately tracking water-body separation point/line, we obtain a thorough understanding of the gravity effect on the characteristics of slamming pressure/load on the object and free-surface profiles. For the cavity problem, we investigate the formation and evolution of an air

cavity behind an object dropped into water (from air) at relatively low Froude numbers where the inertia and gravity effects are comparable. A theoretical solution is newly derived based on a matched asymptotic approach and a fully nonlinear numerical simulation is carried out, for the description of the kinematics and dynamics of the air cavity. Satisfactory quantitative comparisons are obtained among the theoretical predictions, numerical simulations, and existing experimental measurements for the dependence of cavity shape and closure time/height on Froude number and body geometry. For floating structures in waves, our focus is on the understanding of the fundamental mechanism and basic characteristics for coupled unstable heave-pitch motions of floating platforms/vessels. Through stability analyses, we identify that the second-order difference-frequency interaction between surface waves and body motions is the key mechanism for the excitation of unstable resonant motions. Fully nonlinear simulations are conducted to study the development of large-amplitude body motions and investigate quantitatively the dependence of the instability on related physical parameters, such as incident wave amplitude and phase, frequency detuning, body geometry, and system damping. Theoretical analyses and numerical simulations are verified by comparison to available experiments for the coupled unstable motions of a deep draft caisson vessel (DDCV).

Thesis Supervisor: Yuming Liu

Title: Principal Research Scientist, Mechanical Engineering

Acknowledgments

First and foremost, I would like to express my gratitude to my thesis advisor, Dr. Yuming Liu. I cannot thank him enough for the continuous guidance and patience he gave to me in the long journey to getting my Ph.D degree from MIT. Whenever I have questions and problems, he is there to help and would never give me up before I have the answers. Whenever I am frustrated by slow research progress, he is there to encourage me and push me forward. There is an old Chinese saying, "a teacher of one day, a mentor of lifetime". This is exactly how I feel towards Dr. Yuming Liu.

I thank Professor Dick K.P. Yue very much for advising me. His knowledge, his vision, and attitude towards research set up very high standards that always inspire and motivate me to do better. Several times when I was stuck with problems, it is his sharp insights that guided me through the difficult situations. I am truly grateful for all his help.

I thank Professor Michael Triantafyllou for serving in my thesis committee. His insightful questions on my thesis committee meetings helped me look at my research subjects from different angles.

I dedicate my thesis to my family. My parents give me their unconditional love and they are always there for me. My elder brother constantly reminded me that I need to graduate from here and my younger brother is already happy about whatever I do. I am especially indebted to my husband, Ming Tang, for his love, his devotion, and unreserved support all the way along. Meeting and marrying him is the most fortunate thing that happened to me at MIT.

Special thanks go to all the former and current VFRL members. It is you who make here such a nice place to work at. Kelli reviewed part of my thesis. She also helped greatly with my presentations, and so did Areti. Guangyu taught me a lot of computer skills during my early days at MIT. Gabe regularly checked up with my thesis writing progress. Everybody offered me help in many different ways, for which I highly appreciate. All the joyful moments we VFRL members spent together will always be in my fond memories.

Lastly, thank all my friends at MIT. Especially, Yaning and Wenchao are like sisters to me. I cherish our friendship.

Contents

1	Introduction	31
2	Development of Pre-corrected FFT-accelerated Quadratic Boundary Element Method	43
2.1	Introduction	43
2.2	Formulation of the Classical Boundary Element Method	47
2.2.1	Boundary Integral Equation (BIE)	47
2.2.2	Constant Panel Method (CPM)	48
2.2.3	Quadratic Boundary Element Method (QBEM)	49
2.2.4	System Equations	51
2.3	PFFT-accelerated BEMs	52
2.3.1	Source distribution	52
2.3.2	Dipole distribution	56
2.3.3	Mixed boundary-value problem	57
2.4	Numerical implementation	57
2.4.1	Interpolation function $H(\xi)$	58
2.4.2	Direct approach for dipole distribution	60
2.4.3	Treatment of a boundary element not fully covered by a cell	62
2.4.4	Nearby elements/points	62
2.4.5	Solid-angle evaluation	64
2.4.6	Determination of preconditioners	64
2.5	Numerical Results	68
2.5.1	Dependence on governing numerical parameters	68

2.5.2	Comparison of PFFT-CPM with PFFT-QBEM	77
2.5.3	Performance of Parallelized PFFT-BEMs Algorithm	82
2.6	Conclusions	86
2.7	References	87
3	Time simulations of fully nonlinear wave-body interactions using PFFT-QBEM	89
3.1	Introduction	89
3.2	Mathematical formulation	92
3.2.1	The initial boundary value problem (IBVP)	92
3.2.2	The mixed Eulerian Lagrangian (MEL) approach	94
3.2.3	Incident flow/waves	96
3.2.4	Boundary integral equation (BIE) for BVPs	99
3.2.5	Advantages in solving the disturbance velocity potential over the total velocity potential	102
3.3	Numerical implementations	105
3.3.1	Six-degrees-of-freedom body motion	105
3.3.2	Stability analysis of time-integration schemes	108
3.3.3	Wave absorbing zone on free surface	114
3.3.4	Tracking of wave-body intersection line	123
3.4	Applications to sample fully-nonlinear wave-body interactions	128
3.4.1	Forced heave oscillations of a sphere	128
3.4.2	Ringling loads on a vertical cylinder in Stokes waves	131
3.4.3	Wave resistance of a Series 60 ship hull	134
3.5	Concluding Remarks	136
3.6	References	138
4	Cavity Dynamics in Water Entry at Low Froude Numbers	143
4.1	Introduction	143
4.2	Problem statement	145
4.2.1	The initial boundary value problem	145

4.2.2	Physical insight	149
4.3	Asymptotic theory	150
4.3.1	Governing equations	150
4.3.2	Determination of ϕ_b	152
4.3.3	Determination of ϕ_c	153
4.3.4	Time evolution of the cavity	156
4.3.5	Evaluation of the drag	157
4.4	Fully-nonlinear numerical simulation	158
4.5	Results	160
4.5.1	Freely-falling spheres	160
4.5.2	Water entry of a disk with a constant velocity	167
4.5.3	Body geometry effect	171
4.6	Conclusions	174
4.7	References	177

5 Nonlinear Computations of Water Impact of Axisymmetric Bodies 181

5.1	Introduction	181
5.2	Problem Formulation	185
5.3	Numerical Implementation	187
5.3.1	Overall numerical scheme	187
5.3.2	Jet-cutting treatment for cone impact simulation	189
5.3.3	Determination of flow separation from body surface for sphere impacts	193
5.3.4	Evaluation of impact pressure	194
5.4	Numerical results for inverted cone impact	196
5.4.1	Comparisons with existing studies for $Fr = \infty$	196
5.4.2	Gravity effect	198
5.4.3	Geometry effect	203
5.4.4	An approximate similarity solution for cone impact	208
5.5	Numerical results for water impact of spheres	210

5.5.1	Comparison to experimental measurements	212
5.5.2	Impact pressure and slamming force	215
5.5.3	Free surface profile	217
5.6	Conclusions	220
5.7	References	222
6	Coupled Unstable Heave-Pitch Motions of a Large Floating Ves-	
	sel/Structure in Waves	227
6.1	Introduction	227
6.2	Linear stability analysis for motions of a floating body in waves	230
6.2.1	Mathematical formulations for general wave-body interactions	231
6.2.2	The solution method: linear stability analysis	232
6.2.3	Base flow solution at order $O(\epsilon)$	235
6.2.4	Disturbance flow solution	238
6.2.5	Coupled equations for resonant heave-pitch motions	244
6.2.6	Surge motion effect on instability	245
6.2.7	Other possible conditions of instability	246
6.2.8	Numerical analyses on growth rates of coupled unstable heave/pitch motions	247
6.2.9	Summary of the linear stability analysis for floating bodies in waves	255
6.3	Fully nonlinear numerical simulations of unstable motions of floating structures in waves	257
6.3.1	Confirmation of the instability condition	258
6.3.2	Importance of full nonlinearity in highly-nonlinear wave-body interactions	259
6.3.3	Effect of incident wave steepness on instability	261
6.3.4	Frequency detuning effect on instability	266
6.3.5	Influence of body geometry on instability	269
6.3.6	Effect of surge motion on instability	271

6.3.7	Effect of incident wave phase angle on instability	274
6.3.8	Influence of initial disturbances on instability	277
6.4	Comparison to experimental data	277
6.5	Summary and discussions	284
6.6	References	289
7	Conclusions and Future Studies	291
7.1	Conclusions	291
7.2	Future studies	296
7.3	References	297

List of Figures

2-1	A generic nine-node curvilinear element $FE_j^q(x, y, z)$ and its image in parametric space $FE_j^q(s, t) : s \in [-1, 1], t \in [-1, 1]$	50
2-2	Comparisons of the projection errors in the velocity potential of a point dipole as a function of the distance of the field point from the dipole. The plotted are the results obtained with the use of interpolation functions H (—) and \bar{H} (---) for the point dipole at (a) an arbitrarily-chosen non-central location $(-0.01h, 0.39h, 0.26h)$ and (b) the center the cell. The slope of the curve k is indicated.	63
2-3	L_2 norm of the normalized GMRES residual as a function of iteration number for the Dirichlet problem (a), the Neumann problem (b), and the mixed problems with the ratio of the number of Dirichlet elements to that of Neumann elements being 1.0 (c) and 0.2 (d). The plotted are the results obtained without preconditioner (—) and with diagonal preconditioner (- - -) and MN preconditioners including neighboring elements within $d/h=1.5$ (. . .) and $d/h=3.0$ (— . . . —).	68
2-4	Normalized maximum (\circ , \square , and \triangle) and averaged (\boxplus , \boxtimes , and \boxminus) errors in the velocity potential due to a uniform source distribution on a sphere obtained by the PFFT-CPM with the use of (a) linear and (b) quadratic interpretation functions for various values of d/h	70

2-5	Comparison of the CPU time of the conventional CPM (-O-) and the PFFT-CPM with linear (-Δ-) and quadratic (-□-) interpretation functions as a function of the number of boundary elements (N), for the evaluation of velocity potential due to a uniform source distribution on a sphere. The slopes of the curves are indicated in the figure.	71
2-6	Normalized maximum (○) and averaged (□) errors in the velocity potential due to a uniform dipole distribution on a sphere obtained by the PFFT-CPM with the use of (a) linear and (b) quadratic interpretation functions for various values of d/h	73
2-7	Comparison of the CPU time of the conventional CPM (-O-) and the PFFT-CPM with linear (-Δ-) and quadratic (-□-) interpretation functions as a function of the number of boundary elements (N), for the evaluation of velocity potential due to a uniform dipole distribution on a sphere. The slopes of the curves are indicated in the figure.	74
2-8	Normalized maximum (○) and averaged (□) errors in the normal velocity on Dirichlet surface as well as maximum (☆) and averaged (▽) errors in the velocity potential on Neumann surface in the solution of the mixed boundary-value problem obtained by the PFFT-CPM with the use of (a) linear and (b) quadratic interpretation functions for various values of d/h	75
2-9	Comparison of the CPU time of the conventional CPM (-O-) and the PFFT-CPM with linear (-Δ-) and quadratic (-□-) interpretation functions as a function of the number of boundary elements (N), for the solution of a mixed boundary-value problem. The slopes of the curves are indicated in the figure.	76
2-10	Sample discretization of a sphere surface based on equal partition in lateral and longitudinal directions, covered by uniform grids.	78

2-11	Normalized maximum (-○-/-☆-) and averaged (-□-/-▽-) errors on (Dirichlet/Neumann) surface of the mixed boundary-value solution obtained by (a) PFFT-CPM and (b) PFFT-QBEM, as a function of the inverse of the characteristic element size $\Delta\ell$. The discretization of the sphere surface used here is based on equal partition in lateral and longitudinal angles.	79
2-12	Sample discretization of a sphere surface based on the radial projection of the discretization of the inscribed cube. The top (red) surface is the Dirichlet boundary and the rest (blue) is the Neumann boundary. . .	80
2-13	Normalized maximum (-○-/-☆-) and averaged (-□-/-▽-) errors on (Dirichlet/Neumann) surface of the mixed boundary-value solution obtained by (a) PFFT-CPM and (b) PFFT-QBEM, as a function of the inverse of the characteristic element size $\Delta\ell$. The discretization of the sphere surface used here is based on the radial projection of the discretization of the inscribed cube.	81
2-14	Discretization of a cube surface with the top (red) surface as the Dirichlet surface and the rest (blue) as the Neumann surface.	82
2-15	Normalized maximum (-○-/-☆-) and averaged (-□-/-▽-) errors on (Dirichlet/Neumann) surface of the mixed boundary-value solution obtained by (a) PFFT-CPM and (b) PFFT-QBEM, as a function of the inverse of the characteristic element size $\Delta\ell$. The boundary-value problem is for the interior problem of a cube.	83
2-16	CPU time used (a) per convolution process, (b) per GMRES iteration step, and (c) for solving a mixed BVP using parallelized PFFT-CPM, as a function of the number of processors. A number is shown above each curve denoting the number of uniform grids used in that group of numerical tests.	85
3-1	Sketch of the fluid domain separated into two parts: near-field and far-field.	101

3-2	The inertial, local and body-fixed coordinate systems	105
3-3	The stability diagram for the time-marching scheme composed of RK2 and 3-point upwind finite difference approach, at $F_r = 0.4$	113
3-4	Comparison of the stability regions of Scheme 1 (combining RK4 with 3-point central finite difference approach) and Scheme 2 (combining RK4 with 3-point upwind finite difference approach), at $F_r = 0.4$	113
3-5	Comparison of the effects of damping zone sizes on the free-decay heaving motion of a floating cylinder. Three damping zone sizes are tested: $L_D = 0.2\lambda_0$ (—); $L_D = 0.6\lambda_0$ (); and $L_D = \lambda_0$ (- · · -).	118
3-6	Time history of the free-decay heaving motion of a floating cylinder. Comparison between different curves reflects the performance of the absorbing-beach treatments with different specified damping strengths: $\nu_0 = 0.2\omega_0$ (—); $\nu_0 = 0.5\omega_0$ (- · · -); $\nu_0 = \omega_0$ (- · · -); $\nu_0 = 2\omega_0$ (- -); $\nu_0 = 3\omega_0$ (- -).	119
3-7	Performances of absorbing-beach treatments using different damping functions (Quadratic Func.(—); Cosine Func.(); and Hermitian Poly(- · · -)), seen from the time history of a floating cylinder's free heave decay motion.	120
3-8	Influences of different wave-damping schemes on the results of a floating cylinder's free heaving decay motions: Scheme 1 (Eq. (3.69))(—); Scheme 2 (Eq. (3.70))(- · · -); Scheme 3 (Eq. (3.71))(- -); and the scheme used by Dommermuth & Yue (1988)(- · · -);	121
3-9	Hydrodynamic force history on a cylinder undergoing described oscil- latory heave motions at different frequencies: (a) $\omega_1 = 0.7\text{rad/s}$ (—); (b) $\omega_2 = 0.44\text{rad/s}$ (); and (c) $\omega_3 = 0.256\text{rad/s}$ (—). Accurate values (- -) of the hydrodynamic force amplitude are also present in all plots for reference.	124
3-10	Comparison of the hydrodynamic force on a periodically heaving sphere with $A/R = 0.375$ among linear(- · · -), body-nonlinear(- · · -), and fully- nonlinear(—) numerical results.	129

3-11 Comparison of hydrodynamic force on a periodically heaving sphere with different motion amplitudes: linear(—), $A/R = 0.125$ (- · -), $A/R = 0.25$ (), and $A/R = 0.375$ (- · · -). Except the linear one, all results are obtained from fully nonlinear numerical simulations.	129
3-12 Variations of the added-mass (in phase with body acceleration) and damping coefficient (out of phase with body acceleration) of a sphere undergoing periodic heave motion with different A/R . Linear (Hulme 1982, (- -)), body nonlinear (\blacktriangle), and fully nonlinear (\blacksquare) results are all presented.	131
3-13 Comparison of the instantaneous wave profiles induced by the periodically heaving sphere at $t/T = 4$ among linear result(—) and fully nonlinear results with $A/R = 0.125$ (- · -), $A/R = 0.25$ (), and $A/R = 0.375$ (- · · -).	132
3-14 Time histories of the up-wave and down-wave runups on a fixed truncated circular cylinder in a Stokes wave train.	133
3-15 Comparison of wave profiles obtained from linear PFFT-CPM (—), linear PFFT-QBEM (- · -), fully-nonlinear PFFT-QBEM (- -), and experiment measures of Stern <i>et al.</i> (1996) (-■-) and Toda <i>et al.</i> (1991) (-●-), for S60 hull with $F_r = 0.316$	134
3-16 Comparison of wave profiles obtained from fully nonlinear numerical simulations and experiment measures of Stern <i>et al.</i> (1996) (-■-) and Toda <i>et al.</i> (1991) (-●-), for S60 hull with $F_r = 0.316$. Three group of numerical results are present, obtained from PFFT-QBEM using three types of discretizations on half of the ship hull: 8×4 (—), 12×6 (- · -), and 15×8 (- -) QBEM elements.	135
3-17 Comparison of time history of S60 wave-making resistance at $F_r = 0.316$ between the numerical simulations (linear PFFT-CPM (—), linear PFFT-QBEM (- · -), fully-nonlinear PFFT-QBEM (- -)) and experimental data (McCarthy, 1985).	136

4-1	sketch of an air cavity induced by vertical water entry of an axisymmetric body.	147
4-2	Time ($t' = tV_0/D$) evolution of an air cavity in water entry of a billiard ball at $F_r = 5.03$ from the experiment(Kominiarczuk, 2007).	161
4-3	Comparisons of the cavity profile between experimental measurement (*), numerical simulation (—), and theoretical prediction (- - -) for (a) $t' = 1$; (b) $t' = 2$; (c) $t' = 3$; (d) $t' = 4$; (e) $t' = 5$; (f) $t' = 6$; (g) $t' = 6.9$	162
4-4	Trajectory of the freely falling sphere ($F_r = 5.03$) as a function of time: experimental measurement (*), numerical simulation (—), and theoretical prediction (- - -).	163
4-5	The radial trajectory of the cavity wall at $z' = 2.48$ as a function of time ($F_r=5.03$): experimental measurement (*), numerical simulation (—), and theoretical prediction (- - -).	163
4-6	Maximum cavity radius as a function of depth ($F_r=5.03$): experimental measurement (*), numerical simulation (—), and theoretical prediction (- - -).	164
4-7	Time variation of (a) the radial trajectory and (b) velocity of cavity wall at depth $z'=1$ (—), 2 (- - -), 3 (· · ·), and 4 (- · · -), obtained by fully-nonlinear simulations ($F_r = 5.03$).	166
4-8	Comparison of the drag coefficient as a function of time between numerical simulation (—) and asymptotic theory (- - -).	167
4-9	Dependence of (a) cavity closure time T , (b) total height of cavity H , and (c) depth of cavity closure H_c on Froude number F_r : experimental data of Kominiarczuk (2007) (\diamond); experimental data of Duclaux, <i>et al.</i> (2007) (sphere diameter $D=12\text{mm}$ (\blacksquare), $D=15.6\text{mm}$ (\square), and $D=24\text{mm}$ (\bullet)), fully-nonlinear simulation (—), and asymptotic solution (- - -).	168
4-10	Comparison of the cavity shapes obtained by fully-nonlinear simulation (—) and asymptotic analysis (- - -) in the water entry of a circular disk with $F_r = 5$ at time $t' =$: (a) 2, (b) 4, (c) 6, (d) 8, and (e) 9.	169

4-11 Comparisons of (a) total cavity height (H) and (b) depth of cavity closure (H_c) among the experimental data of Glasheen & McMahon (1996) (\circ) and Bergamnn <i>et al.</i> (2008) (Δ), the fully-nonlinear simulation result(—), and the theoretical prediction (\cdot) for a disk with constant dropping velocity.	170
4-12 The drag force on a circular disk dropping vertically in water obtained by asymptotic theory with $F_r=2$ (-●-) and 4 (-▲-), fully-nonlinear simulation with $F_r=2$ (—) and 4 (- - -), and experimental data of Glasheen & McMahon (1996) (Δ).	172
4-13 Schematic of the different (axisymmetric) geometries at the point of flow separation. The flow separation angle α used in the nonlinear simulations are (a) $\alpha=0^\circ$ for the disk; (b) $\alpha=90^\circ - \theta/2$ for the inverted truncated cone; and (c) $\alpha=70^\circ$ prescribed for the sphere.	172
4-14 Cavity profiles in water entry of a disk (—), inverted truncated cones (height $L/D=0.5$, $\theta = 90^\circ$ (- - -); height $L/D=2.75$, $\theta = 40^\circ$ (- -); height $L/D=3.73$, $\theta = 30^\circ$ (- · · -)), and a sphere (- · ·) with $F_r=5$ at different time $t' = tV_0/D$. The results are obtained by fully-nonlinear simulations.	173
4-15 Fully-nonlinear simulation results of (a) total cavity length (H) and (b) cavity closure depth (H_c) in water entry of a disk (—), inverted truncated cones (height $L/D=0.5$, $\theta = 90^\circ$ (- - -); height $L/D=2.75$, $\theta = 40^\circ$ (- -); height $L/D=3.73$, $\theta = 30^\circ$ (- · · -)), and a sphere (- · ·).	175
4-16 Dependence of total cavity length (H) and depth of pinch-off (H_c) on cone vertex angle θ for water entry of inverted truncated cones at $F_r = 5$. Plotted are the asymptotic prediction for H (—) and H_c (\cdot), numerical simulation result of H (■) and H_c (●) for the cones and H (▲) and H_c (▼) for the disk.	176
4-17 Comparison of drags on disk (· · ·), inverted cones with $\theta = 90^\circ$ (- · ·) and $\theta = 45^\circ$ (—), and sphere (- - -) during water entries with $F_r=5$	176

5-1	Schematic of vertical water impact of an inverted cone of deadrise angle α with a constant velocity V	190
5-2	Influences of κ values for jet-cutting on (a) free surface profile, and (b) hydrodynamic pressure distribution on the body surface, in water impact of an inverted cone of $\alpha = 45^\circ$ at $Fr = 0.5$ and 0.8	192
5-3	Schematic of vertical water impact of a sphere with a constant velocity V at: (a) very initial stage; and (b) later stage after flow separation from the body is formed.	194
5-4	Evolution of the normalized (a) water surface profile in the intersection region and (b) impact pressure on the wetted body surface in water impact of an inverted cone with $\alpha = 30^\circ$ and $Fr = \infty$. The plotted are the nonlinear simulation results at $t=0.1$ (- · -); 0.5 (- -); and 1.0 (—).	197
5-5	Comparison of the impact pressure distribution on the wetted body surface in water impact of inverted cones with (a) $\alpha = 30^\circ$ and (b) $\alpha = 60^\circ$ at $Fr = \infty$ among the present nonlinear simulation result (—), nonlinear solution of Zhao & Faltinsen (1998)(- -), and modified Wagner solution of Faltinsen & Zhao (1998)(- · -).	199
5-6	Free surface profiles in water impact of an inverted cone with $\alpha = 45^\circ$ for a range of Froude numbers: $Fr = 2$ (—); $Fr = 0.8$ (· -); $Fr = 0.6$ (—); $Fr = 0.5$ (—); and $Fr = 0.45$ (—).	200
5-7	Wetting factor C_w as a function of Fr in water impact of an inverted cone with $\alpha = 45^\circ$: present nonlinear simulation (—); nonlinear solution of Zhao & Faltinsen (1998)(- -); and generalized Wagner solution of Faltinsen & Zhao (1998) (- · -).	201
5-8	Normalized (a) total pressure, (b) hydrodynamic pressure, and (c) hydrostatic pressure on the wetted surface of an inverted cone with $\alpha = 45^\circ$ vertically impacting the water surface at various Froude numbers: $Fr = \infty$ (· -) (only present in figure (b)); $Fr = 2$ (—); $Fr = 0.8$ (· -); $Fr = 0.6$ (—); $Fr = 0.5$ (—); $Fr = 0.45$ (—).	202

5-9	Normalized (a) total force(—), (b) hydrodynamic force(---), and (c) hydrostatic force (—) on the inverted cone with $\alpha = 45^\circ$ as a function of Fr . Also presented are the nonlinear solution of Zhao & Faltinsen (1998) (- -) and the solution based on the generalized Wagner approach by Faltinsen & Zhao (1998) (- · -) with the gravity effect neglected. (The results of Zhao & Faltinsen (1998) and Faltinsen & Zhao (1998) are graphically indistinguishable).	203
5-10	Normalized free surface profiles in the region of the body-water intersection in water impact of an inverted cone with various values of α and Fr : (a) $\alpha = 15^\circ$ at $Fr = 1.0$ (—); $Fr = 0.3$ (---); $Fr = 0.25$ (—); $Fr = 0.21$ (—); (b) $\alpha = 30^\circ$ at $Fr = 1.0$ (—); $Fr = 0.5$ (---); $Fr = 0.38$ (—); $Fr = 0.33$ (—); $Fr = 0.3$ (—); (c) $\alpha = 60^\circ$ at $Fr = 2.0$ (—); $Fr = 1.0$ (---); $Fr = 0.75$ (—); $Fr = 0.6$ (—); $Fr = 0.5$ (—); (d) $\alpha = 75^\circ$ at $Fr = 2.0$ (—); $Fr = 1.0$ (---); $Fr = 0.8$ (—); $Fr = 0.6$ (—).	204
5-11	Wetting factor C_w as a function of Fr in water impact of an inverted cone with $\alpha = 30^\circ$ (—); 45° (- -); 60° (- · -); and 75° (- -).	205
5-12	Normalized (a) total pressure, (b) hydrodynamic pressure, and (c) hydrostatic pressure on the wetted surface of an inverted cone with $\alpha = 15^\circ$ for $Fr = 1.0$ (—); 0.3 (---); 0.25 (—); and 0.21 (—).	206
5-13	Normalized (a) total pressure, (b) hydrodynamic pressure, and (c) hydrostatic pressure on the wetted surface of an inverted cone with $\alpha = 75^\circ$ for $Fr = \infty$ (---)(only present in figure (b)); 2.0 (—); 1.0 (---); 0.8 (—); and 0.6 (—).	207
5-14	Normalized total force(—), hydrodynamic force(---), and hydrostatic force(—) on inverted cones with (a) $\alpha = 15^\circ$; (b) 30° ; (c) 60° ; and (d) 75° as a function of Fr . Also plotted are the nonlinear simulation result of Zhao & Faltinsen(1998) (- -) and the generalized Wagner solution of Faltinsen & Zhao (1998)(- · -) with the gravity effect neglected. . .	208

5-15	Contributions to the total force from the gravity effect as a function of the similarity parameter $F_r/\alpha^{1/2}$ in water impact of an inverted cone with $\alpha = 15^\circ$ (—), 30° (), 45° (—), 60° (—), and 75° (—). Also plotted is the curve given by Eq. (5.14) (-×-).	210
5-16	Normalized total force(—), hydrodynamic force(), and hydrostatic force(—) (based on conventional definitions) on cones with different deadrise angles: (a) $\alpha = 15^\circ$; (b) $\alpha = 30^\circ$; (c) $\alpha = 45^\circ$; (d) $\alpha = 60^\circ$; and (e) $\alpha = 75^\circ$. Reference forces include the fully nonlinear numerical result by Zhao & Faltinsen(1998) (- -) and the generalized Wagner solution by Faltinsen & Zhao (1998)(- · -), with gravity effect neglected.	211
5-17	Slamming coefficient C_s as a function of the body submergence $\tau = VT/R$ in water impact of a sphere. The plotted are the present numerical result at $F_r = \infty$ (—) and experimental data of Shiffman & Spencer (1945)(- · · -), Nisewanger (1961) (- · -), Baldwin <i>et al.</i> (1975) (- -), and Moghisi & Squire (1981)(- -).	213
5-18	Comparisons of slamming coefficient C_s as a function of the body submergence $\tau = VT/R$ in water impact of a sphere between present numerical result(—) and experimental data of Troesch & Kang (1987)(- · -) at (a) $F_r = 2.203$ and (b) $F_r = 3.816$	214
5-19	Distribution of the hydrodynamic pressure coefficient C_p in water impact of a sphere with $F_r = \infty$ at time $\tau = 0.04$ (—), 0.1 (), 0.2 (—), 0.3 (—), 0.4 (—), and 0.5 (-).	215
5-20	Time history of the normalized hydrodynamic force on the body during water impact of a sphere with $Fr = 0.5$ (—), 0.8 (—), 1.0 (), 2.0 (—), 5.0 (—), and ∞ (-).	216
5-21	Time history of the normalized total force on the body during water impact of a sphere with $Fr = 0.5$ (—), 0.8 (—), 1.0 (), 2.0 (—), 5.0 (—), and ∞ (-).	217

5-22	Free surface profiles near the body in water impact of a sphere with $Fr = \infty$ at different time $\tau = 0.03$ (—), 0.15 (), 0.3 (—), and 0.5 (—). Small squares indicate the instantaneous flow separation locations. . .	218
5-23	Comparison of the free surface profiles in water impact of a sphere at different Froude numbers and time: ($Fr = \infty$ (—) at $\tau = 0.3$ and 0.5 , $Fr = 1.0$ (- -) at $\tau = 0.3$ and 0.5 , and $Fr = 0.5$ (- · · -) at $\tau = 0.3$ and 0.5 .)	219
5-24	Time histories of the separation angle θ during water impact of a sphere at $Fr = 0.5$ (- · · -), 0.8 (- -), 1.0 (), 2.0 (—), 5.0 (- · · -), and ∞ (). .	220
5-25	Wetting factor C_w during water impact of a sphere at $Fr = \infty$ as a function of dimensionless body submergence. Results presented include present fully nonlinear numerical solution(—), experimental data by Shiffman & Spencer(1945)(■), empirical formula by Shiffman & Spencer(1945)(), experimental data by Cooper(1950)(—), and asymptotic solution by Miloh (1991) (—).	221
6-1	Definition sketch of a floating truncated floating circular cylinder in a regular wave.	231
6-2	Contour of the growth rates, $\mathbf{Re}[\gamma_i], i = 1, 2, 3, 4$ (ordered from the maximum to the minimum), as a function of $(kA)^2C'$, for the study of the SPAR's instability.	249
6-3	Growth rates of the SPAR's coupled resonant heave/pitch motions, $\mathbf{Re}[\gamma_i], i = 1, 2, 3, 4$, as a function of incident wave steepness $k A $, with $ C' = 0.01 $ and $\theta = 45^\circ$ fixed.	250
6-4	Growth rates of the SPAR's coupled resonant heave/pitch motions, $Re[\gamma_i], i = 1, 2, 3, 4$, as a function of the phase angle $\theta = \arg[(kA)^2C']$, with $ (kA)^2C' = 0.001$	251
6-5	Maximum growth rate of the SPAR's coupled resonant heave/pitch motions, $\max(\mathbf{Re}[\gamma_i])$, as a function of incident wave steepness $k A $ and phase angle θ , with a fixed $ C' = 10 $	252

6-6	Contour of the growth rates, $\mathbf{Re}[\gamma_i], i = 1, 2, 3, 4$ (ordered from the maximum to the minimum), as a function of $(kA)^2C'$, for the study of a cylindrical FPSO's instability.	253
6-7	Contour of the growth rates, $\mathbf{Re}[\gamma]$ (ordered from the maximum to the minimum), as a function of $(kA)^2C'$, with damping ratios set as $\varsigma_3 = 0.08$ and $\varsigma_5 = 0.02$, for the study of a cylindrical FPSO's instability.	254
6-8	Growth rates of the FPSO's coupled resonant heave/pitch motions, $\max(\mathbf{Re}[\gamma_i])$, visualized by the colors, as a function of wave damping ratios ς_3 and ς_5 , with $ (kA)^2C' = 0.001$ and $\theta = 45^\circ$	255
6-9	Resonant heave and pitch motions are coupled through 2nd-order interactions with base flow of frequency ω	256
6-10	Time histories of (a) surge motion, (b) amplitudes of surge-motion harmonics, (c) heave motion, (d) amplitudes of heave-motion harmonics, (e) pitch motion, and (f) amplitudes of pitch-motion harmonics, obtained by fully-nonlinear simulations for the SPAR in a regular wave of wave steepness $k A = 0.02$, wave frequency $\omega = 0.294$ rad/s, and phase angle $\theta' = 0$	260
6-11	Comparison between solutions of linear(—), body nonlinear(- · -), and fully nonlinear(- -) PFFT-QBEM simulations for the time histories of (a) surge motion, (b) heave motion, and (c) pitch motion of the SPAR in waves. In the simulations, the incident wave has a wave steepness of $kA = 0.02$, a frequency of $\omega = 0.294$ rad/s and a phase angle of $\theta' = 0$.	262
6-12	Time histories of (a) the amplitude of resonant heave motion $ A_{3n} $, (b) $\log(A_{3n})$, and (c) the growth rate γ'_3 of resonant heave motion, with the incident wave phase angle $\theta' = 0$, frequency $\omega = 0.294$ rad/s, and wave steepness $k A =$: 0.01(---), 0.02(- · -), and 0.03(- · -).	263
6-13	Time histories of (a) the amplitude of resonant pitch motion $ A_{5n} $, (b) $\log(A_{5n})$, and (c) the growth rate γ'_5 of resonant pitch motion with the incident wave phase angle $\theta' =$, frequency $\omega = 0.294$ rad/s, and wave steepness $k A =$: 0.01(---), 0.02(---), and 0.03(- · -).	265

6-14	Time histories of (a) heave motion, (b) amplitudes of heave-motion harmonics, (c) pitch motion, and (d) amplitudes of pitch-motion harmonics, obtained by the fully-nonlinear simulations for the SPAR in a regular wave of wave steepness $k A = 0.02$, frequency $\omega = 0.288$ rad/s, and phase angle $\theta' = 0$	267
6-15	Time histories of (a) heave motion, (b) amplitudes of heave-motion harmonics, (c) pitch motion, and (d) amplitudes of pitch-motion harmonics, obtained by the fully-nonlinear simulations for the SPAR in a regular wave of wave steepness $k A = 0.02$, frequency $\omega = 0.279$ rad/s, and phase angle $\theta' = 0$	268
6-16	(a)Growth rate γ'_3 of the resonant heave motion amplitude $ A_{3n} $, (b) maximum value of A_{3n} , (c)growth rate γ'_5 of the resonant pitch motion amplitude $ A_{5n} $, (b) maximum value of A_{5n} in SPAR motions as a function of the incident wave period T . The plotted results are obtained using the fully nonlinear numerical simulations with incident wave of amplitude $ A = 2.264$ m and phase angle $\theta' = 0$. The red line in each figure highlights the position where the incident wave frequency perfectly satisfies the instability condition (Eq. (6.52)) obtained from linear stability analysis.	270
6-17	Time histories of (a) surge motion, (b) amplitudes of surge-motion harmonics, (c) heave motion, (d) amplitudes of heave-motion harmonics, (e) pitch motion, and (f) amplitudes of pitch-motion harmonics, obtained by the fully-nonlinear simulations for the cylindrical FPSO in a regular wave of wave steepness $k A = 0.2$, wave frequency $\omega = 0.7$ rad/s, and phase angle $\theta' = 0$	272
6-18	Comparison of the effects of surge motions with different natural surge periods ($T_{1n} = 0s$ (—), $T_{1n} = 50s$ (- · -), and $T_{1n} = 150s$ (- -)) on the time histories of (a) heave motion and (b) pitch motion of the SPAR from fully nonlinear numerical simulations. For this study, the following parameter settings are adopted: $\omega = 0.294$ rad/s, $k A = 0.02$ and $\theta' = 0$.	273

- 6-19 Comparison of the effects of surge motions with different natural surge periods ($T_{1n} = 0s$ (---) and $T_{1n} = 45s$ (- · -)) on the time histories of (a) heave motion and (b) pitch motion of the cylindrical FPSO from fully nonlinear numerical simulations. For this study, the following parameter settings are adopted: $\omega = 0.7$ rad/s, $k|A| = 0.2$ and $\theta' = 0$ 275
- 6-20 Time histories of (a) surge motion, (b) logarithmic value of the resonant surge motion amplitude, (c) heave motion, (d) logarithmic value of the resonant heave motion amplitude, (e) pitch motion, (f) logarithmic value of the resonant pitch motion amplitude, obtained by the fully-nonlinear simulations for the SPAR in a regular wave of wave steepness $k|A| = 0.02$ and wave frequency $\omega = 0.294$ rad/s. Comparisons are made for results of different incident wave phase angles: $\theta' = 0$ (---), $\theta' = \pi/2$ (- · -), and $\theta' = \pi$ (- -). To avoid curve overlapping, only two groups of data are plotted in the figure (a), (c), and (e). 276
- 6-21 Time histories of (a) surge motion, (b) amplitudes of surge-motion harmonics, (c) heave motion, (d) amplitudes of heave-motion harmonics, (e) pitch motion, and (f) amplitudes of pitch-motion harmonics, obtained by the fully-nonlinear simulations for the cylindrical FPSO. In the study, the dominant incident wave has a frequency $\omega_1 = 0.7$ rad/s, a wave steepness $k|A_1| = 0.2$, and a phase angle $\theta'_1 = 0$ and the disturbance wave has a frequency $\omega_2 = 0.444$ rad/s, a wave steepness $k|A_2| = 0.004$, and a phase angle $\theta'_2 = 0$ 278
- 6-22 Comparison between experimental data (ExxonMobil, 1998)(- -) and fully-nonlinear numerical results (—) for the time histories of the (a) heave motion, and (b) pitch motion. The incident wave has a wave period $T = 22s$ and a wave amplitude $|A| = 6.4m$. In numerical simulations, we set the viscous damping coefficients as $\nu_5 = 7\%$ and $\nu_5 = 10\%$. 281

6-23 Time histories of the logarithmic values of the resonant (a) heave motion, and (b) pitch motion, obtained by ExxonMobil’s model tests in 1998 (—) and fully nonlinear numerical simulations with different linear viscous damping coefficients: $\nu_3 = 7\%$ and $\nu_5 = 10\%$ (—); $\nu_3 = 5\%$ and $\nu_5 = 8\%$ ($\cdot \cdot \cdot$); and $\nu_3 = 3\%$ and $\nu_5 = 4\%$ (- $\cdot \cdot$ -). The incident wave has wave period $T = 22\text{s}$ and wave amplitude $A = 6.4\text{m}$ in both experiments and numerical simulations. 282

6-24 Time histories of the logarithmic values of the resonant (a) heave motion, and (b) pitch motion, obtained by ExxonMobil’s model tests in 1998 with $T = 22\text{s}$ (- $\cdot \cdot$ -) and fully nonlinear numerical simulations with $T = 22\text{s}$ (—), $T = 21.8\text{s}$ ($\cdot \cdot \cdot$), and $T = 21.6\text{s}$ (- $\cdot \cdot$ -). The incident wave has a wave amplitude $|A| = 6.4\text{m}$ and we set the viscous damping coefficients as $\nu_3 = 3\%$ and $\nu_5 = 4\%$ in numerical simulations. 283

6-25 Time histories of the logarithmic values of the resonant (a) heave motion, and (b) pitch motion, obtained by ExxonMobil’s model tests in 1998 with $|A| = 6.4\text{m}$ (- $\cdot \cdot$ -) and fully nonlinear numerical simulations with $|A| = 6.4\text{m}$ (—), $|A| = 5.8\text{m}$ ($\cdot \cdot \cdot$), and $|A| = 5\text{m}$ (- $\cdot \cdot$ -). The incident wave has wave period $T = 22\text{s}$ and we set the viscous damping coefficients as $\nu_3 = 3\%$ and $\nu_5 = 4\%$ in numerical simulations. 285

List of Tables

3.1	Stability conditions of sampled explicit time-marching schemes.	111
3.2	Harmonic force coefficients for the periodically heaving sphere, with different A/R	130
3.3	Comparisons of the (normalized) amplitudes of force harmonics $f_m, m = 1, 2, 3$ on a truncated vertical cylinder ($D/R=3$) under the action of a Stokes wave train ($kA = 0.148$).	133
4.1	Effect of the flow separation angle α_0 upon the cavity closure time T and closure depth H_c in water entry of a freely falling sphere (§4.5.1) at two Froude numbers ($F_r=3.0$ and $F_r=5.0$) obtained by fully-nonlinear simulations. The values inside the parentheses are obtained with doubled panel numbers along $\partial S_B + \partial S_F$ and halved time step in the simulation.	160

Chapter 1

Introduction

Nonlinear effects in the interaction of steep surface waves with floating structures are of fundamental interest in naval architecture and ocean engineering. Large relative velocities of wave and body, extreme slamming pressure, and significant free-surface deformations are involved in violent wave-body interactions. The importance of the nonlinear effects has been increasingly recognized for the accurate prediction of hydrodynamic loads and body motions in seakeeping and operational concerns of offshore structures in severe sea conditions (Liu, Xue & Yue 2001; Koo & Kim 2007).

Under operational conditions when the amplitudes of incident waves and body motions are relatively small, linear theory generally gives good predictions for wave-body interactions. Based on the linear wave theory, a floating body's response to a random sea can be approximated by superposing the body's response to each wave component in the wave spectrum (St. Denis & Pierson 1953). The solution of regular incident wave interactions with floating bodies can be found with free surface and body surface boundary conditions linearized at the undisturbed water surface and mean body position, respectively. Depending on the characteristics of incident waves or the feature of body geometries, further approximation might be made and the resulting problems can therefore be solved analytically. For example, a typical ship hull has its beam and draft much smaller than the ship length ($B, D \ll L$). Under the assumption of short waves ($\lambda \ll L$), a strip theory has been derived for the study of wave loads on body as well as ship motions (Ogilvie & Tuck 1969). On the other hand,

if waves are long, that is, $\lambda \sim O(L)$, a slender-body theory can be implemented for the study of ship hydrodynamics (Newman 1964; Newman & Tuck 1964). However, for general wave-body interactions, numerical schemes, including finite difference, finite element, finite volume, and boundary element methods, must be utilized to evaluate the wave loads and body motions. Among all numerical schemes, the potential-flow-based boundary element methods have gained great popularity due to their efficiency, accuracy, and flexibility (King 1987; Newman & Sclavounos 1988; Newman 1992). From the linear theory, wave-induced body motion resonates wave frequency and has the motion amplitude linearly proportional to the incident wave amplitude.

To avoid possible large responses to the incident waves due to linear wave excitations, offshore marine structures are often designed to have their natural motion frequencies much higher or lower than the dominant ocean wave frequencies. To study the motions of these marine structures in waves, second-order nonlinearity might be a primary concern. Second-order interactions among irregular waves result in new wave components of sum- and difference-frequencies which, if close to the natural frequencies of floating bodies, could excite resonant body motions. Typical examples include the slow-drift motions of moored ships and vertical motions of small-waterplane-area vessels due to difference-frequency excitations, and the high-frequency oscillations of tension-leg-platforms in vertical direction due to sum-frequency forces. Complete second-order analyses have been conducted in many applications, with free surface and body surface boundary conditions satisfied up to the second order in the wave steepness (Ogilvie 1983; Kim & Yue 1989, 1990). Theoretical solutions have been found for special wave-body interaction problems involving vertical circular cylinders (Emmerhoff & Sclavounos 1992; Chau & Taylor 1992, Newman 1996). For the solution of general second-order steady/unsteady seakeeping problems, numerical methods are more practical choices.

There are other existing studies taking into account partial nonlinearity in the wave-body interactions. For practical problems involving large-amplitude body motions but relatively small incident and diffraction waves (e.g. a slender body like naval ships moving forward in mild waves), body nonlinearities are considered to be

more important than free surface nonlinearities. A body-exact numerical method can be implemented with body boundary condition satisfied on the exact (instantaneous) wetted body surface while free surface condition linearized at the undisturbed water surface (Lin & Yue 1990; Faltinsen & Chezhian 2005). This method is adopted in the commercial code LAMP for computations of large-amplitude motions of ships. To move one step further, a weak-scatter theory relaxes the body-exact method's restriction on the incident wave steepness by linearizing the free surface boundary condition on the incident wave profile while satisfying the body boundary condition on the exact body surface. Thus, the weak-scatter theory allows large-amplitude body motions and incident waves, but it still has limitations on the nonlinearity of disturbance flow. Numerical methods based on this theory has been implemented for the study of large ship responses in head or following seas (Pawlowski 1992; Huang 1997). Although the body-exact method and weak-scatter theory outperform the classical linear theory in many aspects if large-amplitude body motions and/or incident waves are involved, inconsistent approximations of nonlinearity are made in these theories and physical quantities like wave run-ups or local hydrodynamic loads cannot be accurately captured.

Fully nonlinear effects are important for wave-body interactions of extreme conditions when severe sea states and large-amplitude body motions are present. Typical examples of highly nonlinear wave-body interactions include water impacts and wave slammings, green water on deck and wave overtopping, violent wave sloshing, and large amplitude ship motions and capsizing. For these problems, fully nonlinear numerical simulations have to be implemented to capture all levels of nonlinearity involved in wave interactions with floating bodies. Within the context of potential flow theorem, the mixed-Eulerian-Lagrangian (MEL) approach combined with a certain boundary element method (BEM) is favored for the study of fully nonlinear two-dimensional (Vinje & Brevig 1981; Grosenbaugh & Yeung 1989) or three-dimensional wave-body interactions of simple body geometries (Dommermuth & Yue 1987; Liu, Xue & Yue 2001). In this scheme, the BEM is used to solve the boundary integral equation for the boundary value problem at each time step and the MEL approach

is used for updating the nonlinear free surface forward in time.

Despite these advances, three-dimensional fully nonlinear numerical results for general wave-body interactions are still very limited. This is due to two primary factors: the extreme computational cost and the complexity in modeling the multi-scale nonlinearities involved. Although boundary-discretization methods (e.g. BEM) are much more efficient than domain-discretization methods (e.g. finite-volume method), the solution of a boundary value problem of N unknowns at each time step demands at least $O(N^2)$ computational effort using a conventional BEM. This greatly limits the practical applications of BEMs on large structures and long-time simulations. At the same time, complex nonlinear physics is associated with the couplings of wave-body interactions and body motions of different modes. Local wave run-ups or water jets of small length scale and global flow features of large length scale co-exist in the system. Computations are challenging in dealing with the unsteadiness, nonlinearity, multiple length/time scales, and flow-body interactions.

In view of above difficulties faced by fully nonlinear three-dimensional studies for general wave-body interactions, this thesis focuses on the development of an efficient and robust numerical scheme for fully nonlinear wave-wave and wave-body interactions and the investigations of nonlinear effects in several highly nonlinear wave-body interaction problems through theoretical analyses and numerical simulations.

Efficiency and accuracy are the two main concerns in the development of an effective numerical scheme for the solution of nonlinear initial boundary value problems. The efficiency of the numerical scheme decides whether the scheme is applicable of practical applications on wave-body interactions of large length scale and long time evolutions. Accuracy, on the other hand, determines the numerical scheme's robustness in dealing with fully nonlinear wave-body interactions of smoothly/non-smoothly connected boundaries. The efficiency and accuracy of a numerical scheme are correlated but not fully dependent on each other. In this thesis, a highly efficient and robust numerical scheme, PFFT-QBEM, is developed for the simulation of nonlinear wave-wave and wave-body interactions in the context of potential flow. PFFT-QBEM allows for reliable computations of nonlinear hydrodynamics useful in ship design

and marine applications, which are forbidden with the traditional methods on the presently available computing platforms.

Before directly applying PFFT-QBEM for large-scale/long-time nonlinear interactions of a floating body with waves, we first investigate a canonical highly nonlinear wave-body interaction problem: vertical water entry of an axisymmetric body. This problem might not demand extensive computations but gives rise to a sequence of complex events. On this subject, research work of this thesis focuses on the following two areas: (i) prediction of impact loads on the body and nonlinear free-surface deformation at the initial stage of water entry; and (ii) understanding of the formation and evolution of the air cavity behind the falling body after the initial impact. Study on initial water impacts is of fundamental significance to the reliable prediction of the hydrodynamic loads in ship slamming and surface wave impact on marine structures under severe sea conditions. Study on the later stage of water entries lays the foundation for understanding more general water entry problems involving complex geometries, such as dropping of military projectile into water and moderately-sized animals running on water surface.

The next nonlinear wave-body interaction problem investigated in this thesis is the coupled resonant motions of a floating body in waves. Understanding of fundamental mechanisms and basic characteristics of resonant responses and instabilities of a floating body in surface waves is of critical importance for the design and operation of such structures. Past experiments (Liu 1999; Haslum & Faltinsen 1999) indicated that a deep draft caisson vessels (DDCV or spars) experiences large-amplitude heave and pitch resonant motions when the incident wave frequency is much larger than the natural heave and pitch frequencies. Such resonant motions cannot be predicted by classical theories without considering nonlinear effects. This nonlinear mechanism has received little attention so far due to the complex nonlinear wave-body dynamics involved. Here we investigate the effect of nonlinear wave-wave and wave-body interactions on dynamic instability of such marine structures.

More specifically, the major work conducted in this thesis includes:

(I) Development of an efficient and robust IBVP solver, PFFT-QBEM

A highly efficient high-order boundary element method is developed for the numerical simulation of nonlinear wave-wave and wave-body interactions. The method is based on the framework of the quadratic boundary element method (QBEM) for the boundary integral equation, given the fact that QBEM is an accurate and robust method to deal with nonlinear wave-wave and wave-body interactions (Xue *et al.* 2001; Liu, Xue & Yue 2001). The pre-corrected fast Fourier transform (PFFT) algorithm is used to accelerate the evaluation of far-field influences of source and/or normal dipole distributions on boundary elements involved in QBEM. The resulting PFFT-QBEM scheme as an efficient boundary value problem (BVP) solver reduces the computational effort of solving the associated boundary-value problem of N unknowns from $O(N^{2\sim 3})$ with the traditional QBEM or any other boundary element methods to $O(N \ln N)$. The characteristics of accuracy and efficiency of the PFFT-QBEM for various boundary-value problems are studied and compared to those of the (low-order) constant panel method (CPM).

Combined with the mixed-Eulerian-Lagrangian (MEL) approach for nonlinear free surface tracking, PFFT-QBEM is further developed into a highly efficient IBVP solver. For the solution of an IBVP involving incident waves, the numerical scheme for solving the disturbance velocity potential outperforms that for solving the total velocity potential, in terms of both efficiency and robustness. Detailed formulations and numerical issues in the development and implementation of the PFFT-QBEM are presented for the study of fully nonlinear wave-body interaction problems. To validate the newly developed PFFT-QBEM and to illustrate its usefulness, we apply PFFT-QBEM to study three typical nonlinear wave-body interactions: the wave radiation by a periodically heaving sphere, the wave diffraction by a fixed truncated vertical cylinder, and the wave generation and resistance of a forward moving ship hull. The prediction of the hydrodynamic loads on body and the wave profiles are compared to existing experimental measurements or/and theoretical/numerical results with satisfactory agreements.

(II) Study on cavity dynamics in water entries

The dynamics of the air cavity created by vertical water entry of a three-dimensional body is investigated theoretically and computationally. The study is focused in the range of relatively low Froude number, $F_r \equiv V(gD)^{-1/2} \leq O(10)$ (where V is the dropping velocity of the body, D its characteristic dimension, and g the gravitational acceleration), when the inertia and gravity effects are comparable.

To understand the dynamics involved in the formation and evolution of cavity, we develop a matched asymptotic theory based on the slender-body theory in the context of potential flow. Direct comparisons with existing experimental data show that the asymptotic theory properly captures the key physical effects involved in the formation and development of the cavity, and in particular gives a reasonable prediction of the maximum size of the cavity and the time of cavity closure. Due to the inherent assumption in the asymptotic theory, it is incapable of accurately predicting the flow details near the free surface and the body, where nonlinear free surface and body boundary effects are important. To complement the asymptotic theory, a fully-nonlinear numerical study using an axisymmetric boundary integral equation is performed. The numerical and asymptotic predictions for the dependencies of the cavity height and closure time on Froude number and body geometry are in excellent agreement with available experiments.

(III) Nonlinear computations of initial water impacts

A fully-nonlinear numerical simulation is employed to investigate water impact of axisymmetric bodies that strike vertically the horizontal free surface from the air. The main objective is to understand the gravity effect on flow/wave kinematics and dynamics and to quantify the range of validity of existing theories and computations that are based on the infinite-Froude number assumption.

Two body geometries are considered: inverted cone and sphere. For the inverted cone, we obtain detailed dependencies of free-surface profile and impact pressure and load on the body on the generalized Froude number ($F_r \equiv (V/gt)^{1/2}$ where V is the impact velocity, g the gravitational acceleration, and t time) and deadrise angle α .

Based on these, we develop an approximate formula for evaluating the contribution of the gravity effect to the total impact force on the body in terms of a similarity parameter $F_r/\alpha^{1/2}$. For the sphere, we develop and apply a pressure-based criterion to follow the evolution of flow separation on the body and to obtain an appropriate description of the free surface profile near the body and accurate evaluation of the impact pressure and load on the body during the entire impact process. The numerical result of impact force on the body agrees well with existing experimental measurements. We confirm that the gravity effect is unimportant in initial impact of the sphere. Significantly, we find that in later stage of impact, flow separation remains at an almost fixed position at an angle $\theta \approx 62.5^\circ$ to the bottom of the sphere for a wide range of Froude numbers, $F_r \equiv V/(gR)^{1/2} \gtrsim 1$, where R is the radius of the sphere.

(IV) Investigation of coupled resonant heave-pitch motions of a floating structure in waves

We first perform linear stability analyses for the motions of floating structures in waves. From the analyses, we identify the incident wave frequency at which wave energy can be transferred to body motions through nonlinear wave-body interactions so that natural heave and pitch motions may grow exponentially with time. The condition for the occurrence of instability and the key characteristic features of unstable natural heave and pitch motions, predicted by the analyses, agree well with experimental measurement.

To quantitatively study the development of unstable body motions, we perform direct numerical simulations for the whole nonlinear wave-body interaction process. As large-amplitude body motions take a long time period to develop, numerical simulation of this physical problem requires a highly efficient and robust numerical scheme. PFFT-QBEM, together with stable time integration method and proper treatment for far-field wave-energy absorption, is applied to systematically investigate the physical mechanism of the instability for two types of floating platforms: a deep-draft caisson vessel (DDCV) and a cylindrical shallow-draft floating production storage and offloading (FPSO) structure. We evaluate the dependence of unstable body motions on all

related physical parameters including incident wave parameters, frequency detuning, body geometry, body surge motions, and damping in the system. Direct comparisons are made between the numerical results and the experimental data (Liu 1999) for the time histories of unstable heave and pitch motions of a DDCV in waves and very good agreement is achieved.

The resonance mechanism identified from the stability analyses and numerical simulations is general and can be applied to the study of other types of floating bodies, such as semi-submersible platforms, TLP, small platforms in shallow water, and ships with forward speed.

This thesis consists of seven chapters in total. The development of the efficient and robust PFFT-accelerated QBEM is described in chapter 2. Dependency of PFFT-QBEM performance on numerical parameters are studied in detail and comparison between PFFT-QBEM and PFFT-CPM is made in solving general boundary value problems. Chapter 3 focuses on the formulations of initial boundary value problems as well as numerical issues involved in the development and implementation of PFFT-QBEM for fully-nonlinear wave-body interaction problems. Studies on the dynamics of air cavity in water entries are presented in chapter 4. A complete asymptotic theory is developed based on slender-body assumption and a fully nonlinear axisymmetric numerical scheme is also carried out, for the development and evolution of air cavities. Chapter 5 focuses on the dynamics and kinematics involved in the initial water impacts. Fully nonlinear numerical results for cone impacts and sphere impacts are analyzed for the understanding of the gravity effect in water impacts. The coupled resonant heave-pitch motions of floating structures in waves are investigated through stability analyses and fully nonlinear numerical simulations in chapter 6. Effects of all related physical parameters on unstable body motions are studied systematically. In chapter 7, we summarize the contributions of this thesis and suggest future studies. Separate introductions and references are provided for each chapter.

References

- Chau, F.P. & Taylor, R.E., Second-order wave diffraction by a vertical cylinder, *Journal of Fluid Mechanics*, vol. 240, pp. 571-599, 1992;
- Dommermuth, D. G. & Dick K. P. Yue, Numerical simulations of nonlinear axisymmetric flows with a free surface, *J. Fluid Mech.*, 1987, vol. 178, pp. 195-219;
- Emmerhoff, O.J. & Scлавounos, The slow-drift motion of arrays of vertical cylinder, *Journal of Fluid Mechanics*, Vol. 242, pp. 31-50, 1992;
- Faltinsen, O.M. & Chezhian, M., A generalized Wagner method for three-dimensional slamming, *Journal of Ship Research*, Vol. 49(4), pp. 279-287, 2005;
- Grosenbaugh, M.A. & Yeung, R.W., Nonlinear free-surface flow at two-dimensional bow, *Journal of Fluid Mechanics*, Vol. 209, pp. 57-75, 1989;
- Huang, Y., Nonlinear ship motions by a Rankine panel method, Ph.D thesis, Massachusetts Institute of Technology, 1997;
- Haslum, H. A., & Faltinsen, O. M., Alternative Shape of Spar Platforms for Use in Hostile Areas, *Offsh. Techn. Conf.*, Houston, Texas, USA, 1999;
- Kim, M.H. & Yue, D. K. P., The complete second-order diffraction solution for an axisymmetric body, Part 1. Monochromatic incident waves, *J. Fluid Mech.*, Vol. 200, pp. 235-264, 1989;
- Kim, M.H. & Yue, D. K. P., The complete second-order diffraction solution for an axisymmetric body, Part 2. Bichromatic incident waves and body motions, *J. Fluid Mech.*, Vol. 211, pp. 557-593, 1990;
- Koo, W.C. & Kim, M.H., Fully nonlinear wave-body interactions with surface-piercing bodies, *Ocean Engineering*, Vol. 34, pp.1000-1012, 2007;
- King, B.W., Time domain analysis of wave exciting forces on ships and bodies, Technical Report 306, The Department of Naval Architecture and Marine Engineering, The University of Michigan, 1987;

Lin, W.M. & Yue, D.K.P., Numerical solutions for large-amplitude ship motions in time domain, Proceedings of the 18th Symposium on Naval Hydrodynamics, Ann Arbor, Michigan, 1990;

Liu, Y.-M., Sub-harmonic instability of heave-pitch response of a floating DDCV platform in waves, Report to ExxonMobil, 1999 (private communication);

Liu, Y.-M., Xue, M., & Dick K. P. Yue, Computations of fully nonlinear three-dimensional wave-wave and wave-body interactions. Part 2. Nonlinear waves and forces on a body, Journal of Fluid Mechanics, Vol. 438, pp. 41-66, 2001;

Newman, J.N., A slender-body theory for ship oscillations in waves, J. Fluid Mech., Vol. 18, pp. 602-618, 1964;

Newman, J.N., & Tuck, E.O., Current progress in the slender-body theory of ship motions, Proc. 5th Symp. Naval Hydro., pp. 129-167, 1964;

Newman, J. N. & Sclavounos, P. D., The computation of wave loads on large offshore structures, 5th International Conference on the behavior of Offshore Structures (BOSS88), Trondheim, Norway, 1988;

Newman, J. N., Panel methods in marine hydrodynamics, Keynote Lecture, Eleventh Australasian Fluid Mechanics Conference, Hobart, Australia, 1992;

Newman, J.N., The second-order wave force on a vertical cylinder, Journal of Fluid Mechanics, Vol. 320, pp. 417-443, 1996;

Ogilvie, T.F. & Tuck, E.O., A rational strip theory for ship motions, Part 1, Technical Report 013, The Department of Naval Architecture and Marine Engineering, The University of Michigan, 1969;

Ogilvie, T. F., Second-order hydrodynamic effects on ocean platforms, International Workshop on Ship and Platform Motions, University of California, Berkeley, Oct. 1983;

Pawlowski, J., A nonlinear theory of ship motions in waves, Proceedings of the 19th

Symposium on Naval Hydrodynamics, Seoul, Korea, 1992;

St. Denis, M. & Pierson, W.J., On the motions of ships in confused seas, Transactions of the Society of Naval Architects and Marine Engineers, Vol. 61, pp. 280-357, 1953;

Vinje, T. & Brevig, P., Nonlinear two-dimensional ship motion, Proceedings of the 3rd International Conference on Numerical Ship Hydrodynamics, Paris, France, 1981;

Xue, M., Xu, H., Liu, Y. & Yue, D.K.P., Computations of fully nonlinear three-dimensional wave-wave and wave-body interactions. Part 1: Three-dimensional steep waves, J. Fluid Mech. Vol.438, pp. 11-39, 2001.

Chapter 2

Development of Pre-corrected FFT-accelerated Quadratic Boundary Element Method

2.1 Introduction

A great deal of success in the computational study of nonlinear ocean wave dynamics and marine object/structure hydrodynamics has been achieved by the use of the boundary element method (BEM) (e.g. Mei *et al.* 2005, Part 2). In BEM, the boundary-value problem for the velocity potential is reformulated as a boundary integral equation with the introduction of a Green function, from which the unknown velocity potential and/or normal velocity of the fluid on the boundary are solved for. After discretization of the boundary into piecewise elements and approximation of the variables on the boundary elements, a system of linear algebraic equations are resulted from the integral equation: $[A]\{X\} = [C]\{Y\}$, where $[A]$ and $[C]$ are the $N \times N$ dense influence coefficient matrices, $\{X\}$ ($\{Y\}$) the vector of N unknown (known) potentials and/or normal velocities on the boundary, and N the total number of unknowns. The main computation effort in BEM consists of constructing $[A]$ and $[C]$ with $O(N^2)$ operations and solving the system of equations with $O(N^2)$

($O(N^3)$) operations by the use of iterative solvers (direct Gauss elimination) (e.g. Xue *et al.* 2001).

Though BEM is computationally more efficient than the volume discretization methods, its use in practical applications is still limited due to its requisite (at least) $O(N^2)$ effort. In ship design evaluation or ship hull optimization, for example, $O(10^6)$ sea-keeping or wave resistance computations are generally involved. A total of $O(10^{6\sim 7})$ CPU hours on Cray XT3 (or XT4) are needed (with $O(1)$ CPU hour for each computation using $N = O(10^3)$) for all these computations. In the simulation of realistic ocean wave-field evolution, $N = O(10^{6\sim 10})$ is typically needed (e.g. Wu 2004) and it is estimated that $O(10^{4\sim 12})$ CPU hours on Cray XT3 is required at only one time step. Useful solutions of general marine hydrodynamic problems cannot be obtained by the conventional BEMs with the presently available computing facilities. More efficient computational algorithms must be developed.

Since $O(N^2)$ effort is needed in the formation of $[A]$ and $[C]$, any algorithm that is more efficient than $O(N^2)$ in solving the boundary integral equation must not explicitly construct these influence coefficient matrices. In the area of cosmology for the ‘N-body simulations’, a number of efficient algorithms have been developed to compute the product of a dense matrix and a vector without construction of the dense matrix. The commonly used algorithms include the tree method, particle-mesh method (PM), particle-particle-particle-mesh (P³M) method, and fast multipole method (FMM)(e.g. Hockney & Eastwood 1988; Bagla 2005). Among these, FMM and P³M methods have also been applied to speed up BEMs in which they are often referred as the fast multipole-expansion (FME) algorithm (e.g. Nabors & White 1991; Korsmeyer *et al.* 1993) and the pre-corrected fast Fourier transform (PFFT) algorithm (e.g. Phillips & White 1997), respectively.

FME employs multipole expansions while PFFT applies the fast Fourier transform for the evaluation of the far-field influence of a source/dipole distribution on the boundary which is the major computational effort in solving the boundary integral equation. For both FME and PFFT, the near-field influence is evaluated by direct computations. As a result, FME needs $O(N)$ effort while PFFT requires $O(N \ln N)$

effort in solving the boundary integral equation. Although FME seems more efficient than PFFT, numerical tests show that PFFT is superior to FME in terms of both execution time and memory use (Phillips & White 1997). Besides, the implementation of FME is more complicated than PFFT, particularly for nonlinear wave-body interaction problems. In view of efficiency and robustness requirement for practical applications, the PFFT algorithm has been more commonly employed to accelerate the computation of BEMs.

The PFFT-accelerated BEMs have been applied with some successes in the design of very large scale integration circuits and in the modeling of complex microelectromechanical system (MEMS) devices (Phillips & White 1997). Most of these applications are associated with Neumann-type boundary-value problems. There are very limited applications of PFFT-accelerated BEMs in the study of surface wave interactions with large floating structures, for which the general mixed Neumann-Dirichlet boundary-value problem is dealt with (Korsmeyer *et al.* 1999; Kring *et al.* 2000). In all the existing PFFT-accelerated BEMs, the PFFT algorithm is integrated with the constant panel method (CPM) because of its simplicity in implementation. Despite its success in many applications, owing to the fundamental shortcomings inherent in the low-order approximations of CPM, the use of the PFFT-accelerated CPM (hereafter referred as PFFT-CPM) is however quite limited particularly for the nonlinear wave-body interaction problems.

To overcome the deficiencies of the traditional CPM, high-order BEMs are developed (e.g. Grilli, Skourup & Svendsen 1989; Xu 1992). Among these, the quadratic boundary element method (QBEM) has been shown to be effective and robust in the study of breaking wave dynamics (e.g. Xue *et al.* 2001) and steep wave interactions with floating bodies with and without forward speed (e.g. Liu, Xue & Yue 2001). Compared to CPM, QBEM generally obtains quadratic to cubic convergence with element size even in the presence of surface intersections with discontinuous boundary slopes. Significantly, for a given accuracy, QBEM is approximately two orders of magnitude more efficient than CPM for general applications (Xue *et al.* 2001). Despite these, the use of QBEM is still limited to relatively small problems and is

impractical for design analysis and evaluation of ships and offshore structures and prediction of large-scale ocean wave-field evolutions. The main objective of this study is thus to integrate the PFFT algorithm with the QBEM to develop an efficient and robust PFFT-accelerated QBEM (hereafter referred as PFFT-QBEM) for the general (nonlinear) wave-wave and wave-body interactions problems.

In this chapter, we describe the detailed formulation in applying the PFFT algorithm to accelerate QBEM for solving the general boundary integral equation. For completeness and comparisons, the integration of the PFFT algorithm with CPM is also presented. The key numerical issues in the implementation of PFFT-CPM and PFFT-QBEM are discussed in detail. We systematically investigate the dependencies of the accuracy of the PFFT algorithm on key numerical parameters. The characteristics of accuracy and efficiency of PFFT-CPM and PFFT-QBEM in solving various boundary-value problems are studied and compared. At the end, we demonstrate that the efficiency of the PFFT-BEMs can be further improved with a properly designed parallelization algorithm on supercomputers or a cluster of workstations.

This chapter is organized as follows. In §2.2, the boundary integral equation for a general wave-body interaction problem and the formulation of the traditional CPM and QBEM are briefly described. The detailed formulation of the PFFT algorithm to accelerate CPM and QBEM for various integral equations are presented in §2.3. The numerical issues including the determination of interpolation functions and pre-conditioners are discussed in §2.4. In §2.5, we present the characteristics of accuracy of the PFFT algorithm and the comparisons of performance of PFFT-CPM and PFFT-QBEM for various boundary-value problems. The performance of a parallelized PFFT-BEM algorithm is also tested. We conclude in §2.6.

2.2 Formulation of the Classical Boundary Element Method

2.2.1 Boundary Integral Equation (BIE)

In solving the (nonlinear) wave-wave and wave-body interaction problems in the time domain, a main challenge is to seek for the boundary-value solution (at each time step) efficiently and accurately. In the context of potential flow formulation, the boundary-value problem (BVP) typically consists of the Laplace equation for the velocity potential $\phi(\vec{x}, t)$ in the fluid domain \mathcal{V} , a specified $\phi(\vec{x}, t)$ on the free surface S_F , and a specified normal velocity of the fluid $\phi_n(\vec{x}, t)$ on the impervious boundary S_B (such as body surface or bottom topography). The key objective in solving the BVP is to determine the unknown normal velocity $\phi_n(\vec{x}, t)$ on S_F and the unknown potential $\phi(\vec{x}, t)$ on S_B .

In the BVP, application of the Green's second identity leads to the following equation for the evaluation of $\phi(\vec{x})$ in \mathcal{V} (e.g. Xue *et al.* 2001):

$$\beta(\vec{x})\phi(\vec{x}) - \iint_S \phi_n(\vec{\xi})G(\vec{x}; \vec{\xi})dS(\vec{\xi}) + \iint_S \phi(\vec{\xi})G_{n(\vec{\xi})}(\vec{x}; \vec{\xi})dS(\vec{\xi}) = 0 \quad (2.1)$$

where $G(\vec{x}; \vec{\xi}) \equiv 1/|\vec{x} - \vec{\xi}|$ is the Rankin source Green function, S the boundary of \mathcal{V} ($S = S_F + S_B$), and $\beta(\vec{x})$ the interior solid angle. The two integrals in (2.1) can be interpreted as the influences of a source distribution of strength ϕ_n and a normal dipole distribution of strength ϕ on S , respectively. It is clear from (2.1) that ϕ inside \mathcal{V} is completely determined provided ϕ_n and ϕ on S are known.

Letting \vec{x} in (2.1) approach to S , we obtain an integral equation for unknown ϕ_n on S_F and unknown ϕ on S_B . In general, this integral equation needs to be solved numerically. To do that, we subdivide S_F and S_B into two sets of small boundary elements:

$$S_F = \sum_{j=1}^{N_F} FE_j, \quad S_B = \sum_{j=1}^{N_B} BE_j \quad (2.2)$$

where FE (N_F) and BE (N_B) represent the boundary element (total number of

elements) on S_F and S_B , respectively. The discretized integral equation can be written in the form:

$$\beta(\vec{x})\phi(\vec{x}) - \sum_{j=1}^{N_F} IF_s(\vec{x}) + \sum_{j=1}^{N_B} IB_d(\vec{x}) = - \sum_{j=1}^{N_F} IF_d(\vec{x}) + \sum_{j=1}^{N_B} IB_s(\vec{x}), \quad \vec{x} \in S_F, S_B \quad (2.3)$$

where the elemental integrals IF_s , IF_d , IB_s and IB_d are defined as

$$IF_s(\vec{x}), IB_s(\vec{x}) = \iint_{FE_j, BE_j} \phi_n(\vec{\xi}) G(\vec{x}, \vec{\xi}) dS(\vec{\xi}) \quad (2.4)$$

and

$$IF_d(\vec{x}), IB_d(\vec{x}) = \iint_{FE_j, BE_j} \phi(\vec{\xi}) G_{n(\vec{\xi})}(\vec{x}, \vec{\xi}) dS(\vec{\xi}). \quad (2.5)$$

One notes that in (2.5), the Cauchy principal part of the singular integral is assumed. For the evaluation of the integrals in (2.4) and (2.5), approximations are usually introduced on the geometry of the boundary elements (FE , BE) as well as the physical quantities on FE and BE . Depending on the scheme and order of the approximations, a variety of boundary element methods have been developed. For completeness, we here describe two representative ones: constant panel method and quadratic boundary element method.

2.2.2 Constant Panel Method (CPM)

CPM employs a piecewise linear approximation for the geometry of the boundary elements, piecewise constant approximations for the physical quantities on each boundary element, and point collocations at panel centroids. Specifically, FE_j (BE_j) is approximated by a quadrilateral element FE_j^c (BE_j^c), and ϕ and ϕ_n over each element are approximated by their values at the centroid of the element:

$$\phi(\vec{x}, t) = \phi_j(\vec{x}_0, t), \quad \phi_n(\vec{x}, t) = \phi_{nj}(\vec{x}_0, t) \quad (2.6)$$

for $\vec{x} \in FE_j^c (BE_j^c)$, where \vec{x}_0 represents the centroid of $FE_j^c (BE_j^c)$. Correspondingly, (2.4) and (2.5) become

$$IF_s(\vec{x}), IB_s(\vec{x}) = \phi_{nj} \iint_{FE_j^c, BE_j^c} G(\vec{x}, \vec{\xi}) dS(\vec{\xi}) \quad (2.7)$$

and

$$IF_d(\vec{x}), IB_d(\vec{x}) = \phi_j \iint_{FE_j^c, BE_j^c} G_{n(\vec{\xi})}(\vec{x}, \vec{\xi}) dS(\vec{\xi}) \quad (2.8)$$

in which the integrals can be evaluated analytically. In CPM, the number of collocation points (or unknowns) N is identical to the total number of boundary elements ($N_e = N_F + N_B$).

CPM is the most commonly used BIE solver because of its simplicity in implementation. However, CPM possesses several fundamental shortcomings which limit its applications to the (nonlinear) wave-wave and wave-body interactions problems. First of all, a relatively large number of panels are required to achieve accurate representations of the geometry and physical quantities because of the low (nearly linear) convergence rate of CPM. Secondly, CPM does not converge for those BVPs with non-smoothly connected boundaries due to numerical discontinuous approximations along the intersection lines. Thirdly, the spatial derivatives of the velocity potential such as velocity and acceleration cannot be evaluated accurately and robustly, especially near the intersections, edges, and corners of S_F and S_B .

2.2.3 Quadratic Boundary Element Method (QBEM)

QBEM is capable of circumventing the shortcomings of CPM and is relatively effective and economical in dealing with various BVPs (e.g. Xu 1992). QBEM assumes each boundary element to be curvilinear quadrilateral where nine collocation points are located. A bi-quadratic isoparametric interpolation is used to represent the geometry and all variables on each element. In doing that, each nine-node element $FE_j^q(\vec{x})$ (or $BE_j^q(\vec{x})$) is mapped into a square $FE_j^q(s \in [-1, 1], t \in [-1, 1])$ (or $BE_j^q(s, t)$) in a parametric space, as shown in 2-1.

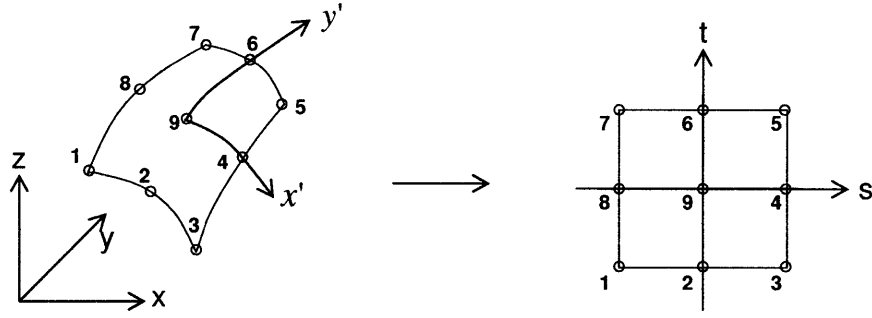


Figure 2-1: A generic nine-node curvilinear element $FE_j^q(x, y, z)$ and its image in parametric space $FE_j^q(s, t) : s \in [-1, 1], t \in [-1, 1]$.

Let Ψ signify a variable from the set of variables (x, y, z, ϕ, ϕ_n) . The value of Ψ at any location of an element is defined in terms of the nine nodal values and Lagrangian interpolation functions

$$\Psi(s, t) = \sum_{m=1}^9 L_m(s, t) \Psi_m \quad (2.9)$$

where Ψ_m being the m -th nodal value of Ψ . The interpolation functions take the form:

$$\begin{cases} L_m(s, t) = \frac{1}{4} s(s + s_m) t(t + t_m), & m = 1, 3, 5, 7 \\ L_m(s, t) = \frac{1}{2} (1 - t_m^2 s^2 - s_m^2 t^2) [t_m t(1 + t_m t) + s_m s(1 + s_m s)], & m = 2, 4, 6, 8 \\ L_9(s, t) = (1 - s^2)(1 - t^2), & m = 9 \end{cases} \quad (2.10)$$

where s_m and t_m represent the coordinates of the m -th node in the parametric space. By the use of (2.9), (2.4) and (2.5) become

$$IF_s(\vec{x}), IB_s(\vec{x}) = \sum_{m=1}^9 (\phi_n)_{jm} \iint_{FE_j^q, BE_j^q} L_m(s, t) G(\vec{x}; s, t) J(s, t) ds dt \quad (2.11)$$

and

$$IF_d(\vec{x}), IB_d(\vec{x}) = \sum_{m=1}^9 \phi_{jm} \iint_{FE_j^q, BE_j^q} L_m(s, t) G_{n(s,t)}(\vec{x}; s, t) J(s, t) ds dt \quad (2.12)$$

where $J(s, t)$ is the Jacobian associated with the transformation of curvilinear element

to its image in parametric space.

In QBEM, the total number of collocation points (i.e. nodal points) N generally differs from the total number of quadratic boundary elements ($N_e = N_F + N_B$). The exact relation between N and N_e depends on the specific configuration and discretization of S_F and S_B . Compared to CPM, QBEM generally obtains quadratic to cubic convergence with element size $\Delta\ell$ in the presence of surface intersections with discontinuous boundary slopes. Significantly, for a given accuracy, QBEM is approximately two orders of magnitude more efficient than CPM for general applications (Xue *et al.* 2001).

2.2.4 System Equations

The imposition of (2.3) at N collocation (or nodal) points on S_F and S_B leads to a system of N linear equations in both CPM and QBEM:

$$[A]\{X\} = \{B\} \quad (2.13)$$

where $[A]$ is a $N \times N$ dense and non-symmetric matrix of influence coefficients, $\{X\}$ the vector of N unknowns (including ϕ_n on S_F and ϕ on S_B at N collocation points), and $\{B\} \equiv [C]\{Y\}$ with $[C]$ (like $[A]$) being a $N \times N$ influence coefficient matrix and $\{Y\}$ the known vector of N specified ϕ on S_F and ϕ_n on S_B . In general, (2.13) can be solved by a direct or iterative approach. The direct method requires $O(N^3)$ computational effort while an iterative solver such as the generalized minimum residual (GMRES) method normally requires $O(N^2)$ effort. Including the construction of the influence coefficient matrices $[A]$ and $[C]$ which needs $O(N^2)$ effort, the conventional BEMs require a minimum of $O(N^2)$ effort in solving the integral equation (2.3). With the present computational capabilities, the $O(N^2)$ effort requirement limits the application of the CPM and QBEM to the (nonlinear) wave-body interaction problems in which a huge number of unknowns and long-time simulations are normally involved. A more efficient boundary-value problem solver is thus called for.

2.3 PFFT-accelerated BEMs

Precorrected-FFT (PFFT) algorithm is an efficient scheme for the evaluation of $[A]\{X\}$ and $[C]\{Y\}$ in (2.13) with an effort of $O(N \ln N)$ without an explicit construction of matrices $[A]$ and $[C]$. This scheme is developed based on the special property of the Rankine source Green function, $G(\vec{x}; \vec{\xi}) = G(\vec{x} - \vec{\xi})$, which enables an efficient evaluation of integrals in (2.1) (for given ϕ and ϕ_n) by taking advantage of the convolution formula. Incorporating the PFFT algorithm into an iterative system-equation solver and combining with the boundary element approximations, we develop efficient PFFT-accelerated BEMs which reduce the requisite computational effort from $O(N^2 \sim N^3)$ to $O(N \ln N)$ in solving the integral equation (2.3).

In this section, we first consider a canonical problem of source distribution to illustrate the PFFT algorithm for efficient evaluation of the first (source) integral in (2.1). The dipole distribution is then considered for efficient evaluation of the second (normal dipole) integral in (2.1) using PFFT. The integration of these two processes into an iterative system-equation solver (e.g. GMRES) forms efficient PFFT-accelerated BEMs for solving various boundary-value problems in wave-wave and wave-body interactions applications.

2.3.1 Source distribution

Given a source distribution on a boundary S , the resulting velocity potential at any point \vec{x} is given by

$$\phi(\vec{x}) = \iint_S \sigma(\vec{\xi}) G(\vec{x}; \vec{\xi}) dS(\vec{\xi}) = \sum_{j=1}^{N_e} \iint_{E_j} \sigma(\vec{\xi}) G(\vec{x}; \vec{\xi}) dS(\vec{\xi}) \equiv \sum_{j=1}^{N_e} I_{sj}(\vec{x}) \quad (2.14)$$

where σ represents the strength of the source distribution, E_j the j -th boundary element, and I_{sj} the velocity potential due to the source on the j -th element. The evaluation of $\phi(\vec{x})$ at N collocation points on S by the PFFT algorithm contains five main steps of operations (Phillips & White 1997): (i) grid definition, (ii) projection; (iii) convolution, (iv) interpolation, and (v) near-field correction.

In the step of *grid definition*, we define N_g ($= N_x \times N_y \times N_z$) grids in a three-dimensional domain covering entire S with N_x , N_y , and N_z uniform grids in the x -, y -, and z -directions, respectively. In general, the grid size (h) can be much larger than the characteristic length of boundary elements ($\Delta\ell$). (Note that the grid size does not necessarily need to be identical in the three directions. Without loss of generality, h is considered to be constant here). A sample array of $8 \times 8 \times 8$ uniform grids which cover a sphere is shown in figure 2-10, where the surface of the sphere is represented by 72 QBEM quadrilateral panels. For description, the cube formed by p^3 ($p=2$ or larger) neighboring grids is hereafter referred as a cell.

In the step of *projection*, the continuous source distribution on the element E_j is projected to point sources at the p^3 vertices of the cell which contains E_j . The projection is based on the requirement that $\phi(\vec{x})$ from the net influence of the point sources at cell vertices is identical to that of the original source distribution. To do that, we represent the Rankine Green function $G(\vec{x}; \vec{\xi})$ (i.e. potential at \vec{x} due to a point source at $\vec{\xi}$) by the net influence of point sources at the vertices of the cell surrounding the point source at $\vec{\xi}$:

$$G(\vec{x}; \vec{\xi}) = \sum_{i=1}^{p^3} H_i(\vec{\xi}) G(\vec{x}; \vec{\xi}_i) \quad (2.15)$$

where $H_i(\vec{\xi})$ is the spatial interpolation function for the i -th vertex of the cube and $\vec{\xi}_i$ the coordinates of the i -th vertex of the cube. With (2.15), we have

$$I_{sj}(\vec{x}) \equiv \iint_{E_j} G(\vec{x}; \vec{\xi}) \sigma(\vec{\xi}) dS(\vec{\xi}) = \sum_{i=1}^{p^3} q_{ji}^n G(\vec{x}; \vec{\xi}_i) \quad (2.16)$$

where

$$q_{ji}^n = \iint_{E_j} \sigma(\vec{\xi}) H_i(\vec{\xi}) dS(\vec{\xi}) . \quad (2.17)$$

Equation (2.17) is used to determine the strength of the projected point source, q_{ji}^n , at i -th vertex of the cell associated with the source distribution on the j -th element. Here the superscript n denotes the global ordering of the grids.

For CPM, based on (2.6), (2.17) becomes

$$q_{ji}^n = \sigma_j \iint_{E_j^c} H_i(\vec{\xi}) dS(\vec{\xi}). \quad (2.18)$$

For QBEM, based on (2.9), (2.17) becomes

$$q_{ji}^n = \sum_{m=1}^9 (\sigma)_{jm} \iint_{E_j^q(s,t)} H_i(s,t) L_m(s,t) J(s,t) ds dt. \quad (2.19)$$

The total strength of the point source at the n -th grid (in global ordering) is given by the sum of the projections of all boundary elements:

$$q_n = \sum_{j=1}^{N_e} q_{ji}^n \quad (2.20)$$

for $n=0, 1, \dots, N_g - 1$.

In the step of *convolution*, we evaluate the velocity potentials at N_g uniform grids due to point sources at these grids:

$$\phi(\vec{x}_\ell) \equiv \phi_\ell = \sum_{n=0}^{N_g-1} q_n G_{\ell-n}, \quad \ell = 0, 1, \dots, N_g - 1 \quad (2.21)$$

where $G_{\ell-n} = G(\vec{x}_\ell; \vec{x}_n) = 1/|\vec{x}_\ell - \vec{x}_n|$. Notice that the summation in (2.21) is in a convolution form and may be evaluated efficiently using the fast Fourier transform (FFT). However, FFT cannot be directly applied to (2.21) since G_0 is singular and the total number of G terms differs from that of q . To overcome these difficulties, we define a supplemental function Φ by:

$$\Phi_\ell = \sum_{n=-N_g+1}^{N_g-1} q'_n G'_{\ell-n}, \quad \ell = -N_g + 1, \dots, 0, 1, \dots, N_g - 1 \quad (2.22)$$

where q' and G' are periodic with the same period $(2N_g - 1)$ and defined as:

$$G'_{\ell-n} = \begin{cases} 0, & \ell = n \\ G_{\ell-n}, & -N_g + 1 \leq \ell - n \leq N_g - 1 \text{ and } \ell \neq n \end{cases}$$

$$q'_n = \begin{cases} 0, & -N_g + 1 \leq j < 0 \\ q_n, & 0 \leq j \leq N_g - 1 \end{cases}$$

Equation (2.22) is in the convolution form of two discrete periodic functions. FFT can be directly applied to evaluate Φ for given q' and G' . With the self influence excluded from ϕ in (2.21), we have $\phi_\ell = \Phi_\ell$, $\ell = 0, 1, \dots, N_g - 1$. Note that the self influences of point sources will be added to the solution in the step of *near-field correction*.

In the step of *interpolation*, we evaluate $\phi(\vec{x})$ at the collocation points on S by the use of interpolation based on the grid values of ϕ obtained in the step of convolution. With the interpolation function H_i , as in (2.15), we have

$$\phi(\vec{\xi}) = \sum_{i=1}^{p^3} H_i(\vec{\xi}) \phi(\vec{\xi}_i) \quad (2.23)$$

where $\vec{\xi}_i, i = 1, \dots, p^3$ is the i -th vertex of the cube surrounding the collocation point $\vec{\xi}$.

From (2.15), it is clear that the accuracy of the representation of $G(\vec{x}; \vec{\xi})$ in terms of $G(\vec{x}; \vec{\xi}_i)$, $i = 1, \dots, p^3$, deteriorates when $|\vec{x} - \vec{\xi}|/h = O(1)$ or smaller. Thus the near-field influence of the source distribution in $\phi(\vec{x})$ evaluated by FFT based on (2.16) needs to be corrected. This is the objective of the *near-field correction* step. To do that, we subtract the near-field contribution included in the convolution step and add the exact near-field contribution which can be evaluated using the direct computation, i.e.

$$\phi(\vec{x}) = \phi_F(\vec{x}) + \Delta\phi(\vec{x}) \quad (2.24)$$

where $\Delta\phi(\vec{x}) \equiv \phi_N(\vec{x}) - \phi_{FN}(\vec{x})$ represents the correction, $\phi_F(\vec{x})$ and $\phi_{FN}(\vec{x})$ respectively the total and near-field influences obtained from (2.23) based on the results

in the convolution step, and $\phi_N(\vec{x})$ the exact influence of near-field elements. For a specified criterion, the near-field elements of any collocation point on S can be easily identified. $\phi_{FN}(\vec{x})$ can be determined by following the same procedures in the steps of projection, convolution, and interpolation with the focus on the near-field boundary element influence only. In this case, the influence of point sources on near-field grid points should be evaluated directly (but not by FFT). $\phi_N(\vec{x})$ is obtained by directly evaluating the boundary element integrals in (2.14).

In summary, the evaluation of the potentials at N collocation points due to a given source distribution on S by the PFFT algorithm involves computational accounts of $O(N_g)$, $O(p^3N)$, $O(N_g \ln N_g)$, $O(N)$, and $O(p^3N)$ in the steps of grid definition, projection, convolution, interpolation, and near-field correction, respectively. Normally, N_g can be chosen in the same order as N . The total requisite computational effort with the PFFT algorithm is thus $O(N \ln N)$ (for $N \gg 1$) in contrast to $O(N^{2-3})$ required by the conventional BEMs.

2.3.2 Dipole distribution

With minor manipulations, the above procedure can be applied to efficiently compute the influence of a normal dipole distribution. For illustration, we consider a normal dipole distribution of strength $\gamma(\vec{\xi})$ on a surface S . The velocity potential at \vec{x} from the influence of this dipole distribution is:

$$\phi(\vec{x}) = \iint_S \gamma(\vec{\xi}) G_{n(\vec{\xi})}(\vec{x}; \vec{\xi}) dS(\vec{\xi}) = I_\xi(\vec{x}) + I_\eta(\vec{x}) + I_\zeta(\vec{x}) \quad (2.25)$$

where

$$I_\xi(\vec{x}) = \iint_S n_\xi(\vec{\xi}) \gamma(\vec{\xi}) G_\xi(\vec{x}, \vec{\xi}) dS(\vec{\xi}) \quad (2.26)$$

$$I_\eta(\vec{x}) = \iint_S n_\eta(\vec{\xi}) \gamma(\vec{\xi}) G_\eta(\vec{x}, \vec{\xi}) dS(\vec{\xi}) \quad (2.27)$$

$$I_\zeta(\vec{x}) = \iint_S n_\zeta(\vec{\xi}) \gamma(\vec{\xi}) G_\zeta(\vec{x}, \vec{\xi}) dS(\vec{\xi}) \quad (2.28)$$

where (n_ξ, n_η, n_ζ) are the three components of the unit normal on $S(\vec{\xi})$. Similarly to $G(\vec{x}, \vec{\xi})$, we have $G_\xi(\vec{x}, \vec{\xi}) = G_\xi(\vec{x} - \vec{\xi})$, $G_\eta(\vec{x}, \vec{\xi}) = G_\eta(\vec{x} - \vec{\xi})$, and $G_\zeta(\vec{x}, \vec{\xi}) = G_\zeta(\vec{x} - \vec{\xi})$. As a result, I_ξ (I_η , I_ζ) can be computed using the PFFT algorithm described in the above with G and σ replaced by G_ξ (G_η , G_ζ) and $n_\xi\gamma$ ($n_\eta\gamma$, $n_\zeta\gamma$), respectively. Clearly, the computational effort for the normal dipole distribution is three times of that for the source distribution for the same numbers of collocation points, boundary elements, and uniform background grids.

2.3.3 Mixed boundary-value problem

Our purpose is to develop a highly efficient method for solving the boundary integral equation (2.3) by combining the PFFT algorithm with the BEMs. Specifically, we solve (2.3) for unknown ϕ on S_B and unknown ϕ_n on S_F for given ϕ_n on S_B and ϕ on S_F . As in the traditional BEMs, an iterative method such as the generalized minimum residual (GMRES) (e.g. Xu 1992) is typically employed to solve (2.3). At each iteration, the main effort is to evaluate the integrals in (2.3) with an updated ϕ on S_B and ϕ_n on S_F . The PFFT algorithm described in the above (for source distribution and dipole distribution problems) provides a unique capability of efficiently evaluating these integrals for any specified ϕ_n (i.e. source) on S_F and ϕ (i.e. normal dipole) on S_B with a requisite $O(N \ln N)$ effort in contrast to $O(N^2)$ effort with the traditional BEMs. By incorporating the PFFT algorithm with the GMRES, we obtain efficient PFFT-accelerated BEMs for solving the integral equation (2.3) of the general BVPs associated with wave-wave and wave-body interactions applications.

2.4 Numerical implementation

In this section, we address a number of numerical issues associated with the implementation of PFFT-CPM and PFFT-QBEM.

2.4.1 Interpolation function $H(\xi)$

The spatial interpolation function $H_i(\vec{\xi})$, $i = 1, 2, \dots, p^3$, is used in both projection and interpolation steps (cf. (2.15), (2.23)). The way to construct H is not unique. A direct approach is to conduct Talor series expansions separately for the left and right hand sides of (2.15) and then match the corresponding coefficients of the expansions. But the process for this approach is tedious. Phillips & White (1997) determined the interpolation function H by setting $\vec{x} = \vec{x}_k^t$, $k = 1, \dots, N_c$ with \vec{x}^t as the test points which distance themselves from the given cell center by a radius r_c . In their scheme, the accuracy of H depends on the choice of test point number N_c and distance r_c between test points and the cell center.

We here describe a generalized but simple way which can essentially obtain the similar H to that based on the Talor series expansion approach. For illustration, we take the Green function G as a sample function and consider a cell with 2^3 vertices, inside which G is regular. Assume that G inside this cell can be represented in terms of a complete set of linear functions in $\vec{\xi}$:

$$G(\vec{x}; \vec{\xi}) = \sum_{k=1}^{m=4} c_k(\vec{x}) f_k(\vec{\xi}) \equiv \{f\}^T(\vec{\xi}) \{c\}(\vec{x}) \quad (2.29)$$

where $f_k(\vec{\xi}) = 1, \xi, \eta, \zeta$ for $k=1, 2, 3, 4$, respectively, $\{f\}^T \equiv \{f_1, f_2, \dots, f_m\}$, and $\{c\} \equiv \{c_1, c_2, \dots, c_m\}^T$. To determine the unknown coefficient vector $\{c\}$, we apply (2.29) at the vertices of the cell $\vec{\xi}_i$, $i = 1, 2, \dots, 8$, to obtain:

$$\{G\}(\vec{x}) \equiv \begin{bmatrix} G_1(\vec{x}, \vec{\xi}_1) \\ G_2(\vec{x}, \vec{\xi}_2) \\ \vdots \\ G_8(\vec{x}, \vec{\xi}_8) \end{bmatrix} = \begin{bmatrix} f_1(\vec{\xi}_1) & f_2(\vec{\xi}_1) & \cdots & f_m(\vec{\xi}_1) \\ f_1(\vec{\xi}_2) & f_2(\vec{\xi}_2) & \cdots & f_m(\vec{\xi}_2) \\ \vdots & \vdots & \ddots & \vdots \\ f_1(\vec{\xi}_8) & f_2(\vec{\xi}_8) & \cdots & f_m(\vec{\xi}_8) \end{bmatrix} \cdot \begin{bmatrix} c_1(\vec{x}) \\ c_2(\vec{x}) \\ \vdots \\ c_m(\vec{x}) \end{bmatrix} \equiv [F] \{c\}(\vec{x}). \quad (2.30)$$

For a given \vec{x} , $\{G\}$ and $[F]$ are known. We thus solve for $\{c\}$ from (2.30) to get:

$$\{c\}(\vec{x}) = [F]^{-1} \{G\}(\vec{x}). \quad (2.31)$$

Substituting (2.31) into (2.29), we obtain $G(\vec{x}, \vec{\xi})$ inside the cell represented in terms of its values at the vertices of the cell:

$$G(\vec{x}; \vec{\xi}) = \{f\}^T(\vec{\xi})[F]^{-1}\{G\}(\vec{x}) . \quad (2.32)$$

Comparing (2.32) with (2.15), we obtain the linear interpolation function:

$$\{H\}(\vec{\xi}) = \{f\}^T(\vec{\xi})[F]^{-1} \quad (2.33)$$

where $\{H\} = \{H_1, H_2, \dots, H_8\}^T$ for a cell of 8 vertices. Note that in (2.30), for $m=4$, the system of equations is over-determined, and $[F]^{-1}$ can be obtained by using the singular value decomposition method.

Inside a cell with 2^3 vertices, instead of using (2.29), we can also approximate the Green function in an alternative form, :

$$G(\vec{x}; \vec{\xi}) = \sum_{k=1}^{m=8} c_k(\vec{x}) f_k(\vec{\xi}) \quad (2.34)$$

where $f_k(\vec{\xi}) = 1, \xi, \eta, \zeta, \xi\eta, \eta\zeta, \xi\zeta, \xi\eta\zeta$ for $k = 1, 2, \dots, 8$, respectively. This form of interpolation has complete linear terms and only partial quadratic/cubic terms. Following the same procedure in (2.30)-(2.33), we obtain another form of the interpolation function $\{H\}$. The result is equivalent to that used in finite-element methods (Huebner *et al.* 2001).

$$H_i(\vec{\xi}) = \frac{1}{8}(1 + \xi\xi_i)(1 + \eta\eta_i)(1 + \zeta\zeta_i) , \quad i = 1, 2, \dots, 8 \quad (2.35)$$

where (ξ_i, η_i, ζ_i) are the coordinates of the cell vertices in a natural coordinate system (as shown in figure 5.18(b) in Huebner *et al.* 2001). Note that in (2.34), any quadratic term in $f_k(\vec{\xi})$ cannot be ξ^2 or η^2 or ζ^2 . Otherwise, the symmetry property of the vertex coordinates makes matrix $[F]$ singular. In addition, although more terms are included in (2.34) than in (2.29), (2.34) does not necessarily give more accurate result for projection and interpolation since the maximum errors from the interpolations in

(2.34) and (2.29) are in the same quadratic order.

If the cell consists of 3^3 vertices, we can obtain a interpolation function $\{H\}$ which contains complete quadratic terms but only partial cubic terms. One way to derive $\{H\}$ based on a 27-vertex cell is to write G in the following form:

$$G(\vec{x}; \vec{\xi}) = \sum_{k=1}^{m=17} c(\vec{x}) f_k(\vec{\xi}) \quad (2.36)$$

where $f_k(\vec{\xi}) = 1, \xi, \eta, \zeta, \xi^2, \eta^2, \zeta^2, \xi\eta, \eta\zeta, \xi\zeta, \xi\eta\zeta, \xi^2\eta, \xi\zeta^2, \xi^2\zeta, \eta\zeta^2, \eta^2\zeta$ for $k = 1, 2, \dots, 17$, respectively. The quadratic interpolation function can then be determined by following a similar procedure described in the above for deriving the linear interpolation function.

In the following, if without special specification, linear and quadratic interpolation functions are referred to the ones derived based on (2.29) and (2.36), respectively.

2.4.2 Direct approach for dipole distribution

For the calculation of the velocity potential due to a normal dipole distribution using the PFFT algorithm, in addition to the indirect approach described in §3.2, there is a direct approach in which the influence of the normal dipole distribution can be approximated by that of point sources at the vertices of cells (e.g. Zhu 2004). For illustration, we take a normal dipole distribution on a boundary element E_j as an example. In this approach, the velocity potential at a (far-field) position \vec{x} from this dipole distribution is approximately represented by the sum of influences of point sources at the vertices of the cell enclosing the boundary element:

$$I_{d_j}(\vec{x}) \equiv \iint_{E_j} G_{n(\vec{\xi})}(\vec{x}; \vec{\xi}) \gamma(\vec{\xi}) dS(\vec{\xi}) = \sum_{i=1}^{p^3} \bar{q}_{ji}^n G(\vec{x}; \vec{\xi}_i) \quad (2.37)$$

where γ is the strength of the normal dipole distribution, and \bar{q}_{ji}^n represents the (projected) point source strength at the i -th vertex of the cell. The challenge here is to properly determine \bar{q}_{ji}^n , $i = 1, 2, \dots, p^3$ such that (2.37) holds. To do that, we take

a normal derivative of the Green function in (2.29):

$$G_{n(\vec{\xi})}(\vec{x}; \vec{\xi}) = \frac{\partial\{f\}^T(\vec{\xi})}{\partial n(\vec{\xi})} \cdot \{c\}(\vec{x}) \quad (2.38)$$

Substituting $\bar{c}(\vec{x})$ obtained from (2.31) into equation (2.38), we obtain

$$G_{n(\vec{\xi})}(\vec{x}; \vec{\xi}) = \frac{\partial\{f\}^T(\vec{\xi})}{\partial n(\vec{\xi})} \cdot [F]^{-1} \cdot \{G\}(\vec{x}) \quad (2.39)$$

By substituting G_n in (2.39) into (2.37), we obtain the projected point source strengths associated with the dipole distribution on E_j :

$$\bar{q}_{ji}^n = \iint_{E_j} \gamma(\vec{\xi}) \bar{H}_i(\vec{\xi}) dS(\vec{\xi}) \quad (2.40)$$

where the interpolation function vector $\{\bar{H}\}(\vec{\xi})$ is given by

$$\{\bar{H}\}(\vec{\xi}) = \frac{\partial\{f\}^T(\vec{\xi})}{\partial n(\vec{\xi})} \cdot [F]^{-1} . \quad (2.41)$$

In (2.41), $\partial\{f\}^T/\partial n \equiv \bar{n}(\vec{\xi}) \cdot \nabla_{\vec{\xi}}\{f\}^T$ is clearly one order lower in $\vec{\xi}$ than $\{f\}(\vec{\xi})$ in (2.33). Therefore, the error in projection with the use of the interpolation function $\{\bar{H}\}(\vec{\xi})$ in (2.41) is an order larger than that with the use of $\{H\}(\vec{\xi})$ in (2.29) or (2.34). In figure 2-2, as an example, we compare the errors in the representation of the velocity potential of a point dipole associated with the indirect and direct approaches. For figure 2-2a, the dipole is located at an arbitrarily chosen position ($\xi = -0.01h$, $\eta = 0.39h$, and $\zeta = 0.26h$) and the cube (of 2^3 vertices and side length h) enclosing the dipole has its center at the origin. The results in figure 2-2a indicate that the relative error in the velocity potential at the field point \vec{x} computed with the use of the linear interpolation function $H(\vec{\xi})$ decays quadratically as the distance R of the field point from the dipole increases, while that with the use of the associated $\bar{H}(\vec{\xi})$ decays only linearly with R . Figure 2-2b shows a similar comparison but with the dipole located at the center of the cube. Interestingly, due to error cancellation associated with symmetry, the relative error from the use of $H(\vec{\xi})$ ($\bar{H}(\vec{\xi})$) decays with

R two (one) orders faster than that when the dipole is not at the center of the cube. For this special dipole location, the decay rate of the error with the use of $\bar{H}(\vec{\xi})$ is two orders slower than that with the use of $H(\vec{\xi})$.

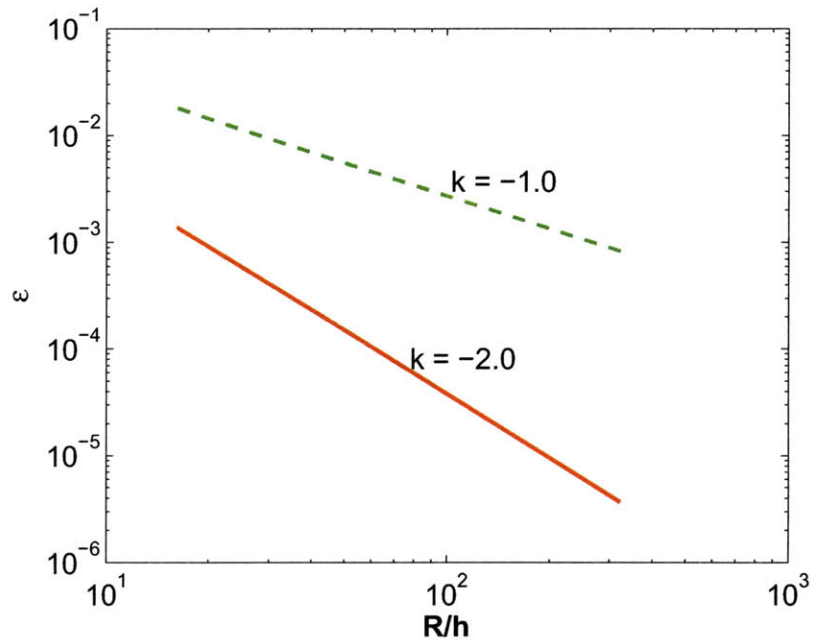
Compared to the indirect approach, at the first glance, the direct approach seems to require only 1/3 of the computational effort associated with the indirect approach. However, to compensate the lower decay rate of the projection error (associated with the use of $\bar{H}(\xi)$), the direct approach requires a near-field domain (in which the solution needs to be corrected) whose size is one order larger than that required by the indirect approach. The resulting total effort (in both memory and CPU time) with the direct approach is in fact much larger than the indirect approach for a prescribed accuracy of the solution.

2.4.3 Treatment of a boundary element not fully covered by a cell

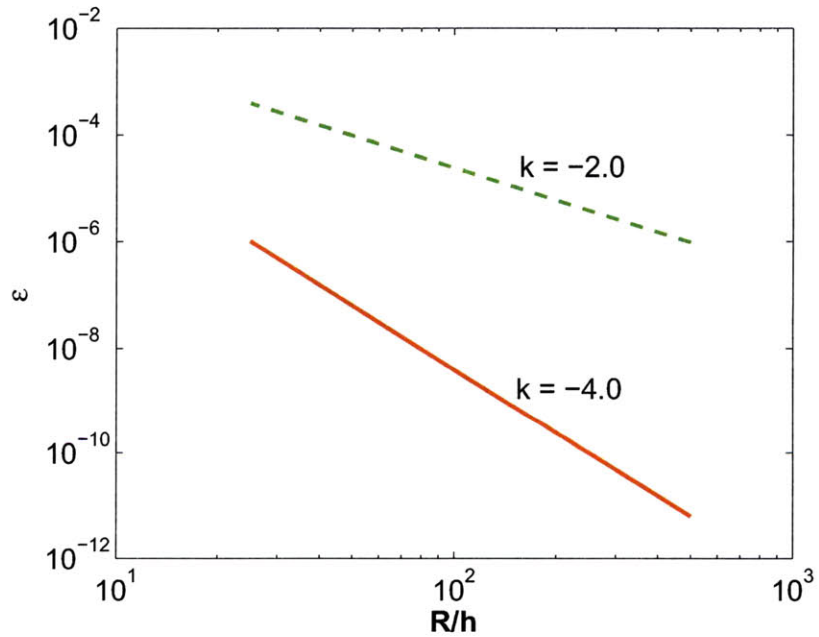
For CPM, the collocation point is located at the center of each element. Thus, any element that crosses cells is projected to the vertices of the cell in which the collocation point of the element resides. For QBEM, the nodes of a quadratic boundary element that crosses the cells can locate in different cells. In this case, two types of treatments can be applied. One is to treat the boundary element as the basis of the projection, i.e. the whole element is projected to the cell in which the 9-th node (i.e. central node) of the element is resides. The other is to assign the cell for each collocation point based on its own location and project source/dipole strength at this collocation point to the vertices of the associated cell based on (2.19). Our numerical tests indicate that the two treatments lead to similar error features. The choice of the treatment depends on the convenience in implementation.

2.4.4 Nearby elements/points

The process of finding the nearby elements/points is commonly referred to as nearest neighboring particle searching (NNPS). A linked-list algorithm is used here (for de-



(a)



(b)

Figure 2-2: Comparisons of the projection errors in the velocity potential of a point dipole as a function of the distance of the field point from the dipole. The plotted are the results obtained with the use of interpolation functions H (—) and \bar{H} (- -) for the point dipole at (a) an arbitrarily-chosen non-central location $(-0.01h, 0.39h, 0.26h)$ and (b) the center the cell. The slope of the curve k is indicated.

tails, see Hockney & Eastwood (1998) in the discussion of short-range forces in particle simulation methods). The implementation of the linked-list algorithm is especially convenient for the PFFT scheme, since it requires mesh overlaid on the problem domain and all the collocation points assigned to cells, which is inherent in the PFFT scheme. Assume the mesh size is h and define a nearby region $d/h = \kappa$. For a chosen collocation point, its neighboring boundary elements/points can only be in the same grid cell or the immediately connecting cells. If the average number of collocation points inside each cell is small, the complexity of the linked-list algorithm is of order $O(N)$.

2.4.5 Solid-angle evaluation

Direct evaluation of the solid angle β in (2.1) is not straightforward in general, since it involves the integration of r^{-2} type of singularity. In CPM, boundary elements are approximated as quadrilateral flat panels and collocation points are located at centers of the panels, and thus the solid angle $\beta(\vec{x}) = 2\pi$ for all collocation points on the boundary. In QBEM, the collocation points are on curved panels or even on the intersection of these panels which are not smoothly connected. In this case, the evaluation of β is nontrivial.

One way to effectively compute β is based on the use of the following formula in QBEM:

$$\beta(\vec{x}) = - \iint_S G_{n(\vec{\xi})}(\vec{x}; \vec{\xi}) dS(\vec{\xi}) \quad (2.42)$$

where the Cauchy principal-value integral is implied. This formula follows by setting ϕ as a constant in (2.1). The PFFT algorithm is applied to evaluate the integral in (2.42). Note that for specified boundary elements of S , β needs to be evaluated only once in solving the integral equation (2.3).

2.4.6 Determination of preconditioners

In addition to efficient evaluation of matrix-vector products, the requisite computational effort in solving the integral equation is also largely affected by the convergence

rate of the iteration method used. A proper choice of a preconditioner can significantly accelerate the convergence of the iteration, and thus reduces the computational cost. Since the PFFT algorithm computes the product of influence coefficient matrix $[A]$ and vector $\{X\}$ without an explicit construction of $[A]$, it is a challenge to properly determine an effective preconditioner for PFFT-BEMs.

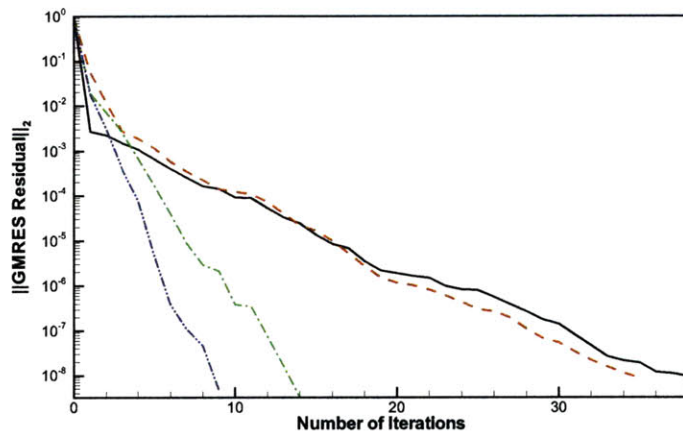
The effectiveness of a preconditioner is normally influenced by the conditioning of coefficient matrix $[A]$. For example, the preconditioner given by $diag([A])$ works quite effectively for the Neumann problem, but not so for the Dirichlet problem for which $[A]$ is not diagonally dominant. It is in general demanding to design a robust preconditioner that is effective for both Neumann and Dirichlet problems. In the present study, we choose to implement the so-called mesh-neighbor-based (MN) preconditioner which allows flexible choices to ensure its effectiveness for various problems (e.g. Vavasis 1992; Chen 1998). Moreover, the MN preconditioner involves information only between neighboring nodes, which is available in the evaluation of $[A]\{X\}$ with the PFFT algorithm, and thus does not require extra computations. This type of preconditioners has been demonstrated to be effective in solving the first kind of the boundary integral equation with the multipole-accelerated iterative method (Nabors 1994).

In figure 2-3, we show the convergence of the L_2 norm of the normalized GMRES residual as a function of iteration numbers with the use of various MN preconditioners for three types of boundary-value problems: the Dirichlet problem, the Neumann problem, and the mixed Dirichlet-Neumann problem. As an example, the BVP considered here represents a simple uniform flow with the velocity potential given by $\phi = Ux + Vy + Wz$ with $U = V = W = 1$. For numerical illustration, the boundary is chosen to be a spherical surface which is approximated by 9600 quadrilateral panels. For the Dirichlet (Neumann) problem, ϕ (ϕ_n) is specified on the whole surface and we solve for ϕ_n (ϕ) on the surface. For the mixed problem, ϕ (ϕ_n) is specified on a portion (the rest) of the surface and we solve for the associated ϕ_n (ϕ) on the surface. For all the solutions shown, zero value is used as the initial guess of the solution. Three different MN preconditioners are used: (i) the diagonal-type preconditioner

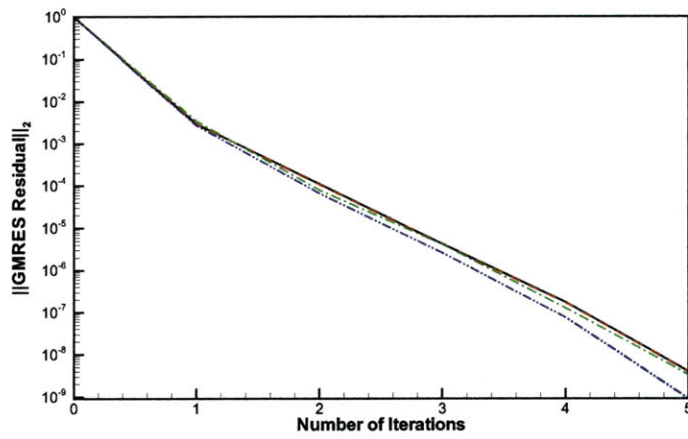
for which only the own element (with no neighboring mesh) is considered; (ii) the MN preconditioner including all neighboring meshes within $d/h=1.5$; and (iii) the MN preconditioner including all neighboring meshes within $d/h=3$, where d is nearby region size. For comparison, the result without the use of any preconditioner is also shown.

Clearly, for the Neumann problem, as shown in figure 2-3b, the residual (L_2 norm) decreases rapidly to $O(10^{-8})$ after 5 iterations even without the use of preconditioner. This indicates that the use of preconditioner is practically unnecessary for the Neumann problem as the associated coefficient matrix $[A]$ is diagonally dominant and well conditioned. For the Dirichlet problem shown in figure 2-3a, on the other hand, the convergence rate of iteration depends on the number of neighboring meshes included in the preconditioner. Specifically, faster convergence obtains with more neighboring meshes included in the preconditioner. In particular, the diagonal-type preconditioner is seen to be completely ineffective. The use of more neighboring meshes in the construction of the preconditioner may however require extra computational effort. Thus there is an optimal value of d/h for a minimum computation requirement for a prescribed accuracy of the BVP solution. This optimal value of d/h is certainly problem dependent.

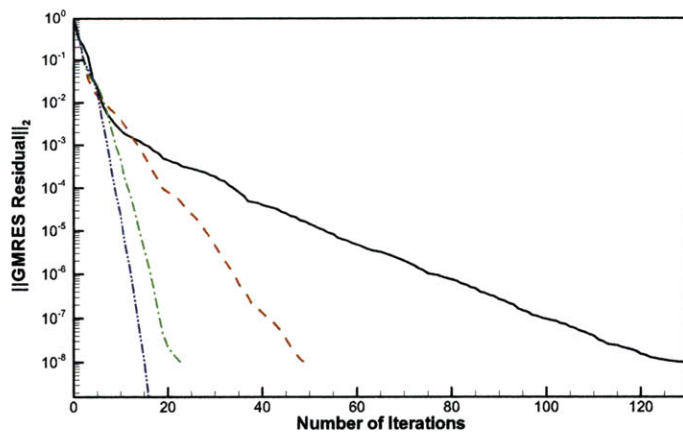
For the mixed BVP problem, both diagonal-type and MN preconditioners can speed up the convergence of GMRES, as shown in figures 2-3b,c. Similarly to the Dirichlet problem, the effectiveness of the MN preconditioner increases as more neighboring meshes are considered in the preconditioner. Importantly, the performance also depends on the ratio between the numbers of Dirichlet and Neumann elements since it affects the conditioning of the coefficient matrix $[A]$. The results in figures 2-3c,d indicate that the same preconditioner is more effective if the problem is less Dirichlet (or more Neumann).



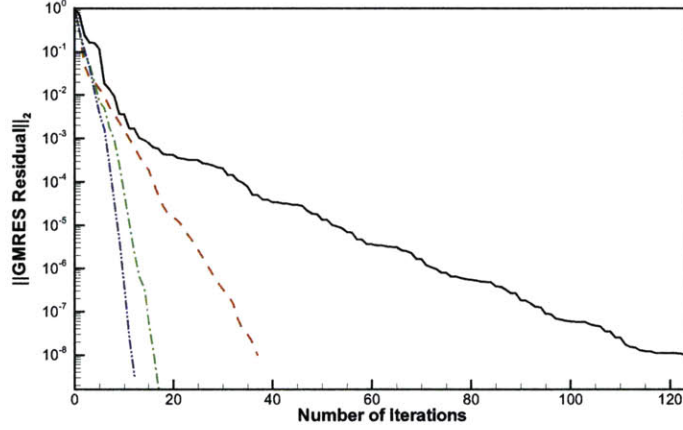
(a)



(b)



(c)



(d)

Figure 2-3: L_2 norm of the normalized GMRES residual as a function of iteration number for the Dirichlet problem (a), the Neumann problem (b), and the mixed problems with the ratio of the number of Dirichlet elements to that of Neumann elements being 1.0 (c) and 0.2 (d). The plotted are the results obtained without preconditioner (—) and with diagonal preconditioner (- - -) and MN preconditioners including neighboring elements within $d/h=1.5$ (- · -) and $d/h=3.0$ (· · ·).

2.5 Numerical Results

2.5.1 Dependence on governing numerical parameters

We first study the dependencies of accuracy and efficiency of the PFFT algorithm on governing numerical parameters for different BVPs. Two important parameters affect the performance of PFFT:

$$\varepsilon = f(\alpha, d/h) \quad (2.43)$$

where ε is the nondimensional relative error of the solution by PFFT-BEMs differing from the solution by direct BEMs for specified BVPs, α the order of the interpolation function with $\alpha=1$ and 2 respectively for linear and quadratic functions, and d/h the critical (nondimensional) distance separating near- and far-field elements. Higher-order interpolation functions and larger range of nearby regions are all expected to reduce the error of PFFT scheme.

Source Distribution problem

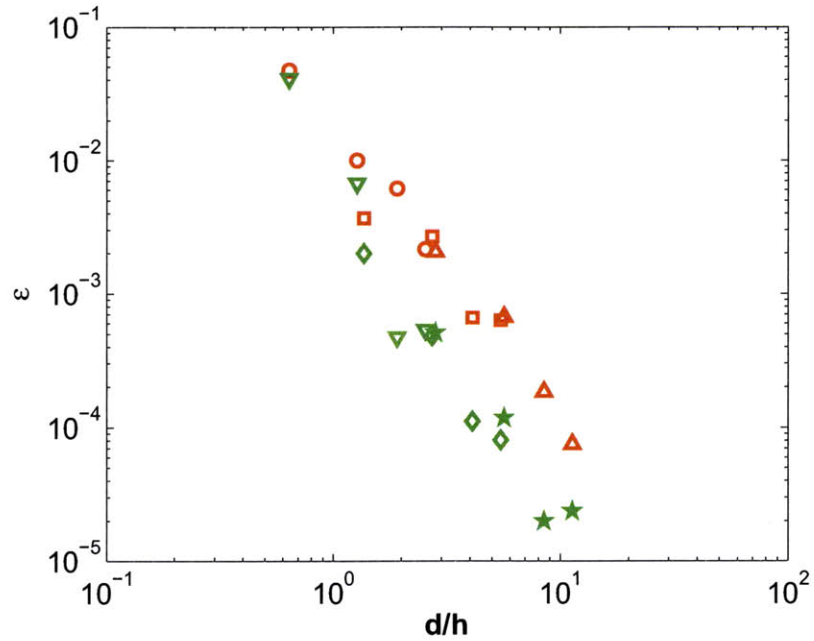
We consider a canonical problem of a spherical surface with a source distribution of constant strength. The nondimensional diameter of the sphere is $D = 1$ and the sphere surface is approximated by $N_e = 3174$ quadrilateral panels. The PFFT-CPM is applied to evaluate the velocity potential on the surface of the sphere. To understand the characteristics of accuracy and efficiency of PFFT-CPM, the result is compared to the solution directly obtained by CPM.

In figure 2-4, the normalized maximum and averaged errors in the velocity potential obtained by PFFT-CPM with $\alpha=1$ and 2 are shown as a function of d/h . Notice that three groups of data (represented by three types of symbols) shown in figure 2-4 are obtained with different values of h used in the PFFT-CPM scheme. Both maximum and averaged errors decay with increasing d/h , as expected. Specifically, the errors decay approximately in a quadratic (cubic) rate with d/h for $\alpha=1$ (2). The use of higher-order interpolation functions leads to faster convergence rate with d/h and thus requires a smaller near-field region for a specified precision of the solution. However, it is more involved and maybe more expensive to evaluate the higher-order interpolation functions.

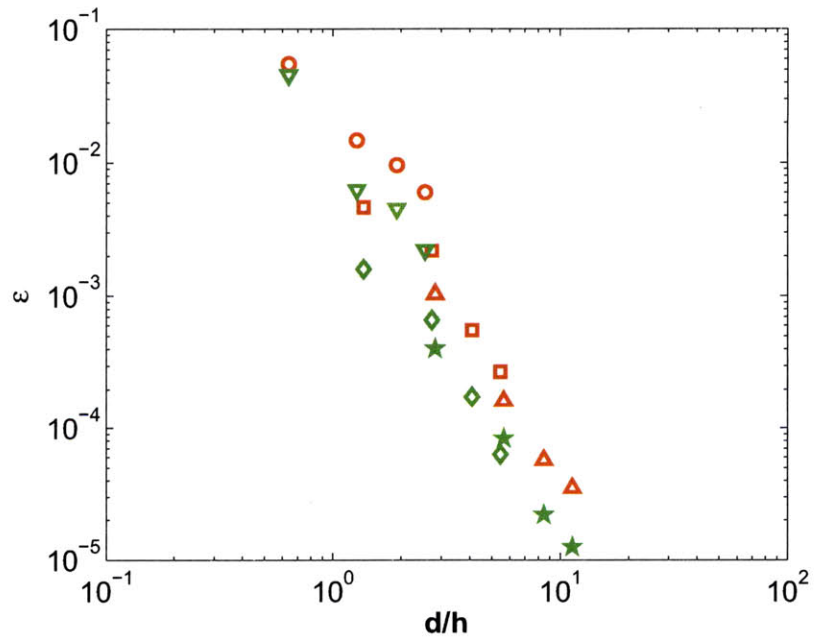
To illustrate the high efficiency of the PFFT algorithm, in figure 2-5, we compare the CPU usage of PFFT-CPM to that of CPM for various numbers of panels (N). The computations are performed on a workstation with Intel Xeon processor. In the PFFT-CPM computations, the relative error is controlled to be within 1 percent, and the number of background grids N_g is chosen to be comparable to N . The results in figure 2-5 confirm that the CPU time with CPM increases (nearly) quadratically while that with PFFT-CPM increases about linearly (for both $\alpha=1$ and 2) with N . For a specified panel number N , PFFT-CPM with $\alpha = 2$ uses slightly more CPU time than that in the $\alpha = 1$ scheme.

Dipole distribution problem

Figure 2-6 presents the relative maximum and averaged errors in the velocity potential due to a uniform dipole distribution on a sphere obtained by PFFT-CPM



(a)



(b)

Figure 2-4: Normalized maximum (\circ , \square , and \triangle) and averaged (∇ , \diamond , and \star) errors in the velocity potential due to a uniform source distribution on a sphere obtained by the PFFT-CPM with the use of (a) linear and (b) quadratic interpretation functions for various values of d/h .

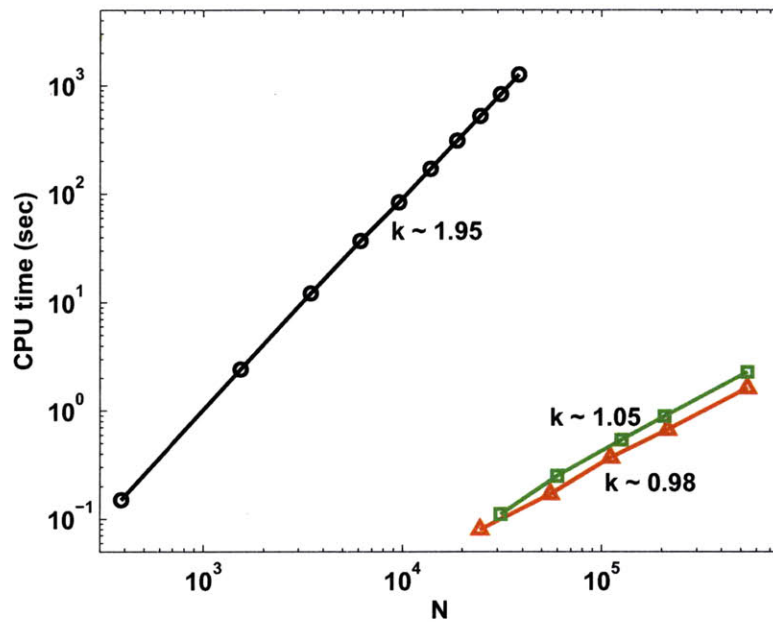


Figure 2-5: Comparison of the CPU time of the conventional CPM (-○-) and the PFFT-CPM with linear (-△-) and quadratic (-□-) interpretation functions as a function of the number of boundary elements (N), for the evaluation of velocity potential due to a uniform source distribution on a sphere. The slopes of the curves are indicated in the figure.

with various values of d/h . The computational parameters used are the same as those for the source distribution in figure 2-4. For both $\alpha=1$ and $\alpha=2$, the convergence rates of the PFFT-CPM solution with increasing d/h in terms of both maximum and averaged errors are quadratic and cubic, respectively, and similar to those for the source distribution. To obtain a solution within an accuracy of 0.1%, we need to use $d/h \simeq 10$ for $\alpha=1$ and $d/h \simeq 5$ for $\alpha=2$.

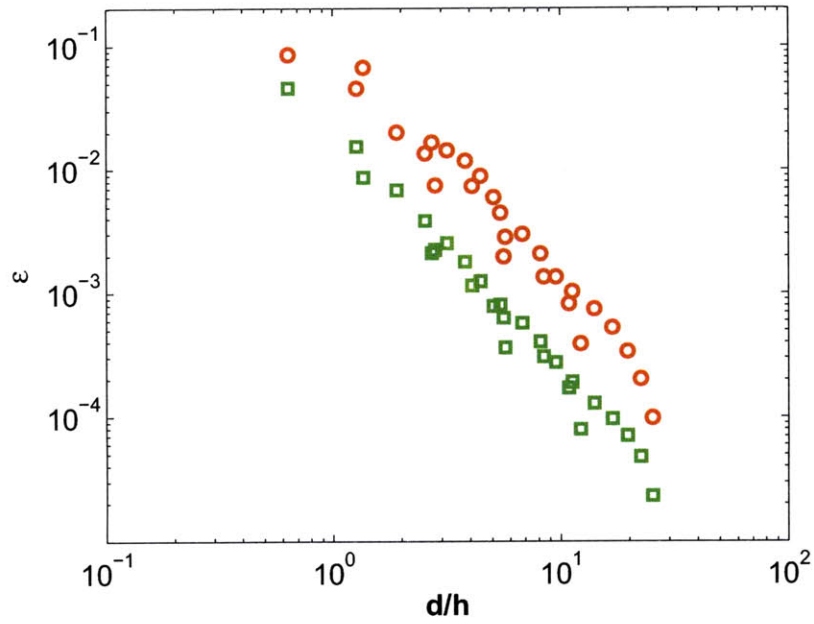
Figure 2-7 compares the CPU usages in PFFT-CPM and CPM for the dipole distribution problem. The computational effort is proportional to about $N^{1.2}$ (N^2) for PFFT-CPM (CPM). Compared to the source distribution case (cf. figure 2-5), the computational effort of PFFT-CPM for the dipole distribution is several times larger due to the use of the indirect approach in the projection and convolution steps.

Mixed boundary-value problem

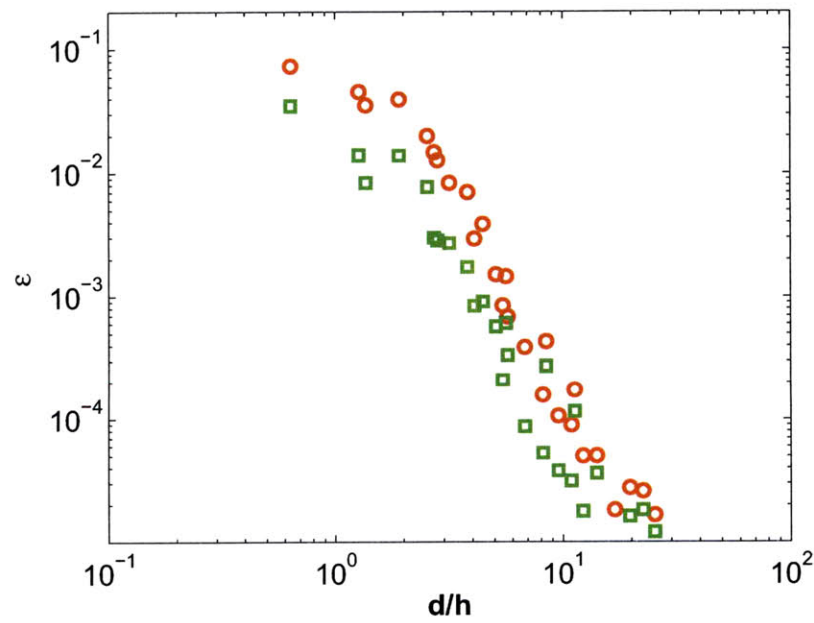
After above source and dipole distribution problems are tested, we investigate the performance of PFFT-CPM, in comparison to CPM, in solving boundary-value problems. The overall performance of the scheme depends on the efficiency of evaluating the influences of source and dipole distributions, the effectiveness of the preconditioner employed, and the properties of the iterative method itself. In this study, GMRES iterative method is adopted for both PFFT-CPM and CPM. A simple diagonal preconditioner is used in PFFT-CPM while a symmetric successive overrelaxation (SSOR) preconditioner is employed in CPM.

As an example, the following BVP is considered here. On the top half surface of the sphere, the velocity potential $\phi = Ux + Vy + Wz$ (U, V, W are constants) is specified and the normal velocity ϕ_n is solved for. This boundary is called Dirichlet surface. On the bottom half surface of the sphere, $\phi_n = Ux_n + Vy_n + Wz_n$ is given and ϕ is solved for. This boundary is called Neumann surface. For comparison, we solve this mixed BVP using both PFFT-CPM and CPM.

The relative maximum and averaged errors of the PFFT-CPM solution on Dirichlet and Neumann surfaces are shown in figure 2-8 as a function of d/h . Similarly to the source and dipole distribution problems, all the errors in the PFFT-CPM solution



(a)



(b)

Figure 2-6: Normalized maximum (\circ) and averaged (\square) errors in the velocity potential due to a uniform dipole distribution on a sphere obtained by the PFFT-CPM with the use of (a) linear and (b) quadratic interpretation functions for various values of d/h .

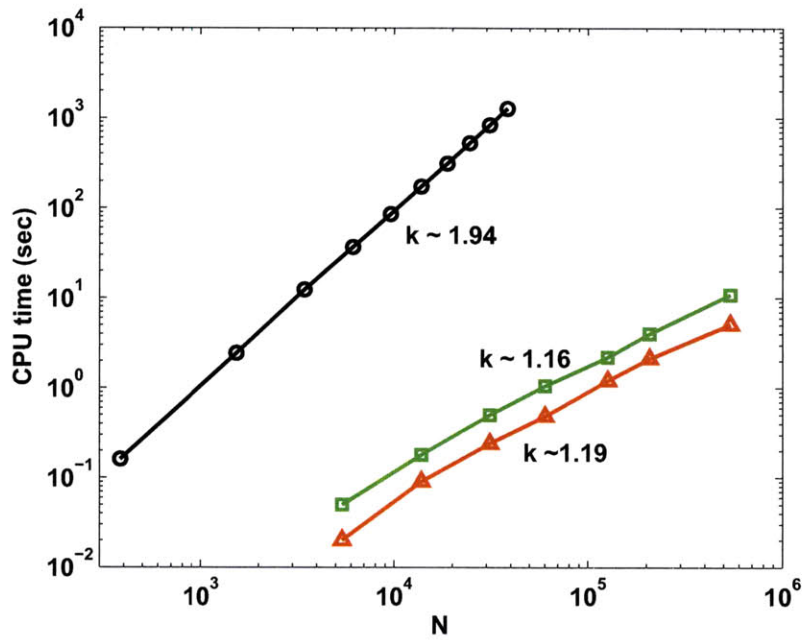


Figure 2-7: Comparison of the CPU time of the conventional CPM (-○-) and the PFFT-CPM with linear (-△-) and quadratic (-□-) interpretation functions as a function of the number of boundary elements (N), for the evaluation of velocity potential due to a uniform dipole distribution on a sphere. The slopes of the curves are indicated in the figure.

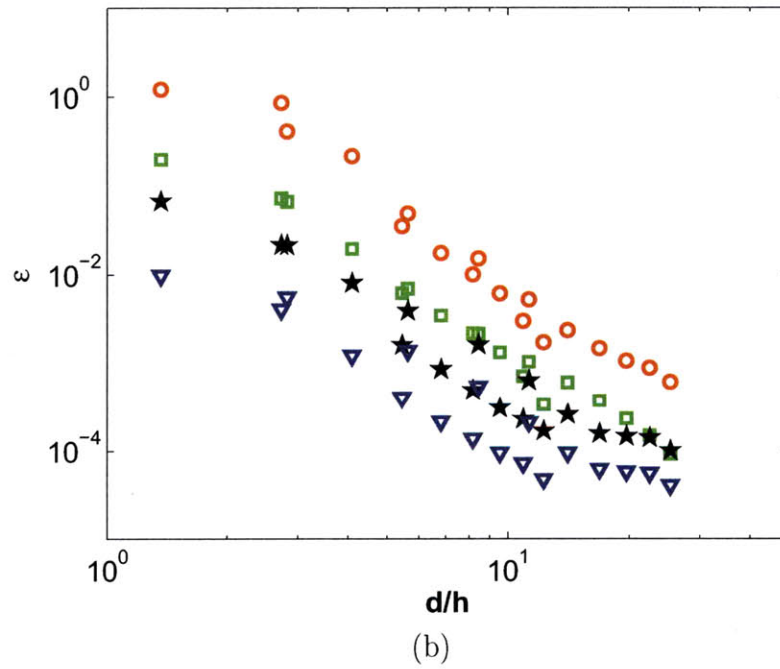
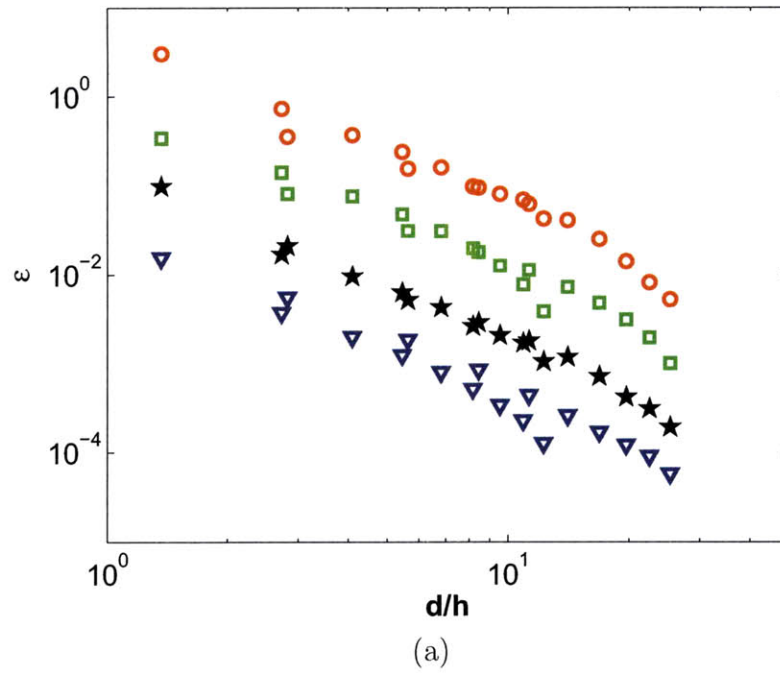


Figure 2-8: Normalized maximum (\circ) and averaged (\square) errors in the normal velocity on Dirichlet surface as well as maximum (\star) and averaged (∇) errors in the velocity potential on Neumann surface in the solution of the mixed boundary-value problem obtained by the PFFT-CPM with the use of (a) linear and (b) quadratic interpretation functions for various values of d/h .

with $\alpha=1$ ($\alpha=2$) decrease quadratically (cubically) with increasing d/h . In general, the errors on Neumann surface are about an order of magnitude smaller than those on Dirichlet surface. Clearly, with fixed values of the computational parameters, better accuracy of the PFFT-CPM solution obtains on Neumann surface and with the use of a quadratic interpolation function.

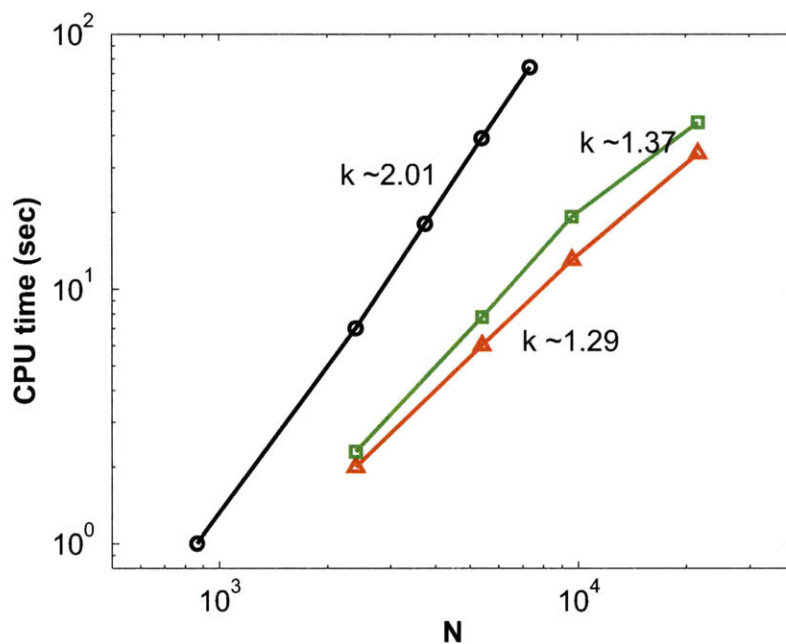


Figure 2-9: Comparison of the CPU time of the conventional CPM (-○-) and the PFFT-CPM with linear (-△-) and quadratic (-□-) interpolation functions as a function of the number of boundary elements (N), for the solution of a mixed boundary-value problem. The slopes of the curves are indicated in the figure.

The comparison of CPU usages with PFFT-CPM and CPM for the mixed BVP is shown in figure 2-9. In PFFT-CPM computations, we set $d/h = 3$ and N_g comparable to N . The computational effort of PFFT-CPM for both $\alpha=1$ and 2 increases with N as $N^{\sim 1.3}$ while that of CPM is proportional to $N^{\sim 2.0}$. For a fixed N , a slightly larger computational effort is needed for PFFT-CPM with $\alpha=2$ than with $\alpha=1$ since the use of a quadratic interpolation function is more computationally involved than the use of a linear interpolation function.

2.5.2 Comparison of PFFT-CPM with PFFT-QBEM

The solution of a BVP obtained by PFFT-BEMs generally contains two sources of errors: one is associated with the application of the PFFT algorithm in evaluation of matrix products, which is studied in the preceding section, and the other is due to approximations in BEMs. We here study the effects of the CPM and QBEM approximations on the PFFT-CPM and PFFT-QBEM performance in solving the general BVPs. To highlight the BEMs' influence on the PFFT-BEMs solution, the value of d/h is chosen to be sufficiently large such that the error associated with the PFFT algorithm is negligibly small and the error in the boundary-value solution is dominated by that due to BEM approximations.

Mixed BVP with smooth boundaries

We first consider a mixed BVP with a smoothly connected boundary. We take a sphere as an example and set up the mixed BVP based on a uniform flow solution of $\phi(\vec{x}) = Ux$. The top (bottom) half sphere is considered as Dirichlet (Neumann) surface with the potential (normal velocity) specified by $\phi = Ux$ ($\phi_n = Un_x$, where n_x is the x -component of the unit normal of the surface). The specified BVP governs the fluid motion inside the sphere. Figure 2-10 illustrates a typical type of discretization of the sphere surface, which is based on equal partition in lateral and longitudinal directions. Both PFFT-CPM and PFFT-QBEM are applied to solve the mixed BVP. The obtained solutions are compared with the known analytical solutions to understand the convergence characteristics of the numerical solutions.

The normalized maximum and averaged errors in ϕ_n on Dirichlet surface and ϕ on Neumann surface are shown in figure 2-11. For both PFFT-CPM and PFFT-QBEM, all the errors decrease for smaller element size ($\Delta\ell$). Specifically, for PFFT-CPM, the maximum/averaged error on Dirichlet surface vanishes approximately linearly/quadratically while both the maximum and averaged errors on Neumann surface decrease quadratically with $\Delta\ell^{-1}$. For PFFT-QBEM, the convergence of all the errors behaves similarly, but with a rate that is two orders of magnitude faster. We note

that with this type of discretization, the maximum errors on Dirichlet and Neumann surfaces for both PFFT-CPM and PFFT-QBEM occur on the (degenerated) elements connected to the poles of the sphere.

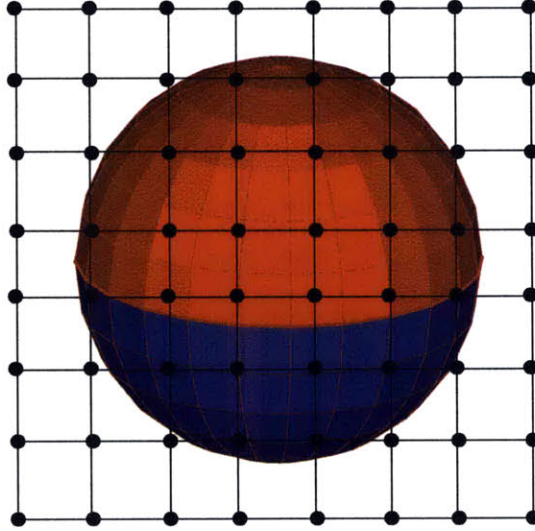
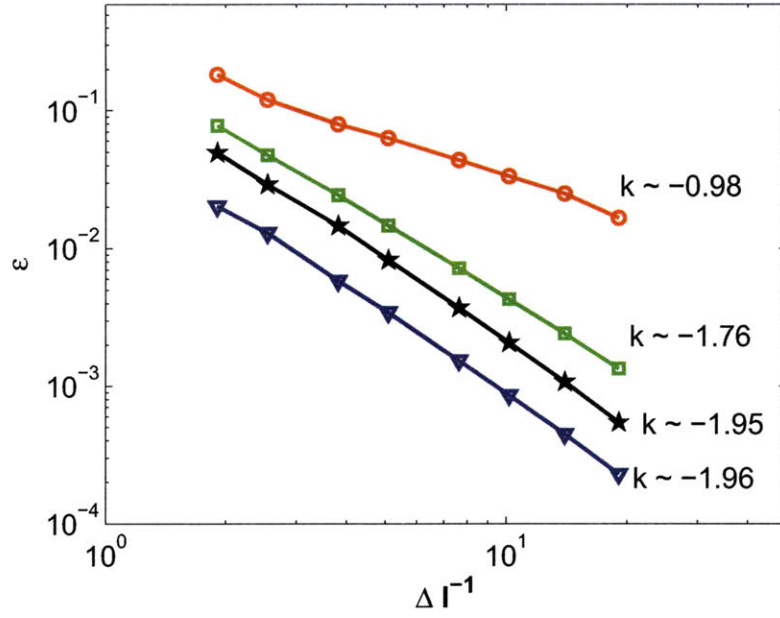


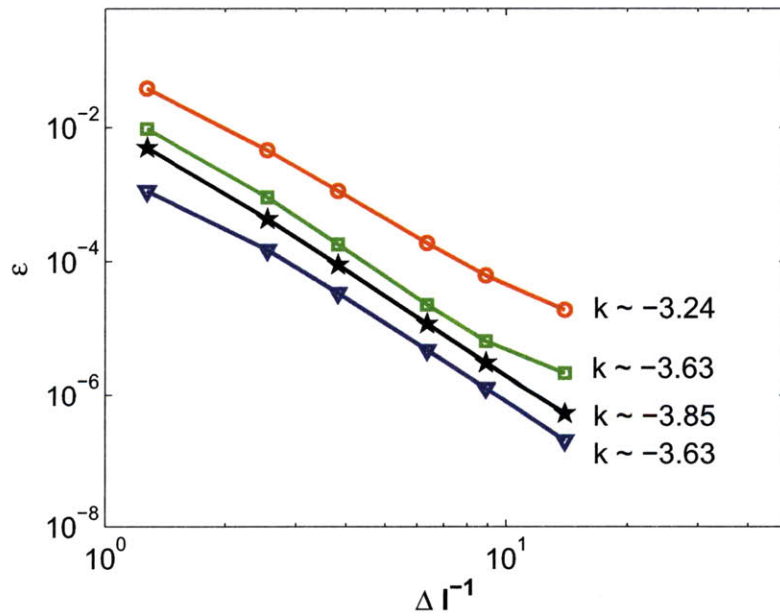
Figure 2-10: Sample discretization of a sphere surface based on equal partition in lateral and longitudinal directions, covered by uniform grids.

In general, the convergence rates of CPM and QBEM are influenced by the discretization of boundaries. To illustrate this, we apply both PFFT-CPM and PFFT-QBEM to solve the same boundary-value problem in the above, but with a different boundary-surface discretization. In this case, we adopt a discretization that is obtained by projecting the element nodes on an equally-discretized inscribed-cube surface to the sphere surface in the radial direction. In this discretization, as shown in figure 2-12, the sizes of the elements are comparable and there is no degenerated element.

The same analytical velocity potential function and normal velocity values are specified on the Dirichlet surface and Neumann surface, respectively. For PFFT-CPM, in figure 2-13a, the maximum error on Dirichlet surface is seen to hardly decay with decreasing $\Delta\ell$ while the other errors behave similarly to those with equal lateral and longitudinal angle discretizations in figure 2-11a. For PFFT-QBEM, however, the maximum error on Dirichlet surface decays quadratically with $\Delta\ell^{-1}$, as shown in



(a)



(b)

Figure 2-11: Normalized maximum (-○-/-☆-) and averaged (-□-/-▽-) errors on (Dirichlet/Neumann) surface of the mixed boundary-value solution obtained by (a) PFFT-CPM and (b) PFFT-QBEM, as a function of the inverse of the characteristic element size $\Delta \ell$. The discretization of the sphere surface used here is based on equal partition in lateral and longitudinal angles.

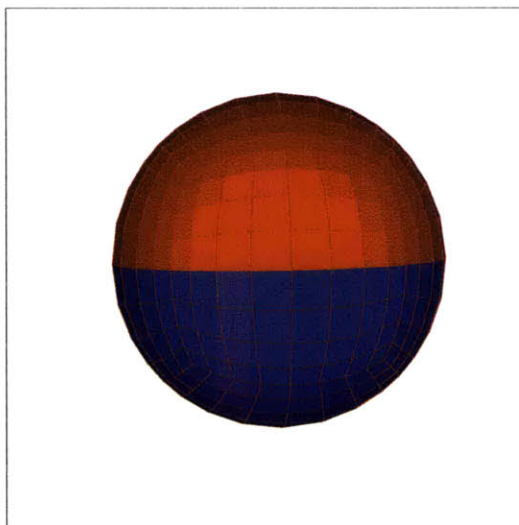


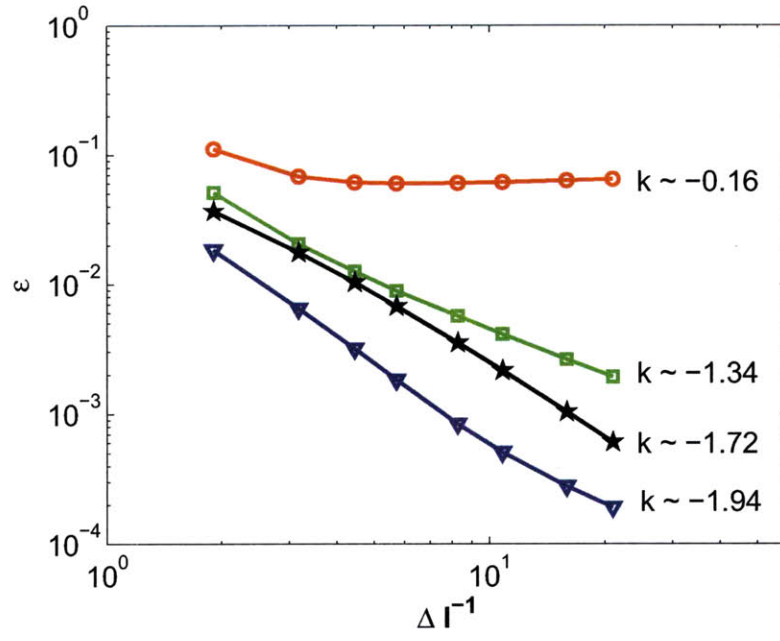
Figure 2-12: Sample discretization of a sphere surface based on the radial projection of the discretization of the inscribed cube. The top (red) surface is the Dirichlet boundary and the rest (blue) is the Neumann boundary.

figure 2-13b. Compared to the results in figure 2-11b, the convergence rates of both maximum and averaged errors on both Dirichlet and Neumann surfaces deteriorates by one order of magnitude. We note that in this type of discretization, the maximum error (on Dirichlet surface) occurs near/at the intersection of Dirichlet and Neumann surfaces for PFFT-CPM/PFFT-QBEM.

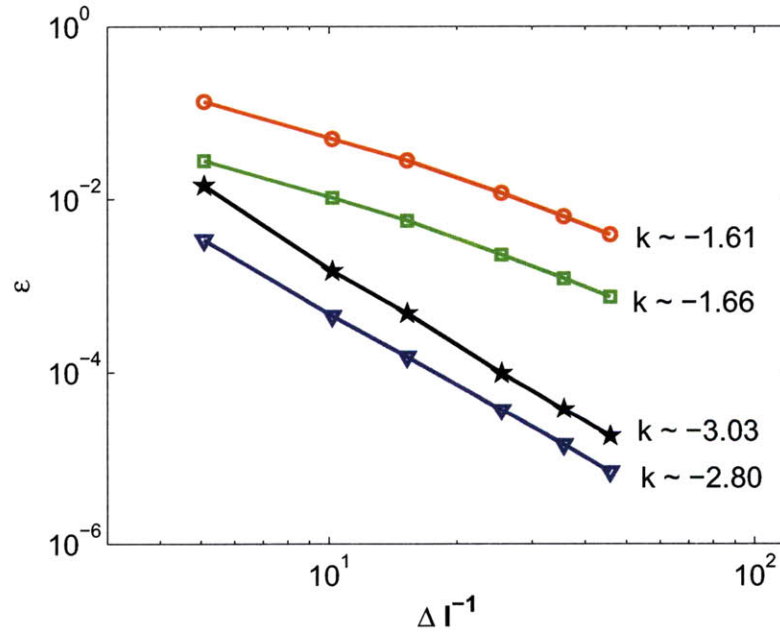
Mixed boundary-value problem with non-smooth boundaries

The convergence characteristics of BEMs is also affected by the smoothness of the boundaries of the boundary-value problem. As an example, we consider the interior problem of a cube whose surface discretization is shown in figure 2-14. The mixed boundary-value problem is set with the top surface as the Dirichlet boundary and the rest as the Neumann boundary based on an analytic velocity potential function $\phi(\vec{x}) = \sin(k_x x + k_y y) \exp(k_z z)$ with $k_x = 0.5$, $k_y = 1.0$, $k_z = (k_x^2 + k_y^2)^{1/2} = 1.12$.

Figures 2-15a,b show the variations of the maximum and averaged errors in the solutions obtained by PFFT-CPM and PFFT-QBEM with decreasing element size $\Delta\ell$. For PFFT-CPM, the maximum error on Dirichlet surface, which always obtains



(a)



(b)

Figure 2-13: Normalized maximum (-○-/-☆-) and averaged (-□-/-▽-) errors on (Dirichlet/Neumann) surface of the mixed boundary-value solution obtained by (a) PFFT-CPM and (b) PFFT-QBEM, as a function of the inverse of the characteristic element size $\Delta \ell$. The discretization of the sphere surface used here is based on the radial projection of the discretization of the inscribed cube.

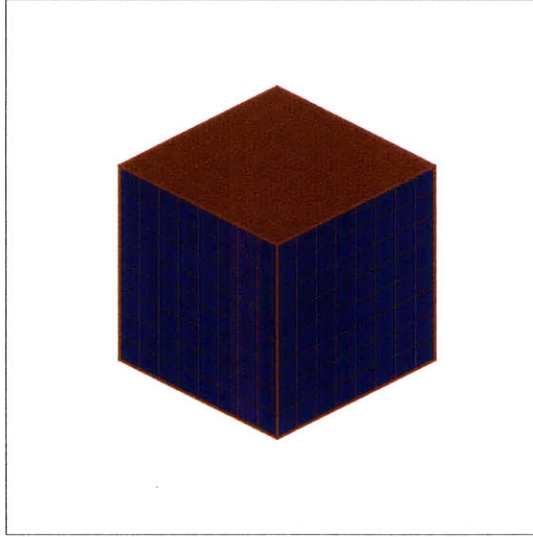


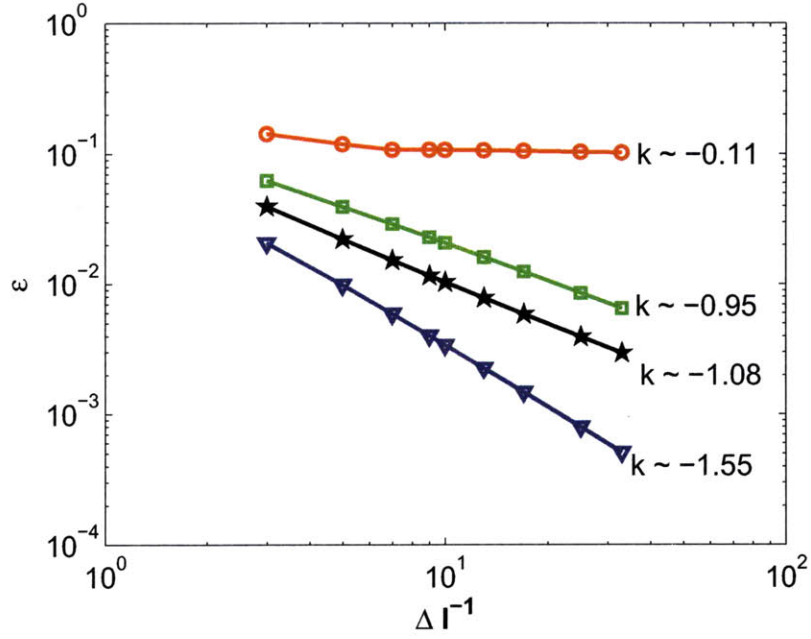
Figure 2-14: Discretization of a cube surface with the top (red) surface as the Dirichlet surface and the rest (blue) as the Neumann surface.

at the edge elements of Dirichlet surface, almost does not decay with $\Delta\ell$ while all the other errors decay approximately linearly with decreasing $\Delta\ell$. For PFFT-QBEM, both the maximum and averaged errors on Dirichlet/Neumann surface vanish nearly quadratically/cubically. Such a superior performance of PFFT-QBEM makes it a useful and effective method for the computation of wave-body interaction problems for which PFFT-QBEM can obtain a convergent solution at the body intersection with water surface.

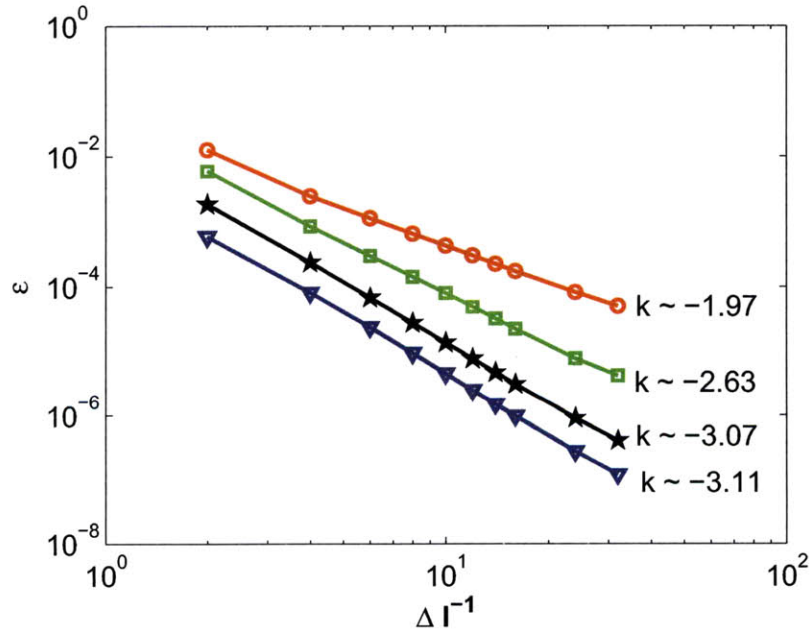
From the above study, we can conclude that PFFT-QBEM has a much better performance than PFFT-CPM in terms of the convergence and accuracy of the solution for a general boundary value problem with smoothly or non-smoothly connected boundaries.

2.5.3 Performance of Parallelized PFFT-BEMs Algorithm

The PFFT-BEMs have been proved to be an $O(N \ln N)$ algorithm on a single-processor-based computer. Here N is the total number of unknowns involved in the boundary value problem and assumed to be comparable to the total number of uniform grids N_g . From both computational complexity and memory requirement



(a)



(b)

Figure 2-15: Normalized maximum (-○-/-☆-) and averaged (-□-/-▽-) errors on (Dirichlet/Neumann) surface of the mixed boundary-value solution obtained by (a) PFFT-CPM and (b) PFFT-QBEM, as a function of the inverse of the characteristic element size $\Delta\ell$. The boundary-value problem is for the interior problem of a cube.

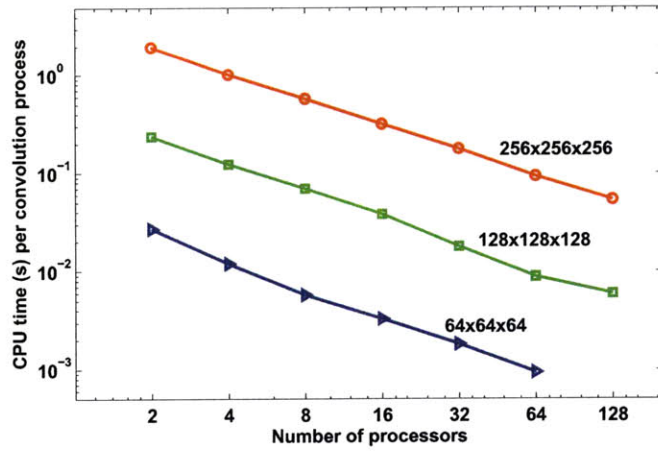
points of view, we want to further exploit the performance of PFFT-BEMs on supercomputers or a cluster of scientific workstations. In this section, the performance of PFFT-BEMs with a properly designed message passing interface(MPI)-based parallelization scheme is briefly demonstrated.

In the PFFT-BEM algorithm, the projection, interpolation, and pre-correction processes only involve local operations among neighboring boundary elements and uniform grids and these steps can be parallelized in a straightforward way. Key parts that determine the overall performance of parallelized PFFT-BEMs are the convolution process and the GMRES solver used for the solution of the system equation (2.13) as their operations are global and take most computational effort.

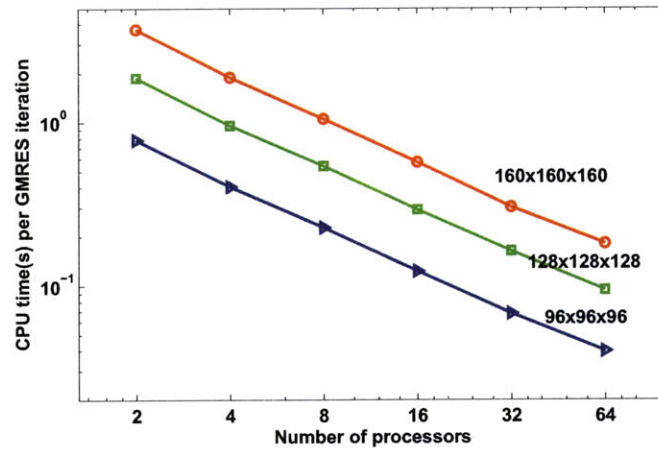
For the convolution process, the customized parallel FFT software, FFTW, is adopted in our computations and the CPU time per convolution process is plotted in figure 2-16a, as a function of the number of processors. Results show that for a specified number of uniform grids (with comparable number of boundary elements), the computational time used for the convolution process has a linear dependence on the number of processors.

To solve the system equation obtained from PFFT-BEMs, we develop parallel code to be in accordance with the open software package, PETSc, and implement the GMRES algorithm together with a Jacobian preconditioner (contained in PETSc). Note that we do not have the explicit forms of the matrices in (2.13) from the PFFT-BEMs algorithm and as a result, the system equation is solved in a matrix-free form within the parallelization scheme. The parallel GMRES solver is then numerically tested and figure 2-16b shows that its CPU time usage decays in a linear rate with the number of processors.

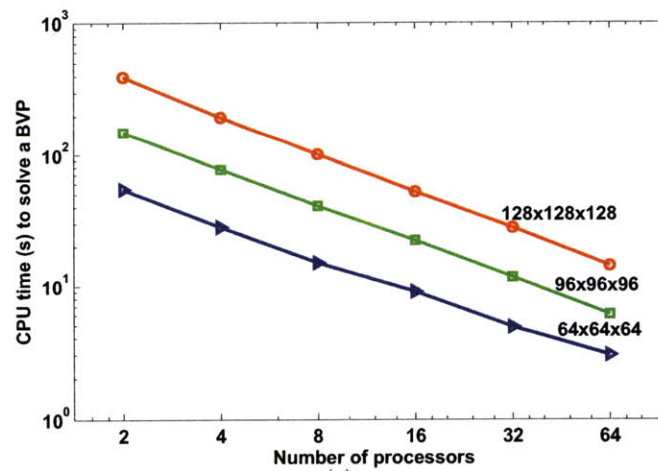
Finally, we combine the parallel algorithms used for each step involved in PFFT-BEMs and evaluate the efficiency of the overall algorithm by solving a general mixed boundary value problem. Taking the parallelized PFFT-CPM as an example, we show in figure 2-16c how the total CPU time varies with the number of processors, for several specified uniform grid numbers. Nearly linear scalability of the parallelized PFFT-CPM is achieved on a nested cluster machine with up to $O(100)$ processors.



(a)



(b)



(c)

Figure 2-16: CPU time used (a) per convolution process, (b) per GMRES iteration step, and (c) for solving a mixed BVP using parallelized PFFT-CPM, as a function of the number of processors. A number is shown above each curve denoting the number of uniform grids used in that group of numerical tests.

2.6 Conclusions

We develop an efficient high-order boundary element method for the numerical simulation of large-scale nonlinear wave-wave and wave-body interactions. The method is based on the integration of the pre-corrected fast Fourier transform (PFFT) algorithm into the quadratic boundary element integral equation solver (QBEM). The developed PFFT-QBEM reduces the computational operations for the boundary-value solution from $O(N^{2\sim 3})$ (required by the traditional boundary element methods) to $O(N \ln N)$ where N is the number of boundary unknowns.

Compared to the existing low-order boundary element methods, like constant panel method (CPM), PFFT-QBEM is robust and accurate, particularly near the intersections of non-smoothly connected boundary surfaces. The characteristics of accuracy and efficiency of the PFFT-QBEM and their dependencies on key numerical parameters are investigated for various boundary-value problems with different boundary geometries. From the numerical tests for the performance of PFFT-BEMs on a cluster of workstations, we obtain a nearly linear scalability from the parallel PFFT-BEMs algorithm.

From our study, we demonstrate the high efficiency and robustness of PFFT-QBEM for solutions of general BVPs when the number of uniform grids (N_g) used in the PFFT scheme is comparable with the number of boundary unknowns (N) adopted in QBEM. There are practical problems which might demand a much larger N_g than N in order to obtain solutions with certain prescribed accuracy. One representative example of such problems is for the study of the water-bottom topography effects on surface waves/motions of floating bodies especially when the water depth is neither too shallow nor too deep. For this type of problems, the performance of PFFT-QBEM (PFFT-BEMs) needs to be further studied.

2.7 References

- Bagla, J.S., Cosmological N-body simulation: Techniques, scope and status, *Current science*, Vol.88, pp. 1088-1100, 2005;
- Chen, K., On a class of preconditioning methods for dense linear systems from boundary elements, *SIAM J. ACI. COMPUT.*, Vol.20, pp.684-698, 1998;
- Grilli, S.T., Guyenne, P., Dias, F., A fully non-linear model for three-dimensional overturning waves over an arbitrary bottom, *Int. J. Numer. Methods Fluid*, Vol.35, pp.829-867, 2001;
- Huebner, K.H., Dewhurst, D.L., Smith, D.E., Byrom, T.G., *The Finite Element Method for Engineers*, Fourth Edition, A Wiley-Interscience Publication, 2001;
- Hockney, R.W., Eastwood, J. W., *Computer Simulation Using Particles*, Institute of Physics Publishing, 1988;
- Korsmeyer, F.T., Yue, D.K.P., Nabors, K., White, J.K., Multipole-accelerated preconditioned iterative methods for three-dimensional potential problems, *BEM15 Worcester*, MA, 1993;
- Korsmeyer, F.T., Klemas, T., White, J.K., Phillips, J., Fast Hydrodynamic Analysis of Large Offshore Structures, 9th *Int. J. Offshore Polar Eng.*, pp.27-34, 1999;
- Kring, D., Korsmeyer, T., Singer, J., White, J., Analyzing mobile offshore bases using accelerated boundary-element methods, *Mar. struct.*, Vol.13, pp.301-313, 2000;
- McCarthy, J.H., Collected experimental resistance component and flow data for three surface ship model hulls, Report No. DTNSRDC-85/011, 1985;
- Mei, C.C., Stiassnie, M., Yue, D.K.P., *Theory and Applications of Ocean Surface Waves*, World Scientific, 2005;
- Nabors, K., Korsmeyer, F.T., Leighton, F.T., White, J., Preconditioned, adaptive, multipole-accelerated iterative methods for three-dimensional first-kind integral equa-

- tions of potential theory, SIAM J. SCI. COMPUT., Vol.15 pp.713-735, 1994;
- Nabors, K., White, J.K., Fastcap: a multipole accelerated 3D capacitance extraction program, IEEE Trans. Comput. Aided Des. Integr. Circuits Syst., Vol.10, pp.1447-1459, 1991;
- Phillips, J.R., White, J.K., A precorrected-FFT method for electrostatic analysis of complicated 3D structures, IEEE Trans. Comput. Aided Des. Integr. Circuits Syst., Vol.16, pp.1059-1072, 1997;
- Stern, F., Longo, J., Zhang, Z.J., Subramani, A.K., Detailed bow-flow data and CFD for a Series 60 $C_B = 0.6$ ship model for Froude number 0.316, J. Ship Res., Vol.40, pp.193-199, 1996;
- Toda, Y., Stern, F., Longo, J., Mean-flow measurements in the boundary layer and wake and wave field of a Series 60 $C_B=0.6$ ship model – Part 1: Froude numbers 0.16 and 0.316, J. Ship Res., Vol.36, pp.360-377, 1992;
- Vavasis, S.A., Preconditioning for boundary integral equations, SIAM J. MATRIX ANAL. APPL., Vol.13, pp.905-925, 1992;
- Wu, G.-Y., Direct simulation and deterministic prediction of large-scale nonlinear ocean wave field, Ph.D Thesis, MIT, 2004;
- Xu, H.-B., Numerical study of fully nonlinear water waves in three dimensions, PhD thesis, MIT, 1992;
- Zhu, Z.-H., Efficient integral equation based algorithms for parasitic extraction of interconnects with smooth or rough surface, PhD thesis, MIT, 2004.

Chapter 3

Time simulations of fully nonlinear wave-body interactions using PFFT-QBEM

3.1 Introduction

Computational fluid dynamics has been widely employed in the design and performance analysis of surface vessels and offshore structures. Most of the existing computational tools are developed based on the assumption of mild surface waves and small amplitude body motions (Mei 1989). They provide accurate and useful predictions of hydrodynamic loads and responses of structures under operating conditions. Their use is, however, limited under surviving conditions in which steep surface waves are often present and large amplitude body motions can be encountered. In these extreme environments, fully nonlinear effects in wave-body interactions are of importance and must be properly accounted for in order to obtain a reliable prediction of hydrodynamic loads and responses of floating/fixed structures. Numerical simulation of fully-nonlinear three-dimensional wave-body interactions is challenging at present in virtue of two primary factors: requirement of high computational cost and complexity in modeling the multi-scale nonlinear processes involved (Tsai & Yue 1996).

Most computational burden in the time simulations of nonlinear wave-body interactions is induced in seeking the solution of the boundary-value problem (BVP) at each time step. As shown in chapter 2, using the pre-corrected fast Fourier transform (PFFT) algorithm to accelerate a boundary element method (BEM) can reduce the requisite computational effort in solving the BVP (with N unknowns) from $O(N^{2-3})$ to $O(N \ln N)$. As the quadratic boundary element method (QBEM) is accurate and robust in computations of BVP solutions and in evaluations of velocity quantities even along the intersections of non-smoothly connected boundary surfaces (Xue *et al.* 2001; Liu *et al.* 2001), the combination of PFFT and QBEM leads to a highly efficient and accurate BVP solver.

Our ultimate goal of developing PFFT-QBEM is to provide an effective and practical simulation capability for nonlinear wave-wave and wave-body interactions in marine hydrodynamics. To realize our goal, we combine PFFT-QBEM with the mixed-Eulerian-Lagrangian (MEL) approach to make a powerful tool for the study of general initial boundary value problems (IBVP) including fully nonlinear three-dimensional wave-body interaction problems. The focus of this chapter is to illustrate the numerical scheme and address the numerical issues in implementing PFFT-QBEM for fully nonlinear wave-body interactions.

Related to the numerical scheme used for the solution of an IBVP involving incident waves, one can choose to solve for either the total velocity potential ϕ or the disturbance velocity potential ϕ_D , in principle. Most existing studies of nonlinear wave-body interactions adopt the former approach (Liu, Xue & Dick 2001; Bai & Taylor 2006). As ϕ_D decays with distance away from the floating body, several important advantages are associated with the use of the latter scheme: significant reduction of the computational domain size, great savings in computational effort, effective far-field damping beach treatment, and evident relief in computational complexity. In the present numerical scheme, we choose to solve for the disturbance velocity potential.

There are several numerical issues critical to the successful implementation of a numerical scheme for the study of nonlinear wave-body interactions. These include:

- (1) accuracy in evaluation of body motions. The time history of body motions determines the instantaneous body position and velocity upon which the BVP at each time step is defined. The equations of body motion could be complicated if rotational body motions are involved in the problem.
- (2) stability in time-integration methods. In the MEL approach, after the BVP at each time step is solved, the kinematic and dynamic free-surface boundary conditions need to be integrated in time to obtain the position of free surface and velocity potential on it for the next time step. Unstable time integration scheme leads to a failure of the overall numerical simulation.
- (3) absorption of wave energy in the (far-field) damping zone. When a finite computational domain is used in the numerical simulation, wave absorbing treatment is normally adopted near the outer boundary of the truncated free surface. Ineffective damping treatment induces significant numerical errors due to wave reflections from the damping zone.
- (4) tracing of wave-body intersection line. Proper evaluation of the waterline position is of importance to the global accuracy of the numerical scheme as well as the local accuracy in the prediction of wave run-up and wave loads on the body.

In this chapter, we will conduct systematic investigations on all these numerical issues.

To illustrate the effectiveness of the newly-developed IBVP solver, we carry out numerical simulations for three representative nonlinear wave-body interaction problems: wave-radiation of a periodically heaving sphere, wave diffraction of a fixed vertical cylinder, and wave generation of a forward moving ship hull. Satisfactory comparisons are made between the fully nonlinear numerical results and existing experimental data and/or theoretical/numerical results. The effect of nonlinearity is also investigated for these wave-body interaction problems.

This chapter is organized as follows. In §3.2, the initial boundary value problem and the associated MEL/BIE formulations for general wave-body interaction problems are presented. Numerical issues involved in the time-domain fully nonlinear

numerical simulations are addressed in §3.3. We carry out computations of several typical wave-body interaction problems and discuss the related key nonlinear effects in §3.4. Conclusions are given in §3.5.

3.2 Mathematical formulation

3.2.1 The initial boundary value problem (IBVP)

IBVP for total flow

For general initial boundary value problems, the flow can be described by a velocity potential $\phi(\vec{x}, t)$ which, for continuity, satisfies the Laplace equation in the whole fluid domain $\mathcal{V}(t)$:

$$\nabla^2 \phi(\vec{x}, t) = 0, \quad \vec{x} \in \mathcal{V}(t), \quad (3.1)$$

On free surface $\mathcal{F}(t)$, the kinematic and dynamic boundary conditions are, in their Lagrangian forms:

$$\frac{D\vec{x}}{Dt} = \nabla \phi, \quad \vec{x} \in \mathcal{F}(t), \quad (3.2)$$

and

$$\frac{D\phi}{Dt} = \frac{1}{2} |\nabla \phi|^2 - gz - P_{\mathcal{F}}/\rho, \quad \vec{x} \in \mathcal{F}(t), \quad (3.3)$$

where D/Dt is the material derivative, $P_{\mathcal{F}}$ the pressure on water surface, ρ the fluid density, and g the gravitational acceleration. On the impervious boundary surface $\mathcal{B}(t)$, the normal velocity of the flow is equal to that of the boundary:

$$\frac{\partial \phi}{\partial n} = \nabla \phi \cdot \vec{n}, \quad \vec{x} \in \mathcal{B}(t), \quad (3.4)$$

where \vec{n} is the unit normal (out of fluid domain) of body surface. For deep water, the far-field (radiation) condition is:

$$\nabla(\phi - \phi_I) \rightarrow 0, \quad \text{as } r \equiv \sqrt{x^2 + y^2 + z^2} \rightarrow \infty, \quad (3.5)$$

When an incident wave field is involved in the wave-body interaction study, ve-

locity potential ϕ is composed of two parts:

$$\phi = \phi_I + \phi_D \quad (3.6)$$

where ϕ_I describes incident wave and ϕ_D is the disturbance velocity potential. In general, ϕ_D includes the influence of body existence on background flow (diffraction problem) and the effect of body motions (radiation problem).

IBVP for incident waves

Governing equations for the incident wave velocity potential, ϕ_I , are summarized as:

$$\nabla^2 \phi_I(\vec{x}, t) = 0, \quad \vec{x} \in \mathcal{V}(t) \quad (3.7)$$

$$\frac{\partial \phi_I}{\partial t} + \frac{1}{2} |\nabla \phi_I|^2 + g\eta_I = 0, \quad \text{on } (S_F)_I \quad (3.8)$$

$$\frac{\partial \phi_I}{\partial z} = \frac{\partial \eta_I}{\partial t} + \frac{\partial \phi_I}{\partial x} \frac{\partial \eta_I}{\partial x} + \frac{\partial \phi_I}{\partial y} \frac{\partial \eta_I}{\partial y}, \quad \text{on } (S_F)_I \quad (3.9)$$

where $(S_F)_I$ is the incident wave free surface on which $z = \eta_I(x, y, t)$. Besides, ϕ_I also needs to satisfy the far-field boundary condition in the horizontal plane and the water-bottom condition if water depth is finite.

IBVP for the disturbance flow

In Eq. (3.6), the disturbance velocity potential, ϕ_D , satisfies the Laplace equation in the fluid domain

$$\nabla^2 \phi_D(\vec{x}, t) = 0, \quad \vec{x} \in \mathcal{V}(t), \quad (3.10)$$

On the free surface, $\mathcal{F}(t)$, the dynamic boundary condition for ϕ_D can be derived from Eq. (3.3) and Eq. (3.8):

$$\frac{D\phi_D}{Dt} = -\frac{\partial \phi_I}{\partial t} + \frac{1}{2} (\nabla \phi_I + \nabla \phi_D) \cdot (\nabla \phi_D - \nabla \phi_I) - gz - P_{\mathcal{F}}/\rho, \quad \vec{x} \in \mathcal{F}(t), \quad (3.11)$$

The kinematic boundary condition on free surface in Lagrangian form is

$$\frac{D\vec{x}}{Dt} = \nabla\phi_I + \nabla\phi_D, \quad \vec{x} \in \mathcal{F}(t), \quad (3.12)$$

If we consider the most general unsteady body motion with six degrees of freedom, ϕ_D must satisfy the boundary condition

$$\frac{\partial\phi_D}{\partial n} = -\frac{\partial\phi_I}{\partial n} + \vec{U}(\vec{x}, t) \cdot \vec{n} + \vec{\Omega} \cdot (\vec{r}' \times \vec{n}), \quad \vec{x} \in \mathcal{B}(t), \quad (3.13)$$

on the body boundary $\mathcal{B}(t)$. Here \vec{n} is taken to be positive when pointing out of the fluid volume, $\vec{U}(\vec{x}, t)$ is the translational velocity of the body, $\vec{\Omega}$ the angular velocity of the body, and \vec{r}' the distance vector from the center of rotation.

The far-field condition for ϕ_D is

$$\nabla\phi_D \rightarrow 0, \quad as \ r \equiv \sqrt{x^2 + y^2 + z^2} \rightarrow \infty. \quad (3.14)$$

Above equations completely define the flow involved in body-wave interaction problems. To solve this type of initial boundary value problems, one can choose to either solve the total velocity potential ϕ directly based on equations (3.1) ~ (3.5) or obtain ϕ_I from equations (3.7) ~ (3.9) and ϕ_D from equations (3.10) ~ (3.14), separately. Almost all existing studies on fully-nonlinear wave-body interactions adopt the former scheme (Liu, Xue & Dick 2001; Bai & Eatock Taylor 2006), but we find that there are several advantages in using the latter scheme (which will be discussed in the following section §3.2.5). So, here we will focus on the implementation of the latter scheme in solving for the incident wave velocity potential ϕ_I and the disturbance velocity potential ϕ_D .

3.2.2 The mixed Eulerian Lagrangian (MEL) approach

At each time step, with incident flow information, specified body boundary $\mathcal{B}(t)$, body instantaneous velocity $U/\Omega(x \in \mathcal{B}, t)$, free surface $\mathcal{F}(t)$ and ϕ_D on it, the boundary value problem (BVP) is completely defined for ϕ_D satisfying Eq. (3.10). The mixed-

Eulerian-Lagrangian method using quadratic boundary elements is applied to the study of fully nonlinear body-wave interactions. This solution procedure involves the following four main steps:

- I. Obtain incident wave information including $\nabla\phi_I$ and $\partial\phi_I/\partial t$ on instantaneous boundary surfaces, $\mathcal{B}(t)$ and $\mathcal{F}(t)$;
- II. Given $\mathcal{B}(t)$ and disturbance normal velocity $\partial\phi_D/\partial n$ on it, $\mathcal{F}(t)$ and disturbance velocity potential ϕ_D on it, solve the BVP for unknown ϕ_D on $\mathcal{B}(t)$ and unknown $\partial\phi_D/\partial n$ on $\mathcal{F}(t)$. Evaluate $\nabla\phi_D$ and $\partial\phi_D/\partial t$ (based on ϕ_D obtained at consecutive time steps) on $\mathcal{B}(t)$ and $\mathcal{F}(t)$;
- III. Compute pressure distribution on wetted body surface based on Bernoulli equation, evaluate forces and moments acting on the floating body by integration of pressure, and obtain the structure's translational and angular acceleration velocities from equations of body motion;
- IV. Integrate in time the dynamic and kinematic free-surface boundary conditions Eq. (3.11) and Eq. (3.12) for free surface \mathcal{F} and disturbance velocity potential ϕ_D on it at the new time $t + \Delta t$; Integrate in time the instantaneous acceleration velocities to obtain body velocities, \vec{U} and $\vec{\Omega}$, at $t + \Delta t$; Integrate in time one more time for new body boundary position $\mathcal{B}(t + \Delta t)$.

Starting from the initial conditions, repeat the above process to obtain the time simulation of nonlinear wave-body interactions for an arbitrary duration of time.

Related to step I, in general, a fully-nonlinear irregular incident wave field in the absence of floating bodies, by itself, is hard to obtain in numerical simulations. Much research work is being conducted currently in this topic (Xue *et al.* 2001; Wu 2004). Since this part is not the focus of present work, only a special example of fully nonlinear incident wave, monochromatic Stokes wave train, will be explained in the following section §3.2.3.

Step II dominates the computation time and storage used for wave-body interaction studies, as ϕ_D has to be solved numerically from a boundary-integral equation.

This part will be briefly explained in section §3.2.4.

Body motions are important physical quantities of interest. The governing equations of motion, used in Step III, are not trivial especially when rotational body motions are involved. Detailed formulations of these equations will be shown in section §3.3.1.

Step IV relates to the stability issue involved in numerical calculations for updating the free-surface and body-surface boundaries in time, which will be analyzed in section §3.3.2.

3.2.3 Incident flow/waves

As shown in Eq. (3.11), (3.12), and (3.13), explicit incident wave information, $\nabla\phi_I$ and $\partial\phi_I/\partial t$ on $\mathcal{F}(t)$ and $\nabla\phi_I$ on $\mathcal{B}(t)$, need to be pre-evaluated in order to solve for ϕ_D -related information. In addition, after the boundary value problem for ϕ_D is solved, $\partial\phi_I/\partial t$ is required on $\mathcal{B}(t)$ to compute pressure distribution on the instantaneous body surface. Note that here the free surface $\mathcal{F}(t)$ is different from the incident wave surface $(S_F)_I$ due to the disturbance of the body in waves. At locations where $\mathcal{F}(t)$ is above $(S_F)_I$, it might be hard to understand the physical meaning of $\nabla\phi_I$ and $\partial\phi_I/\partial t$. But mathematically, ϕ_I can be any function if it can satisfy the Laplace equation in the whole fluid domain (Eq. (3.7)) and free surface boundary conditions defined in Eq. (3.8) and (3.9). (Flow of infinite-depth is considered hereafter, if not stated explicitly otherwise.)

One simple example of ϕ_I which can satisfy all the equations (Eq. (3.7), (3.8) and (3.9)) is $\phi_I = ax + by + cz$ where a , b , and c are arbitrary constants. The physical fluid defined by this ϕ_I is the superposition of three uniform streams with velocities a , b , and c in x , y and z directions, respectively. Consider a special case of wave-body interactions: a ship hull moving forward with a steady speed U in calm water. With respect to the coordinate system fixed on the ship, the problem can be viewed as a fixed ship being placed in an incident uniform flow of speed U and the corresponding

velocity potential can be written as

$$\phi = -Ux + \phi_D \quad (3.15)$$

for which the incident flow information is known everywhere in space.

For general fully nonlinear incident waves, solutions satisfying Eq. (3.7), (3.8) and (3.9) are hard to obtain even numerically on free surface boundary $(S_F)_I$. But if we linearize the dynamic and kinematic boundary conditions (Eq. (3.8) and (3.9)) on $z = 0$, analytical solutions of incident wave velocity potential ϕ_I and wave elevation η_I can be written as

$$\phi_I(\vec{x}, t) = \frac{gA}{\omega} e^{kz} \sin(kx - \omega t + \varphi) \quad (3.16)$$

and

$$\eta_I(x, y, t) = A \cos(kx - \omega t + \varphi) \quad (3.17)$$

with specified wave frequency ω or wave number k and phase angle φ . Based on Eq. (3.16), $\nabla\phi_I$ and $\partial\phi_I/\partial t$ can be readily evaluated at any location \vec{x} .

The problem of steady progressive fully-nonlinear free-surface waves is classical in fluid mechanics. Stokes (1849) proposed a solution by means of a perturbation expansion for finite as well as infinite water depths, although the convergence of Stokes' solution is slow when the ratio of water depth to wavelength is small (Stokes, 1880). Besides, Stokes' expansion has been found to be incapable of yielding the highest wave for any value of the water depth (Schwartz, 1974). Approximate solution for the so-called solitary wave was found by Boussinesq in 1871 for the extreme case as the ratio of water depth over wavelength approaching zero. When the ratio is small but finite, Korteweg & de Vries (1895) gave a solution known as the cnoidal wave. Schwartz (1974) extended Stokes' infinitesimal-wave expansion to high order for steady progressive free-surface waves and used a computer-based coefficient arithmetic to obtain high accuracy for most values of the wave height and water depth.

In our work, Schwartz's scheme is implemented numerically and accurate data about Stokes wave velocity potential ϕ_I , wave elevation η_I , and flow velocities $\nabla\phi_I$

are obtained on wave free surface, with specified wave amplitude A_I , wavelength λ_I , and water depth h . From Schwartz's scheme, we can also evaluate Stokes wave's fundamental wave frequency ω_0 and wave speed c (defined as $c = \omega_0 \lambda / 2\pi$). After knowing incident wave information on wave free surface $(S_F)_I$, how can we obtain $\nabla \phi_I$ and $\partial \phi_I / \partial t$ at any specified position on $\mathcal{F}(t)$ and $\mathcal{B}(t)$? Here we propose a simple but effective approach. First, evaluate $((\eta_I)_i, (\phi_I)_i)$ at x_i for $i = 1, \dots, N$ with x_i covering a complete Stokes wave length. Then, assume

$$\phi_I(x, z) = \sum_n C_n e^{-ik_n x} e^{|k_n|z}, \quad n = -M/2, \dots, M/2 - 1 \quad (3.18)$$

where $k_n = 2\pi n / \lambda_I$. Equation (3.18) is discretized at the N collocation points on free surface, (x_i, η_i) , so that N equations are built to obtain M unknowns, C_n . If $N > M$, this will be an over-determined system. After C_n is solved, ϕ_I is fully determined by Eq. (3.18) at any position within one wave length and velocities will be easily evaluated as:

$$\frac{\partial \phi_I}{\partial x}(x, z) = \sum_n (-i) C_n k_n e^{-ik_n x} e^{|k_n|z}, \quad n = -M/2, \dots, M/2 - 1 \quad (3.19)$$

and

$$\frac{\partial \phi_I}{\partial z}(x, z) = \sum_n C_n |k_n| e^{-ik_n x} e^{|k_n|z}, \quad n = -M/2, \dots, M/2 - 1 \quad (3.20)$$

Based on Schwartz's scheme, wave elevation η_I can be evaluated at any location on the Stokes wave surface. But if we want to simplify our computations and make use of only the N values of $(\eta_I)_i$ obtained above to approximate η_I at any specified position, the following equation can be assumed:

$$\eta_I(x) = \sum_n D_n e^{-ik_n x}, \quad n = -M/2, \dots, M/2 - 1. \quad (3.21)$$

M unknowns D_n will be solved in a similar way as that for C_n in Eq. (3.18). (As will be explained in the following section for damping zone implementation, η_I is explicitly needed on part of the free surface \mathcal{F} .)

Stokes wave is a steady progressive wave and the time dependence of Stokes wave solution can be written as

$$\eta_I(x, t) = f(x - ct); \quad \phi_I(x, z, t) = g(x - ct) \quad (3.22)$$

As a result, the time derivative of Stokes wave's velocity potential is

$$\frac{\partial \phi_I}{\partial t} = -c \frac{\partial \phi_I}{\partial x}. \quad (3.23)$$

Besides, Stokes wave is periodic in space so that $\phi_I(x) = \phi_I(x + m\lambda)$ for an arbitrary integer number m . By now, we have outlined an approach to compute Stokes wave information including $(\eta_I, \phi_I, \partial \phi_I / \partial t, \nabla \phi_I)$ at any specified position (x, z) in space.

3.2.4 Boundary integral equation (BIE) for BVPs

In solving the nonlinear wave-body interaction problems in time domain, the most computational effort is placed at solving the BIE which controls the boundary-value problem at each time:

$$\beta(\vec{x})\phi(\vec{x}) - \iint_S \phi_n(\vec{\xi})G(\vec{x}; \vec{\xi})dS(\vec{\xi}) + \iint_S \phi(\vec{\xi})G_{n(\vec{\xi})}(\vec{x}; \vec{\xi})dS(\vec{\xi}) = 0 \quad (3.24)$$

where S is the boundary of the whole fluid domain ($S = \mathcal{F} + \mathcal{B}$), G the Rankine source Green function, and $\beta(\vec{x})$ the so-called interior solid angle which is defined as

$$\beta(\vec{x}) = - \iint_S G_n(\vec{x}; \vec{\xi})dS(\vec{\xi}) \quad (3.25)$$

Eq. (3.24) is the BIE for total velocity potential ϕ . If the BVP for the disturbance velocity potential ϕ_D (in Eq. (3.6)) is to be solved, the BIE will be:

$$\beta(\vec{x})\phi_D(\vec{x}) - \iint_S (\phi_D)_n(\vec{\xi})G(\vec{x}; \vec{\xi})dS(\vec{\xi}) + \iint_S \phi_D(\vec{\xi})G_{n(\vec{\xi})}(\vec{x}; \vec{\xi})dS(\vec{\xi}) = 0 \quad (3.26)$$

General procedure can be referred to chapter 2 for implementing PFFT-QBEM

(PFFT-BEMs) to solve unknowns in Eq. (3.24) or Eq. (3.26), velocity potential on \mathcal{B} and normal velocity on \mathcal{F} , with specified velocity potential on \mathcal{F} and normal velocity on \mathcal{B} .

In this section, we focus on investigating the main differences of Eq. (3.24) and Eq. (3.26) in numerical implementations for the evaluation of far-field contributions in the boundary integrals.

A: Treatment of far-field contribution in Eq. (3.24)

Consider general three-dimensional wave-body interactions in an infinite fluid domain. Free surface \mathcal{F} can be viewed as the combination of two parts: surface close to the floating body \mathcal{F}_{in} and surface in far field \mathcal{F}_{out} , as demonstrated in Figure 3-1. Along \mathcal{F}_{in} , both incident waves and disturbance waves are important while on \mathcal{F}_{out} , disturbance waves are negligible due to the decaying feature of disturbance waves with distance away from the body. One possible way to account for contributions from surface of far-field in Eq. (3.24) is to match the nonlinear inner solution to a general linearized wavefield by implementing transient linearized free-surface Green function on \mathcal{F}_{out} (Dommomuth & Yue 1987; Lin & Yue 1990; Xue & Yue 1998). However, this matching technique cannot be extended to a general problem involving (highly) nonlinear incident wavefield. Another choice for far-field closure is to impose doubly-periodic (outer) boundary conditions and adopt the doubly-periodic Green function G_p in Eq. (3.24) (Liu, Xue & Yue 2001). But this approach significantly limits the numerical simulation time in order to avoid the boundary effect getting into the system.

In our study, we propose a different scheme to account for far-field influence. By splitting \mathcal{F} into near- and far-field parts, Eq. (3.24) can be rewritten as:

$$\beta(\bar{x})\phi(\bar{x}) - \iint_{\mathcal{B}+\mathcal{F}_{in}} \phi_n(\bar{\xi})G(\bar{x};\bar{\xi})dS(\bar{\xi}) + \iint_{\mathcal{B}+\mathcal{F}_{in}} \phi(\bar{\xi})G_{n(\bar{\xi})}(\bar{x};\bar{\xi})dS(\bar{\xi}) = B_I(\bar{x}) \quad (3.27)$$

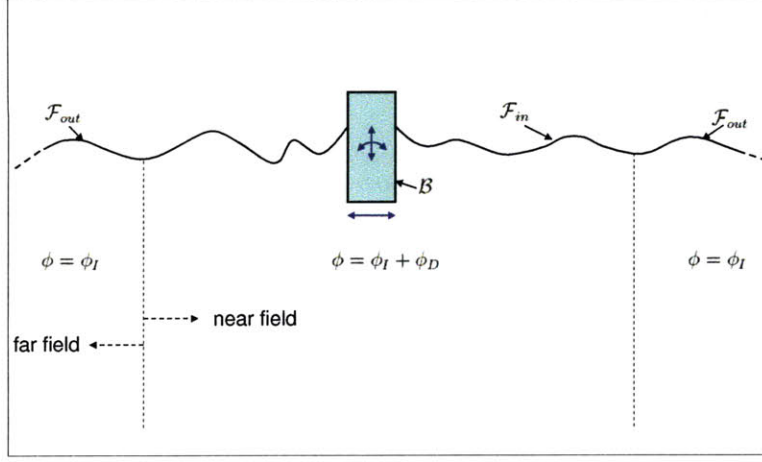


Figure 3-1: Sketch of the fluid domain separated into two parts: near-field and far-field.

where $B_I(\vec{x})$ is the contribution of the incident wave from far-field:

$$B_I(\vec{x}) = \iint_{\mathcal{F}_{out}} (\phi_I)_n(\vec{\xi}) G(\vec{x}; \vec{\xi}) dS(\vec{\xi}) - \iint_{\mathcal{F}_{out}} \phi_I(\vec{\xi}) G_{n(\vec{\xi})}(\vec{x}; \vec{\xi}) dS(\vec{\xi}) \quad (3.28)$$

Since ϕ_I satisfies Laplace equation (Eq. (3.7)), by applying Green's second identity to ϕ_I and the Rankine Green function G , we have

$$B_I(\vec{x}) = \iint_{\mathcal{F}'_{in}} [-(\phi_I)_n(\vec{\xi}) G(\vec{x}; \vec{\xi}) + \phi_I(\vec{\xi}) G_{n(\vec{\xi})}(\vec{x}; \vec{\xi})] dS(\vec{\xi}) + \beta'(\vec{x}) \phi_I(\vec{x}) \quad (3.29)$$

where surface \mathcal{F}'_{in} combines with \mathcal{F}_{out} to make a closed boundary $(S_F)'_I$. Note that \mathcal{F}'_{in} is not uniquely defined here as long as it is inside the fluid domain. So, we have freedom to choose \mathcal{F}'_{in} to be (a) \mathcal{F}_{in} as used in Eq. (3.27), (b) the near-field incident wave surface $(S_F)_I$, or (c) an arbitrarily-shaped surface for computational convenience. Suppose the fluid domain enclosed by $(S_F)'_I$ is \mathcal{V}' . Depending on the relative position of \vec{x} to \mathcal{V}' , $\beta'(\vec{x})$ in Eq. (3.29) has different values:

$$\beta'(\vec{x}) = \begin{cases} 0, & \text{if } \vec{x} \text{ is outside } \mathcal{V}' \\ 2\pi, & \text{if } \vec{x} \text{ is on the (smooth) boundary } \mathcal{F}'_{in} \\ 4\pi, & \text{if } \vec{x} \text{ is inside } \mathcal{V}' \end{cases} \quad (3.30)$$

If we choose \mathcal{F}'_{in} in Eq. (3.29) the same as \mathcal{F}_{in} in Eq. (3.27), $\beta'(\vec{x}) = \beta(\vec{x})$.

As we can see, it is not a trivial issue to take care of far-field closure in Eq.(3.24).

B: Treatment of far-field contribution in Eq. (3.26)

If we choose to solve the disturbance velocity potential using Eq. (3.26), by neglecting the disturbance wave on far-field surface \mathcal{F}_{out} , we can obtain:

$$\beta(\vec{x})\phi_D(\vec{x}) - \iint_{\mathcal{B}+\mathcal{F}_{in}} (\phi_D)_n(\vec{\xi})G(\vec{x};\vec{\xi})dS(\vec{\xi}) + \iint_{\mathcal{B}+\mathcal{F}_{in}} \phi_D(\vec{\xi})G_{n(\vec{\xi})}(\vec{x};\vec{\xi})dS(\vec{\xi}) = 0 \quad (3.31)$$

All the computational effort used to evaluate the term $B_I(\vec{x})$ in Eq. (3.27) can be saved in this scheme.

Another issue worth to mention here is the evaluation of solid angle $\beta(\vec{x})$ in both Eq. (3.24) and Eq. (3.26), especially when boundary surface S is not smoothly connected at \vec{x} . Based on Eq. (3.25), numerical integration needs to be carried out over the whole (closed) boundary S (with $S = \mathcal{F}_{in} + \mathcal{F}_{out} + \mathcal{B}$) to obtain β accurately. Since the contribution from \mathcal{F}_{out} cannot be computed directly, we use the following equation to evaluate β , instead:

$$\beta(\vec{x}) = - \iint_{\mathcal{B}+\mathcal{F}_{in}} G_n(\vec{x};\vec{\xi})dS(\vec{\xi}) - \iint_{\mathcal{F}'_{out}} G_n(\vec{x};\vec{\xi})dS(\vec{\xi}) \quad (3.32)$$

where surface \mathcal{F}'_{out} can be arbitrarily chosen as long as it is inside the fluid domain. If \mathcal{F}'_{out} is constructed as the combination of several flat surfaces, analytical formulae exist for the evaluation of the second integral in the RHS of Eq. (3.32) (Hess & Smith 1964).

3.2.5 Advantages in solving the disturbance velocity potential over the total velocity potential

The scheme of splitting total velocity potential ϕ into incident wave velocity potential ϕ_I and disturbance wave velocity potential ϕ_D is popular in the study of linear

wave-body interactions, as the linear incident wave can be easily obtained. For general three-dimensional fully nonlinear wave-body interactions, existing studies (with very few exceptions (Ferrant 1996; Ferrant *et al.* 2003)) choose to solve total velocity potential mainly due to the difficulty in obtaining explicit nonlinear incident wave information. But indeed, solving the total velocity potential ϕ cannot avoid the demand of incident wave information within the scheme. First of all, wave-body interactions are simulated as an initial boundary value problem (IBVP) and (η_I, ϕ_I) on \mathcal{F} and $\nabla\phi_I$ on \mathcal{B} have to be provided at $t = 0$ to start the simulation. Secondly, to account for far-field influence of incident wave in Eq. (3.28), ϕ_I and $(\phi_I)_n$ need to be known at each time step.

For fully-nonlinear wave-body interaction studies, the approach of solving ϕ_D based on Eqs. (3.10 ~ 3.14) and Eq. (3.26) deserves more attention. Here we summarize the advantages in solving the IBVP for ϕ_D by comparing with the numerics in solving for ϕ :

- I. Significant reduction of the numerical computational domain. As discussed in §3.2.4, BIE for ϕ_D (Eq. (3.31)) only needs to include the boundary integration of near-field free surface \mathcal{F}_{in} while contribution of ϕ_I on far-field free surface \mathcal{F}_{out} has to be taken into account in the BIE for ϕ (Eq. (3.27)).
- II. Great saving in computational time and storage. Since evaluating accurately $B_I(\bar{x})$ in Eq. (3.27) requires considerable computational effort, avoiding the evaluation of $B_I(\bar{x})$ in the procedure of solving ϕ_D results in big saving in computation cost. There is another important contributor of numerical saving in the ϕ_D scheme. Due to the decreasing energy density of diffracted and radiated waves with radial distance away from the floating body (in three-dimensions), disturbance waves are significant only in the neighborhood of the body. As a result, for the boundary element method used for solving the BIE of ϕ_D , fine grids are required only on the boundary surface near the body and grids with increasing size can be implemented away from the body. On the contrary, to get accurate result from the BIE of ϕ , grids of similar size are required on whole

boundaries, as ϕ in far-field is comparable with ϕ in near-field. The saving of the ϕ_D scheme in computational time and storage is vital for the study of floating structures' large-amplitude or unstable motions which are in general developed in long-time periods.

III. Easier treatment for wave absorbing zone. Finite computational domain has to be used to solve the BVPs either for ϕ or ϕ_D . To minimize (numerically) reflected waves, certain damping treatment is in general adopted along the outer computational domain (i.e., along the outer edge of \mathcal{F}_{in}). As far as ϕ_D is concerned, an effective damping-beach treatment can be relatively easier to develop due to the fact that the value of ϕ_D is small in the outer computational domain. But ϕ_I , as the main component of ϕ near the wave-absorbing zone, does not decay with distance and it brings big challenges to the design of an effective damping treatment. Especially when the incident wave is steep, reflection from the wave absorbing zone due to the existence of η_I and ϕ_I is hard to avoid (Xue 1997). In view of long-time numerical simulations, if numerical errors induced by the reflected waves from outer boundaries cannot be limited, the overall numerical solutions could be damaged.

IV. Less influence from numerical smoothing schemes. For long-time fully nonlinear numerical simulations of wave-wave or wave-body interactions, to suppress the development of the so-called 'saw-tooth' instability of the free surface, certain numerical smoothing technique needs to be applied on the free surface. Since any smoothing treatment would affect the (true) solution more or less, numerical experiments show that substantial part of the energy in the system could be lost after smoothing treatments are applied on ϕ and η for certain period of time especially when a highly nonlinear incident wave is involved. By contrast, smoothing on ϕ_D and $\eta - \eta_I$ results in very limited consequences.

3.3 Numerical implementations

We address here the key issues associated with the numerical implementation of the newly-developed IBVP solver, PFFT-QBEM together with MEL scheme, for the solutions of fully nonlinear wave-body interaction problems. (Most of the issues discussed here are common in the numerical schemes for solving for either ϕ or ϕ_D .)

3.3.1 Six-degrees-of-freedom body motion

Define the following three coordinate systems, as shown in Figure 3-2: (1) an inertia coordinate system (global system), $OXYZ$, fixed in space; (2) a local system, $oxyz$, with origin o at the body's center of gravity and axes $(x-,y-,z-)$ parallel to the ones in the global system $(X-,Y-,Z-)$; and (3) a body-fixed coordinate system, $ox'y'z'$, which shares the origin with the local coordinate system.

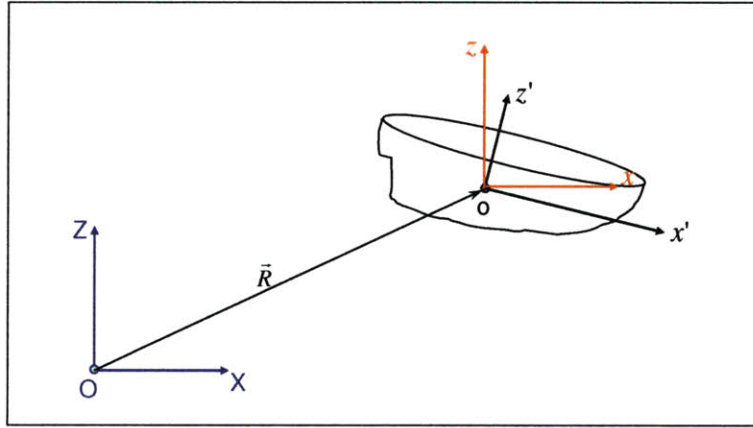


Figure 3-2: The inertial, local and body-fixed coordinate systems

The global and local coordinate systems are related by the position vector $\vec{R} = \vec{O}o$ while the local system and the body-fixed system are related by three Euler angles $\underline{\Theta}^T = (\psi, \theta, \phi)$ defined by the sequence of rotations:

$$(xyz) \xrightarrow[\text{about } oz]{\text{rotate } \psi} (xyz)_* \xrightarrow[\text{about } oy_*]{\text{rotate } \theta} (xyz)_{**} \xrightarrow[\text{about } ox_{**}]{\text{rotate } \phi} (ox'y'z') \quad (3.33)$$

Corresponding to the general motions of ships, ψ , θ , and ϕ are the yaw, pitch and

roll angles. By convention, the Euler angles are defined in the following ranges: $0 \leq \psi < 2\pi$; $-\pi/2 \leq \theta \leq \pi/2$; $0 \leq \phi < 2\pi$.

The components of any vector can be transformed between the local coordinate system and body-fixed systems through the rotation matrix \underline{L} :

$$\underline{v}' = \underline{L} \underline{v} \quad (3.34)$$

with \underline{v} being a general column vector in the local system and \underline{v}' being the transformation of \underline{v} in the body-fixed system. The rotational matrix, \underline{L} , is defined as

$$\underline{L} = \begin{bmatrix} \cos\psi\cos\theta & \sin\psi\cos\theta & -\sin\theta \\ -\sin\psi\cos\phi + \cos\psi\sin\theta\sin\phi & \cos\psi\cos\phi + \sin\psi\sin\theta\sin\phi & \cos\theta\sin\phi \\ \sin\psi\sin\phi + \cos\psi\sin\theta\cos\phi & -\cos\psi\sin\phi + \sin\psi\sin\theta\cos\phi & \cos\theta\cos\phi \end{bmatrix} \quad (3.35)$$

Note that \underline{L} is an orthogonal transformation so that $\underline{v} = \underline{L}^T \underline{v}'$.

The velocity of the body's gravitational center, \vec{v}_o , and \vec{R} are related by

$$\vec{v}_o = \dot{\vec{R}} \quad (3.36)$$

The rate of change of the Euler angles, $\underline{\Theta}$, is given by, in terms of the angular velocity of the ship, $\underline{\omega}'$ (in the body-fixed coordinate system)

$$\dot{\underline{\Theta}} = \underline{W} \underline{\omega}' \quad (3.37)$$

where \underline{W} is defined as

$$\underline{W} = \begin{bmatrix} 1 & \sin\phi\sin\theta/\cos\theta & \cos\phi\sin\theta/\cos\theta \\ 0 & \cos\phi & -\sin\phi \\ 0 & \sin\phi/\cos\theta & \cos\phi/\cos\theta \end{bmatrix} \quad (3.38)$$

Note that equation (3.38) is not defined when $\theta = \pm\pi/2$ which corresponds to the so-called gimbal lock.

To obtain the instantaneous body motions and body position, equations of rigid body motions need to be solved. The equation of body translational motion, with respect to the center of gravity o , can be written as:

$$\frac{d}{dt}(m\vec{v}_o) = \vec{F}_o \quad (3.39)$$

where m is the body mass and \vec{F}_o the total external force acting on the body. In our fully nonlinear numerical simulations of wave-body interactions, the total force, \vec{F}_o , can be evaluated by integrating the total pressure over wetted body surface. Comparatively, in the linear numerical simulations, components of \vec{F}_o induced by the diffraction problem, radiation problem, and the hydrostatics have to be evaluated separately and the equations of body motions are complex.

The equation of rotational body motion is, referred to o :

$$\frac{d\vec{H}_o}{dt} = \vec{M}_o \quad (3.40)$$

where \vec{M}_o is the external moment on body and \vec{H}_o the angular momentum (all with respect to the center of gravity o and referred to the local coordinate system). In the body-fixed coordinate system, we have

$$\underline{H}'_o = \underline{I}'_o \underline{\omega}' \quad (3.41)$$

where \underline{I}'_o is the body-frame moments and products of inertia matrix with size of 3×3 and it is time invariant ($\frac{d\underline{I}'_o}{dt} = 0$). The rate of change of the angular momentum in the body-fixed system can be written as

$$\frac{d\underline{H}'_o}{dt} = \underline{I}'_o \underline{\dot{\omega}}' + \underline{\omega}' \times \underline{I}'_o \underline{\omega}' \quad (3.42)$$

In view of equations (3.34) and (3.42), equation (3.40) can be reformed as

$$\underline{M}_o = \underline{L}^T (\underline{I}'_o \underline{\dot{\omega}}' + \underline{\omega}' \times \underline{I}'_o \underline{\omega}') \quad (3.43)$$

Notice that above rotational equation of motion in our fully nonlinear numerical scheme is also much simpler than that used in the linear numerical simulations.

Combining equations (3.36), (3.37), (3.39), and (3.43), we obtain the following system of equations governing the body motions in waves:

$$\frac{d}{dt} \begin{bmatrix} \underline{v}_o \\ \underline{\omega}' \\ \underline{R} \\ \underline{\Theta} \end{bmatrix} = \begin{bmatrix} \underline{E}^{-1} \underline{q} \\ \underline{v}_o \\ \underline{W} \underline{\omega}' \end{bmatrix} \quad (3.44)$$

where

$$\underline{E} = \begin{bmatrix} \underline{m} & \underline{0} \\ \underline{0} & \underline{L}^T \underline{I}'_o \end{bmatrix} \quad (3.45)$$

and

$$\underline{q} = \left\{ \begin{array}{c} \underline{F}_o \\ \underline{M}_o - \underline{L}^T (\underline{\omega}' \times \underline{I}'_o \underline{\omega}') \end{array} \right\} \quad (3.46)$$

3.3.2 Stability analysis of time-integration schemes

Different time integration schemes can be employed to advance η and ϕ (or ϕ_D) on free surface based on Eq. (3.3) and Eq. (3.2) (or Eq. (3.11) and Eq. (3.12)). For illustration, we consider the case of linearized boundary conditions on free surface and analyze the stability of different time integration schemes. For simplicity, as an example, we discuss here only the treatment of two-dimensional problems.

For problems involving only oscillatory body motions (with $U = 0$)

If the floating body does not has forward speed and experiences oscillatory motions about its equilibrium position, the dynamic and kinematic boundary conditions on free surface, (Eq. (3.3) and Eq. (3.2) taken as an example), can be linearized as the following

$$\phi_t(x, y, z, t) = -g\eta, \quad \eta_t(x, y, t) = \phi_z, \quad \text{at } z = 0 \quad (3.47)$$

A typical first-order explicit scheme, Euler method, for updating η and ϕ based on Eq. (3.47) is

$$\eta^{n+1} = \eta^n + \Delta t \phi_z^n, \quad \phi^{n+1} = \phi^n - \Delta t g \eta^n \quad (3.48)$$

where the superscripts represent time step number ($\eta^n = \eta(t = n\Delta t)$). For illustration, the simple semi-implicit scheme, modified Euler method, can be written as

$$\eta^{n+1} = \eta^n + \frac{\Delta t}{2}(\phi_z^n + \phi_z^{n+1}), \quad \phi^{n+1} = \phi^n - \frac{g\Delta t}{2}(\eta^n + \eta^{n+1}) \quad (3.49)$$

Depending on the numerical accuracy and complexity required, numerous alternative schemes exist for the time integration of Eq. (3.3) and Eq. (3.2), including the commonly used Runge-Kutta second order method (RK2), predictor-corrector method, Runge-Kutta fourth order method (RK4) and so on.

The stability characteristics of different time-marching schemes can be analyzed by a Fourier-von Neumann approach (Yeung 1982). Set

$$\phi(x, y, z, n\Delta t) \equiv \phi^n e^{i(k_x x + k_y y)} e^{kz} \quad (3.50)$$

where k_x , k_y , and k are wave numbers and $k = \sqrt{k_x^2 + k_y^2}$. Based on Eq. (3.50), we have $\phi_z^n = k\phi^n$. Let η be of the form

$$\eta(x, y, n\Delta t) = \eta^n e^{i(k_x x + k_y y)} \quad (3.51)$$

By substituting Eq. (3.50) and Eq. (3.51) into any time-marching scheme, we will obtain the following relation

$$\begin{bmatrix} \phi^{n+1} \\ \eta^{n+1} \end{bmatrix} = [G] \begin{bmatrix} \phi^n \\ \eta^n \end{bmatrix} \quad (3.52)$$

where matrix $[G]$ is the so-called amplification matrix (or growth matrix) whose spectral radius, R , decides the stability feature of the time-marching scheme. (Let the eigenvalues of $[G]$ be $\lambda^{(1)}$ and $\lambda^{(2)}$. The spectral radius of $[G]$ is $R = R(\Delta t, \Delta x, k) =$

$\max(|\lambda^{(1)}|, |\lambda^{(2)}|)$.) The von Neumann's condition for stability is that $R \leq 1$ for all wave number k (Lax & Richtmyer 1956).

The eigenvalues for the Euler method shown in Eq. (3.48) are:

$$|\lambda^{(i)}| = (1 + gk\Delta t^2)^{1/2} \quad i = 1, 2 \quad (3.53)$$

So, the Euler scheme is always unstable. While the modified Euler method in Eq. (3.49) results in the following eigenvalues

$$|\lambda^{(i)}| = 1 \quad i = 1, 2 \quad (3.54)$$

which indicates that this modified Euler scheme is a stable one, although error induced by the scheme does not decay, either. But since the modified Euler method is implicit, higher computational cost is needed for repeated evaluations. As we can see, this von Neumann stability analysis is simple but informative.

For completeness, we also study the stability regions of several other (explicit) schemes and obtain the following conclusions: RK2 is unconditionally unstable; the predictor-corrector scheme's stability condition is

$$\Delta t^2 \leq \frac{\Delta x}{g\pi} \quad (3.55)$$

and for a stable RK4, the following condition has to be satisfied:

$$\Delta t^2 \leq \frac{8\Delta x}{g\pi}. \quad (3.56)$$

For problems involving a steady forward body motion (with $U \neq 0$)

When the body has a steady forward speed U , the linearized boundary conditions for the disturbance velocity potential (ϕ_D in Eq. (3.15)) on free surface are, in the

moving coordinate system fixed on the body:

$$(\phi_D)_t(x, y, z, t) = -g\eta_D + U(\phi_D)_x, \quad (\eta_D)_t(x, y, t) = (\phi_D)_z + U(\eta_D)_x, \quad \text{at } z = 0 \quad (3.57)$$

For Eq. (3.57), the way to evaluate $(\phi_D)_x$ and $(\eta_D)_x$ affect the stability of the overall time-marching scheme. Different finite-difference methods, including upwind, central difference, and downwind schemes, are all choices for $(\phi_D)_x$ and $(\eta_D)_x$ evaluations. For demonstration, we take several explicit time-marching schemes (RK2, Precorrector/Corrector, and RK4) combined with specified approaches for $(\phi_D)_x$ and $(\eta_D)_x$ evaluations as examples to show their stability characteristics in Table 3.1:

	RK2	Predictor/Corrector	RK4
3-pt U	$ 1 + \lambda_1 + \lambda_1^2/2 \leq 1$	$ 1 + \lambda_1 + \lambda_1^2 \leq 1$	$ 1 + \lambda_1 + \lambda_1^2/2 + \lambda_1^3/6 + \lambda_1^4/24 \leq 1$
3-pt C	unstable	$ 1 + \lambda_2 + \lambda_2^2 \leq 1$	$ 1 + \lambda_2 + \lambda_2^2/2 + \lambda_2^3/6 + \lambda_2^4/24 \leq 1$
3-pt D	unstable	unstable	unstable
5-pt U	$ 1 + \lambda_3 + \lambda_3^2/2 \leq 1$	$ 1 + \lambda_3 + \lambda_3^2 \leq 1$	$ 1 + \lambda_3 + \lambda_3^2/2 + \lambda_3^3/6 + \lambda_3^4/24 \leq 1$
5-pt C	unstable	$ 1 + \lambda_4 + \lambda_4^2 \leq 1$	$ 1 + \lambda_4 + \lambda_4^2/2 + \lambda_4^3/6 + \lambda_4^4/24 \leq 1$
5-pt D	unstable	unstable	unstable

Table 3.1: Stability conditions of sampled explicit time-marching schemes.

In Table 3.1, U, C, and D represent the upwind, central difference, and downwind finite difference schemes, respectively. Also,

$$\lambda_1 = i\Delta t \left\{ \frac{U}{2\Delta x} [(4 \sin \theta - \sin 2\theta) + i(3 - 4 \cos \theta + \cos 2\theta)] \pm \sqrt{gk} \right\}$$

$$\lambda_2 = i\Delta t \left(\frac{U}{\Delta x} \sin \theta \pm \sqrt{gk} \right)$$

$$\lambda_3 = i\Delta t \left\{ \frac{U}{12\Delta x} [(48 \sin \theta - 36 \sin 2\theta + 16 \sin 3\theta - 3 \sin 4\theta) + i(25 - 48 \cos \theta + 36 \cos 2\theta - 16 \cos 3\theta + 3 \cos 4\theta)] \pm \sqrt{gk} \right\}$$

$$\lambda_4 = i\Delta t \left(\frac{U}{3\Delta x} \sin \theta (4 - \cos \theta) \pm \sqrt{gk} \right)$$

where $\theta = k \cdot \Delta x \in [-\pi, \pi]$ so that $k \in [-\frac{\pi}{\Delta x}, \frac{\pi}{\Delta x}]$.

Based on Table 3.1, we can determine the combination of $(\Delta t, \Delta x)$ for certain specified time integration scheme so that values of $\phi_D(t + \Delta t)$ and $\eta_D(t + \Delta t)$ can be obtained stably based on Eq. (3.57). For example, if the 3-point central difference approach is used to evaluate $(\phi_D)_x$ and $(\eta_D)_x$ and the predictor/corrector method is applied for the time marching of $(\phi_D)_t$ and $(\eta_D)_t$, stability requires the following condition to be satisfied:

$$\Delta t \left(\frac{U}{\Delta x} \sin \theta + \sqrt{\frac{g\theta}{\Delta x}} \right) \leq 1 \quad (3.58)$$

for any $\theta \in [-\pi, \pi]$. The combination of 5-point central difference approach and RK4 as the time integration scheme results in the following stability region:

$$\Delta t \left(\frac{U}{3\Delta x} \sin \theta (4 - \cos \theta) + \sqrt{\frac{g\theta}{\Delta x}} \right) \leq \sqrt{8}. \quad (3.59)$$

The normalized form of Eq. (3.57) is

$$(\phi_D)_t(x, y, z, t) = -\eta_D + F_r \cdot (\phi_D)_x, \quad (\eta_D)_t(x, y, t) = (\phi_D)_z + F_r \cdot (\eta_D)_x, \quad \text{at } z = 0 \quad (3.60)$$

where $F_r = \frac{U}{\sqrt{gL}}$ with L as the characteristic length in the physical problem under study. For illustration, we show in Figure 3-3 the stability region of the time-marching scheme combining RK2 and 3-point upwind finite difference method, at $F_r = 0.4$. Along the black curve in Figure 3-3, the combination of normalized $(\Delta t, \Delta x)$ makes the amplitude of the spectral radius R of the amplification matrix $[G]$ be equal to 1. Below this curve, the overall time-marching scheme is stable (i.e., $|R| < 1$) while above the curve, numerical errors involved in the IBVP will grow with time. Inside the stable region, a larger Δx determines a wider choice of Δt value.

Figure 3-4 compares the stability region of Scheme 1 (combining RK4 with 3-point central difference method) and Scheme 2 (combining RK4 with 3-point upwind finite difference method), at $F_r = 0.4$. Clearly, Scheme 1 has a larger stable region than that of Scheme 2. From the numerical accuracy concern, central difference method over-performs upwind finite difference method. So, the overall performance of Scheme 1 is better.

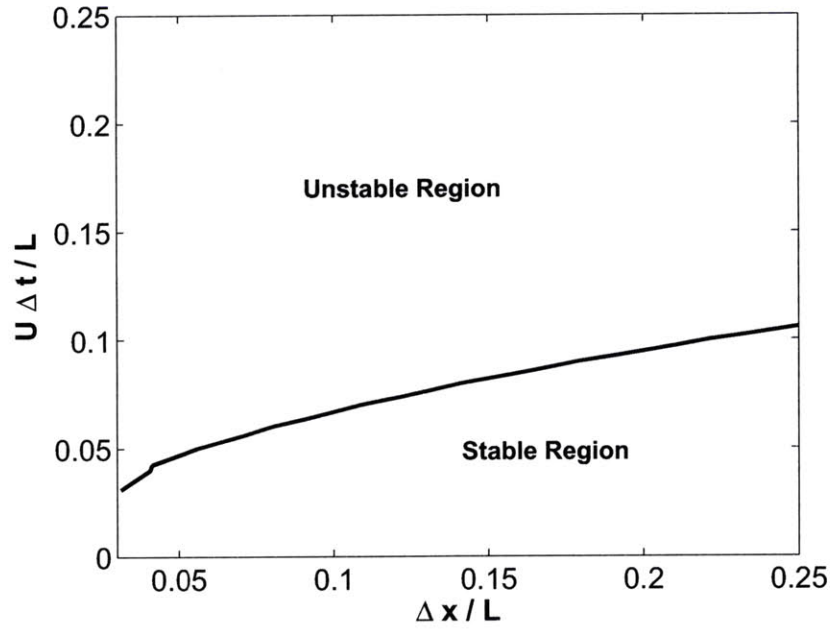


Figure 3-3: The stability diagram for the time-marching scheme composed of RK2 and 3-point upwind finite difference approach, at $F_r = 0.4$.

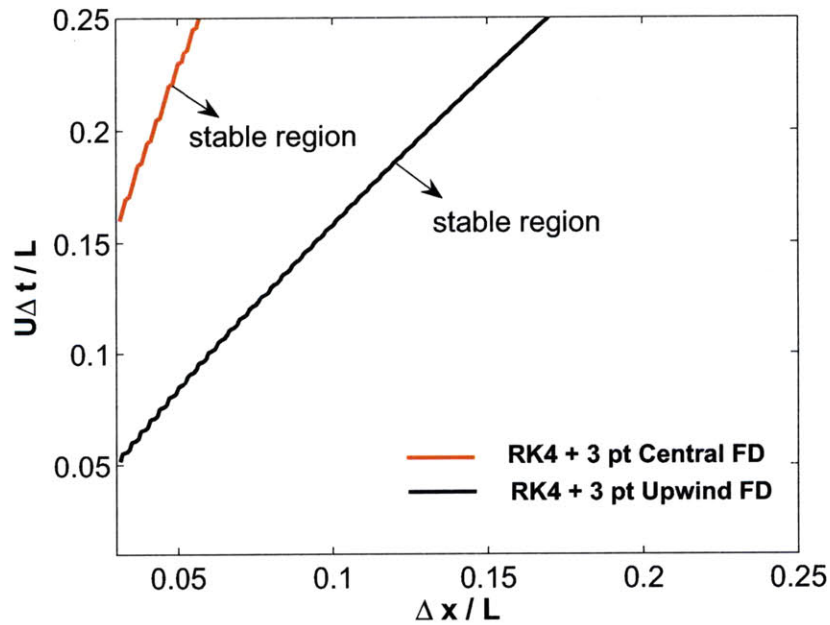


Figure 3-4: Comparison of the stability regions of Scheme 1 (combining RK4 with 3-point central finite difference approach) and Scheme 2 (combining RK4 with 3-point upwind finite difference approach), at $F_r = 0.4$.

Although our stability analysis for different time-marching schemes is based on the linearized forms of the free surface conditions (Eq. (3.57)), the conclusions obtained above can provide a guidance for the stability analysis of a specified time-marching scheme for fully nonlinear numerical problems. For instance, Table 3.1 shows that any time-marching scheme with backward finite difference approach involved is always unstable, no matter how the time integration schemes, time step Δt , and grid size Δx are chosen. Consider the waterline along the stern part of a body which moves forward in waves. To evaluate the quantities of $(\eta_D)_x$ and $(\phi_D)_x$ on the waterline, only downwind finite difference method can be employed, which means instability can easily appear and special care has to be taken near the stern part of the body in numerical computations.

3.3.3 Wave absorbing zone on free surface

As shown in Eq. (3.31), finite region of free surface, \mathcal{F}_{in} , will be used in numerical simulations of wave-body interactions. Mathematically, the size of \mathcal{F}_{in} needs to be large enough so that outside of \mathcal{F}_{in} , disturbance wave is negligible. On the one hand, due to the out-traveling feature of disturbance waves, the outer boundary of \mathcal{F}_{in} with any fixed size will be eventually reached. On the other hand, available computational capacity limits the size of \mathcal{F}_{in} that can be implemented numerically. Damping zone, also called numerical beach or sponge layer, will be placed along the outer boundary of \mathcal{F}_{in} to minimize the (numerically) reflected waves and reduce numerical errors induced by the truncated free surface. Different damping zone treatments have been used in literature (Dommermuth & Yue 1988; Yonghwan Kim 1999; Koo & Kim 2006). Focuses of this section are to conduct brief theoretical analysis on general absorbing-beach schemes and then discuss the numerical issues related to the implementation of these schemes.

General absorbing-beach schemes

To simplify the theoretical analysis, we assume linearized free surface boundary conditions on the outer part of \mathcal{F}_{in} where absorbing-beach treatments are applied. (This assumption is valid since disturbance waves are small far away from the floating body.) With the most general damping treatment applied, the linearized kinematic and dynamic boundary conditions can be written as:

$$\frac{\partial \eta_D}{\partial t} = \frac{\partial \phi_D}{\partial z} + \alpha_1 \eta_D + \beta_1 \phi_D + \gamma_1 \frac{\partial \phi_D}{\partial n} \quad \text{on } z = 0 \quad (3.61)$$

$$\frac{\partial \phi_D}{\partial t} = -g\eta_D + \alpha_2 \eta_D + \beta_2 \phi_D + \gamma_2 \frac{\partial \phi_D}{\partial n} \quad \text{on } z = 0 \quad (3.62)$$

where α_i , β_i , and γ_i for $i = 1, 2$ are all damping parameters. In the above two equations, $\frac{\partial \phi_D}{\partial n}$ can be replaced by $\frac{\partial \phi_D}{\partial z}$ due to the linear wave assumption.

Suppose a (linear) disturbance wave with wave amplitude A , wave frequency ω , and wave number k ($k = \omega^2/g$) entering the damping zone. Its wave elevation and velocity potential can be written as:

$$\eta_D = \text{Re}\{Ae^{i(kx-wt)}\}, \quad \phi_D = \text{Re}\left\{\frac{Ag}{w}e^{kz}e^{i(kx-wt)}\right\} \quad (3.63)$$

By substituting Eq. (3.63) into Eq. (3.61) and Eq. (3.62), we can check how the damping treatment changes the incoming disturbance wave. The corresponding dispersion relation becomes

$$gk = \omega^2 - i\omega(\alpha_1 + \beta_2 + k\gamma_2) + (k\alpha_2 - g\beta_1 - gk\gamma_1 + \alpha_2\beta_1 - \alpha_1\beta_2 + k\alpha_2\gamma_1 - k\alpha_1\gamma_2) \quad (3.64)$$

To ensure the incident disturbance wave is damped, the ideal dispersion relation would be

$$gk = (\omega - i\nu)^2 \quad (3.65)$$

with $\nu > 0$. Comparing Eq. (3.64) and Eq. (3.65), we have

$$2\nu = \alpha_1 + \beta_2 + k\gamma_2 \quad (3.66)$$

and

$$\nu^2 = -(k\alpha_2 - g\beta_1 - gk\gamma_1 + \alpha_2\beta_1 - \alpha_1\beta_2 + k\alpha_2\gamma_1 - k\alpha_1\gamma_2) \quad (3.67)$$

Under these conditions, the damped wave elevation and velocity potential of disturbance wave inside the damping zone become:

$$\eta_D = \text{Re}\{Ae^{-\nu t}e^{i(kx-wt)}\}, \quad \phi_D = \text{Re}\left\{\frac{Ag}{w}e^{-\nu t}e^{kz}e^{i(kx-wt)}\right\} \quad (3.68)$$

which shows the absorbing-beach treatment effectively makes the amplitude of incident waves decrease with time.

There is a lot of freedom to choose the values of those damping parameters (α_i , β_i , and γ_i for $i = 1, 2$) to make Eq. (3.66) and Eq. (3.67) hold. In the following, several popular combinations of these damping parameters are listed for demonstration:

$$(1) \alpha_1 = -2\nu; \beta_1 = \nu^2/g; 0 \text{ for all others} \quad (3.69)$$

$$(2) \alpha_1 = -\nu; \beta_2 = -\nu; 0 \text{ for all others} \quad (3.70)$$

$$(3) \alpha_1 = -\nu; \gamma_2 = -\nu/k; 0 \text{ for all others} \quad (3.71)$$

It's desirable to make the parameter ν in Eq. (3.65) smoothly vary over the damping zone to minimize reflection resulted from any sudden change of the free surface boundary conditions. The general expression for ν would be

$$\nu(x, y) = \begin{cases} 0 & \text{for } r < r_0 \\ \nu_0 f\left(\frac{r-r_0}{L_D}\right) & \text{for } r_0 < r < r_0 + L_D \end{cases} \quad (3.72)$$

where ν_0 is a constant, called the damping strength, $r(= \sqrt{x^2 + y^2})$ the transverse distance from body center, r_0 the transverse distance between the center of the body and the inner edge of damping zone, and L_D the width of damping zone.

When it comes to the fully-nonlinear free surface boundary conditions for disturbance velocity potential after certain damping scheme (say, scheme 3 defined in Eq.

(3.71)) is applied, Eq. (3.11) and Eq. (3.12) can be revised as:

$$\frac{D\eta}{Dt} = \frac{\partial\phi_I}{\partial z} + \frac{\partial\phi_D}{\partial z} - \nu(x, y)(\eta - \eta_I), \quad \bar{x} \in \mathcal{F}(t), \quad (3.73)$$

and

$$\frac{D\phi_D}{Dt} = -\frac{\partial\phi_I}{\partial t} + \frac{1}{2}(\nabla\phi_I + \nabla\phi_D)(\nabla\phi_D - \nabla\phi_I) - gz - \frac{\nu(x, y)}{k_I}(\phi_D)_n, \quad \bar{x} \in \mathcal{F}(t) \quad (3.74)$$

where k_I can be set as the dominant incident wave number.

Key numerical issues in the implementation of damping-zone treatment

There are several questions to be answered before we can implement absorbing-beach treatments in the free surface boundary conditions: what is a proper damping zone size, L_D ? How would damping treatments perform with different combinations of damping strength ν_0 and damping function f in Eq. (3.72)? which damping scheme is better? and how would damping treatments perform when incident wave has multiple wave components? Systematic numerical tests are conducted to address these issues.

The first example we choose to demonstrate the performance of absorbing-beach treatment is the numerical simulation for the free decay of a truncated circular cylinder's heave motion. With the absorbing-beach treatments applied along the outer boundary of the computational free surface, the time history of the body's motion is recorded. The cylinder has a diameter $D = 91.6\text{m}$ and a draft $H = 27\text{m}$. The weight of this cylinder is $m = 1.778 \times 10^8\text{kg}$. Based on the long-wave approximation (Faltinsen 1990), we can estimate the added mass of this cylinder as $A_{33} = \rho\pi D^3/12$. The hydrostatic restoring coefficient, from linear theory, can be evaluated as $C_{33} = \rho g A_{wp}$ with A_{wp} being the mean water-plane area of the cylinder. From above information, the natural period of body heave motion is approximated using the formula: $T_0 = 2\pi/\sqrt{\frac{C_{33}}{m+A_{33}}} = 15.2\text{s}$. The corresponding natural wave length λ_0 as well as wave number κ_0 can then be determined. For the numerical results to be presented, T_0 and $1/\kappa_0$ are taken as the time and length scales for parameter normalization.

At $t = 0$, water surface is flat and the cylinder has an initial displacement in z direction, δ_0 , off its equilibrium position. The body is then set free at $t = 0^+$. A linearized IBVP solver, based on the efficient PFFT-QBEM, is adopted for the numerical simulations. With a big wave damping coefficient B_{33} , the body's heave motion amplitude decays fast with time. Ideally, body motion will be diminishing if no reflection waves come back to the system from the outer computational boundary.

(1) Effect of damping zone size L_D

First of all, the second wave-damping scheme in Eq. (3.70) is implemented and the time histories of body heave motions for different damping zone sizes are compared in Figure 3-5. In the simulations, the undamped computational domain has the size of two wave lengths in all directions, that is, $r_0 = 2\lambda_0$. Damping strength is set to be the natural heave frequency, i.e., $\nu_0 = \omega_0$. In addition, a quadratic damping function is used, i.e., $f(s) = s^2$.

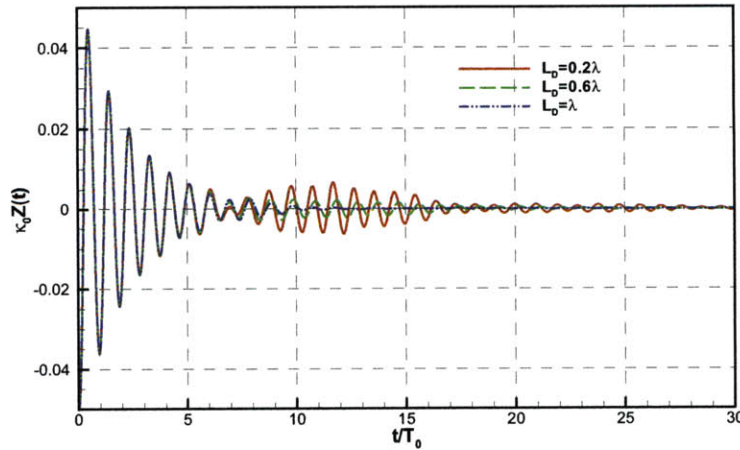


Figure 3-5: Comparison of the effects of damping zone sizes on the free-decay heaving motion of a floating cylinder. Three damping zone sizes are tested: $L_D = 0.2\lambda_0$ (—); $L_D = 0.6\lambda_0$ (---); and $L_D = \lambda_0$ (- · - ·).

From Figure 3-5, we can see that different damping zone sizes result in different amounts of reflected waves whose effects are visible for $t/T_0 > 5$. Results show that the size of $0.2\lambda_0$ is too small for the damping zone to be effective and increasing damping

zone size helps to reduce wave reflection from outer computational boundary. But increasing damping zone size results in growing computational effort as larger overall computational domains are involved in the computations. A proper damping zone size is eventually decided by both the accuracy required for numerical results and computational cost limited by the computational capacity.

(2) Effects of damping strength ν_0 and damping function f

With all other settings fixed (second scheme in Eq. (3.70), $r_0 = 3\lambda_0$, $L_D = 0.5\lambda_0$, $f(s) = s^2$ in Eq. (3.72)), by varying only the damping strength ν_0 , we plot the time histories of the cylinder's free decay motions in Figure 3-6. Too small (e.g., $0.2\omega_0$) or too big (e.g., $2\omega_0 \sim 3\omega_0$) damping strengths all results in strong wave reflections from the damping zone. Based on the numerical tests, we propose $0.5\omega_0 \sim 1\omega_0$ a reasonable range for ν_0 to achieve effective wave-damping effect.

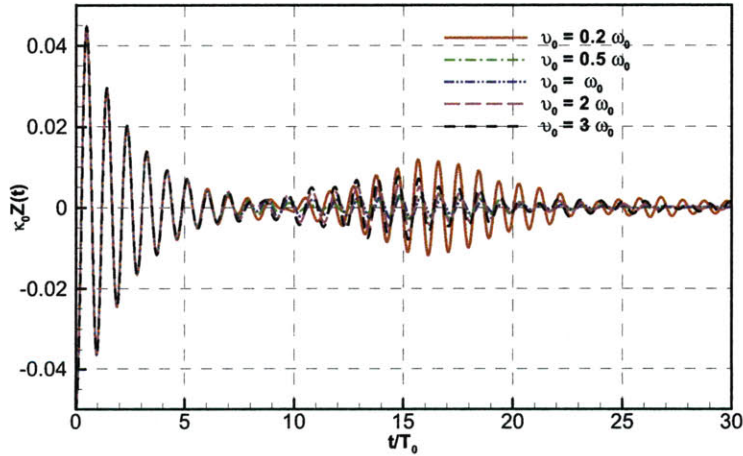


Figure 3-6: Time history of the free-decay heaving motion of a floating cylinder. Comparison between different curves reflects the performance of the absorbing-beach treatments with different specified damping strengths: $\nu_0 = 0.2\omega_0$ (—); $\nu_0 = 0.5\omega_0$ (- -); $\nu_0 = \omega_0$ (- · · -); $\nu_0 = 2\omega_0$ (- · -); $\nu_0 = 3\omega_0$ (- - -).

The choice for damping function f in Eq. (3.72) is quite flexible. For instance, a quadratic function $f(s) = s^2$ was used by Yonghwan Kim (1999) and a cosine function $f(s) = 1 - \cos(\frac{\pi}{2}s)$ was implemented by Koo & Kim (2006). To see whether a highly

smooth damping function improves the performance of the absorbing-beach scheme, we also test f as the Hermitian polynomial defined as:

$$f(s) = 1 - \Pi(s) \text{ with } \Pi(s) = 1 - 462s^6 + 1980s^7 - 3465s^8 + 3080s^9 - 1386s^{10} + 252s^{11}. \quad (3.75)$$

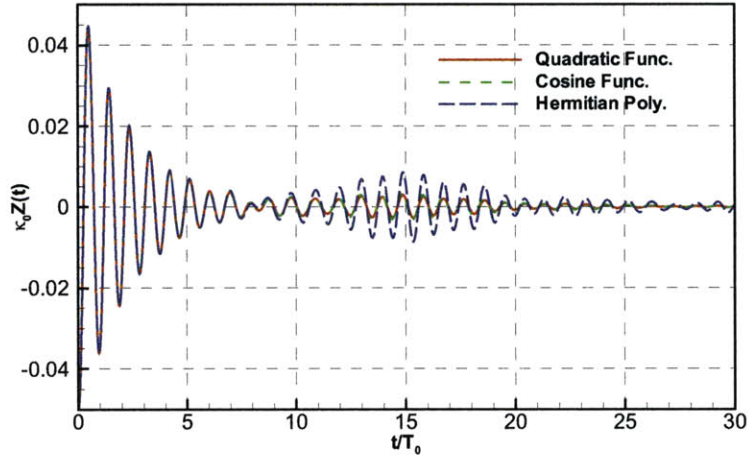


Figure 3-7: Performances of absorbing-beach treatments using different damping functions (Quadratic Func.(—); Cosine Func.(- - -); and Hermitian Poly.(- · · -)), seen from the time history of a floating cylinder’s free heave decay motion.

Figure 3-7 compares the performance of damping zone treatments with different damping functions. Among all, the Hermitian polynomial produces the most significant wave reflection and the quadratic function over-performs the cosine function. (For this group of results, the second scheme in Eq. (3.70) is implemented with $r_0 = 3\lambda_0$, $L_D = 0.5\lambda_0$, and $\nu_0 = \omega_0$.)

(3) Comparison of different absorbing-beach schemes

Based on the theoretical analysis for general damping treatments, schemes listed in Eq. (3.69) ~ Eq. (3.71) should result in same wave-damping effect and they are all expected to make the waves entering the damping zone decay exponentially at the rate of $-\nu t$, as shown in Eq. (3.68). By setting $r_0 = 3\lambda$, $\nu_0 = \omega_0$, $f(s) = s^2$, and $L_D = 0.5\lambda$, we implemented all these three wave-damping schemes and compare their

performances in Figure 3-8. Effects of wave reflections using these three schemes do not differ much and comparatively speaking, the scheme defined in Eq. (3.71) has the best performance.

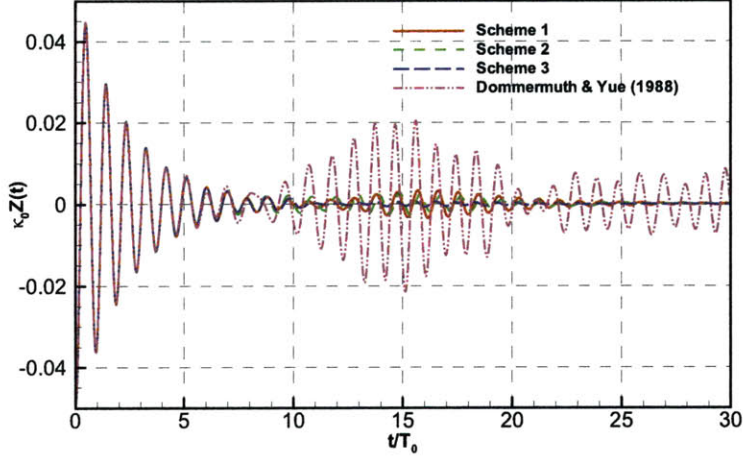


Figure 3-8: Influences of different wave-damping schemes on the results of a floating cylinder's free heaving decay motions: Scheme 1 (Eq. (3.69))(—); Scheme 2 (Eq. (3.70))(- -); Scheme 3 (Eq. (3.71))(- -); and the scheme used by Dommermuth & Yue (1988)(- · · -);

For demonstration, we also include in Figure 3-8 the performance of the wave-damping approach used by Dommermuth & Yue (1988). In their scheme, the kinematic and dynamic free surface boundary conditions were not adjusted by any damping terms. Instead, they directly multiply wave elevation and wave velocity potential by a tapering function $\Omega(x, y, r_0, L_D)$ inside the damping zone. Their tapering function takes the following form:

$$\Omega(x, y, r_0, L_D) = \begin{cases} 1 & \text{for } r < r_0 \\ \Pi\left(\frac{r-r_0}{L_D}\right) & \text{for } r_0 < r < r_0 + L_D \end{cases} \quad (3.76)$$

where Π is the Hermitian polynomial defined in Eq. (3.75). From Figure 3-8, we can see that this absorbing-beach scheme has too weak wave damping effect and it should not be a favorable choice for the numerical studies of general wave-body interactions.

(4) Performance of damping treatments for waves of multiple components

In the above example of the cylinder's free decay heave motions, we know the disturbance wave coming into the damping zone has the (dominant) natural heave frequency so that we can adjust the damping strength ν_0 and damping zone size L_D accordingly in relation with wave parameters ω_0 and λ_0 . But in general wave-body interaction problems, disturbance waves may contain many wave components due to body motions excited by incident waves of multiple frequencies. In numerical simulations, (transient) disturbance waves of multiple frequencies could be caused by the initial startup of the computations.

How should we choose damping parameters to minimize wave reflections in multiple wave frequencies? Damping zone size L_D may be relatively easy to decide in theory based on our previous studies. If L_D can be tuned in accordance with the longest wavelength and all other damping parameters are properly set, wave damping effect should be good for all wave components. But note that the upper bound of L_D is restricted by overall computational cost. Proper value of damping strength ν_0 is difficult to determine. With a specified wave frequency ω , the reasonable choice of ν_0 is around $0.5\omega \sim 1\omega$. Depending on the frequency range of the waves entering damping zone, we might not be able to find a value of ν_0 which makes the overall performance of damping treatment acceptable.

In the following, we use a simple numerical example to show how a damping scheme with all damping parameters fixed performs for different wave frequencies. The same cylinder as in the last numerical example is forced to have oscillatory heave motion with amplitude A_h and frequency ω , i.e.,

$$Z(t) = -A_h \sin(\omega t). \quad (3.77)$$

This radiation problem with three different heave frequencies ($\omega_1 = 0.7$ rad/s, $\omega_2 = 0.44$ rad/s, and $\omega_3 = 0.256$ rad/s) are numerically simulated in time domain. The damping scheme defined in Eq. (3.71) is implemented with the following parameter settings: $\nu_0 = 0.6\omega_1$, $L_D = 0.5\lambda_1$, and $r_0 = 3\lambda_1$ with λ_1 being the corresponding wave

length for wave frequency ω_1 . The hydrodynamic force $F_D(t)$ on the cylinder is evaluated as:

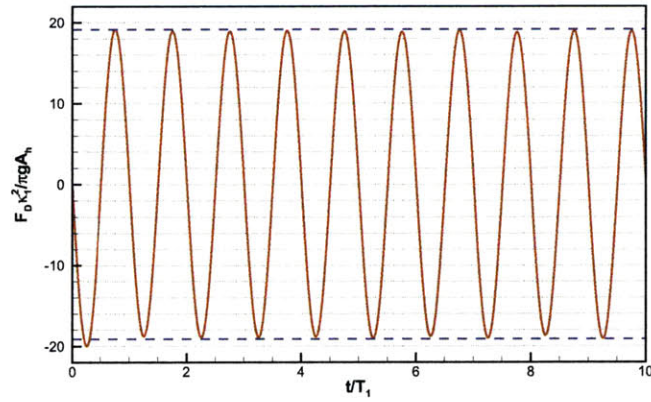
$$F_D = -A_{33}(\omega)\frac{dZ^2(t)}{dt^2} - B_{33}(\omega)\frac{dZ(t)}{dt} \quad (3.78)$$

where A_{33} and B_{33} are added mass and damping coefficient and they are all functions of wave frequency. The time histories of the hydrodynamic force on the cylinder at these three wave frequencies are shown in Figure 3-9, with time and force normalized by $2\pi/\omega_1$ and $\rho g A_h/\kappa_1^2$, respectively. Accurate values of the amplitudes of hydrodynamic forces (evaluated from a frequency-domain BVP solver which is also developed from PFFT-QBEM) are included in Figure 3-9 (in blue dashed line) for reference.

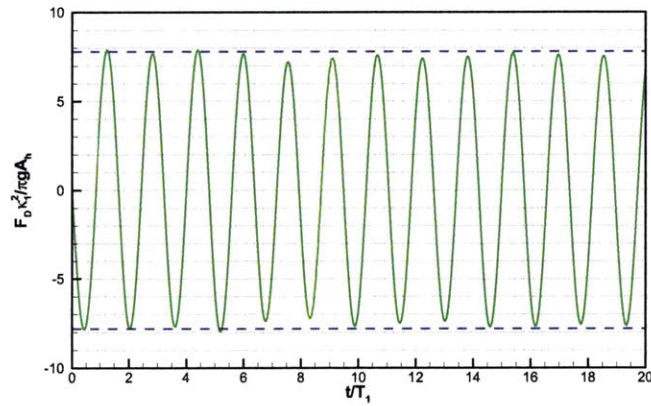
Since current damping parameter setting well suits incident wave with frequency ω_1 , the effect of wave reflection from damping zone on $F_D(\omega_1, t)$ is negligible, as confirmed by Figure 3-9a. The damping zone size $L_D = 0.5\lambda_1$ is small for incident wave at frequency ω_2 as $L_D \approx 0.2\lambda_2$ and effect of wave reflection on the hydrodynamic force can be observed in Figure 3-9b. With respect to the wave frequency ω_3 , current value of L_D becomes too small and more importantly, the whole undamped computational domain r_0 is only $\sim 0.4\lambda_3$. As a result, obvious difference can be observed between present numerical result for the amplitude of F_D and the accurate force-amplitude value. But overall, from the engineering point of view, these numerical results may be acceptable, because the damping effects become gradually stabilized with time, for all three specified wave frequencies.

3.3.4 Tracking of wave-body intersection line

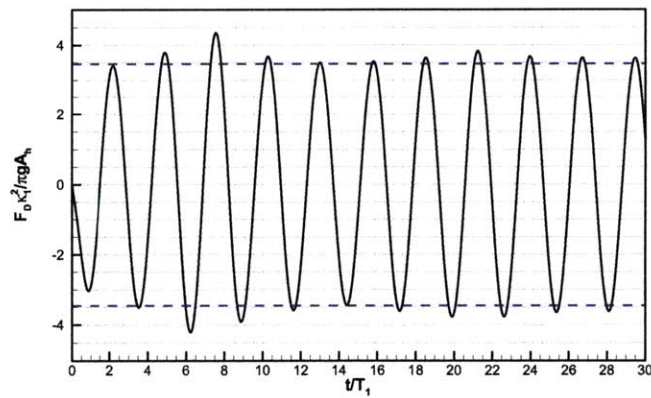
Obtaining the position of the wave-body intersection line is crucial for fully nonlinear numerical simulations of wave-body interactions as the intersection line determines the instantaneous wetted body surface over which the BVP at each time step is defined and pressure is integrated to obtain wave loads acting on body. Wave loads then directly connect to body motions and waterline-position tracking is related to the overall accuracy of numerical solutions. In practice, the information of wave profile (decided by the wave-body intersection line) along body surface is very important for



(a)



(b)



(c)

Figure 3-9: Hydrodynamic force history on a cylinder undergoing described oscillatory heave motions at different frequencies: (a) $\omega_1 = 0.7\text{rad/s}$ (—); (b) $\omega_2 = 0.44\text{rad/s}$ (—); and (c) $\omega_3 = 0.256\text{rad/s}$ (—). Accurate values (- -) of the hydrodynamic force amplitude are also present in all plots for reference.

the design of marine structures' geometry configurations.

In the MEL approach, the evolution of the wave-body intersection line is determined by following the motions of Lagrangian points. The velocities of these Lagrangian points need to be evaluated accurately in order for a reliable tracing of the wave-body intersection evolution. Our fully nonlinear numerical scheme, PFFT-QBEM, allows the collocation at the exact wave-body intersection. Double-node technique is applied along the intersection to treat the confluence of different types of boundary conditions (Dirichlet boundary condition *vs.* Neumann boundary condition). Numerical tests using canonical boundary value problems show that double-node technique can provide reliable predictions of the velocity potential and normal velocity on the wave-body intersection line, which is a great advantage of QBEM-based BVP solver over CPM-based scheme. (See double-node treatment applications also in Lin, Newman & Yue 1984; Dommermuth & Yue 1987; and Liu, Xue & Yue 2001).

Even with the effective double-node treatment applied along the intersection line, updating waterline position accurately over time is still quite challenging for the numerical study of general nonlinear wave-body interactions. Depending on the physical problems, there are several possible factors contributing to this difficulty:

- (1) lower accuracy in velocity evaluation along the wave-body interaction line. From the Green-theorem based BIE, ϕ and ϕ_n are known on all boundary surfaces after BVP is solved at each time step. To update waterline position, we need the information of tangential velocity ϕ_τ which combines ϕ_n to give velocities in all directions. ϕ_τ can be evaluated from ϕ using finite different (FD) method on boundary surfaces, but only one-side FD method can be adopted for collocation points along waterline as the body surface does not smoothly connect with the free surface in general. This results in deterioration in the accuracy of velocity evaluation there. With more collocation points available along and near the intersection, more accurate velocity could be obtained there, but larger computational effort is demanded as well.

- (2) stability concern along the waterline especially for problems involving forward body motions. From previous stability analysis, we know that stability criteria cannot be satisfied along the waterline on the stern part of the body surface, no matter which time integration scheme is adopted.
- (3) existence of singularity along the waterline on the bow part of body surface, if body has an impulsively-started forward motion ($U \neq 0$) (Lin, Newman & Yue 1984).
- (4) deviation of intersection line from body surface. Due to the finite time step size used in numerical integrations of intersection velocity, the newly updated intersection position might depart from body surface. Any extra numerical treatment to fix this problem will deteriorate the overall accuracy of the scheme to some extent.

Due to the reasonings in (2) and (3), tracking the accurate wave-body intersection for the case of forward moving body ($U \neq 0$), like ships, is in general more difficult than that for zero-speed ($U = 0$) case. In many existing numerical studies for the forward-moving Wigley hull (Lin, Kuang & Reed 2005; Tarafder & Suzuki 2008), large discrepancies can be observed between numerical results and experimental measurements for the wave profile along the body surface, but Fuat *et al.* (2007) obtained good agreement for that waterline position. In the work of Fuat *et al.* (2007), a nonlinear constant-panel-based *source formulation method* is implemented for the solution of the IBVP. The results of Fuat *et al.* (2007) motivated our study on the performance of source formulation for general wave-body interaction problems.

By skipping all the numerical scheme details, we only summarize here the conclusions achieved from our numerical study about the strength and weakness of the source formulation method as a BVP solver, in comparison with our Green-theorem-based approach. The appealing feature of the source formulation method is that once the source strength on each boundary element is solved, velocity (in any direction) can be readily evaluated with similar accuracy as that for the computations of the

velocity potential (on Neumann surface) or the normal velocity (on Dirichlet surface). However, for the source formulation method, it is not reasonable to place sources along the intersection of discontinuous surfaces since the resulting velocity values along the intersection would be infinity. As a result, for velocity evaluations along waterline, certain extrapolation scheme has to be used based on velocity distributions on interior boundary surfaces. In contrary, the Green-theorem-based method combining with QBEM collocates along sharp edges of boundary surfaces and fast-converged solutions for velocity potential and normal velocities can be obtained there. The shortage of the Green theorem method, though, is that the accuracy in (tangential) velocity evaluation is inferior than that for velocity potential or normal velocities on boundary surfaces.

Systematical numerical experiments are conducted for both the source formulation and the Green-theorem scheme to solve well-defined canonical two-dimensional and three-dimensional interior/exterior problems with/without continuous boundaries. By comparing with the solutions obtained from Green theorem scheme for velocity potential and normal velocities, source formulation method obtains not only larger errors on both the interior and edges of surfaces but also slower convergence rate. Besides, source formulation method does not provide better accuracy in velocity evaluation than Green-theorem method for problems with continuous/discontinuous boundary surfaces.

Several other numerical issues are also important for fully-nonlinear numerical simulations of wave-body interactions. These include smoothing of free surface to avoid saw-tooth instability, free-surface grid generation and regeneration, and specification of initial conditions on body surface for the solution of IBVP. Successful analyses/treatments for these issues can be found in many existing studies (Xue 1997; Liu, Xue & Yue 2001; Bai & Taylor 2006).

3.4 Applications to sample fully-nonlinear wave-body interactions

The newly-developed efficient IBVP solver, which combines the PFFT-QBEM (as the BVP solver) with the 4th order Runge-kutta (RK4) time integration method, is implemented for the simulations of fully nonlinear three-dimensional wave-body interactions. To validate this IBVP solver and to investigate the effect of nonlinearity on wave-body interactions, we choose to study the following representative wave-body interaction problems including a radiation problem, a diffraction problem, and a wave resistance problem.

3.4.1 Forced heave oscillations of a sphere

A sphere of radius R undergoes forced periodic heave oscillations with $Z(t) = -A \sin \omega t$ for $t > 0$. Three different numerical schemes, including linear, body nonlinear, and fully nonlinear PFFT-QBEM, are implemented with the purpose of investigating effects of various level of nonlinearity. Initially, the sphere is semi-submerged and the water surface is undisturbed. In the simulations, we use $\omega^2 R/g = 1$, 36 collocation points per wavelength, and 60 time steps per wave period.

The time histories of the hydrodynamic force (normalized by $\rho g \pi R^2 A$ with A being the amplitude of forced heave motion) from the linear, body nonlinear, and fully nonlinear simulations (with a fixed motion amplitude $A = 0.375R$) are compared in figure 3-10. In this case, body nonlinearity is seen to account for most of the nonlinear effect in the radiation force magnitude.

To see the effect of body motion amplitude on the hydrodynamic force, we plot in figure 3-11 the time histories of the (normalized) vertical hydrodynamic forces acting on the sphere, obtained from linear and fully nonlinear (for different A/R values) numerical simulations. As expected, the difference grows between the nonlinear curves and the linear one as A/R increases. Corresponding to larger heave amplitudes, the curves show sharper and higher peaks and shallower troughs.

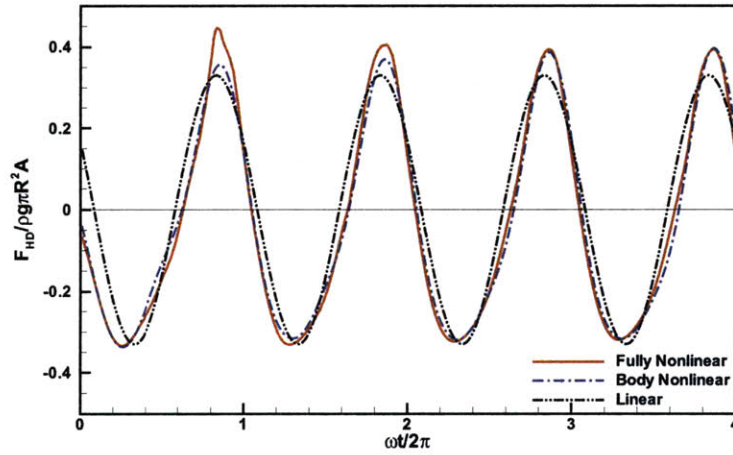


Figure 3-10: Comparison of the hydrodynamic force on a periodically heaving sphere with $A/R = 0.375$ among linear(- · · -), body-nonlinear(- - -), and fully-nonlinear(—) numerical results.

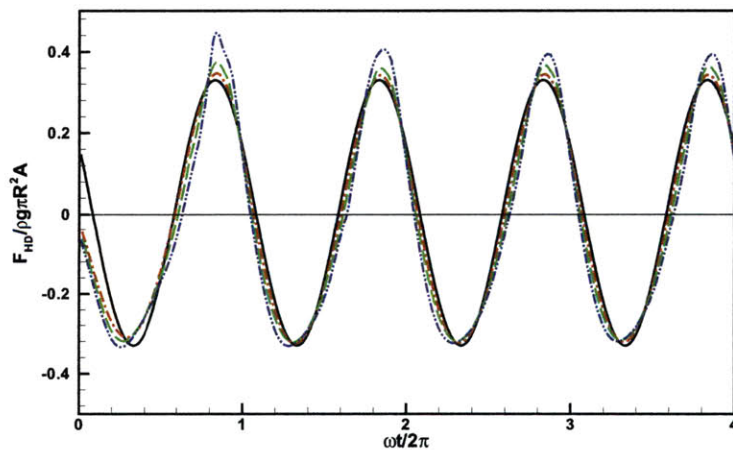


Figure 3-11: Comparison of hydrodynamic force on a periodically heaving sphere with different motion amplitudes: linear(—), $A/R = 0.125$ (- · · -), $A/R = 0.25$ (- - -), and $A/R = 0.375$ (- · · -). Except the linear one, all results are obtained from fully nonlinear numerical simulations.

A/R	$f_0/\rho g \pi R A^2$	$ f_1 /\rho g \pi R^2 A$		$ f_2 /\rho g \pi R A^2$
	hydrodynamic	hydrodynamic	total	hydrodynamic
Linear	—	0.3323	0.7341	—
0.125	-0.0864	0.3328	0.7267	0.174
0.25	-0.0808	0.3338	0.7178	0.179
0.3	-0.0789	0.3392	0.7102	0.187
0.375	-0.0768	0.3449	0.7007	0.193

Table 3.2: Harmonic force coefficients for the periodically heaving sphere, with different A/R .

A detailed analysis of the frequency components of the hydrodynamic force can be conducted on the steady-state time history of the force through Fourier transform. We define the frequency components of the force as:

$$F(t) = \Re[f_0 + f_1 e^{i\omega t} + f_2 e^{i2\omega t} + \dots] \quad (3.79)$$

Table 3.2 shows the normalized form for the hydrodynamic as well as the total force harmonics, obtained from linear and fully nonlinear numerical calculations for different A/R settings. As we can see, the mean hydrodynamic force on the sphere is negative and its amplitude (after normalization) decreases slowly with heave motion amplitude. The first- and second- harmonic components have normalized hydrodynamic forces growing with the value of A/R . But the normalized amplitude of the first-harmonic total force reaches its maximum value as $A/R \rightarrow 0$ (i.e., from the linear calculation).

Figure 3-12 shows the normalized force components of f_1 (at body motion frequency) in phase and out of phase with body acceleration. These quantities are referred as the large-amplitude added mass and damping coefficient and their normalized values, based on the fully nonlinear solution, all slowly increase with sphere heave amplitude. The linear result also presented in Figure 3-12 agrees perfectly with Hulme's (1982) theoretical solution derived based on linear wave assumption. Body nonlinear results show a decreasing (increasing) tendency of the added mass (damping) and the difference between body-nonlinear results and fully-nonlinear results

reflects the effect of free surface nonlinearity. Note that the body-nonlinear results in Figure 3-12 agree with those of Lin & Yue (1990) (which also used body-nonlinear scheme) in the variation trend of added mass/damping coefficient but not the exact values. We believe that this is due to the low accuracy associated in the low-order panel method (CPM) used in Lin & Yue (1990).

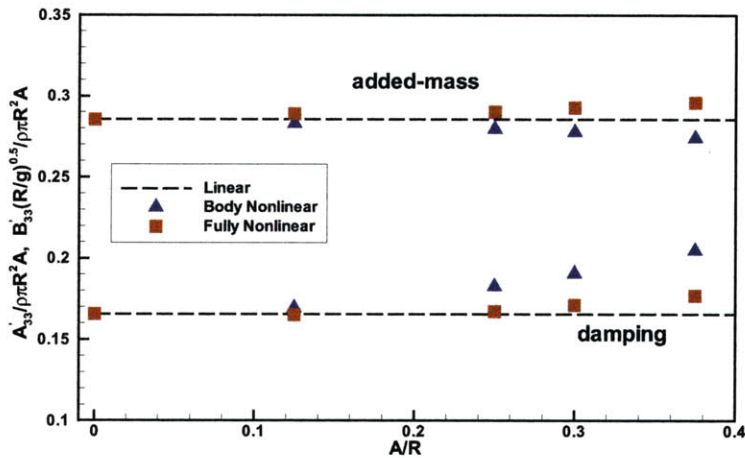


Figure 3-12: Variations of the added-mass (in phase with body acceleration) and damping coefficient (out of phase with body acceleration) of a sphere undergoing periodic heave motion with different A/R . Linear (Hulme 1982, $---$), body nonlinear (\blacktriangle), and fully nonlinear (\blacksquare) results are all presented.

For completeness, we also compare the wave profiles induced by the heaving oscillation of the sphere at $t/T = 4$ with different A/R values, based on fully nonlinear numerical simulations. For larger body heave amplitudes, the wave profiles are more deformed away from the linear (smooth) one.

3.4.2 Ringing loads on a vertical cylinder in Stokes waves

The diffraction of steep Stokes waves by a fixed truncated vertical circular cylinder is studied using fully nonlinear PFFT-QBEM simulations. The purpose is to demonstrate the capability of present numerical scheme in evaluating high-order high-harmonic ringing loads on the cylinder due to steep wave diffraction.

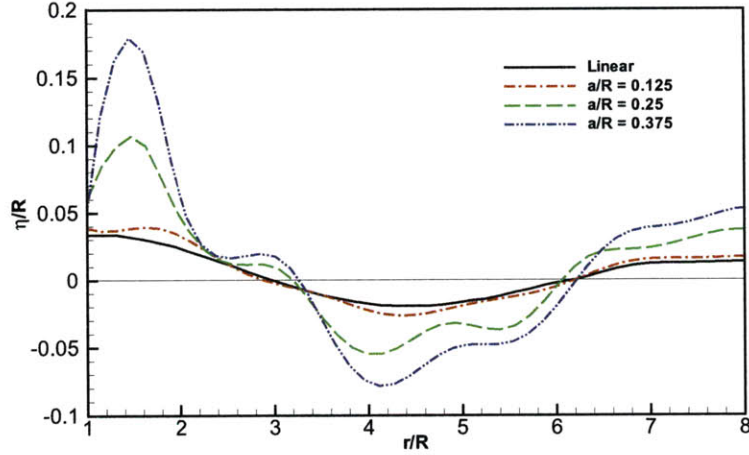


Figure 3-13: Comparison of the instantaneous wave profiles induced by the periodically heaving sphere at $t/T = 4$ among linear result(—) and fully nonlinear results with $A/R = 0.125$ (- - -), $A/R = 0.25$ (- - -), and $A/R = 0.375$ (- · · -).

The surface-piercing cylinder has a radius R and draught H , in the presence of an exact Stokes wave train with wave amplitude A , wave number k and fundamental wave period T . For illustration, we present here the results for $kR = 0.39$, $kA = 0.148$, and $H/R = 3$. In the computation, we use 156 QBEM elements on the body surface, 24 nodes per wavelength, and 100 time-steps per wave period.

The time histories of up-wave and down-wave runups are shown in Figure 3-14. Highly nonlinear and high harmonic features are displayed in the record in view of the incident wave amplitude.

The normalized amplitudes of force harmonics, $f_m, m = 1, 2, 3$ (defined in Eq. (3.79)), are listed in Table 3.3. (Note that the force harmonics are normalized the same way as that in Liu, Xue & Yue 2001.) Comparisons are made among experimental measurements (Krokstad & Stansberg 1995, MARINTEK), present fully nonlinear numerical result (PFFT-QBEM), (frequency-domain) small-body asymptotic theory (Faltinsen et al. 1995, FNV), and the second-order frequency-domain computations (Kim & Yue 1989, KY). Among the numerical and asymptotic results, present fully nonlinear numerical result agrees the best with the experimental measurements (MARINTEK).

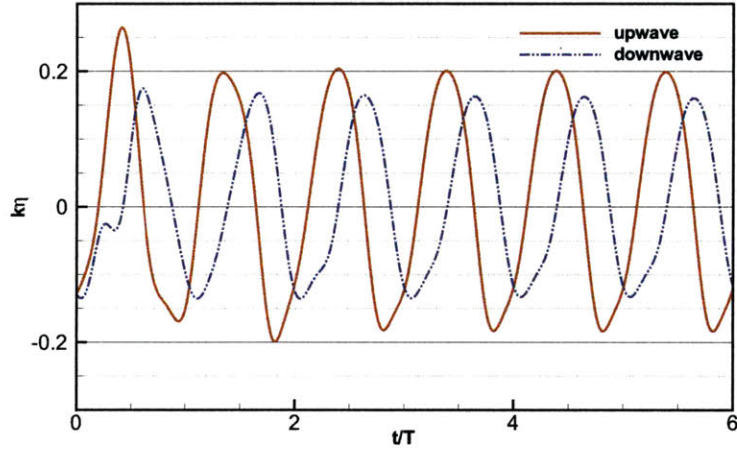


Figure 3-14: Time histories of the up-wave and down-wave runups on a fixed truncated circular cylinder in a Stokes wave train.

	$ f_1 (kA)/\rho g R^3$	$ f_2 (kA)^2/\rho g R^3$	$ f_3 (kA)^3/\rho g A^3$
MARINTEK	11.07	3.04	0.50
PFFT-QBEM	11.15	2.83	0.49
FNV	11.31	9.85	0.95
KY	10.99	4.38	—

Table 3.3: Comparisons of the (normalized) amplitudes of force harmonics $f_m, m = 1, 2, 3$ on a truncated vertical cylinder ($D/R=3$) under the action of a Stokes wave train ($kA = 0.148$).

3.4.3 Wave resistance of a Series 60 ship hull

We simulate the wave resistance problem of a Series 60 (S60) ship hull with block coefficient $C_B = 0.6$ moving with a constant forward speed ($F_r = V/\sqrt{gL} = 0.316$). The hull is held fixed in trim and sinkage. On half of the ship hull surface, we use 72 QBEM panels in the fully nonlinear PFFT-QBEM simulations. For comparison, numerical results from linear PFFT-QBEM and linear PFFT-CPM are also provided, for which 72 QBEM panels and 325 CPM panels are used on half of the S60 hull, respectively.

The steady wave profiles along S60 hull are compared in Figure 3-15 among numerical results obtained from fully nonlinear PFFT-QBEM, linear PFFT-QBEM, and linear PFFT-CPM. Also presented in Figure 3-15 are experimental data from Stern *et al.* (1996) and Toda *et al.* (1991). It can be seen that among all numerical results, the fully-nonlinear result agrees the best with experimental data although discrepancy exists especially near the bow region where flow is highly nonlinear. The numerical result from linear PFFT-QBEM compares better with experimental data than that from linear PFFT-CPM.

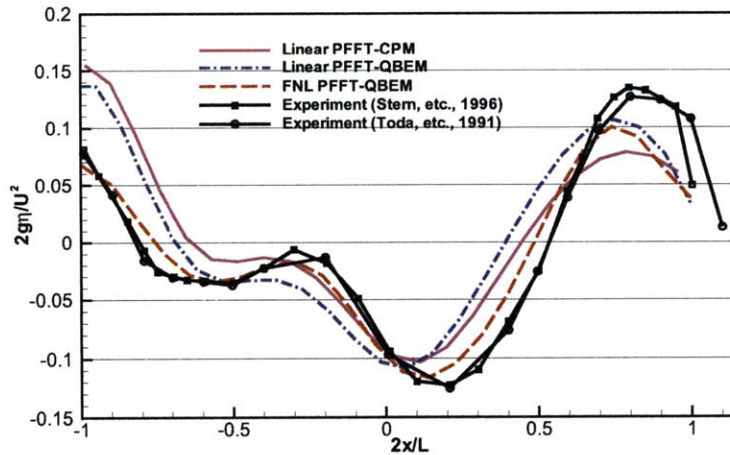


Figure 3-15: Comparison of wave profiles obtained from linear PFFT-CPM (—), linear PFFT-QBEM (- · -), fully-nonlinear PFFT-QBEM (- -), and experiment measures of Stern *et al.* (1996) (-■-) and Toda *et al.* (1991) (-●-), for S60 hull with $F_r = 0.316$.

It's a great challenge to obtain accurate ship bow wave profile from numerical simulations as the flow there is extremely complex and tracking the precise position of the waterline is difficult. But increasing boundary panel number on body surface and free surface can improve the accuracy in the evaluation of waterline position. To demonstrate the convergence of the fully-nonlinear PFFT-QBEM for the bow wave profile, figure 3-16 shows three groups of fully nonlinear numerical results obtained from PFFT-QBEM using the following three types of discretizations on half S60 hull: 8×4 , 12×6 , and 15×8 elements, respectively. With finer boundary elements, numerical results for the bow wave profile get closer to the experimental measurements.

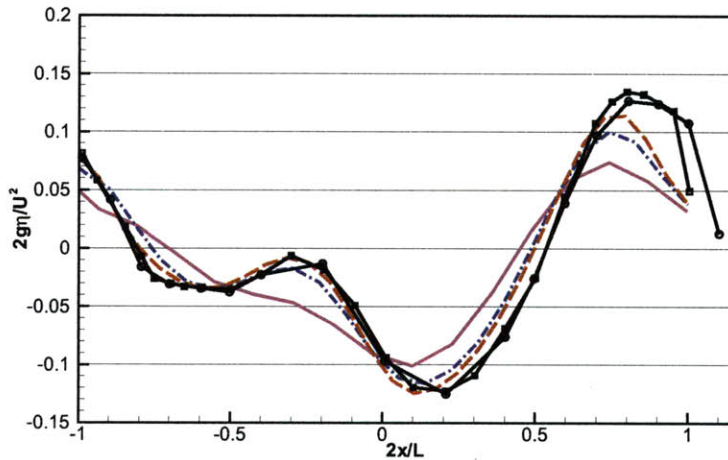


Figure 3-16: Comparison of wave profiles obtained from fully nonlinear numerical simulations and experiment measures of Stern *et al.* (1996) (-■-), and Toda *et al.* (1991) (-●-), for S60 hull with $F_r = 0.316$. Three group of numerical results are present, obtained from PFFT-QBEM using three types of discretizations on half of the ship hull: 8×4 (—), 12×6 (- · -), and 15×8 (- -) QBEM elements.

Numerically evaluated S60 wave making resistance C_x is shown in Figure 3-17 as a function of time and compared with ITTC experimental measurement for the steady value of C_x (McCarthy 1985). Note that in Figure 3-17, the time t is normalized by $T_0 \equiv 8\pi U/g$ which is the asymptotic result for the decaying oscillation period of C_x (Wehausen 1964) and the wave resistance F_x is normalized by $0.5\rho U^2 S$ where S is the mean wetted surface area of the hull. The C_x curve has sharp initial transients

because of the non-smooth starts of the numerical simulations. The agreements with experimental data are satisfactory for numerical results from both linear and fully nonlinear PFFT-QBEM while the linear PFFT-CPM significantly over-predicts the wave resistance of S60.

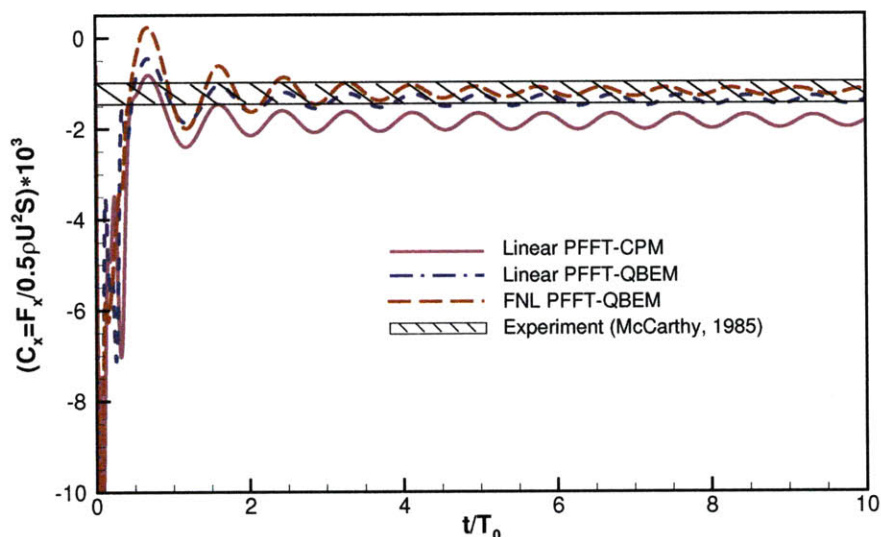


Figure 3-17: Comparison of time history of S60 wave-making resistance at $F_r = 0.316$ between the numerical simulations (linear PFFT-CPM (—), linear PFFT-QBEM (- · -), fully-nonlinear PFFT-QBEM (- · -)) and experimental data (McCarthy, 1985).

3.5 Concluding Remarks

We develop and apply a highly efficient fully nonlinear simulation capability using the PFFT-QBEM for general three-dimensional wave-body interactions. First of all, the QBEM-based IBVP solver is robust in dealing with general fully nonlinear problems as QBEM provides accurate solution of BVP at each time step even on non-smoothly connected boundary surfaces. Secondly, using the PFFT algorithm to accelerate QBEM, the computational effort in solving a BVP at each time step can be reduced to $O(N \ln N)$ from the conventional $O(N^{2\sim 3})$ and the efficiency of overall IBVP solver is much improved. These are the foundations for our numerical scheme to be competent for the study of large-scale/long-time fully nonlinear wave-body interactions.

To further improve the efficiency of the IBVP solver, disturbance velocity potential ϕ_D , instead of total velocity potential ϕ , is solved for in the present numerical scheme. By making use of the decaying feature of ϕ_D over distance away from the floating body, we can design the scheme such that it achieves great reduction in the requisite computational domain size, significant savings in computational storage and time, as well as effective absorption of wave energy in the far-field sponge zone. The success of current numerical scheme also relies on the stability of time integration approaches, effectiveness of absorbing-beach treatment, and robustness in tracking waterline position, which are all investigated systematically in this chapter.

For validation, present numerical scheme is implemented for the study of three sample nonlinear three-dimensional wave-body interaction problems: wave radiation of a periodically heaving sphere, wave diffraction of a fixed vertical cylinder, and wave generation of a forward moving ship hull. For all these problems, our fully nonlinear simulation results compare well with existing experimental data and theoretical/numerical results. The presence of discrepancy in the wave profile along the bow region of S60 hull between the present numerical results and experimental measurements manifests the challenge of tracking accurately the evolution of the wave-body intersection, especially in the presence of a forward body motion. Comparisons among the linear, body nonlinear, and fully nonlinear numerical results demonstrate various nonlinear effects in these wave-body interaction problems.

The highly efficient and robust IBVP solver, PFFT-QBEM, provides an effective and practical simulation capability of nonlinear wave-wave and wave-body interactions for the design and analysis of surface ships and marine structures. The efficiency and robustness of this powerful numerical tool will be further illustrated in the detailed study of important fully-nonlinear free surface hydrodynamic problems in the following chapters.

3.6 References

Bai, W. & Eatock Taylor, R., Higher-order boundary element simulation of fully nonlinear wave radiation by oscillating vertical cylinders, *Applied Ocean Research*, Vol.28, pp.247-265, 2006;

Dommermuth, D. G. & Dick K. P. Yue, Numerical simulations of nonlinear axisymmetric flows with a free surface, *J. Fluid Mech.*, Vol.178, pp.195-219, 1987;

Dommermuth, D. G. & Dick K. P. Yue, The nonlinear three-dimensional waves generated by a moving surface disturbance, 17th Symposium on Naval Hydrodynamics, 1988, The Hague, The Netherlands;

Faltinsen, O. M., *Sea Loads on Ships and Offshore Structures*, Cambridge University Press, 1993;

Faltinsen, O. M., Newman, J. N., and Vinje, T., Nonlinear Wave Loads on a Slender Vertical Cylinder, *J. Fluid Mech.*, Vol.289, pp.179-198, 1995;

Ferrant, P., Simulation of strongly nonlinear wave generation and wave-body interactions using a 3-D MEL model, Twenty-First Symposium on Naval Hydrodynamics, pp.93-109, 1996;

Ferrant, P., Touze, D. L., & Pelletier, K., Non-linear time-domain models for irregular wave diffraction about offshore structures, *International Journal for Numerical Methods in Fluids*, Vol.43, pp.1257-1277, 2003;

Hulme, A., The wave forces acting on a floating hemisphere undergoing forced periodic oscillations, *J. Fluid Mech.*, Vol.121, pp.443-463, 1982;

Hess, J. L. & Smith, A. M. O., Calculation of non-lifting potential flow about arbitrary three-dimensional bodies, *Journal of Ship Research*, Vol.8, pp.22-44, 1964;

Ikehata, M., Tanaka, H., Adachi, H., Namimatsu, M., & Ogiwara, S., The summary of the Cooperative Experiment on Wigley Parabolic Model in Japan, *Proceedings of the second DTNSRDC Workshop on ship Wave-Resistance Computations*, pp.5-35,

1983, Bethesda, Md;

Kara, F., Tang, C.-Q., Vassalos, D., Time domain three-dimensional fully nonlinear computations of steady body-wave interaction problem, *Ocean Engineering*, Vol.34, pp.776-789, 2007;

Kim, H. M. and Yue, D. K. P., The Complete Second-order Diffraction Solution for an Axisymmetric Body, Part I. Monochromatic Incident Waves, *J. Fluid Mech.*, Vol.200, pp.235-264, 1989;

Kim, Y., Computation of higher-order hydrodynamic forces on ships and offshore structures in waves, PhD Thesis, MIT, 1999;

Krokstad, J. R. and Stansberg, C. T., Ringing Load Models Verified Against Experiments, *Proc. Intl Conf. on Offshore Mechanics and Arctic Engineering*, Copenhagen, Denmark, 1995;

Koo, W. C. & Kim, M. H., Fully nonlinear wave-body interactions with surface-piercing bodies, *Ocean Engineering*, Vol.34, pp.1000-1012, 2007;

Lax, P. D., & Richtmyer, R. D., Survey of the stability of linear finite difference equations, *Comm. Pure Appl. Math.*, Vol.9, pp.267-293, 1956;

Lin, W.-M., & Dick K. P. Yue, Numerical Solutions for Large-Amplitude Ship Motions in the Time Domain, *Eighteenth Symposium on Naval Hydrodynamics*, 1990;

Lin, W.-M, Newman, J.N., & Yue, D,K.P., Nonlinear forced motions of floating bodies, *The 15th Symposium on Naval Hydrodynamics*, Hamburg, Germany, Sep. 1984;

Lin, R.-Q, Kuang, W., Reed, A.M., Numerical modeling of nonlinear interactions between ships and surface gravity waves, Part 1: ship waves in calm water, *Journal of ship research*, Vol.49 (1), pp.1-11, 2005;

Liu, Y.-M., Xue, M., & Dick K. P. Yue, Computations of fully nonlinear three-dimensional wave-wave and wave-body interactions. Part 2. Nonlinear waves and

- forces on a body, *J. Fluid Mech.*, Vol.438, pp.41-66, 2001;
- Mei, C.C., *The Applied Dynamics of Ocean Surface Waves*, World Scientific, 1989;
- McCarthy, J. H., *Collected Experimental Resistance Component and Flow Data for Three Surface Ship Model Hulls*, Report No. DTNSRDC-85/011, 1985;
- Schwarz, L. W., *Computer extension and analytical contribution of Stokes' expansion for gravity waves*, *J. Fluid Mech.*, Vol.62, pp.553-578, 1974;
- Stern, F., Longo, J., Zhang, Z.-J., & Subramani, A. K., *Detailed bow-flow data and CFD for a Series 60 CB=0.6 ship model for Froude number 0.316*, *Journal of Ship Research*, Vol.40(3), pp.193-199, 1996;
- Tsai, W.T. & Yue, D.K.P., *Computation of nonlinear free-surface flows*, *Ann. Rev. Fluid Mech.*, Vol.28, pp.249-278, 1996;
- Tarafder, Md. S., & Suzuki, K., *Numerical calculation of free-surface potential flow around a ship using the modified Rankine source panel method*, *Ocean Engineering*, Vol.35, pp.536-544, 2008;
- Troesch, A. W. & Wang, M.-L., *An experimental study for slamming flow and green water on deck*, Final report, No.327, September, 1994, The university of Michigan;
- Troesch, W. W. & Kang, C.-G., *Hydrodynamic Impact Loads on Three-Dimensional Bodies*, *Proceedings of the 16th Symposium on Naval Hydrodynamics*, Berkeley, pp.537-558, July 1986;
- Wehausen, J.V., *Effect of the initial acceleration upon the wave resistance of ship models*, *J. Ship Res.*, Vol. 7, pp. 38-50, 1964;
- Wu, G.-Y., *Direct simulation and deterministic prediction of large-scale nonlinear ocean wave-field*, PhD thesis, MIT, 2004;
- Xue, M., *Three-dimensional fully-nonlinear simulations of waves and wave body interactions*, PhD Thesis, MIT, 1997.

Xue, M. & Dick K. P. Yue, Nonlinear free-surface flow due to an impulsively started submerged point sink, *Journal of Fluid Mechanics*, 'Vol.364, pp.325-347, 1998;

Xue, M, Xu, H., Liu, Y., Yue, D.K.P., Computations of fully nonlinear three-dimensional wave-wave and wave-body interactions. Part 1: Three-dimensional steep waves, *J. Fluid Mech.* Vol.438, pp.11-39, 2001;

Yeung, R. W., Numerical methods in free-surface flows, *Ann. Rev. Fluid Mech.* Vol.14, pp.395-442, 1982.

Chapter 4

Cavity Dynamics in Water Entry at Low Froude Numbers

4.1 Introduction

An air cavity forms when a solid enters into water or other liquids. The focus of this chapter is on the understanding of the formation and evolution of the cavity behind the falling body after the initial impact, and for relatively low Froude numbers where both inertia and gravity effects are of relevance.

The dynamics of water impact and air cavities was first considered by Worthington & Cole (1900). The study on this subject got intensified during World War II for the design of military projectiles entering water at high speed (Gilbarg & Anderson 1948; Richardson 1948; May & Woodhull 1948; May 1951, 1952). Most of these early studies were experimental and focused on high Froude numbers, for which the gravity effect is relatively unimportant. Due to basic scientific interest and practical importance, recent studies have expanded to relatively low Froude numbers, where gravity effects are comparable to inertia effects. An important application in naval architecture is the large hydrodynamic loads on surface ships and offshore structures due to water entry/impact as a result of large-amplitude relative motions (e.g. Korobkin & Pukhnachov 1988; Greenhow 1988). The formation of air cavity also significantly influences the dynamics and trajectory of low-speed projectiles such as mines deployed

from ships or airplanes (e.g. Holland *et al.* 2004; Chu *et al.* 2004). On a much smaller scale, the water impact and subsequent cavity formation play an important role in the locomotion of water animals such as shore birds and lizards (e.g. Laerm 1974; Glasheen & MaMahon 1996).

In addition to experiments, there are also theoretical and numerical studies of air cavity dynamics associated with water entry. Levinson (1945) developed an asymptotic solution for the evolution of the cavity behind an axisymmetric body moving through an ideal fluid with the gravity effect neglected. A two-dimensional analytic model was used to study the cavity dynamics by Birkhoff & Zrantonello (1957) and Lee, Longoria & Wilson (1997). Results derived from this model contain an arbitrary constant which was introduced to account for the three-dimensional flow effect. The value of this constant was determined by matching the theoretical prediction with experimental data and/or nonlinear numerical simulations. Duclaux *et al.* (2007) developed an analytical model for the time evolution of the cavity based on the Besant-Rayleigh equation. In this model, an arbitrary coefficient is introduced in the determination of the kinetic energy of the fluid in the initial expansion of the cavity. In addition, similarly to the model of Birkhoff & Zrantonello (1957) and Lee, Longoria & Wilson (1997), this model also introduces an arbitrary radius to approximate the three-dimensional flow effect. These coefficient are then determined by matching with experimental data. So far, there has been no complete theoretical model that does not employ such empirical coefficient(s). Owing to complexity of the unsteady nonlinear flow, numerical studies on the cavity dynamics associated with water entry are limited. Gaudet (1998) performed a fully nonlinear simulation of water entry of circular disks at low Froude numbers ($F_r = 0.1 \sim 14$, see definition of F_r shortly) in the context of potential flow based on the use of a constant panel method. His numerical results are in good agreement with the experimental measurements of Glasheen & McMahan (1996).

In this work, we focus on the investigation of the air cavity dynamics in the water entry problem at relatively low Froude numbers through theoretical analysis and fully-nonlinear numerical simulations. The theoretical analysis and numerical com-

putation are based on the potential-flow formulation (§4.2). An asymptotic solution is developed, based on the slender body assumption, for the description of cavity formation and evolution till the occurrence of pinch off (§4.3). Unlike the existing analytic models, the present solution is complete and does not contain an arbitrary constant (to be determined by matching with experimental data or nonlinear numerical simulations). To understand the detailed flow characteristics near the free surface and in the neighborhood of the body where the asymptotic solution is inaccurate, we apply fully-nonlinear computations to simulate the development of air cavity in vertical water entry of an axisymmetric body. The nonlinear simulation is based on a boundary integral equation method together with the mixed-Eulerian-Lagrangian (MEL) approach for tracking nonlinear free surface motion (§4.4). The characteristics of the cavity kinematics and profile and the pinch-off process in the evolution of the cavity as well as their dependency on Froude number and body geometry are systematically studied (§4.5). To verify the validity and accuracy of the asymptotic theory and numerical simulation and to understand the effects not accounted for in theoretical analysis and numerical computation, comparisons are made between the asymptotic and numerical result and available experimental measurements. We find that the potential-flow based formulation properly describes the development and evolution of air cavity in water entry till the moment pinch off occurs. In particular, the asymptotic theory gives an accurate prediction of the time and cavity height for pinch-off to occur. These are concluded in §4.6.

4.2 Problem statement

4.2.1 The initial boundary value problem

We address the hydrodynamic problem of air cavity development in vertical water entry of an axisymmetric body with relatively low Froude numbers, $F_r \equiv V(gD)^{-1/2} = O(10^{0-1})$, where V is the characteristic dropping velocity of the body, D the characteristic length of the body, and g the gravitational acceleration. In general, the

evolution of the air cavity may be influenced by the dropping velocity, body geometry and surface condition, densities of air, water and body, surface tension, viscosity, gravity, and air dynamics.

We take the interesting case of basilisk lizard walking on water surface as an example to see the influence of each physical parameter on the air cavity evolution. A moderately-sized basilisk lizard weighs around $90g$. Basilisks have large hind feet with flaps of skin between each toe and we approximate a mature lizard's foot as a thin disk with diameter $D \sim 0.06m$. The impact velocity of lizards' feet on water surface is $V \sim 2.25m/s$. Let σ represent water surface tension and we can evaluate the Bond number as $Bo \equiv \rho g D^2 / \sigma = 504$ or the Weber number as $We \equiv \rho V^2 D / \sigma = 4340$ where ρ is the density of water. From these nondimensional values, we may conclude that surface tension effect is not important for cavity evolution except possibly near pinch-off stage. Reynolds number, based on above data setting, can be checked as $Re \equiv DV / \nu = 1.35 \times 10^5$, where ν is the kinematic viscosity coefficient of water. Corresponding to this Reynolds number, water viscous effect is negligible here. Experiments (May 1951; Duclaux *et al.* 2007) show that the cavity formed by relatively high-speed water entry is practically independent of the body surface state. For simplicity, we assume perfectly smooth hydrophobic body surface condition in our study. As for the air dynamics effect on cavity, we approximate the air velocity is in the order of the body falling velocity. Since the air density is much smaller than water density, the air dynamics will play trivial role in the cavity evolution except for the water jet formation above original water surface.

By conclusion, the dynamics of cavity formation will be mainly affected by body entry velocity, body geometry, density of body material, and gravity. From scaling laws, we summarize the controlling nondimensional parameters for water-entry problem under study will be Froude number $F_r \equiv V(gD)^{-1/2}$, body geometry, and density ratio between body and water $\gamma = \rho_b / \rho$. Since the effect of γ is predictable, we will focus our study on the influences of Froude number and body geometry on cavity dynamics.

We define a cylindrical coordinate system $\mathbf{x} \equiv (r, \theta, z)$ with r as the radial coordi-

nate, θ the azimuthal coordinate, and z the vertical coordinate positive downwards. The origin is on the undisturbed free surface. The flow of the problem is axisymmetric (i.e. independent of θ), as shown in figure 4-1.

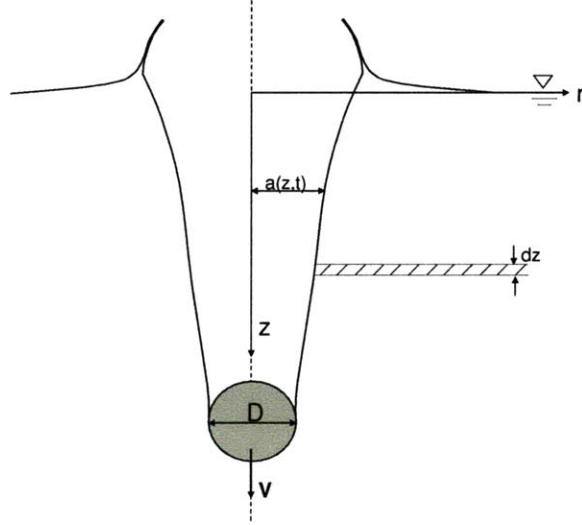


Figure 4-1: sketch of an air cavity induced by vertical water entry of an axisymmetric body.

We assume that the fluid motion is irrotational. The flow is described by a velocity potential ϕ which satisfies Laplace's equation in the fluid domain \mathcal{V} :

$$\nabla^2 \phi(\mathbf{x}, t) = \frac{\partial^2 \phi}{\partial r^2} + \frac{1}{r} \frac{\partial \phi}{\partial r} + \frac{\partial^2 \phi}{\partial z^2} = 0, \quad \mathbf{x} \in \mathcal{V}(t), \quad (4.1)$$

where t is time. On the free surface $S_F(\mathbf{x}, t)$ which includes the wall of the cavity, ϕ satisfies the kinetic boundary condition in a Lagrangian form

$$\frac{D\mathbf{x}}{Dt} = \nabla \phi, \quad \text{on } S_F(\mathbf{x}, t) \quad (4.2)$$

where $D/Dt \equiv \partial/\partial t + \nabla \phi \cdot \nabla$ denotes material derivative. The dynamic boundary condition on $S_F(\mathbf{x}, t)$ in Lagrangian form is

$$\frac{D\phi}{Dt} = \frac{1}{2} |\nabla^2 \phi| + gz - P_F, \quad \text{on } S_F(\mathbf{x}, t) \quad (4.3)$$

where P_F is the pressure on $S_F(\mathbf{x}, t)$. Unless the impact speed is very high, aerodynamic effects are small, and we set P_F to be equal to the atmospheric pressure which is constant in this study. (After cavity closure, the pressure on the cavity surface may become time dependent, see e.g. Wang 2004). On the wetted body boundary, $S_B(\mathbf{x}, t)$, the normal velocity of the flow is identical to that of the boundary,

$$\nabla\phi \cdot \mathbf{n} = V(t)n_z, \quad \text{on } S_B(\mathbf{x}, t) \quad (4.4)$$

where $\mathbf{n} \equiv (n_r, n_z)$ is the unit normal pointing out of the fluid, and $V(t)$ the body velocity that may be time dependent. In addition, a far-field condition

$$\nabla\phi \rightarrow 0, \quad \text{for } |\mathbf{x}| \rightarrow \infty \quad (4.5)$$

is imposed. Initially, the body is assumed to touch the water surface slightly with the impact velocity $V_0 \equiv V(t = 0)$. Thus, we apply zero initial condition on the undisturbed free surface

$$\phi = 0, \quad \text{on } S_F(\mathbf{x}, t = 0). \quad (4.6)$$

The above equations completely define the initial boundary-value problem for ϕ .

If the body drops freely in the water, its motion is governed by the equation of motion:

$$Mg + F(t) = M \frac{dV(t)}{dt} \quad (4.7)$$

where M is the mass of the body and $F(t)$ the total hydrodynamic and hydrostatic force:

$$F(t) = \int_{S_B(t)} p n_z ds \quad (4.8)$$

where the pressure p on the wetted body surface is given by Bernoulli's equation:

$$\frac{p}{\rho} = -\frac{\partial\phi}{\partial t} - \frac{1}{2}|\nabla\phi|^2 + gz. \quad (4.9)$$

4.2.2 Physical insight

Before we carry out the detailed asymptotic analysis and nonlinear computations, it is helpful to obtain a heuristic understanding of the cavity development and evolution. The water entry of a body and the subsequent cavity formation behind consist of two main phases. Assuming a constant dropping velocity V , the body position $z_b(t) (> 0)$ after initial impact (at time $t = 0$) is $z_b = Vt$. At some height z_0 , the cavity begins to form at $t_0(z_0) = z_0/V$ with an initial radius $a(z_0, t_0) \approx D/2$ where $D/2$ is the body radius (assuming an axi-symmetric body). Initially, the cavity expands ($\partial a/\partial t > 0$ for $t > t_0(z_0)$) as the body continues to descend below z_0 . After some expansion time $\delta t_1(z_0)$, the cavity reached maximum radius, $a(z_0, t_0 + \delta t_1) = R_m(z_0)$, and then starts to contract, eventually collapsing the cavity. There is generally a height $z = H_c$ at which the cavity first closes, at closure time $t = T$, when $a(H_c, T) = 0$. This initial cavity closure can occur above the free surface (“surface closure”, $H_c < 0$) or below the free surface (“deep closure” or “pinch-off”, $H_c > 0$) depending on the value of the Froude number. Deep closure usually occurs for relatively low Froude numbers, while surface closure generally occurs for larger Froude numbers (Birkhoff & Zrantonello 1957).

For the contraction phase, a heuristic estimate of closure time at any height z_0 can be obtained by assuming steady state, with a constant radial velocity approximated by Bernoulli equation, $-\partial a/\partial t = u(z_0) = (2gz_0)^{1/2}$ for $t > t_0 + \delta t_1$. The time of collapse at z_0 , $t_c(z_0) = t_0 + \delta t_1 + \delta t_2$, can be estimated by $\delta t_2(z_0) \approx 0.5D/u(z_0)$. For some body shapes (for example, a long vertical cylinder), the expansion phase is short compared to the collapsing phase, $\delta t_1 \ll \delta t_2$. Under this condition, one may neglect δt_1 to obtain the closure time, $T = \min_{z_0} [t_0(z_0) + \delta t_2(z_0)]$. Substituting the value of δt_2 in terms of z_0 , we obtain finally: $TV/D \approx (3/2^{5/3})F_r^{2/3}$, corresponding to a pinch off position $z = H_c = H/3$, where $H = TV$ is the total cavity height at pinch off time $t = T$. (Details of this can be found in Mann (2005) and Mann *et al.* (2007)).

Despite the simple model, the above estimate obtains good agreement with measurements in the case of relatively long vertical cylinders (Duclaus *et al.* 2007), and

remarkably for the case of a sphere entering into soft sand (Lohse *et al.* 2007). For general body shapes, however, the heuristic estimate fails. For example, experimental data show an almost linear dependence of TV/D and H/D on F_r , and $H_c \simeq H/2$, for water entry of circular disks (entering normally) (Glasheen & MaMahon 1996) and spheres (Lohse *et al.* 2007).

4.3 Asymptotic theory

To understand the basic mechanism governing the evolution of air cavity in water entry of a body, we derive an asymptotic solution of the above problem by assuming the diameter of the cavity d small relative to its length h (for example, at $F_r \approx 5.0$, $d/h \approx 0.14$ for spheres (Duclaux *et al.* 2007) and $d/h \approx 0.12$ for circular disks (Glasheen & McMahon 1996) near cavity closure). Of particular interest is the dependence of key cavity dynamics parameters such as closure time and cavity height on the Froude number.

4.3.1 Governing equations

Fluid motion associated with the evolution of a slender air cavity bears a strong similarity to that from a slender ship motion. We thus follow the slender body analyses in ship hydrodynamic (Newman 1977) to derive an asymptotic solution for the development of air cavity.

We define a slenderness parameter, $d/h = \varepsilon \ll O(1)$, where d is the characteristic diameter of the cavity, and h the characteristic length of the cavity. In terms of this small parameter, the flow in the near field of the cavity can be simplified to be two-dimensional. In the near field of the cavity ($r/h = O(\varepsilon)$), we have

$$\frac{\partial \phi}{\partial z} \ll \frac{\partial \phi}{\partial r}, \quad r/h = O(\varepsilon). \quad (4.10)$$

The Laplace equation in (4.1) can be simplified as

$$\frac{\partial^2 \phi}{\partial r^2} + \frac{1}{r} \frac{\partial \phi}{\partial r} = 0, \quad r \ll h, \quad (4.11)$$

The kinematic boundary condition (4.2) on the cavity wall ($r = a(z, t)$) can be rewritten as:

$$\frac{\partial a}{\partial t} = \phi_r - \phi_z \frac{\partial a}{\partial z}, \quad \text{at } r = a(z, t). \quad (4.12)$$

After applying the slender assumption and linearization, kinematic boundary condition (4.12) becomes

$$\frac{\partial a}{\partial t} = \phi_r + O(\varepsilon), \quad \text{at } r = R \quad (4.13)$$

which is now imposed on the fixed vertical surface $r = R$ with R being the characteristic transverse dimension of the dropping body. Similarly, the dynamic boundary condition (4.3) can also be linearized and imposed on the fixed surface $r = R$:

$$\frac{\partial \phi}{\partial t} = gz + O(\varepsilon), \quad \text{at } r = R. \quad (4.14)$$

Since the free surface extends to infinity, its deformation is negligible except in the region close to the cavity where water splash is formed. In deriving the asymptotic solution, we neglect the splash effect and assume a flat free surface with the boundary condition:

$$\phi = 0, \quad \text{at } z = 0. \quad (4.15)$$

In the far field of the cavity ($r/h \geq O(1)$), the flow is three-dimensional with ϕ satisfying the three-dimensional Laplace equation (4.1) and the simplified free-surface boundary condition (4.15) and the far-field condition (4.5).

In solving the above formulated problem, to account for the effect of cavity motion on the flow, we distribute a line source with unknown strength $q(z, t)$ along the center line of the cavity. For the effect of the body, we place a point source with strength $m(t)$ at the bottom of the cavity. In order to satisfy the free-surface boundary condition (4.15), negative images of the line source and point source with respect to

the free surface $z=0$ need to be added. As a result, the velocity potential of the flow is represented as the sum of influences from the line sources and point sources:

$$\phi(z, r, t) = \phi_b + \phi_c \quad (4.16)$$

where ϕ_c and ϕ_b are the velocity potentials induced by the line sources and point sources, respectively.

In (4.16), ϕ_b is determined by choosing $m(t)$ such that the body boundary condition (4.4) is satisfied. As in the slender-body analysis of ship hydrodynamics, we solve for ϕ_c using the method of matched asymptotic expansions, where the inner and outer solutions are treated as complementary approximations, each of which is valid in its own domain. Specifically, the inner solution ϕ_{in} needs to satisfy the two-dimensional Laplace equation (4.11) and the boundary conditions on the cavity wall, (4.13) and (4.14). The outer solution ϕ_{out} is governed by the three-dimensional Laplace equation (4.1) and the far-field condition (4.5). These two solutions need to be matched in the *overlap* region (far from the cavity in the inner region but very close to the body in the outer region):

$$\phi_{in} \approx \phi_{out}, \quad \varepsilon h \ll r \ll h. \quad (4.17)$$

4.3.2 Determination of ϕ_b

A moving point source with strength $m(t)$ is used to approximate the effect of the falling body on the fluid motion. The exact position of the point source is not critical as long as it is close to the body, since the discrepancy introduced on cavity kinematics is within the accuracy of the slender body approximation. In this study, the point source is placed at cavity depth $h(t)$ (or body centroid). The resulting velocity potential by this point source and its image is:

$$\phi_b(z, r, t) = -\frac{m(t)}{4\pi} \frac{1}{\sqrt{(h-z)^2 + r^2}} + \frac{m(t)}{4\pi} \frac{1}{\sqrt{(h+z)^2 + r^2}} \quad (4.18)$$

with $h(t)$ represents the position of the body.

A conceptually clear way to specify the strength $m(t)$ is to use ϕ_b in (4.16) to account for the *vertical* volume flux due to the body. Thus the value of $m(t)$ for (4.18) is obtained by matching the vertical volume flux across the wetted body surface S_B given by (4.4) to that across the front ($z > h$) portion of the Rankine half body formed by the single point source (this flux equals $0.36m$ which we shall simply approximate as $m/3$ below). For the sphere, S_B depends on the (assumed) location of the detachment line, which, if we specify it to be at maximum radius, say, obtains: $m(t) = 2\pi R^2 V(t)$. For the inverted truncated cone in §4.5.2, the separation line is at the top edge, yielding $m(t) = 3\pi R^2 V(t) \sin(\theta/2)$, where θ is the cone vertex angle. The circular disk is simply the limit of $\theta = \pi$ giving $m(t) = 3\pi R^2 V(t)$. We remark that the decomposition (4.16) in principle leaves some freedom in the specification of m in (4.18). The present choice which frees ϕ_c from satisfying the vertical flux due to the body is a theoretically elegant one, and, as we shall show in §4.5, gives remarkably good predictions relative to fully-nonlinear simulations and experiments.

4.3.3 Determination of ϕ_c

Inner solution

In the inner region of the cavity, the problem is two-dimensional. The velocity potential due to the influence of the line source can be written as:

$$(\phi_c)_{in}(z, r, t) \simeq \frac{q(z, t)}{2\pi} \log\left(\frac{r}{2h}\right) + f_1(z, t), \quad r \ll h \quad (4.19)$$

where $q(z, t)$ is the unknown source strength, and $2h$ is the total length of the line source and its image with respect to the free surface $z = 0$. In the above, (4.19) contains an arbitrary function $f_1(z, t)$ (independent of r) that is to be determined by matching the *inner* solution with the *outer* solution in the overlap region. Clearly, the inner solution (4.19) diverges as $r \rightarrow \infty$, and cannot be reconciled with the far-field condition (4.5).

Outer solution

In the outer region of the cavity, the problem is three-dimensional. The *outer* solution of ϕ_c is given by

$$(\phi_c)_{out}(z, r, t) = - \int_{-h}^h \frac{q(\xi, t)}{4\pi} \frac{1}{\sqrt{(\xi - z)^2 + r^2}} d\xi \quad (4.20)$$

which represents the influence of a line source of length $2h$ in the three-dimensional domain.

Asymptotic matching

For matching $(\phi_c)_{in}$ with $(\phi_c)_{out}$ in the overlap region, we develop the inner expansion of the outer solution (4.20) for $r/h \ll 1$. By matching the resulting expansion with $(\phi_c)_{in}$ in (4.19), the function $f_1(z, t)$ is uniquely determined to be:

$$f_1(z, t) = \frac{1}{4\pi} \int_z^h \frac{\partial q(\xi, t)}{\partial \xi} \log[2(\xi - z)/(2h)] d\xi - \frac{1}{4\pi} \int_{-h}^z \frac{\partial q(\xi, t)}{\partial \xi} \log[2(z - \xi)/(2h)] d\xi \quad (4.21)$$

The potential for the whole fluid domain is now uniquely determined once the strength of the line source $q(z, t)$ is known. Since the focus of this study is on the dynamics of the air cavity, hereafter only the *inner* solution is relevant:

$$\phi_{in}(z, r, t) = (\phi_c)_{in} + \phi_b \quad (4.22)$$

Determination of line source strength $q(z, t)$

The dynamic boundary condition (4.14) is imposed on ϕ_{in} to determine unknown $q(z, t)$. Upon integrating (4.14) with respect to time, we obtain

$$\phi_{in}(z, R, t) = gz(t - t_0(z)) + C(z) \quad (4.23)$$

where $t_0(z)$ is the time when the body arrives at the depth z

$$z = \int_0^{t_0} V(t) dt . \quad (4.24)$$

In (4.23), the integration constant $C(z)$ is equal to the velocity potential on the cavity wall at depth z at $t = t_0$:

$$C(z) = \phi_{in}(z, R, t_0) = \phi_{b0} + f_2(z) \quad (4.25)$$

where ϕ_{b0} and $f_2(z)$ are given by

$$\phi_{b0} = -\frac{m(t_0)}{4\pi} \frac{1}{R} + \frac{m(t_0)}{4\pi} \frac{1}{\sqrt{4z^2 + R^2}} , \quad (4.26)$$

$$f_2(z) = f_1(z, t_0) = -\frac{1}{4\pi} \int_{-z}^z \frac{\partial q(\xi, t_0)}{\partial \xi} \log[2(z - \xi)/(2z)] d\xi . \quad (4.27)$$

Note that in the determination of $C(z)$, the line source strength at the end of the line source is considered to be zero as it is connected to the point source.

At any time $t > t_0$, substitution of (4.22) evaluated at $r = R$ into (4.23) gives an integral equation for the unknown linear source strength $q(z, t)$:

$$q(z, t) = \frac{2\pi}{\log \frac{R}{2h}} \left\{ gz(t - t_0) - \phi_b + \phi_{b0} - f_1(z, t) + f_2(z) \right\} \Big|_{r=R} , \quad t > t_0 . \quad (4.28)$$

This equation can be solved easily after applying an asymptotic expansion for $q(z, t)$:

$$q(z, t) = q_1(z, t) + q_2(z, t) + O(\varepsilon) , \quad t > t_0 \quad (4.29)$$

where $q_1 = O(\log \varepsilon)$ and $q_2 = O(1)$. After substituting (4.29) into (4.28), we obtain the solution:

$$q_1(z, t) = \frac{2\pi}{\log \frac{R}{2h}} \left\{ gz(t - t_0) - \phi_b + \phi_{b0} \right\} \Big|_{r=R} , \quad (4.30)$$

$$q_2(z, t) = \frac{2\pi}{\log \frac{R}{2h}} \left\{ -f_1(z, t) + f_2(z) \right\} \Big|_{r=R} . \quad (4.31)$$

Note that $q=q_1$ is used in the evaluation of $f_1(z, t)$ and $f_2(z)$ in (4.31). After the line source strength $q(z, t)$ is known, the velocity potential in the *inner* region of the cavity is fully determined from (4.22).

We remark that in the existing analytic models of Birkhoff & Zrantonello (1957) and Lee, Longoria & Wilson (1997), the strip theory is applied with the flow at each depth z assumed to be purely two-dimensional. The effects of ϕ_b and the matching term $f_1(z, t)$ in (4.19) are not considered. The three-dimensional far-field effect is approximated by introducing an empirical coefficient to the two-dimensional velocity potential. The present analysis overcomes these shortcomings of the existing models and provides a complete asymptotic solution including three-dimensional body and far-field effects.

4.3.4 Time evolution of the cavity

The radial velocity of the cavity is:

$$\phi_r = \frac{q(z, t)}{2\pi r} + \frac{\partial\phi_b}{\partial r}, \quad \text{at } r = R. \quad (4.32)$$

The radius $a(z, t)$ of the cavity at any time can be evaluated by integration of the kinematic boundary condition (4.13) with respect to t :

$$a(z, t) = R + \int_{t_0}^t \phi_r dt. \quad (4.33)$$

The decomposition (4.16) now allows us to obtain a clear qualitative description of the phases of cavity development discussed in §4.2.2: (a) For small $(t-t_0)V/R$, at any depth z_0 , $q \sim q_0 \sim (t-t_0)$ from (4.30), and $(\phi_b)_r$ dominates the radial velocity (4.32). Since $(\phi_b)_r > 0$ from (4.18) (for $m(t) > 0$), this accounts for the initial expansion phase of the cavity at this depth. (b) As $t-t_0$ increases, it can be shown from (4.30) (and (4.31)) that $q(z_0, t) < 0$ (so that $(\phi_c)_r < 0$) for $(t-t_0) \gtrsim VR/(gz_0)$, with a magnitude that increases with $t-t_0$. In the meantime, $(\phi_b)_r \sim (t-t_0)^{-3}$ decreases, so that at

some time $t = t_0 + \delta t_1(z_0)$, the two competing contributions balance, at the point when the cavity reaches maximum radius $R_m(z_0)$. (c) For $t > t_0 + \delta t_1(z_0)$, ϕ_r reverses sign (dominated by $(\phi_c)_r$), and the cavity eventually collapses at this location using time $t_c - t_0 - \delta t_1 = \delta t_2(z_0)$.

At depth z_0 , $\delta t_1(z_0)$ is determined from setting $\phi_r = 0$ in (4.32); and $R_m(z_0)$ from (4.33) with $t = t_0(z_0) + \delta t_1(z_0)$. The time of collapse, $t_c(z_0) = t_0 + \delta t_1(z_0) + \delta t_2(z_0)$ is then the upper limit of the integral to t_c in (4.33) to obtain $a=0$. Finally, the closure time of the cavity itself T is defined as the minimum of $t_c(z_0)$ over all z_0 of the cavity, given by:

$$\left. \frac{dt_c(z_0)}{dz_0} \right|_{z_0=H_c} = 0, \quad (4.34)$$

where $z_0 = H_c$ is the depth at which this (first) pinch off occurs. The total cavity height H at this closure time T is simply $\int_0^T V dt$.

4.3.5 Evaluation of the drag

For later reference, for the case of freely falling bodies, it is necessary to determine the (drag) force on the body. The drag force on the body, $F(t)$, can be evaluated in terms of the rate at which total energy E is imparted into the fluid at that time, which is in principle now known (from §4.3.3). One approach leading to an approximation can be obtained by accounting for this energy in terms of the total energy in the 2D plane, $E_{2D}(z)$:

$$E(t) = \int_0^{z_b(t)} E_{2D}(z, t) dz, \quad (4.35)$$

where $z_b(t)$ is the current position of the body. Thus:

$$F(t) = \frac{1}{V} \frac{dE}{dt} = E_{2D}(z_b, t) + \frac{1}{V} \int_0^{z_b(t)} \frac{dE_{2D}}{dt} dz. \quad (4.36)$$

We now make the slender body assumption that the energy $E_{2D}(z)$ in each 2D plane is conserved (Birkhoff & Zarantonello 1957), which gives:

$$F(t) \approx E_{2D}(z_b, t) \approx \int_0^{R_m(z_b)} (\rho g z_b) 2\pi r dr = \pi \rho g z_b R_m^2(z_b), \quad (4.37)$$

where the second approximation is obtained from the slender body approximation and equating the total energy E_{2D} to the maximum potential energy of the fluid displaced by the cavity at the current body depth $z_b(t)$.

We note that, in comparing (4.36) and (4.37), it can be seen that the second (neglected) term in (4.36) is generally negative. The reasoning is clear again because of the decomposition (4.16). $E_{2D}(z)$ is due to both ϕ_b and ϕ_c . The contribution due to the line source ϕ_c satisfies approximately slender body assumption (so that the time change at any depth is small). The contribution due to the body source ϕ_b is negative for $z < z_b$ (see (4.18)), so that the net contribution is negative and (4.37) is expected to somewhat overestimate the drag on the body (see Figure 8).

4.4 Fully-nonlinear numerical simulation

The matched asymptotic analysis is not expected to be good for the flow near the free surface or close to the body. To provide an independent check of its validity and to provide a simulation capability for general entry body geometries and Froude numbers we develop here a fully-nonlinear numerical method based on a mixed Eulerian-Lagrangian (MEL) ring-source boundary-integral equation method. The general approach follows closely that of Dommermuth & Yue (1987) and Xue & Yue (1998); for completeness, we outline here the key steps.

The nonlinear initial boundary-value problem (in the axi-symmetric z - r plane) in §4.2 is solved in the time domain starting from initial conditions. At each time, the unknown normal velocities on the trace of the free surface/cavity S_F , ∂S_F , and the unknown velocity potential on the trace of the body surface S_B , ∂S_B , are obtained by solving the integral equation (Dommermuth & Yue 1987):

$$\beta(z, r, t)\phi(z, r, t) = \int_{\partial S_F + \partial S_B} \left(\frac{\partial \phi}{\partial n'} - \phi \frac{\partial}{\partial n'} \right) G(z, r; z', r') r' d\ell', \quad (z, r) \in \partial S_F + \partial S_B \quad (4.38)$$

where β is the subtended solid angle and $G = \int_0^{2\pi} R^{-1} d\theta'$, $R = [(z-z')^2 + (r-r' \cos \theta')^2 + (r' \sin \theta')^2]^{1/2}$, is the Rankine ring-source Green function (Hulme 1983). Because

of the transient nature of the problem, the special far-field closure treatments of Dommermuth & Yue (1987) and Xue & Yue (1998) are not important here. On the other hand, the treatment of flow separation from the body must be considered with some care. For bodies with sharp edges or corners (such as the disk or the inverted truncated cone in §4.5.2), the separation point (from which the flow leaves tangentially from the body) is well defined.

For general smoothed geometries such as spheres, the separation point may be affected by the Froude number and body surface properties (Duez *et al.* 2007). In the numerical method, the separation position may be determined based on the requirement of satisfying both the free-surface and body boundary conditions, but sensitively depends on numerical resolution (e.g. Dommermuth & Yue 1987; Liu, Xue & Yue 2001). For the present problem, the separation point is observed in the experiments to be relatively invariant during the development of cavity. Thus, in this study, we presume the separation angle α_0 (measured from the downward vertical) and assume the flow detaches the body surface (at $\alpha = \alpha_0$) tangentially. Table 1 shows the dependence of cavity closure time and closure depth on prescribed value of separation angle α_0 for a freely falling sphere for two different F_r values. The results indicate that the key cavity closure parameters are relatively insensitive to α_0 in the low Froude number range. For a horizontal circular cylinder impact, Lin & Shieh (1997) observed that the separation point remains unchanged after separation with $\alpha_0 = 70^\circ \sim 80^\circ$ for $F_r = O(1)$. In water entry of small hydrophobic spheres, Aristoff & Bush (2009) found that $\alpha_0 = 70^\circ \sim 80^\circ$ for $F_r = O(10^{-1}) \sim O(10^2)$. Based on the above, we set $\alpha_0 = 70^\circ$ in this study for the sphere entry problem.

Finally we comment on the numerics. For axisymmetric problems, the present method requires discretization only along a (1D) line. In this study, we typically use 40 panels along ∂S_B , 300 panels on ∂S_F , and dimensionless time step $\Delta t = 0.005$. With these parameters, the numerical errors are converged to less than 1%. Table 1 shows a sample convergence result with two discretizations. (Extensive convergence tests and numerical validations can be found in Dommermuth & Yue 1987 and Xue & Yue 1998).

α_0	$F_r=3$		$F_r=5$	
	TV_0/D	H_c/D	TV_0/D	H_c/D
60°	4.38	1.76	7.10	2.74
65°	4.38	1.76	7.09	2.72
70°	4.36 (4.36)	1.74 (1.73)	7.04 (7.03)	2.71 (2.72)
75°	4.32	1.70	6.94	2.68
80°	4.23	1.65	6.78	2.64

Table 4.1: Effect of the flow separation angle α_0 upon the cavity closure time T and closure depth H_c in water entry of a freely falling sphere (§4.5.1) at two Froude numbers ($F_r=3.0$ and $F_r=5.0$) obtained by fully-nonlinear simulations. The values inside the parentheses are obtained with doubled panel numbers along $\partial S_B + \partial S_F$ and halved time step in the simulation.

4.5 Results

We first investigate the characteristics of air cavity development associated with water entry of freely falling spheres. The focus is on the evolution of the kinematics and profile of cavity wall, and the dependence of closure time and pinch-off height on Froude number. Theoretical analysis and fully-nonlinear simulation are compared with available laboratory experiments to understand the validity and limitations of the theory and simulation. We then apply our asymptotic theory and fully-nonlinear simulation to study the body geometry effect on the dynamics of air cavity by comparing the results associated with circular disks, inverted cones with different vertex angles and spheres. In the case of circular disks, comparisons are also made between the simulation result and asymptotic solution with existing experimental data.

The results shown below are all normalized in terms of length D (the radius of the sphere or disk), velocity V_0 (the initial water entry velocity of the body), and time D/V_0 if not explicitly stated otherwise. The normalized quantities are represented by primed symbols.

4.5.1 Freely-falling spheres

Figure 4-2 displays a sequence of pictures taken in experiment (Kominiarczyk, 2007) which clearly illustrate the evolution of air cavity starting from initial formation till

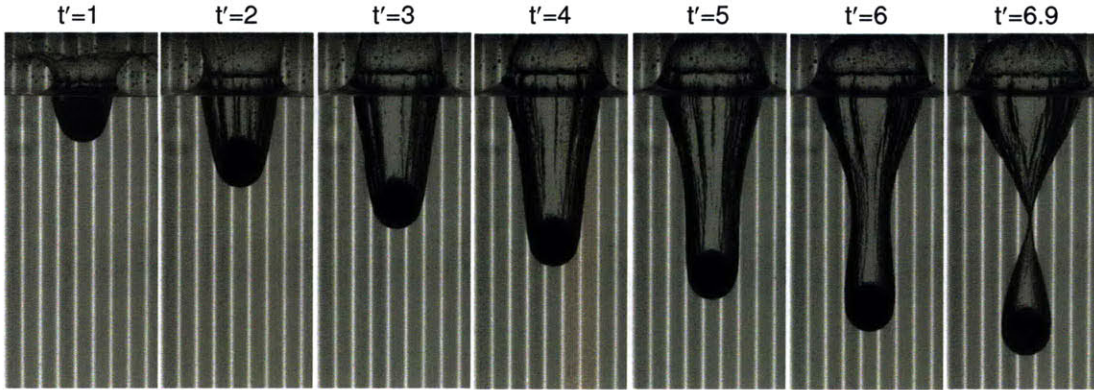


Figure 4-2: Time ($t' = tV_0/D$) evolution of an air cavity in water entry of a billiard ball at $F_r = 5.03$ from the experiment (Kominiarczuk, 2007).

occurrence of pinch off. The experiment is conducted by dropping a billiard ball from a height of 0.72m above the free surface. This gives the ball an initial impact velocity of $V_0 = 3.76$ m/s corresponding to $F_r = 5.03$. (In the following studies of sphere entries, if not specified, the experiment specifically means the one conducted by Kominiarczuk (2007) for the vertical water entry of a billiard ball (with diameter 5.72cm, made of phenolic resin ($\rho_b/\rho \approx 1.73$)).)

Detailed comparisons of the cavity profiles (for the case in figure 4-2 with $F_r = 5.03$) among the experimental data, theoretical prediction, and fully-nonlinear computation are shown in figure 4-3. Excluding the spray which is hard to obtain in experiments, the result from the fully-nonlinear simulation agrees well with the experimental data in view of the overall cavity shape and size, body position, as well as the cavity pinch-off position. The asymptotic solution also captures the main features of the cavity, and agrees well with the fully-nonlinear numerical simulation and experimental data except near the free surface where the slender body assumption is invalid. The cavity profile near the body is surprisingly well predicted by the asymptotic theory. Small discrepancies between the theory and nonlinear simulation and experimental data are seen, when pinch off nearly occurs, with the theory slightly overpredicts the deceleration of the body during its free fall.

Figure 4-4 compares the trajectories of the freely falling sphere (with $F_r=5.03$) as a function of time till the instant of pinch off, obtained by the experiment, fully-

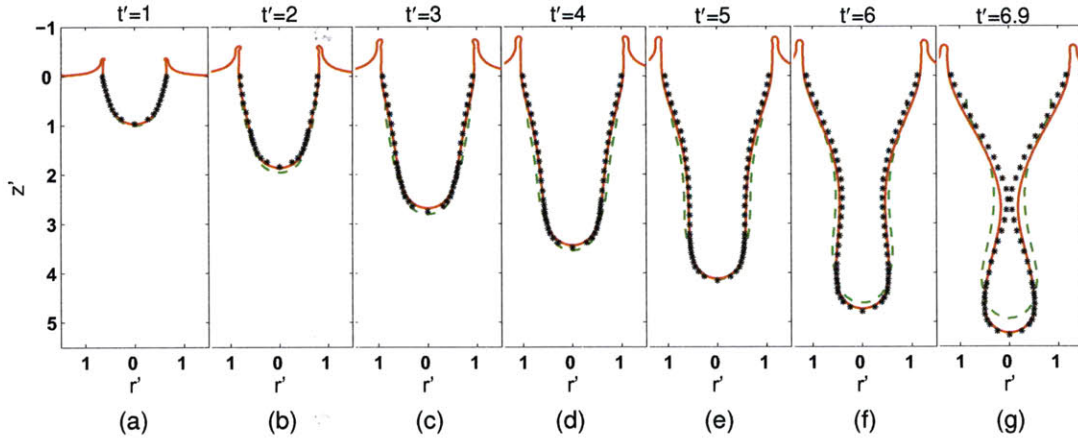


Figure 4-3: Comparisons of the cavity profile between experimental measurement (*), numerical simulation (—), and theoretical prediction (- - -) for (a) $t' = 1$; (b) $t' = 2$; (c) $t' = 3$; (d) $t' = 4$; (e) $t' = 5$; (f) $t' = 6$; (g) $t' = 6.9$.

nonlinear simulation, and theoretical prediction. Agreements among them are excellent except near the time of pinch off the theory slightly underestimated the dropping of the sphere.

The radial trajectory of the cavity wall at depth $z' = 2.48$ where pinch-off happens in the experiment is shown in figure 4-5. From figure 4-4, the experiment, asymptotic analysis, and numerical simulation give a close prediction on the time for the body to reach the depth $z' = 2.48$. Therefore, they should predict the cavity wall at this depth starting to expand at a similar time. The results in figure 4-5 indicate that in the theoretical prediction, the cavity grows wider than those obtain in the nonlinear simulation and experiment. The maximum radius R_m is reached at about the same time. Both asymptotic analysis and numerical simulation obtain a slightly slower contraction rate than the experimental data.

Figure 4-6 shows the maximum cavity size $R_m(z)$ reached at each depth. $R(m)$ decreases with depth in general. This can be explained qualitatively. At smaller depth, the body has a higher falling speed and more momentum can be transferred to the fluid from the body motion so that the cavity can expand to a larger radius. In addition, the hydrostatic pressure increases with depth, which makes the cavity at deeper depth harder to move outwards. Overall, the theoretical prediction, nonlinear

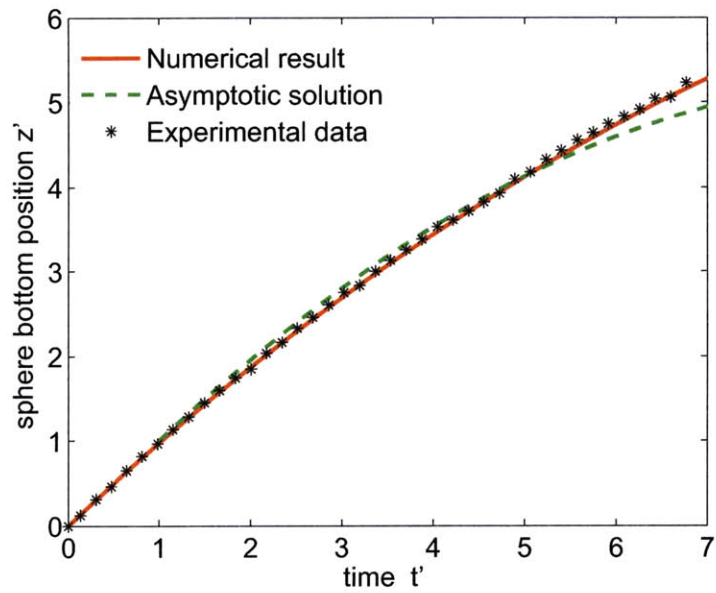


Figure 4-4: Trajectory of the freely falling sphere ($F_r = 5.03$) as a function of time: experimental measurement (*), numerical simulation (—), and theoretical prediction (- - -).

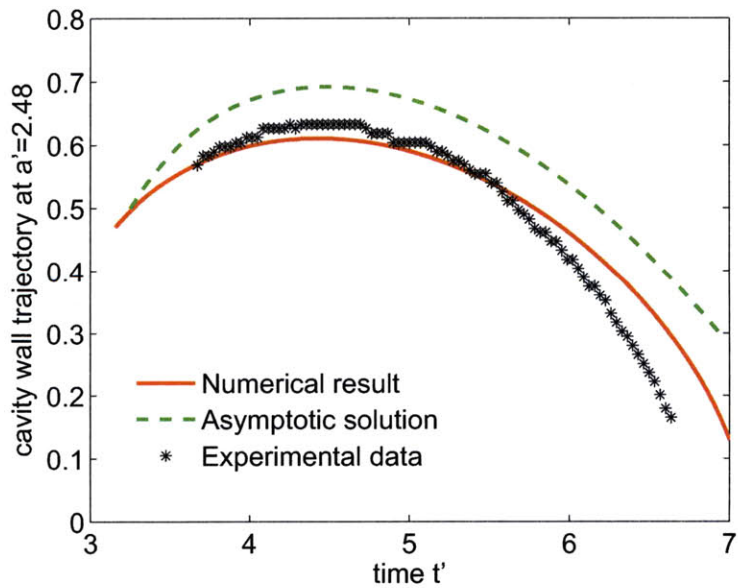


Figure 4-5: The radial trajectory of the cavity wall at $z' = 2.48$ as a function of time ($F_r = 5.03$): experimental measurement (*), numerical simulation (—), and theoretical prediction (- - -).

simulation, and experimental data agree each other reasonably well. The theory and nonlinear simulation slightly overpredict the value of R_m except in the region near the free surface where the asymptotic theory is invalid and nonlinear simulation slightly underestimates R_m , which may be due to the neglect of splash effects in the initial water impact process.

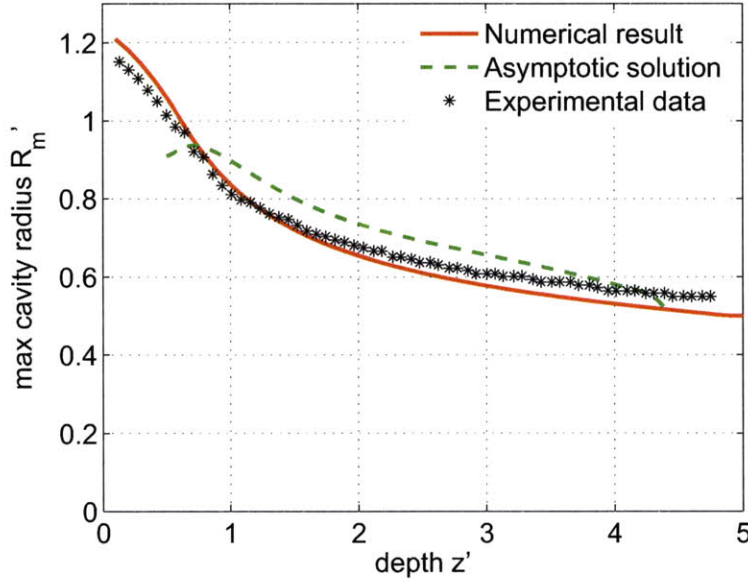


Figure 4-6: Maximum cavity radius as a function of depth ($F_r=5.03$): experimental measurement (*), numerical simulation (—), and theoretical prediction (- - -).

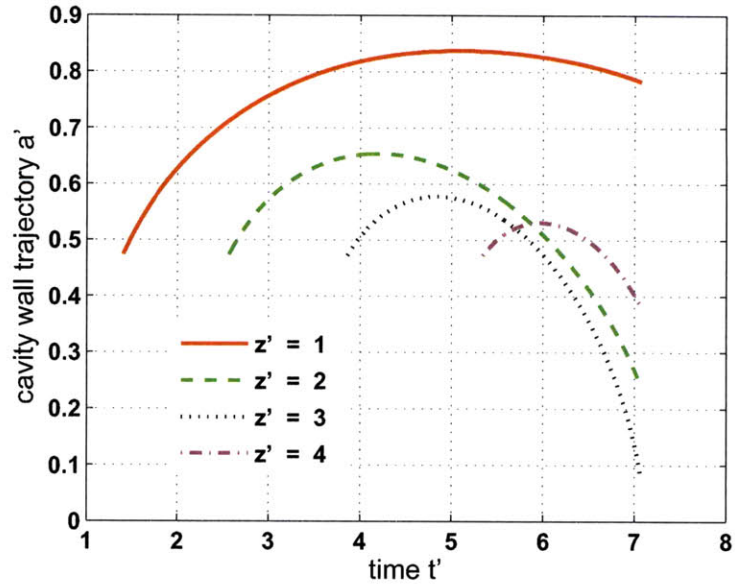
To understand the dependence of cavity wall evolution on water depth, we show nonlinear simulation results of the radial trajectory $a(z, t)$ and radial velocity $a_t(z, t)$ of cavity wall at several different depths in figure 4-7. Once the body arrives at depth z_0 at time $t_0(z_0)$, the cavity wall starts to move outwards with a decreasing (positive) velocity. After a time period ($\delta t_1(z_0)$) of expansion, the cavity reaches its maximum radial position $R_m(z_0)$ and starts to contract with an increasing (negative) velocity. Pinch off occurs after a time period ($\delta t_2(z_0)$) of contraction. In addition to the observation that $R_m(z)$ decreases with depth (as shown in figure 4-6), both δt_1 and δt_2 are seen from figure 4-7 to decrease with depth, which causes cavity closure to occur in relatively deep water. Owing to the increasing hydrostatic pressure, the radial acceleration of the cavity wall generally increases with depth as inferred by

the slope of the velocity curve in 4-7b. Moreover, unlike the prediction by the two-dimensional theoretical models (G. Birkhoff & E. H. Zrantonello (1957) and M. Lee, R. G. Longoria, & D. E. Wilson (1997)), the contraction process is not inversely symmetric to the expansion process (with respect to $r = R_m$ due to three-dimensional effects).

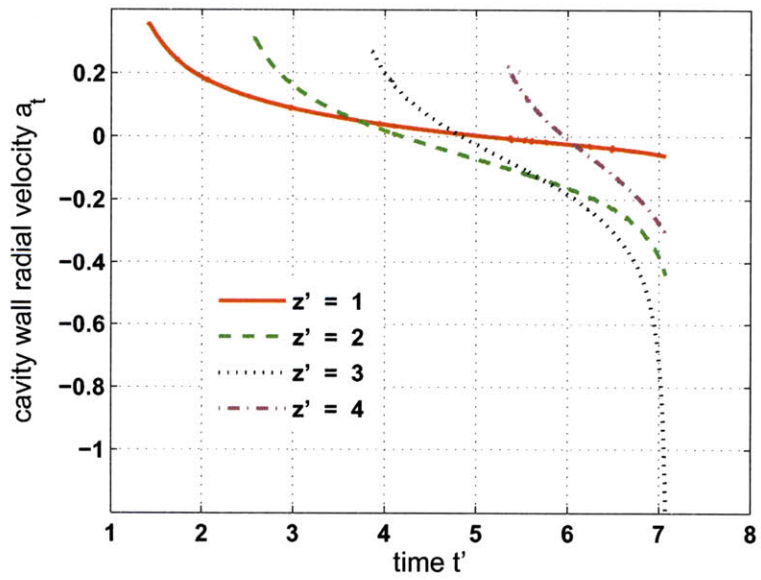
The comparison of the drag force on the freely falling sphere in water entry ($F_r = 5.03$) between the asymptotic theoretical prediction and fully-nonlinear simulation is shown figure 4-8. The drag coefficient is defined as $C_D = F(t)/0.5\rho_w V_0^2 S$ with S being the maximum body cross-section area. Both theory and numerical simulation predict that C_D is nearly a constant except in the initial stage where C_D varies sharply owing to the water impact effect. The prediction of C_D by the asymptotic theory is about 30% larger than that by the nonlinear simulation. As can be seen from the above results, this rather large difference in C_D does not cause much discrepancy in the prediction of the detailed kinematics and profile of the cavity.

Finally, we examine the dependence of cavity development on Froude number for the freely falling sphere. Figure 4-9 plots pinch-off time T , position H_c , and total cavity height at pinch off H for $F_r = 1 \sim 7$. We include for comparison also the experimental measurements of Duclaux *et al.* (2007) (who use glass spheres of specific densities ranging from 2.36 to 7.74, relative to our value of $\rho_b/\rho \approx 1.73$). The results are generally in agreement especially for the dependence of dimensionless pinch-off time TV_0/D on F_r . As expected, for the higher density spheres of Duclaux *et al.* (2007) the values for H/D and H_c/D are somewhat greater (especially for larger F_r) corresponding to greater (average) V/V_0 . If we think of the Froude number in terms of the average V/V_0 , denser spheres have effectively greater Froude numbers, which explains the steeper slopes of the H/D and H_c/D versus F_r curves for denser spheres.

As observed by Duclaux *et al.* (2007) and others (e.g. Glasheen & McMahon 1996 for dropping disks) in experiments and by the numerical simulation of Gaudet (1998) (for the disk); and consistent with (two-dimensional) theories (e.g. Birkhoff & Zrantonello 1957; Lee *et al.* 1997); T , H_c , and H are all approximately linear increasing functions of F_r . Our results capture this linear dependence with excellent



(a)



(b)

Figure 4-7: Time variation of (a) the radial trajectory and (b) velocity of cavity wall at depth $z'=1$ (—), 2 (---), 3 (···), and 4 (-·-), obtained by fully-nonlinear simulations ($F_r = 5.03$).

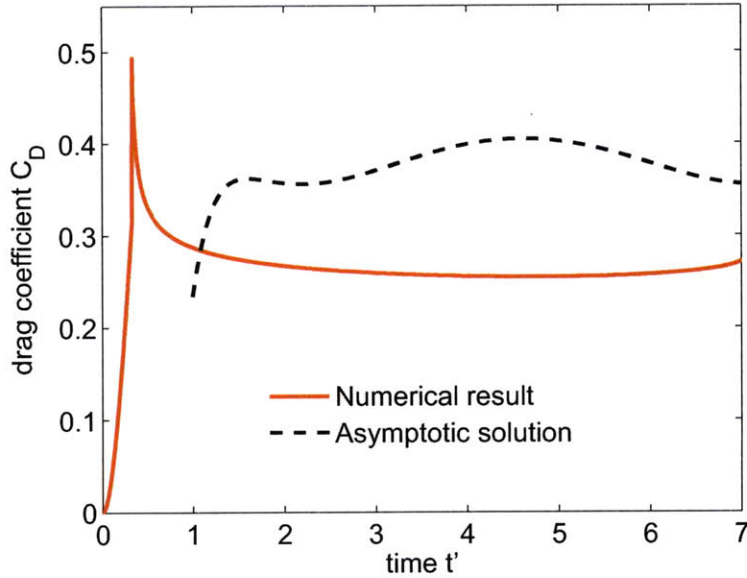


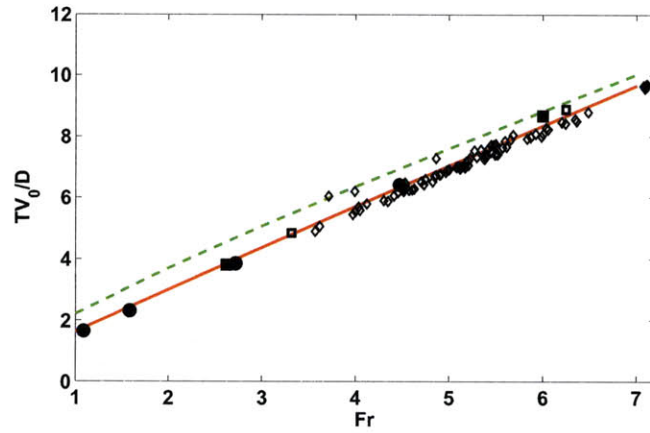
Figure 4-8: Comparison of the drag coefficient as a function of time between numerical simulation (—) and asymptotic theory (- - -).

comparison between the nonlinear simulation and measurements. The asymptotic solution predicts the slope but somewhat overpredicts the value of $T(F_r)$. The theory slightly underpredicts $H_c(F_r)$ and $H(F_r)$ especially for higher F_r . As pointed out in Figures 4-5, 4-6, and 4-8, the asymptotic theory overpredicts the drag force which (among other effects) delays the arrival of the body and evolution of the cavity.

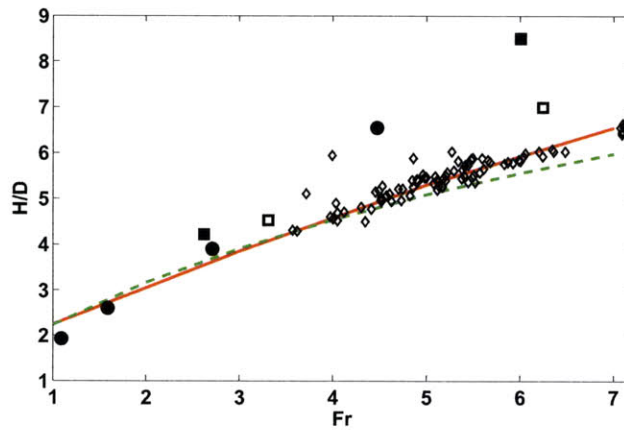
4.5.2 Water entry of a disk with a constant velocity

In this section, we present the results of our study for water entry of a disk with a prescribed constant velocity. Kutta condition is applied in fully nonlinear numerical simulations along the disk edge where flow separation occurs.

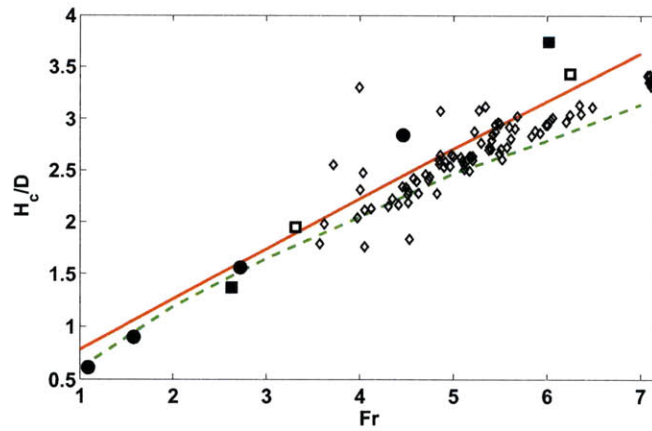
For illustration, the asymptotic theory prediction is shown and compared to numerical results for cavity profiles in disk entries with $F_r=5$ (Figure 4-10). The asymptotic solution is seen to agree with the nonlinear simulation result excellently except in the region near the free surface where the asymptotic analysis is invalid (results are omitted). In particular, the cavity shape near the body is well predicted by the



(a)



(b)



(c)

Figure 4-9: Dependence of (a) cavity closure time T , (b) total height of cavity H , and (c) depth of cavity closure H_c on Froude number Fr : experimental data of Kominarczuk (2007) (\diamond); experimental data of Duclaux, *et al.* (2007) (sphere diameter $D=12\text{mm}$ (\blacksquare), $D=15.6\text{mm}$ (\square), and $D=24\text{mm}$ (\bullet)), fully-nonlinear simulation ($—$), and asymptotic solution ($- -$).

theoretical analysis. This indicates that the simple treatment of the body effect in the asymptotic analysis is quite effective.

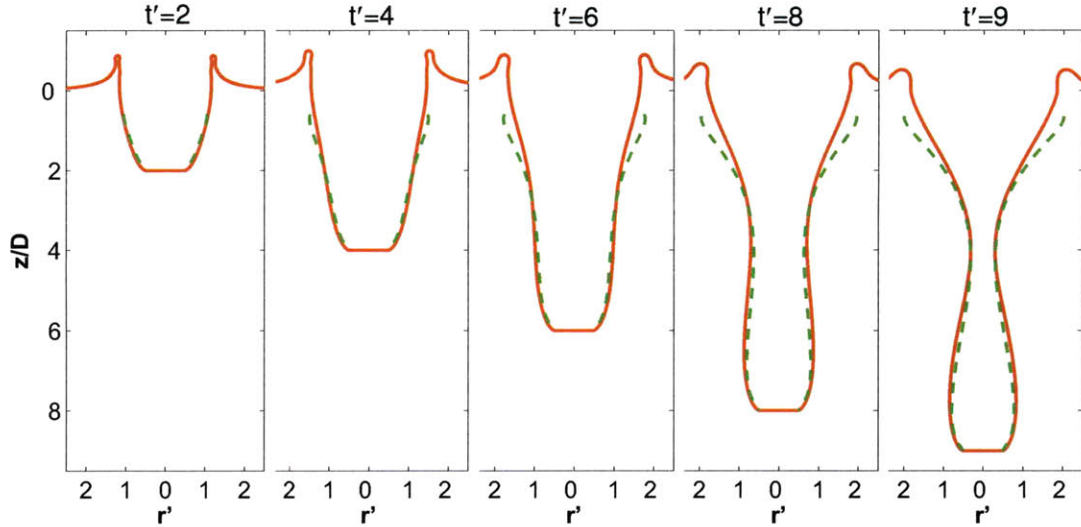
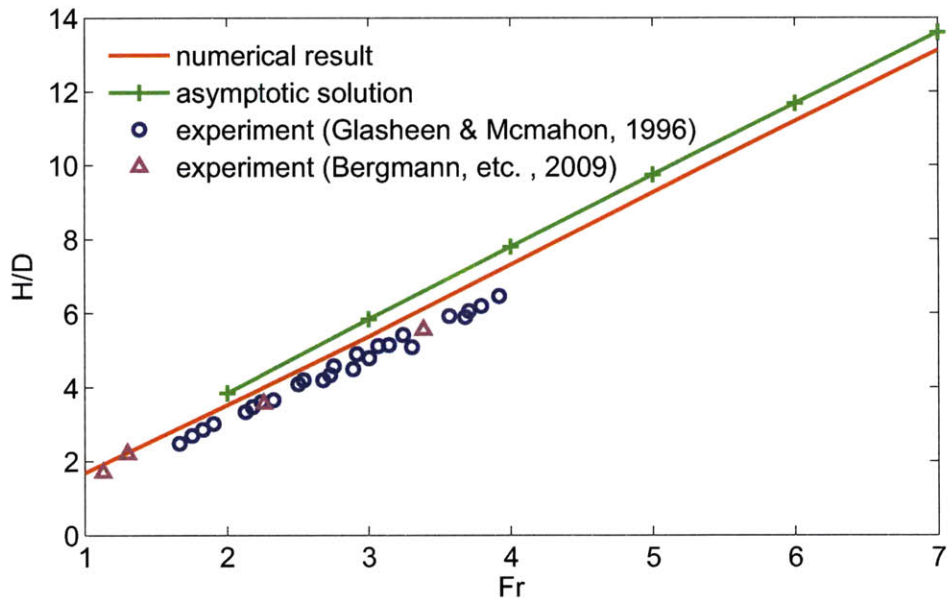
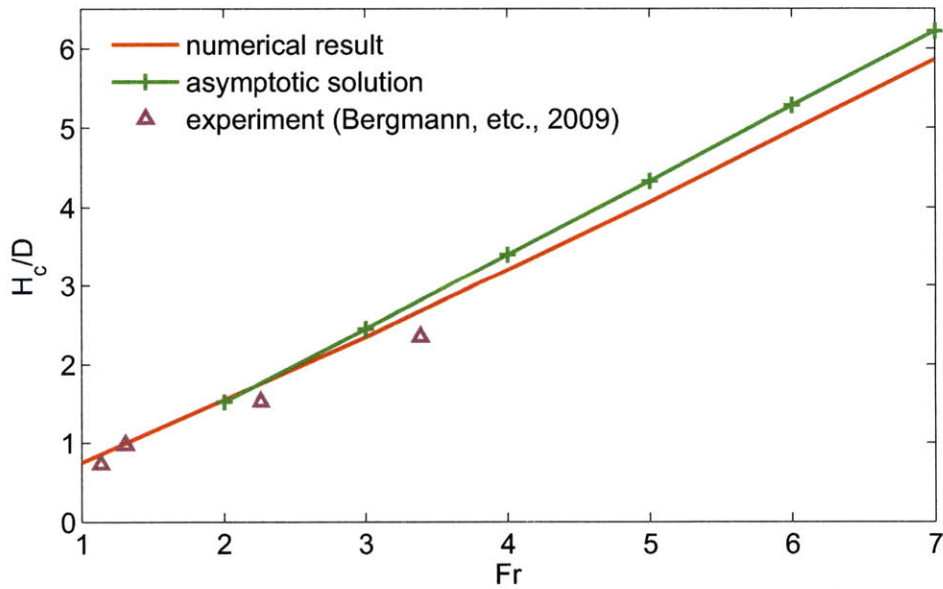


Figure 4-10: Comparison of the cavity shapes obtained by fully-nonlinear simulation (—) and asymptotic analysis (- - -) in the water entry of a circular disk with $F_r = 5$ at time $t' =$: (a) 2, (b) 4, (c) 6, (d) 8, and (e) 9.

In Figure 4-11, we show the comparisons of H and H_c as a function of F_r , in the case of disks, among the theoretical prediction, fully-nonlinear simulation, and the experimental data of Glasheen & McMahon (1996) and Bergamnn *et al.*(2009). Similarly to the sphere case, a nearly linear dependence of both H and H_c on F_r is obtained by the theory, nonlinear simulation, and experimental measurements. Both the theory and nonlinear simulation slightly overpredict H and H_c compared to both experimental data. We note that in the experiments of Glasheen & McMahon (1996), an abrupt velocity reduction in the initial impact (up to $\sim 7\%$) and an almost linear reduction of the velocity in the late stage of water entry are encountered. It is thus reasonable to obtain a lightly larger prediction of H and H_c as a constant dropping velocity is considered in the present theory and nonlinear simulation. In the experiments of Bergamnn *et al.*(2009), the velocity of the disk during its falling is controlled to be nearly constant, the measurement of H would be expected to be slightly larger than that in Glasheen & McMahon (1996). Nevertheless, they are seen to be close to each other.



(a)



(b)

Figure 4-11: Comparisons of (a) total cavity height (H) and (b) depth of cavity closure (H_c) among the experimental data of Glasheen & McMahon (1996) (\circ) and Bergmann *et al.*(2008) (\triangle), the fully-nonlinear simulation result(—), and the theoretical prediction ($-+$) for a disk with constant dropping velocity.

We compare the drag force on the disk evaluated in the asymptotic analysis and fully-nonlinear simulation to the experimental data of Glasheen & McMahon (1996), in figure 4-12. Following Glasheen & McMahon (1996), to include the hydrostatic pressure effect, we define the drag coefficient as $C_D^* = F(t)/[(0.5\rho v_0^2 + \rho gh)S]$, and plot C_D^* as a function of the so-called water-entry cavitation number $\sigma_{we} = gh/(0.5\rho V_0^2)$, where $h(t)$ represents the depth of the instantaneous body position. The experimental data of Glasheen & McMahon (1996) did not explicitly indicate the effect of Froude number. In the theoretical analysis and nonlinear simulation, two Froude numbers of $F_r=2$ and 4 are considered. Both the theoretical analysis and nonlinear simulation predict that unless very close to the free surface, C_D^* varies slowly with σ_{we} and approaches to a constant at large values of σ_{we} for which the hydrostatic effect is dominant in $F(t)$. This in general agrees with the experimental data of Glasheen & McMahon (1996). The asymptotic theory somewhat over-predicts the value of C_D^* compared to the nonlinear simulation and experimental measurements. The analysis and nonlinear simulation also show that C_D^* is not very sensitive to the value of F_r , particularly when σ_{we} is large. For small values of σ_{we} corresponding to small $h(t)$, C_D^* from the fully-nonlinear simulation decreases sharply due to the hydrodynamic effect of initial water impact. At small σ_{we} , the asymptotic theory is invalid and experimental data is not available.

4.5.3 Body geometry effect

To understand the effect of body geometry, we conduct nonlinear numerical simulations for the cavity development behind inverted truncated cones of different heights and compare these to the sphere and disk (see Figure 4-13). For the numerics, flow separation is enforced at the sharp edges for the inverted truncated cones (and the disk). For simplicity we set imposed constant downward velocity V_0 in all cases.

Figure 4-14 compares the numerically obtained profiles of the cavity associated with water entry of the different bodies. As expected, the cavity lateral size (corresponding to the same time) increases with the bluntness of the body geometry, in particular with decreasing flow separation angles α . Note that the profiles for the

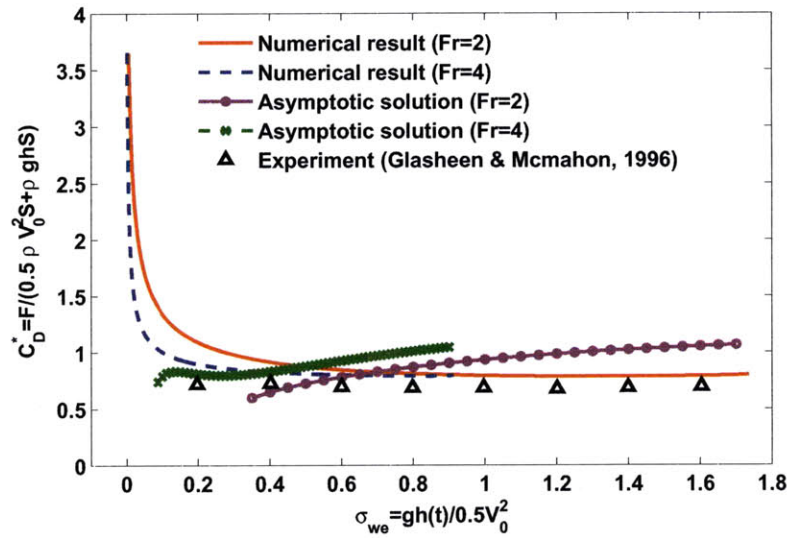


Figure 4-12: The drag force on a circular disk dropping vertically in water obtained by asymptotic theory with $F_r=2$ (-•-) and 4 (-*-), fully-nonlinear simulation with $F_r=2$ (—) and 4 (- - -), and experimental data of Glasheen & McMahon (1996) (Δ).

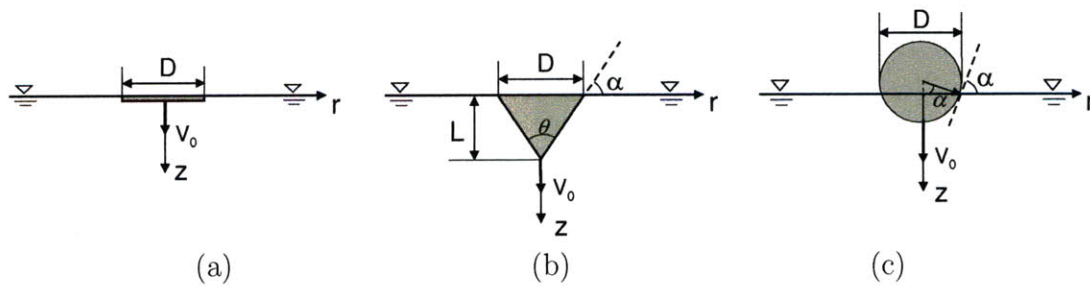


Figure 4-13: Schematic of the different (axisymmetric) geometries at the point of flow separation. The flow separation angle α used in the nonlinear simulations are (a) $\alpha=0^\circ$ for the disk; (b) $\alpha=90^\circ - \theta/2$ for the inverted truncated cone; and (c) $\alpha=70^\circ$ prescribed for the sphere.

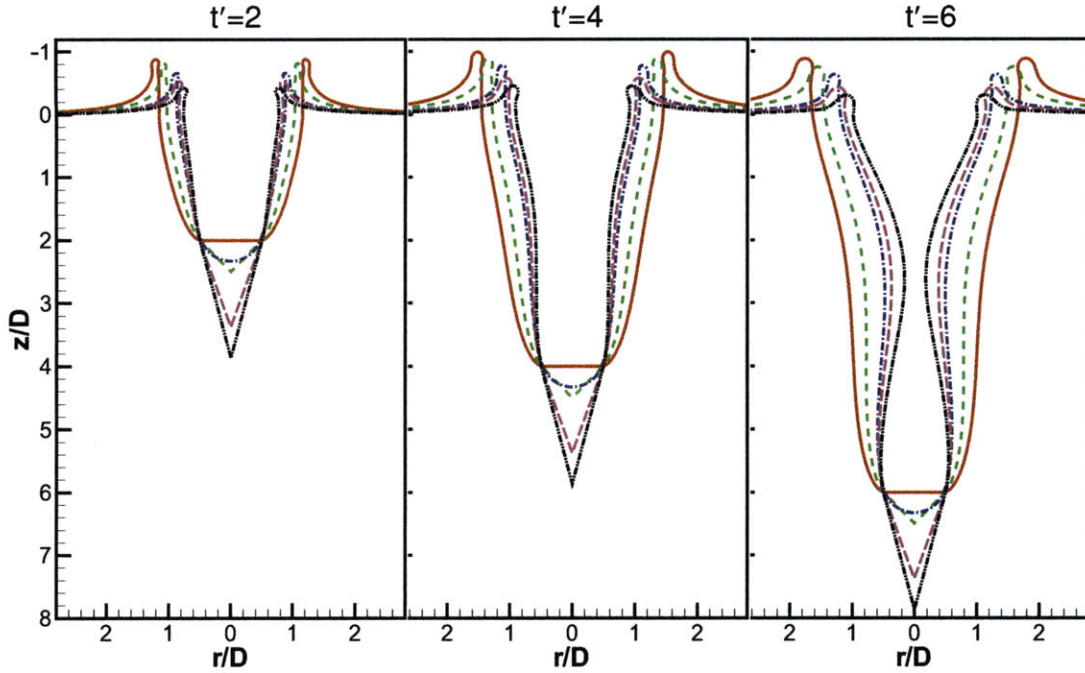


Figure 4-14: Cavity profiles in water entry of a disk (—), inverted truncated cones (height $L/D=0.5$, $\theta = 90^\circ$ (- - -); height $L/D=2.75$, $\theta = 40^\circ$ (- · -); height $L/D=3.73$, $\theta = 30^\circ$ (- · · -)), and a sphere (- · · -) with $F_r=5$ at different time $t' = tV_0/D$. The results are obtained by fully-nonlinear simulations.

inverted truncated cone of vertex angle $\theta=40^\circ$ ($\alpha=70^\circ$) is slightly narrower than that of the sphere (with the same value of α) due to the difference of the wetted body geometry.

Figure 4-15 compares the total cavity length H ($=TV_0$) and closure depth H_c of different body geometries as functions of F_r . The linear dependencies observed earlier (for the sphere and disk) obtain here. The slopes of the $H(F_r)$ and $H_c(F_r)$ curves increase with body bluntness. This qualitative behavior of H and H_c increasing with body bluntness shown in Figure 4-15 can be explained from the asymptotic theory where the point source strength m increases with bluntness. Larger m strengthens the expansion phase of the cavity development and thus leads to greater H and H_c . Figure 4-16 shows the asymptotic theory prediction of H and H_c for a wide range of vertex angle θ for inverted truncated cones at $F_r=5.0$. The asymptotic solution agrees well with the nonlinear simulation. H and H_c monotonically increase with θ

as m does.

We remark here that from the (near) linear dependencies of H and H_c on F_r in Figure 4-15 (and the fact that H and H_c vanish for $F_r \rightarrow 0$), it follows that the ratio H_c/H is (nearly) constant and independent of F_r for a given geometry (Lee *et al.* 1997; Duclaux *et al.* 2007; Bergmann *et al.* 2009).

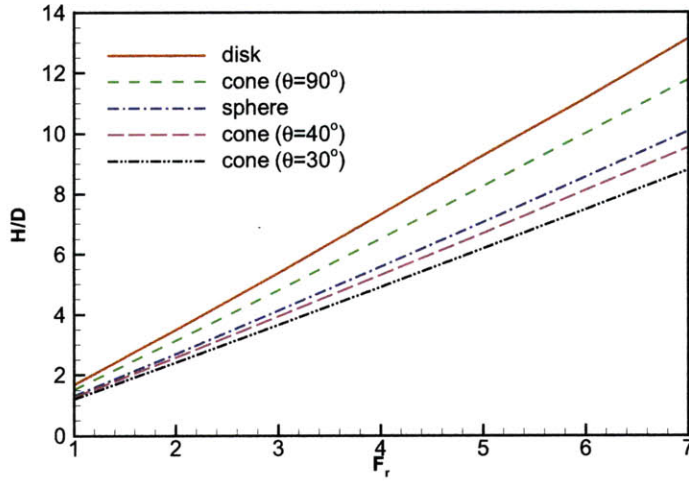
The drag forces for different body geometries obtained from fully nonlinear numerical evaluations are compared in figure 4-17, with $F_r=5$. It is seen that the disk experiences the largest drag among the geometries being tested. If a body is subject to a larger (drag) force, more energy is transferred from body into water to make the air cavity wider. The conclusion drawn here from the drag comparison is consistent with the results shown in figures 4-14 and 4-15 for cavity kinematics.

4.6 Conclusions

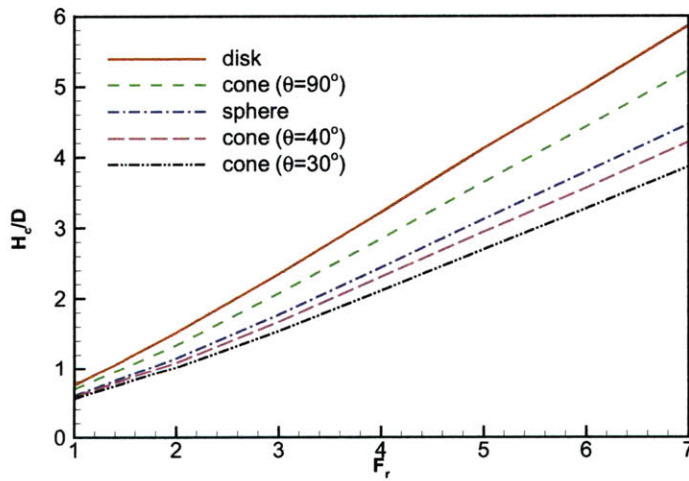
We consider the hydrodynamic problem of air cavity development and evolution in vertical water entry of an axi-symmetric body. The problem is studied using asymptotic analysis and fully nonlinear numerical simulations in the context of potential flow. The focus is in the range of relatively low Froude number, $F_r \leq O(10)$ where gravity effects cannot be neglected.

Using a matched asymptotic approach, we derive a theoretical solution for the description of the dynamics of the air cavity including three-dimensional body and flow effects. The asymptotic solution provides useful insights into the understanding of salient features and associated dynamics in the evolution of the air cavity. To validate and complement the asymptotic analysis, we then develop a nonlinear numerical simulation which includes full body and nonlinear free-surface wave effects.

Satisfactory quantitative comparisons among the asymptotic theory predictions, nonlinear numerical simulations, and existing experimental measurements are obtained for the freely dropping sphere including predictions of the cavity shape, maximum radius, pinch off position, closure time and closure height. To understand the effect of body geometry on cavity properties, we apply the matched asymptotic so-



(a)



(b)

Figure 4-15: Fully-nonlinear simulation results of (a) total cavity length (H) and (b) cavity closure depth (H_c) in water entry of a disk (—), inverted truncated cones (height $L/D=0.5$, $\theta = 90^\circ$ (- - -); height $L/D=2.75$, $\theta = 40^\circ$ (- - -); height $L/D=3.73$, $\theta = 30^\circ$ (- · · -)), and a sphere (- · · -).

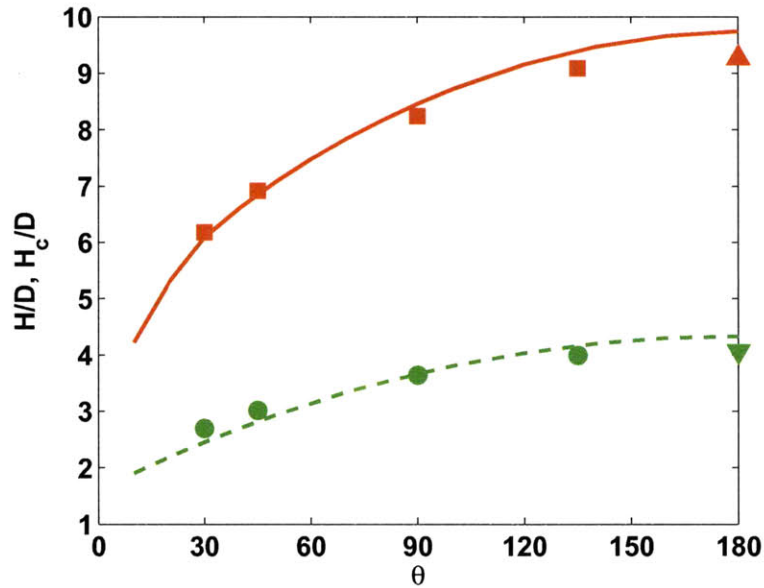


Figure 4-16: Dependence of total cavity length (H) and depth of pinch-off (H_c) on cone vertex angle θ for water entry of inverted truncated cones at $F_r = 5$. Plotted are the asymptotic prediction for H (—) and H_c (---), numerical simulation result of H (■) and H_c (●) for the cones and H (▲) and H_c (▼) for the disk.

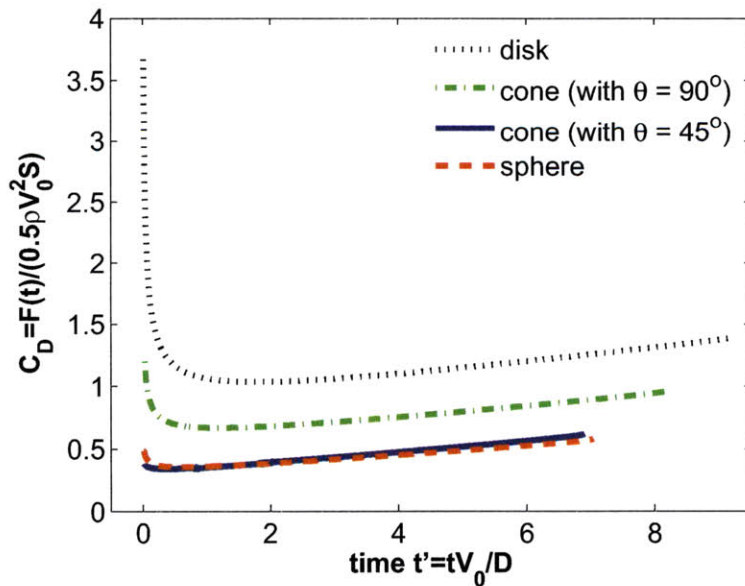


Figure 4-17: Comparison of drags on disk ($\cdot \cdot \cdot$), inverted cones with $\theta = 90^\circ$ ($- \cdot -$) and $\theta = 45^\circ$ (—), and sphere ($- - -$) during water entries with $F_r = 5$.

lution and numerical simulations to circular disk and inverted truncated cones. The asymptotic solution is found to be remarkably robust. For the disk, our analytical and numerical predictions agree well with available measurements.

These results underscore the importance of air cavity dynamics in bluff body water entry. The dynamics of the body differs significantly before and after cavity closure and depends critically on cavity closure parameters. In the low Froude number regime, in particular, depth of cavity closure and total cavity height increase linearly with the Froude number independent of body geometry. This study lays the foundation for understanding more general water impact/entry problems involving complex geometries, such as ship bow impact, projectile entry, and animals running on water surface.

4.7 References

- Aristoff, J.M. & Bush, J.W.M, Water entry of small hydrophobic spheres, *J. Fluid Mech.*, Vol.619, pp.45-78, 2009;
- Bergmann,R., van der Meer, D., Gekle, S., van der Bos, A., & Lohse, D., Controlled impact of a disk on a water surface: Cavity dynamics, *F. Fluid Mech.*, Vol.633, pp.381-409, 2009;
- Birkhoff, G. ,Zarantonello, E.H., *Jets, Wakes, and Cavities*, In Academic Press Inc, New York, 1957;
- Chu, P. C., Fan, C. W., Evans, A. D., & Gilles, A. F., Triple coordinate transforms for prediction of falling cylinder through the water column, *J. Applied Mech.*, Vol.71, pp.292-298, 2004;
- Dommermuth, G., & Yue, D.K.P., Numerical simulations of nonlinear axisymmetric flows with a free surface, *J. Fluid Mech.*, Vol.178, pp.195-219, 1987;
- Duclaux, V., Caille, F., Duez, C., Ybert, C., Bocquet, L., & Clanet, C., Dynamics of transient cavities, *J. Fluid Mech.*, Vol.591, pp.1-19, 2007;

Gaudet, S., Numerical simulation of circular disks entering the free surface of a fluid, *Physics of Fluids*, Vol.10(10), pp.2489-2499, 1998;

Glasheen, J.W., & McMahon, T.A., Vertical water entry of disks at low Froude numbers, *Physics of Fluids*, Vol.8(8), pp.2078-2083, 1996;

Gilbarg, D., & Anderson, R.A., Influence of atmospheric pressure on the phenomena accompanying the entry of spheres into water, *Journal of Applied Physics*, Vol.19(2), pp.127-139, 1948;

Greenhow, M. Water-entry and -exit of a horizontal circular cylinder, *Appl. Ocean Res.*, Vol.10(4), pp.191-198, 1988;

Holland, K. T., Green, A. W., Abelev, A. & Valent, P. J., Parameterization of the in-water motions of falling cylinders using high-speed video, *Experiments in Fluids*, Vol.37(5), pp.690-700, 2004;

Hulme, A., A ring source integral equation method for the calculation of hydrodynamic forces exerted on floating bodies of revolution, *J. Fluid Mech.*, Vol.128, pp.387-412, 1983;

Kominiarczyk, J. K., Cavity and projectile dynamics in intermediate Froude number water entry, SB thesis, Massachusetts Institute of Technology, Cambridge, MA, 2007;

Korobkin, A. A. & Pukhnachov, V. V., Initial stage of water impact, *Ann. Rev. Fluid Mech.*, Vol.20, pp.159-185, 1988;

Laerm, J., A functional analysis of morphological variation and differential niche utilization in basilisk lizards, *Ecology*, Vol.55, pp.404-411, 1974;

Lee, M., Longoria, R.G., & Wilson, D.E., Cavity dynamics in high-speed water entry, *Physics of Fluid*, Vol.9(3), pp.540-550, 1997;

Levinson, N., On the asymptotic shape of the cavity behind an axially symmetric nose moving through an ideal fluid, *Annals of Mathematics*, Vol. 47(4), pp. 704-730,

1946;

Lin, M.C. & Shieh, L.D., Simultaneous measurements of water impact on a two-dimensional body, *Fluid Dyn. Res.*, Vol.19, pp.125-148, 1997;

Liu, Y., Xue, M., & Yue, D.K., Computations of fully nonlinear three-dimensional wave-wave and wave-body interactions, Part 2. Nonlinear waves and forces on a body, *J. Fluid Mech.*, Vol.438, pp.41-66, 2001;

Mann, J. L., Deterministic and Stochastic Modeling of the Water Entry and Descent of Three-Dimensional Cylindrical Bodies, M.S. Thesis, MIT, Cambridge, MA, 2005;

Mann, J. L., Liu, Y., Kim, Y. & Yue, D. K. P., Deterministic and stochastic predictions of motion dynamics of cylindrical mines falling through water, *IEEE Journal of Ocean Engineering*, Vol.32(1), pp.21-33, 2007;

May, A., & Woodhull, J.C., Drag coefficients of steel spheres entering the water vertically, *J. Appl. Phys.*, Vol.19, pp.1109-1121, 1948;

May, A., Effect of surface condition of a sphere on its water-entry cavity, *Journal of Applied Physics*, Vol.22(10), pp.1219-1222, 1951;

May, A., Vertical entry of missiles into water, *Journal of Applied Physics*, Vol.23, pp.1362-1372, 1952;

Newman, J.N., *Marine Hydrodynamics*, The MIT Press, Cambridge, Massachusetts, 1977;

Richardson, E.G., The impact of a solid on a liquid surface, *Proc. Phys. Soc. London, Sect. A*, Vol.61(352), pp.352-367, 1948;

Truscott, T. T. & Techet, A. H., Water-entry of spinning spheres, *J. Fluid Mech.*, Vol.625, pp.135-165, 2009;

Wang, Q.X., Numerical simulation of violent bubble motion, *Phys. Fluids*, Vol.16(5), pp.1610-1619, 2004;

Worthington, A. M. & Cole, R. S., Impact with a liquid surface studied by the aid of instantaneous photography. Paper II, Phil. Trans. R. Soc. Lond. A, Vol.194, pp.175-199, 1900;

Xue, M. & Yue, D.K., Nonlinear free-surface flow due to an impulsively started submerged point sink, J. Fluid Mech., Vol.364, pp.325-347, 1998.

Chapter 5

Nonlinear Computations of Water Impact of Axisymmetric Bodies

5.1 Introduction

Understanding of the water impact phenomenon is of fundamental significance to the reliable prediction of the hydrodynamic loads in ship slamming and surface wave impact on marine structures under severe sea conditions. Impulsive loads with high pressure peaks accompany water impact as a result of the large relative velocity of a body and water. Impact load may cause severe structure damages and induce violent body motions that can affect maneuverability and operation capacity of the marine structures.

Most of the studies on the initial water impact focus on the two-dimensional problem. The pioneering work by Von Karman (1929) analyzed the impact of a wedge-shaped nearly flat body with the purpose of estimating the maximum pressure on seaplanes during landing. Wagner (1931) modified Von Karman's theory by including the water splash-up effect on the body surface. Cointe (1989) and Wilson (1989) provided the classical Von Karman and Wagner theories with a firmer theoretical basis using matched asymptotic expansions. All of these theories were derived based on the assumptions of small deadrise impact angles and small body penetration depth during the impact. To account for the effects of body geometry

and free-surface nonlinearity, various numerical computations have been developed. These include typically the generalized Wagner approach that considers the nonlinear body geometry but linear free-surface effects (e.g. Zhao & Faltinsen 1998) and the fully nonlinear simulations using Cauchy's integral theorem (e.g. Greenhow 1987; Mei, Liu & Yue 1999) and Green-theorem based boundary integral equation method (e.g. Zhao & Faltinsen 1993).

Due to high nonlinearity and unsteadiness involved, studies of the three-dimensional water impact problem are relatively fewer and mainly focus on the vertical water entry of axisymmetric bodies. Moghisi & Squire (1981) conducted an experimental investigation of the initial impact load on a sphere. Shiffman & Spencer (1951) derived a theoretical solution for vertical water entry of spheres and cones by approximating the flow during the impact as that around an ellipsoid. Miloh (1981; 1991) developed an analytical expression for the small-time slamming coefficient and wetting factor for water entry of a sphere by making use of the added mass coefficient for a double spherical bowl. Zhao & Faltinsen (1998) applied the three-dimensional constant boundary element method to numerically study the problem of vertical water entry of axisymmetric bodies.

Despite these advances, there exist at least a couple of fundamental issues that must be further addressed in order to obtain a reliable prediction of the impact hydrodynamics for practical applications. The first one is the gravitational effect on the impact loads and water surface kinematics. In the existing theoretical and numerical studies, the gravity effect is simply neglected (Miloh 1991; Zhao & Faltinsen 1993), which is strictly valid for an infinite Froude number. As a result, the formulation of the impact problem is largely simplified with the free surface becoming an equipotential (or zero-gravity) surface (e.g. Zhao & Faltinsen 1998). In particular, this simplified formulation leads to a self-similarity solution in the water entry of wedges (Dobrovol 1969) and cones (Shiffman & Spencer 1951). In naval architecture and marine engineering applications, the water impact associated with ship slamming and wave impact on offshore structures often occur at Froude numbers of $O(1)$. In these situations, the gravity effect is of significance. Properly accounting for gravity effect

in the analysis of water impact is a challenge and has received little attention so far.

Another issue that has not been robustly dealt with in numerical simulations is flow separation from the body surface, which might occur during the impact. For bodies with sharp edges, flow separation is considered to be fixed at the discontinuous surface location as in the case of knuckles (e.g. Zhao & Faltinsen 1998). For bodies with continuous curved surface, however, the position of flow separation is in general unknown. To accurately evaluate the impact pressure distribution and hydrodynamic load on the body, the location of flow separation on the body needs to be determined properly. Also, in the time simulation of the water impact process, the flow-body intersection line should be a priori at each time step since different boundary conditions need to be applied on the body and the free surface. By brute-force keeping the jet flow attached to the body surface and not detecting body-flow separation properly in the simulation, nonphysical (negative) pressure distribution would be resulted in a considerable portion of the body surface near the jet root (e.g. Greenhow 1987; Battistin & Iafrati 2003).

In this chapter, we focus on the understanding of the gravity effect in the impact phenomenon using numerical nonlinear simulations within the context of potential flow (e.g. Miloh 1991). In addition, we develop effective and robust treatments to properly account for the effect of flow separation on body surface in the impact process. A fully-nonlinear simulation, based on an axisymmetric boundary element method with the mixed Eulerian-Lagrangian approach (MEL), is employed to study the water entry problem with a wide range of Froude numbers. Two types of body geometries are considered: inverted cones with different deadrise angles and spheres.

For the inverted cone impact problem, there is no explicit physical length scale. The governing dimensionless parameters are found to be the deadrise angle α and the (generalized) Froude number $F_r = \sqrt{V/gt}$ (with Vt as the length scale) where V is the impacting velocity of the body, t the time, and g the gravitational acceleration. The gravity effect in the impact process is measured by the dependence of the results on F_r . As in water impact of any blunt body, a thin jet flow is developed on the surface of the cone, which is associated with the square-root singularity along the intersection

of the body surface and free surface (e.g. Miloh 1991). To properly treat the thin jet flow in the simulation is of critical importance to the accurate computations of impact pressure distribution and free-surface deformation. Zhao & Faltinsen (1993) developed an effective numerical treatment by cutting away the jet flow in the study of two-dimensional wedge impact at the infinitely large Froude number. In our study, we extend and further develop this approach for the three-dimensional impact problem. With the improved treatment for jet flow, we are able to simulate the complete impact process and obtain the overall features of free surface evolution under the gravity effect. Based on these simulations, we obtain the dependencies of the impact pressure, impact loads, and free-surface profiles upon F_r and α , from which the gravity effect is assessed.

For the sphere impact problem, there are also two governing parameters: the conventional Froude number $F_r = V/(gR)^{1/2}$ and the nondimensional time $\tau = Vt/R$ where R is the radius of the sphere. In the (very) initial stage of the impact when the wetted body surface is almost flat, flow does not separate from but attaches to the sphere surface. After the initial (near-flat) impact, unlike in the inverted cone impact, flow separation from the sphere surface can occur. To model this process, we apply the physical requirement of zero total pressure to determine the position of flow separation on the sphere, at which the flow detaches from the body freely during the impact. This modeling is shown to be effective and reliable with the predicted impact load from the simulation matching with the experimental measurements reasonably. With this modeling, we are able to simulate the complete impact process of spheres at various Froude numbers, and obtain the dependencies of the sphere impact quantities on the governing parameters F_r and τ .

This chapter is organized as follows. In §5.2, the mathematical formulation of the initial boundary-value problem for the general three-dimensional axisymmetric water impact problem is described. The application of the boundary integral equation method with the MEL approach to solve the initial boundary-value problem is also presented briefly. In §5.3, we explain and discuss the important numerical treatments implemented in the simulations. Detailed results for the vertical impact of inverted

cones and spheres obtained by fully-nonlinear numerical simulations are presented in §5.4 and §5.5, respectively. We conclude in §5.6.

5.2 Problem Formulation

We consider the initial slamming stage of axisymmetric bodies in vertical water entries. Unless otherwise stated, the drop velocity of the body is assumed to be constant during the impact in this study. We define a cylindrical coordinate system $\mathbf{x} \equiv (r, \theta, z)$ with r as the radial coordinate, θ the azimuthal coordinate, and z the axis pointing upwards. The origin is placed on the undisturbed free surface. Referring to this coordinate system and assuming the flow to be circumferentially stable, all physical quantities such as the velocity of the flow and the pressure distribution on the body are independent of θ .

We assume the fluid motion to be irrotational everywhere and consider the existence of a velocity potential ϕ which satisfies Laplace's equation in the fluid domain \mathcal{V} :

$$\nabla^2 \phi(\mathbf{x}, t) = \frac{\partial^2 \phi}{\partial r^2} + \frac{1}{r} \frac{\partial \phi}{\partial r} + \frac{\partial^2 \phi}{\partial z^2} = 0, \quad \mathbf{x} \in \mathcal{V}(t), \quad (5.1)$$

On the free surface $S_F(\mathbf{x}, t)$, ϕ satisfies the kinetic and dynamic boundary conditions which can be written in a Lagrangian form:

$$\frac{D\mathbf{x}}{Dt} = \nabla \phi, \quad \text{on } S_F(\mathbf{x}, t) \quad (5.2)$$

and

$$\frac{D\phi}{Dt} = \frac{1}{2} |\nabla \phi|^2 - gz - P_F/\rho, \quad \text{on } S_F(\mathbf{x}, t) \quad (5.3)$$

where $D/Dt \equiv \partial/\partial t + \nabla \phi \cdot \nabla$ denotes the material derivative and P_F is the atmospheric pressure on $S_F(\mathbf{x}, t)$. In this study, we set $P_F = 0$. We assume that the body is rigid. On the body surface, $S_B(\mathbf{x}, t)$, the normal velocity of the fluid is equal to that of the body:

$$\nabla \phi \cdot \mathbf{n} = V n_z, \quad \text{on } S_B(\mathbf{x}, t) \quad (5.4)$$

where \mathbf{n} is the unit normal pointing outside of the fluid domain, n_z the vertical component of \mathbf{n} , and V the dropping velocity of the body. In addition, we specify a suitable far-field condition:

$$\nabla\phi \rightarrow 0, \quad \text{for } |\mathbf{x}| \rightarrow \infty. \quad (5.5)$$

As initial conditions (at $t=0$), we assume that the body (with vertical velocity V) just touches the free surface so that the free surface is flat and ϕ is zero on the free surface.

The force exerted on the falling body by the fluid, $F(t)$, including both the hydrodynamic and hydrostatic components, is given by

$$F(t) = \int_{S_B(t)} P n_z ds \quad (5.6)$$

where P is the total pressure on the wetted body surface which can be evaluated based on Bernoulli's equation:

$$\frac{P}{\rho} = -\left(\frac{\partial\phi}{\partial t} + \frac{1}{2}|\nabla\phi|^2 + gz\right) \quad (5.7)$$

in which ρ is the fluid density.

We apply the boundary integral equation method with the mixed Eulerian-Lagrangian approach for free-surface tracking to solve the stated nonlinear initial boundary-value problem. Starting from $t=0$, the time simulation of the nonlinear water impact problem consists of two major operations: (I) solve the mixed boundary-value problem for ϕ to obtain the normal free-surface velocity, ϕ_n on $S_F(\mathbf{x}, t)$, and the velocity potential on the body, ϕ on $S_B(\mathbf{x}, t)$; and (II) integrate the nonlinear free-surface boundary conditions, (5.2) and (5.3), with time to update the position of the free surface and the velocity potential on the free-surface, $S_F(\mathbf{x}, t + \Delta t)$ and $\phi(\mathbf{x}, t + \Delta t)$. At the same time, obtain the new position of the body, $S_B(\mathbf{x}, t + \Delta t)$ by integrating the equation of body motion with time.

To solve the boundary-value problem at any time t , we apply Green's second iden-

tity to obtain the following boundary integral equation (for details see Dommermuth & Yue 1987)

$$\beta(r, z, t)\phi(r, z, t) = \int_{\partial S(t)} r' \left(\frac{\partial \phi}{\partial n'} - \phi \frac{\partial}{\partial n'} \right) G(r, z; r', z') d\mathbf{x}', \quad (r, z) \in \partial S \quad (5.8)$$

where β is the solid angle at \mathbf{x} and G the Rankine ring source Green function. The above line integral is along the trace $\partial S(t) = \partial S_F \cup \partial S_B \cup \partial S_\infty$ of $S(t)$ where $S(t)$ is the total boundary of the fluid domain including the free surface S_F , the wetted body surface S_B , and the far-field boundary S_∞ . One notes that the principal-value Cauchy integral is implied in (5.8). In (5.8), ϕ_n on ∂S_B is given by (5.4), and ϕ on ∂S_F is obtained from the operation (II). By the use of an axisymmetric boundary element method, we can solve (5.8) for unknown ϕ on ∂S_B and ϕ_n on ∂S_F . Once the normal free-surface velocity is obtained from the boundary-value solution, the time integration in operation (II) can be carried out in a straightforward way.

5.3 Numerical Implementation

5.3.1 Overall numerical scheme

The fully-nonlinear time-domain simulation of the water impact problem is achieved by repeating operations (I) and (II) starting from the initial condition. In these two operations, (I) requires the most of the computational time and memories while (II) affects the stability of the simulation. From the simulation, we obtain the time history of the impact pressure distribution and hydrodynamic load on the body as well as the evolution of the free-surface deformation. Based on these, we can study the gravity effect and understand the characteristics of the impact phenomenon.

The objective of operation (I) at each time step, say t_0 , is to solve the integral equation (5.8) for unknown ϕ_n on S_F and ϕ on S_B . The free-surface position $S_F(t_0)$, the wetted body surface $S_B(t_0)$, ϕ on $S_F(t_0)$ (i.e. Dirichlet boundary), and ϕ_n on $S_B(t_0)$ (i.e. Neumann boundary) are all specified. The axisymmetric linear boundary element method of Dommermuth & Yue (1987) is used to numerically solve (5.8). In

this method, the boundary trace $\partial S(t_0)$ is approximated by cubic splines and divided into a number of small line segments ∂S_j , $j = 1, 2, \dots, N$. Along each element, ϕ and ϕ_n are assumed to be piecewise linear. With these approximations, the imposition of (5.8) at collocation points of ∂S results in a system of linear equations, from which unknown ϕ_n (ϕ) on S_F (S_B) are determined.

In principle, $S_F(t_0)$ extends to infinity in space. The contribution from the far-field boundaries in (5.8) must be properly considered in the numerical simulation using a finite computational domain. As discussed in Chapter 3, there are several ways to account for the far-field boundary effects in the study of wave-body interactions. These include the use of periodic boundary conditions (e.g. Vinje & Brevig 1981; Liu, Xue & Yue 2001), the match of the near-field nonlinear solution to an approximate far-field solution (e.g. Faltinsen 1977; Dommermuth & Yue 1987), and the use of artificial damping to absorb the outgoing disturbances (e.g. Xue 1997; Kim *et al.* 1998; Kim 1999). Since the time duration of water impact is relatively short, the impact-induced waves do not have enough time to travel a large distance from the body. As a result, the far-field boundary effect is relatively easy to deal with in this study. Following the damping-zone treatment adopted by Dommermuth & Yue (1989), we use a simple tapering function (Hermitian polynomial) to smooth the free surface elevation η and the velocity potential ϕ in the damping-zone at each time step.

After ϕ_n on $S_F(t_0)$ is obtained from (5.8), we can evaluate $\nabla\phi$ on $S_F(t_0)$. We then integrate (5.2) and (5.3) with time to obtain the new position of the free surface $S_F(t_0 + \Delta t)$ and the updated $\phi(t_0 + \Delta t)$ on $S_F(t_0 + \Delta t)$. A modified fourth-order Runge-Kutta (RK4) method is used for the time integration. In the intermediate steps of RK4, we only update ϕ and ϕ_n but not S_F . Comparing with the exact RK4 scheme, this treatment can greatly save the computational effort with a slight sacrifice of numerical accuracy (Dommermuth & Yue 1987). If the body follows a prescribed dropping, the new position of the body $S_B(t_0 + \Delta t)$ and the updated $\phi_n(t + \Delta)$ on $S_B(t_0 + \Delta t)$ are easily specified. For the free fall motion, we need to compute the impact force on the body from (5.6) and then integrate the equation of motion of the body with time to obtain the new position of the body and the body velocity at

$t_0 + \Delta t$, with which we get the updated $\phi_n(t + \Delta t)$ on $S_B(t_0 + \Delta t)$. This completes the computations in operation (II).

Since the water impact is a highly transient problem, adaptive time stepping is used in the simulation with the time step determined by

$$\Delta t \leq C \frac{(\Delta l)_{min}}{|(\nabla\phi)_{S_F}|_{max}} \quad (5.9)$$

where $|(\nabla\phi)_{S_F}|_{max}$ is the maximum velocity on the free surface, $(\Delta l)_{min}$ the minimum panel size on the free surface, and C the Courant number which is typically chosen to be 0.2 in this study. The condition (5.9) requires that the Lagrangian particles on the free surface do not move more than one grid size in one time step to ensure the stability of (explicit) time integration (e.g. Xue 1997).

In the nonlinear time simulation of the water impact problem, an important numerical issue is to properly update the position of the intersection between the body and the free surface. The intersection line determines the instantaneous wetted body surface which affects the evaluation of the impact pressure and hydrodynamic load on the body. Near the intersection line, a thin jet flow with a relatively large fluid velocity is normally developed. Properly updating the intersection position and including the thin jet flow effect are challenging in the time simulation of the impact problem. In this study, we apply an effective jet-cutting treatment for the inverted cone impact problem and develop a pressure based criterion to determine the instantaneous position of flow separation for the sphere impact problem.

5.3.2 Jet-cutting treatment for cone impact simulation

In water impact of an inverted cone, figure 5-1, a jet flow is typically observed in the region of the intersection of the body with the free surface. Since the jet flow near its tip is very thin, numerical simulations based on the boundary element method easily break down. As the pressure inside the thin jet is almost equal to the atmospheric pressure, it does not provide a significant contribution to the impact load on the body. To overcome this numerical difficulty, we thus follow Zhao & Faltinsen (1993)

to simply cut the tip portion of the jet flow off the computational domain, as shown in figure 5-1.

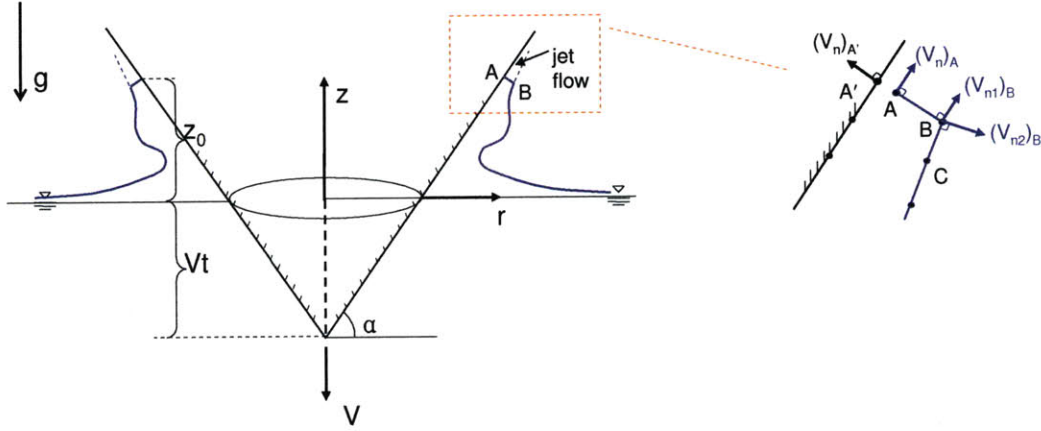


Figure 5-1: Schematic of vertical water impact of an inverted cone of deadrise angle α with a constant velocity V .

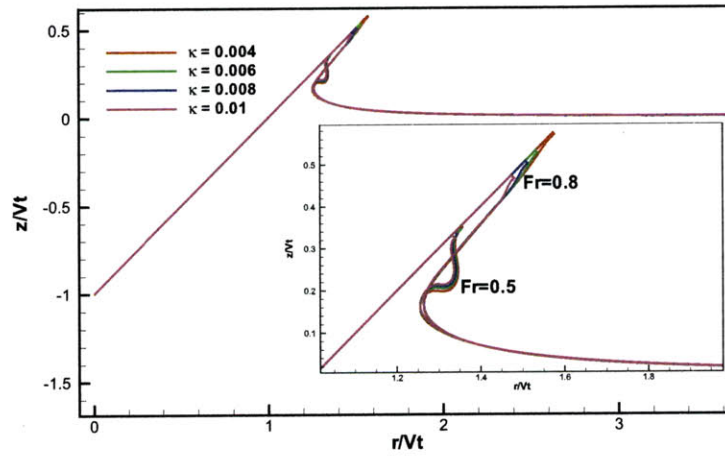
The jet-cutting treatment was first adopted by Zhao & Faltinsen (1993) in the study of the two-dimensional wedge water entry problem. It is now widely applied in the simulation of the similar water impact problems (e.g. Battistin & Iafrati 2003; Sun & Faltinsen 2006). In their approach, the jet-cutting treatment is imposed in the simulation once the angle between the boundary element on the water surface next to the top element, i.e. **BC** in figure 5-1, and the body surface is smaller than a preset value. This type of treatment works well for the impact problems without the gravity effect, since the flow preserves self-similarity and the free surface shape does not vary much with time after the initial transient disturbance is radiated away from the body.

In the present study, with the gravity effect being taken into account, the free surface shape varies significantly with time during the impact process. The existing jet-cutting treatment needs to be modified to accommodate the various characteristic flows encountered in water impact of inverted cones under the gravity effect. In the present simulation, the first cut of the jet can be treated in the same way as in Zhao & Faltinsen (1993) with the top element **AB** on the water surface set to be perpendicular to the body surface. Subsequent cuttings are applied to the portion of

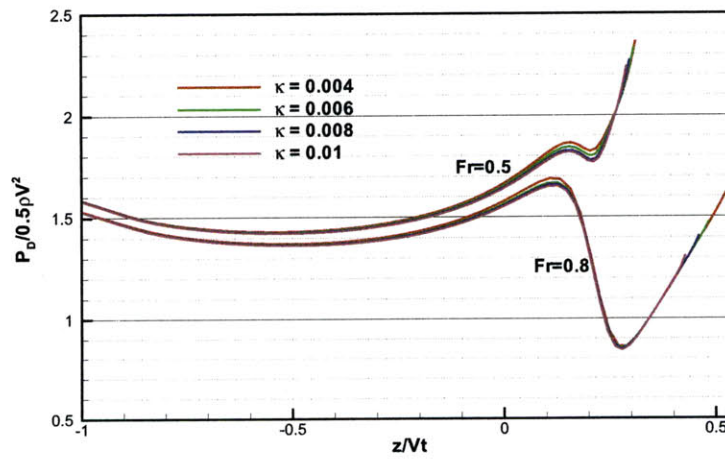
the jet whose thickness is smaller than the (panel size) criterion $\ell_c(t, \alpha) = \kappa V t / \tan \alpha$, where κ is a preset small constant coefficient. The length criterion $\ell_c(t, \alpha)$ varies with t and α , similarly to the radius of the cross section of the inverted cone at the still water plane. This makes sense as the size of the up jet flow is proportional to the amount of water displaced by the body. (Note that at late stage of impact when the free surface near the body does not show an apparent jet flow feature, the value of ℓ_c becomes noncritical as jet cutting may not be necessary).

With the modified jet-cutting treatment, our numerical simulations show that the impact load and free-surface features are insensitive to the choice of small κ value. Taking the inverted cone with $\alpha = 45^\circ$ as an example, figure 5-2 shows the influence of κ values on the free surface shape and the hydrodynamic pressure distribution on the body at $F_r = 0.5$ and 0.8. Results with κ varying from 0.004 to 0.01 are seen to be nearly indistinguishable graphically. For the results shown in later sections, $\kappa = 0.005$ is used.

Special cares need to be taken in solving the boundary-value problem for unknowns associated with the top element **AB** and in updating the position of **AB** with time. First of all, a weak singularity exists at the intersection of the body with the free surface due to the confluence of boundary conditions (e.g. Miloh 1980). To overcome this computational difficulty, an effective double-node treatment is applied at the water-body intersection (e.g. Lin 1984). As seen in figure 5-1, two nodes, **A** and **A'**, are placed at the same physical position. By using the linear boundary element method, (5.8) is imposed at the end points of all panels. At **A'**, we specify its normal velocity $(V_n)_{A'}$ and solve for the velocity potential $\phi_{A'}$. At **A**, the condition $\phi_A = \phi_{A'}$ is imposed while its normal velocity $(V_n)_A$ is solved for. At the other endpoint **B** of the top element, two normal directions exist. We set $(V_{n1})_B = (V_n)_A$ and solve for $(V_{n2})_B$. After the boundary-value problem is solved at each time step, the position of the top element is updated with time using the normal velocities $(V_n)_A$ and $(V_{n2})_B$.



(a)



(b)

Figure 5-2: Influences of κ values for jet-cutting on (a) free surface profile, and (b) hydrodynamic pressure distribution on the body surface, in water impact of an inverted cone of $\alpha = 45^\circ$ at $Fr = 0.5$ and 0.8 .

5.3.3 Determination of flow separation from body surface for sphere impacts

Flow separation from the body surface is often observed in water entry of a blunt body. Determination of the separation position is of significance for a reliable prediction of the impact load on the body and the free-surface deformation in the impact. If flow separation is not properly considered in the computation, a negative pressure distribution on the body surface that is nonphysical could be resulted (e.g. Greenhow 1987; Battistin & Iafrati 2003). There is no robust algorithm or treatment that can effectively model the evolution of flow separation in water entry of a general bluff body as it is influenced by multiple factors such as body geometry and surface condition, fluid density and viscosity, and fluid surface tension. In the present study, we develop a simple procedure that can give a proper determination of the flow separation location on the body surface and effectively account for its effect in the simulation of sphere impact in the context of potential flow.

At the (very) initial stage of sphere impact, a thin jet is developed along the sphere surface. In the simulation, as shown in figure 5-3a, we cut off the small tip region of the jet with the main part of the jet preserved similarly to the treatment applied in the computation of the inverted cone impact problem. As the impact process continues, the jet flow is allowed to freely separate from the sphere surface at the place where the total pressure is zero, as illustrated in figure 5-3b.

After the free-surface and body positions are updated at each time step in the simulation, the new position of flow separation on the body needs to be located for the next time step. To do that, we evaluate the total pressure at the water-body intersection at the current time step. If the pressure is slightly negative, it indicates that the separation point is moved a bit too fast in the previous time step. We fix the separation point at the current position for the next time step. On the other hand, if the pressure is slightly positive, the separation point is moved a bit too slowly in the previous time step. We update the separation point upwards along the body surface for the next time step. Since the time step used in the simulation is always very small

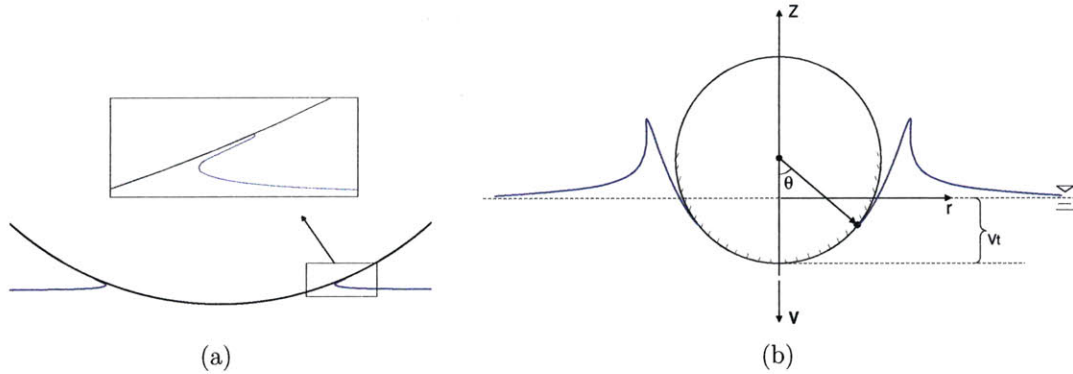


Figure 5-3: Schematic of vertical water impact of a sphere with a constant velocity V at: (a) very initial stage; and (b) later stage after flow separation from the body is formed.

(cf. equation (5.9)), the pressure at the separation point is ensured to be very close to zero in the simulation of the entire impact process. We note that in principle, the separation point can be placed at the exactly zero-pressure position that can be obtained by an iterative process at each time step. The above simplified treatment adopted in our simulations, however, saves a substantial amount of computational effort with a slightly decreased accuracy compared to the iterative approach.

The zero-pressure criterion for the determination of the flow separation point makes sense physically since the pressure on the free surface is always zero and there should be no jump in the pressure along the boundary from the body surface to the free surface. Our numerical results in §5.5 show that the separation position obtained in this way evolves smoothly with time and the predicted impact load agrees well with available experimental measurements.

5.3.4 Evaluation of impact pressure

An accurate evaluation of the pressure on the body surface is crucial for the determination of the flow separation location and the evaluation of the impact load on the body in the water impact problem.

From (5.7), it is clear that $\frac{\partial\phi}{\partial t}$ must be properly evaluated in order to obtain an accurate pressure computation on the body. One way to evaluate $\frac{\partial\phi}{\partial t}$ (at any grid

point on the body surface) is based on the formula:

$$\frac{\partial\phi}{\partial t} = \frac{D\phi}{Dt} - V_p \cdot \nabla\phi \quad (5.10)$$

where V_p is the velocity of the grid under consideration. The material derivative as well as the fluid velocity $\nabla\phi$ can be evaluated using the finite difference method based on the velocity potentials on the body obtained at consecutive time steps. This approach gives a satisfactory computation of the pressure for the problems with zero or small amplitude body motions. For the water impact problem, the pressure obtained in this way is susceptible to nonphysical oscillations when the jet flow is cut off or when the body discretization is modified in the simulation (e.g. Wu & Eatock Taylor 1996; Battistin & Iafrati 2003).

An alternative way to compute $\frac{\partial\phi}{\partial t}$ is to solve the following integral equation:

$$\beta(r, z, t)\phi_t(r, z, t) = \int_{\partial S(t)} r' \left(\frac{\partial\phi_t}{\partial n'} - \phi_t \frac{\partial}{\partial n'} \right) G(r, z; r', z') d\mathbf{x}', \quad (r, z) \in \partial S. \quad (5.11)$$

This equation is obtained by taking the partial time derivative of (5.8). In order to solve the above integral equation, we need to determine $\frac{\partial\phi}{\partial t}$ on the free surface, which can be easily realized based on the Bernoulli equation:

$$\frac{\partial\phi}{\partial t} = -\frac{1}{2}|\nabla\phi|^2 - gz. \quad (5.12)$$

In addition, we need to know $\frac{\partial\phi_t}{\partial n}$ on the body, which can be obtained from the formula (e.g. Battistin & Iafrati 2003):

$$\frac{\partial\phi_t}{\partial n} = -\frac{\partial V}{\partial t} n_z + V \frac{\partial\phi_z}{\partial n} \quad (5.13)$$

where V is the vertical dropping velocity of the body. With $\frac{\partial\phi}{\partial t}$ on the free surface and $\frac{\partial\phi_t}{\partial n}$ on the body determined, we can solve (5.11) for $\frac{\partial\phi}{\partial t}$ on the body. Our numerical tests show that $\frac{\partial\phi}{\partial t}$ obtained from (5.11) is more stable than that by the finite difference method.

5.4 Numerical results for inverted cone impact

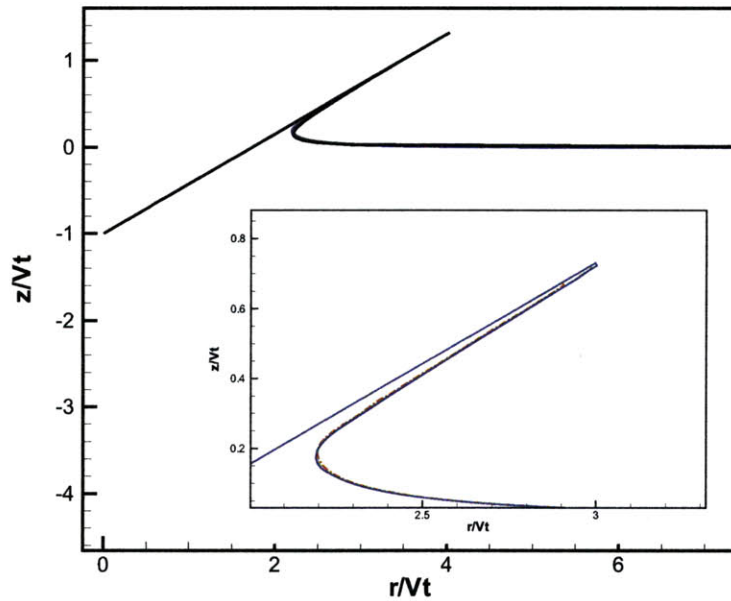
In this section, we investigate the impact problem of an inverted cone that strikes the water surface vertically with a constant velocity V . The focus is on the understanding of the characteristics of the impact pressure and hydrodynamic load on the body as well as the free surface shape near the body with the inclusion of the gravity effect. Since the problem does not have an apparent physical length scale, we can define the generalized Froude number as $F_r = (V/gt)^{1/2}$ by using Vt as the length scale (in an analogy to the similarity parameter defined in unsteady motion of a flat plate in viscous fluid (Newman 1977)). In addition to F_r , the solution of this impact problem also depends on the deadrise angle of the inverted cone, α . Fully nonlinear numerical simulations in the time domain are performed to quantify the influence of F_r and α on the dynamics and kinematics involved in the water impact of inverted cones. Of particular interest is the gravity effect which is characterized by the dependence of the solution on F_r .

5.4.1 Comparisons with existing studies for $F_r = \infty$

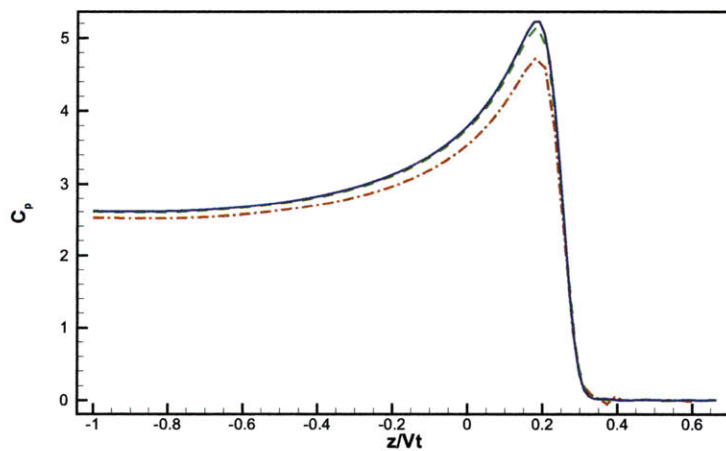
Before the detailed study of the gravity effect, we verify our numerical scheme by comparing the present simulations with the existing theoretical and numerical results for the case of $F_r = \infty$ in which the gravity effect is ignored.

As discussed by Shiffman & Spencer (1951), the fluid motion in water entry of an inverted cone (with any α) is self-similar for $F_r = \infty$. As a first validation, we examine the self-similarity feature of the flow dynamics obtained in the present simulations with various values of α . Since there is no gravity effect, the term gz in (5.3) is removed. The simulation is started with a small portion of the tip of the cone submerged in the water at $t = 0$ and approaches to the self-similarity solution as the initial transient effect radiates away. Figure 5-4 shows a sample result on the evolution of the free surface profile near the body and the impact pressure distribution on the wetted body surface for a cone with $\alpha = 30^\circ$. The free-surface profile (normalized by the length Vt) in figure 5-4a and the impact pressure coefficient (defined as

$C_p = P/(\frac{1}{2}\rho V^2)$ in figure 5-4b are seen to converge to the self-similar solution as the simulation time increases.



(a)



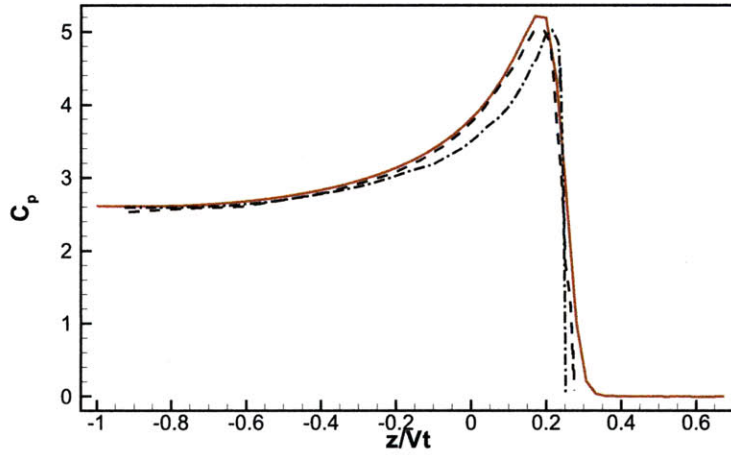
(b)

Figure 5-4: Evolution of the normalized (a) water surface profile in the intersection region and (b) impact pressure on the wetted body surface in water impact of an inverted cone with $\alpha = 30^\circ$ and $F_r = \infty$. The plotted are the nonlinear simulation results at $t=0.1$ (- · -); 0.5 (- -); and 1.0 (—).

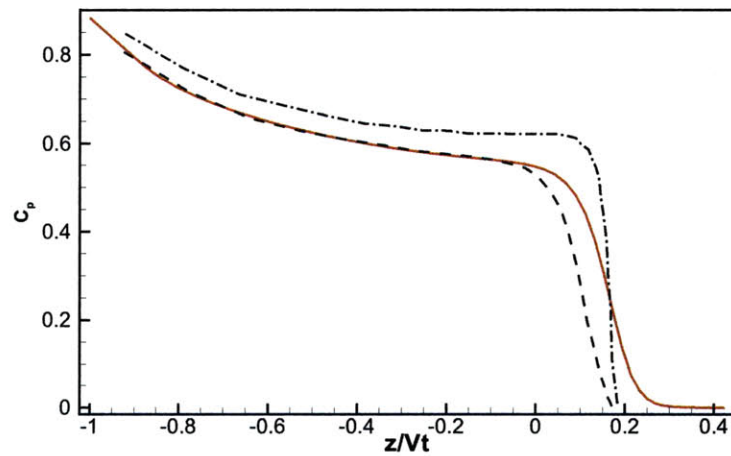
To further validate our simulations, we compare our converged self-similarity result of the impact pressure with the nonlinear solution of Zhao & Faltinsen (1998) and the modified Wagner solution of Faltinsen & Zhao (1998). The comparisons are shown in figure 5-5 for cones with $\alpha = 30^\circ$ and 60° . Owing to the simplifications made in the Wagner approach, an apparent difference is seen between the modified Wagner’s solution and the fully nonlinear predictions. Overall the present nonlinear simulation result agrees well with that of Zhao & Faltinsen (1998) except in the small neighborhood of the intersection between the body and the free surface, where a thin jet flow occurs. There are two main factors contributing to the discrepancy of the solutions. First, the constant panel method (CPM) used by Zhao & Faltinsen (1998) collocates at the center of each panel and thus does not obtain an accurate prediction of the velocity of the jet flow (e.g. Zhao & Faltinsen 1993). In the present simulation, on the contrary, the linear boundary element method is employed and a robust double-node technique is applied to obtain a more accurate solution at the intersection (e.g. Lin, Newman & Yue 1984; Dommermuth & Yue 1987; Liu, Xue & Yue 2001). Secondly, we only cut off the small tip part of the jet flow and a major portion of the jet flow is included in the simulation while most part of the jet flow is cut off in Zhao & Faltinsen (1998). Therefore, the present numerical scheme and conservative jet-cut treatment lead to a more accurate prediction of the impact pressure distribution in the intersection region.

5.4.2 Gravity effect

The gravity effect on water impact of inverted cones can be inferred from the dependence of the solution on F_r . Figure 5-6 compares the normalized free-surface profile in the neighborhood of the intersection between the body and the free surface for F_r in the range of $[0.45, 2.0]$ with a fixed $\alpha = 45^\circ$. Note that the free-surface profile for $F_r > 2$ is graphically indistinguishable from that of $F_r = 2$ and is thus not shown. In the far field of the body, the free surface remains nearly flat and hardly deforms from its initial position. For relatively high Froude numbers ($F_r \gtrsim 0.8$), the free surface reflects the characteristic feature of a sharp jet flow. For smaller Froude numbers,



(a)



(b)

Figure 5-5: Comparison of the impact pressure distribution on the wetted body surface in water impact of inverted cones with (a) $\alpha = 30^\circ$ and (b) $\alpha = 60^\circ$ at $F_r = \infty$ among the present nonlinear simulation result (—), nonlinear solution of Zhao & Faltinsen (1998)(- -), and modified Wagner solution of Faltinsen & Zhao (1998)(- · -).

the apparent jet flow feature disappears and the free surface gradually overturns as a result of the gravity effect.

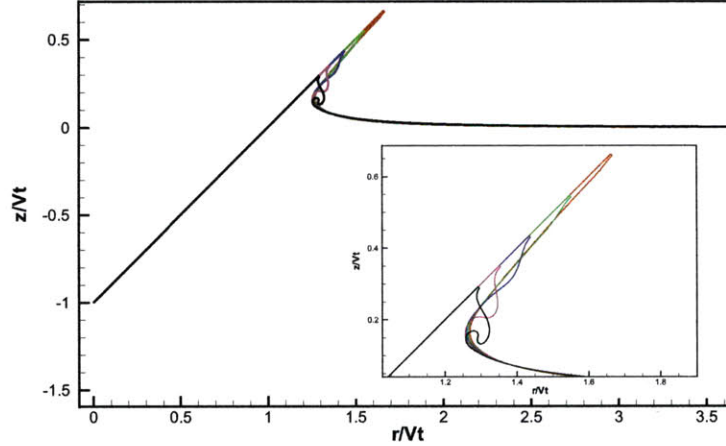


Figure 5-6: Free surface profiles in water impact of an inverted cone with $\alpha = 45^\circ$ for a range of Froude numbers: $Fr = 2$ (—); $Fr = 0.8$ (—); $Fr = 0.6$ (—); $Fr = 0.5$ (—); and $Fr = 0.45$ (—).

In addition to the change in the characteristic free-surface profile, the gravity effect also causes a variation in the position of the intersection of the body with the free-surface, which affects the area of the wetted body surface. To quantitatively describe this effect, figure 5-7 shows the wetting factor C_w as a function of Fr in the impact of an inverted cone with $\alpha = 45^\circ$. We here follow Faltinsen & Zhao (1998) to define the wetting factor by $C_w = h_I/Vt$ where h_I is the vertical distance of the intersection point from the cone vertex. For comparisons, the results of Zhao & Faltinsen (1998) and Faltinsen & Zhao (1998) at $Fr = \infty$ (and $\alpha = 45^\circ$) are also shown. These results are respectively obtained from a fully nonlinear simulation and the generalized Wagner approach. At large Froude numbers ($Fr \gtrsim 0.8$), the gravity effect in the impact process is negligible, as expected. C_w by the present nonlinear simulation is about 30% larger than those of Zhao & Faltinsen (1998) and Faltinsen & Zhao (1998) which are obtained by cutting off the most part of the jet in the simulation or without including the jet flow effect. At low Froude numbers, our simulation result indicates that C_w decreases rapidly as Fr decreases (cf. figure 5-6).

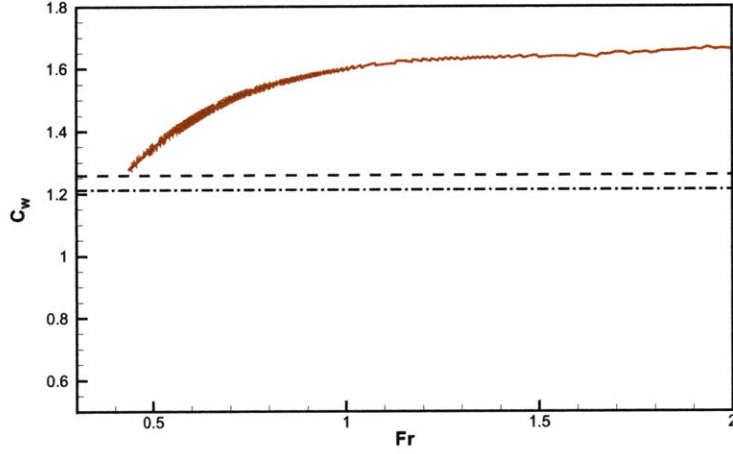
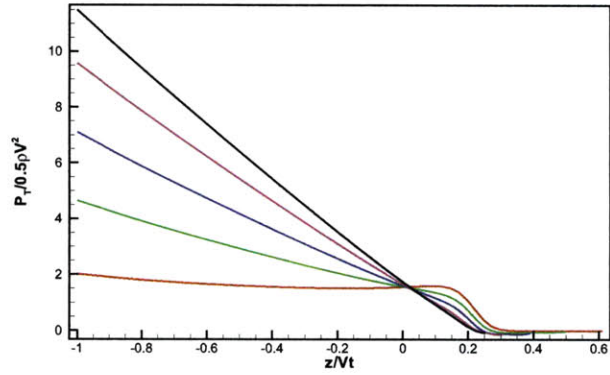


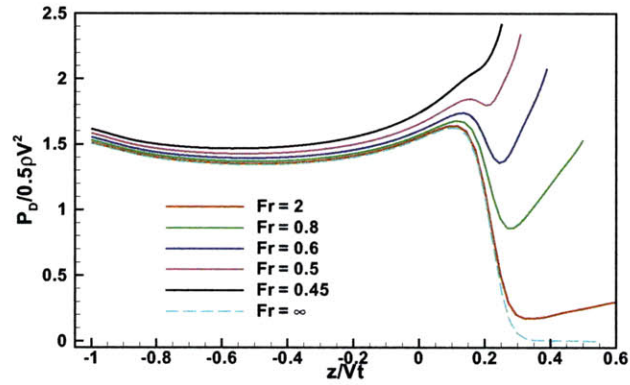
Figure 5-7: Wetting factor C_w as a function of Fr in water impact of an inverted cone with $\alpha = 45^\circ$: present nonlinear simulation (—); nonlinear solution of Zhao & Faltinsen (1998)(- -); and generalized Wagner solution of Faltinsen & Zhao (1998) (- · -).

Figure 5-8 compares the distribution of the impact pressure coefficient on the cone surface for various Fr values ranging from $Fr = \infty$ to $Fr = 0.45$ when the free surface is near breaking. The total pressure (P_T) and its hydrodynamic component ($P_D = -\rho(\partial\phi/\partial t + |\nabla\phi|^2/2)$) and hydrostatic component ($P_S = -\rho gz$) are all shown for comparisons. From figure 5-8b, we see that for relatively small Froude numbers, P_D significantly increases as Fr decreases in the neighborhood of the body intersection with the free surface. Such an increase in P_D is much reduced in the area away from the body-water intersection region. Due to the effect of P_S in figure 5-8c, the total pressure P_T in (away from) the body-water intersection region decreases (increases) as Fr decreases, as shown in figure 5-8a. In the thin jet flow, P_T is near zero, and thus the large positive P_D is balanced by the negative P_S that is linearly dependent on the jet flow height.

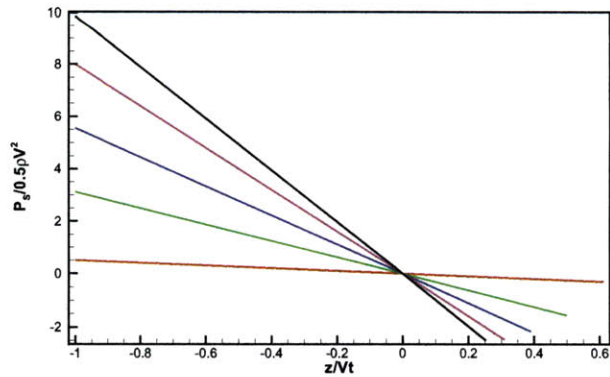
The total, hydrodynamic, and hydrostatic forces on the falling inverted cone are presented in figure 5-9 as a function of Fr . For comparison, the results at $Fr = \infty$ of Zhao & Faltinsen (1998) and Faltinsen & Zhao (1998) are also shown. Following existing studies, the force on the body is normalized by the factor of $\rho V^2 \pi (Vt)^2 / (2 \tan^2 \alpha)$.



(a)



(b)



(c)

Figure 5-8: Normalized (a) total pressure, (b) hydrodynamic pressure, and (c) hydrostatic pressure on the wetted surface of an inverted cone with $\alpha = 45^\circ$ vertically impacting the water surface at various Froude numbers: $Fr = \infty$ (—) (only present in figure (b)); $Fr = 2$ (—); $Fr = 0.8$ (—); $Fr = 0.6$ (—); $Fr = 0.5$ (—); $Fr = 0.45$ (—).

At relatively low Froude numbers ($F_r \lesssim 2.0$), the hydrodynamic force coefficient is overall underestimated by 10% to 40% without the inclusion of the gravity effect. The total force coefficient is also under-predicted similarly if the gravity effect is neglected. (A slightly negative hydrostatic force is resulted from the thin jet flow effect). At (very) low Froude number $F_r \lesssim 0.8$, the total force coefficient is seen to increase rapidly as F_r decreases. This is primarily due to the hydrostatic effect.

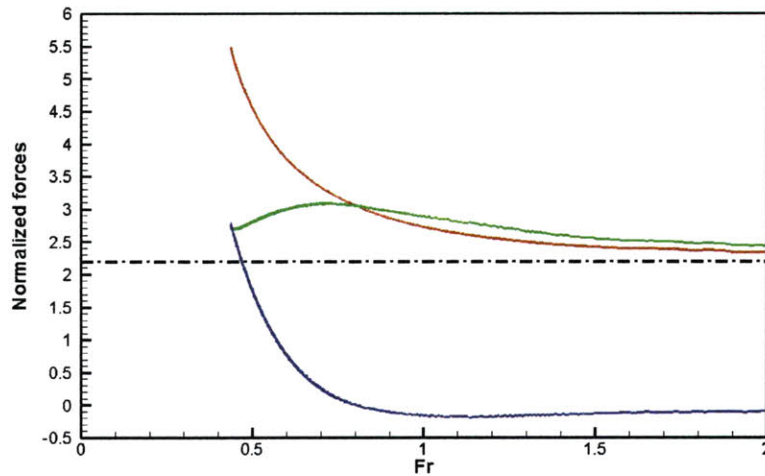


Figure 5-9: Normalized (a) total force(—), (b) hydrodynamic force(—), and (c) hydrostatic force (—) on the inverted cone with $\alpha = 45^\circ$ as a function of F_r . Also presented are the nonlinear solution of Zhao & Faltinsen (1998) (- -) and the solution based on the generalized Wagner approach by Faltinsen & Zhao (1998) (- · -) with the gravity effect neglected. (The results of Zhao & Faltinsen (1998) and Faltinsen & Zhao (1998) are graphically indistinguishable).

5.4.3 Geometry effect

The deadrise angle α is the only parameter governing the geometry of inverted cones. The geometry effect on the impact of an inverted cone can be understood by the study of the dependence of the impact solutions on α .

Figure 5-10 displays the free-surface profiles in water impact of inverted cones with $\alpha = 15^\circ$, $\alpha = 30^\circ$, $\alpha = 60^\circ$ and $\alpha = 75^\circ$. For each α , a range of F_r values are considered, over which the characteristic free-surface profiles are obtained. For small deadrise

angles such as $\alpha = 15^\circ$, sharp jet flow obtains even at very low Fr (e.g. $Fr \sim 0.2$). For moderately large deadrise angles, such as $\alpha = 30^\circ$ and 45° (cf. figure 5-6), the free surface changes from a sharp jet flow to an overturning wave shape as Fr decreases from 2.0 to 0.5. At large deadrise angles, such as $\alpha = 60^\circ$ and 75° , the overturning feature of the free surface disappears and the steep wave feature obtains at lower Fr .

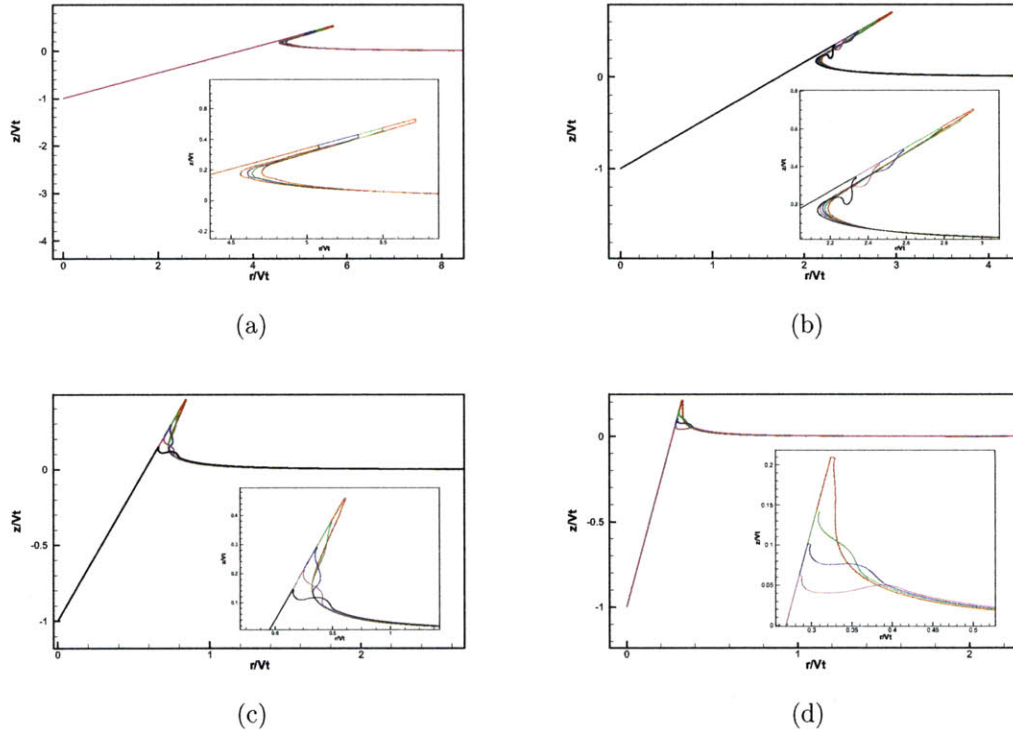


Figure 5-10: Normalized free surface profiles in the region of the body-water intersection in water impact of an inverted cone with various values of α and Fr : (a) $\alpha = 15^\circ$ at $Fr = 1.0$ (—); $Fr = 0.3$ (—); $Fr = 0.25$ (—); $Fr = 0.21$ (—); (b) $\alpha = 30^\circ$ at $Fr = 1.0$ (—); $Fr = 0.5$ (—); $Fr = 0.38$ (—); $Fr = 0.33$ (—); $Fr = 0.3$ (—); (c) $\alpha = 60^\circ$ at $Fr = 2.0$ (—); $Fr = 1.0$ (—); $Fr = 0.75$ (—); $Fr = 0.6$ (—); $Fr = 0.5$ (—); (d) $\alpha = 75^\circ$ at $Fr = 2.0$ (—); $Fr = 1.0$ (—); $Fr = 0.8$ (—); $Fr = 0.6$ (—).

The associated wetting factors C_w as a function of Fr are shown in figure 5-11. For a fixed Fr , larger C_w is generally obtained with smaller α . For a fixed α , C_w decreases as Fr decreases in the low Fr range due to the gravity effect. The range of Fr values over which the gravity effect plays an important role shifts to lower Fr values for smaller α . This indicates that neglect of the gravity effect is a reasonable assumption for the near-flat body impact.

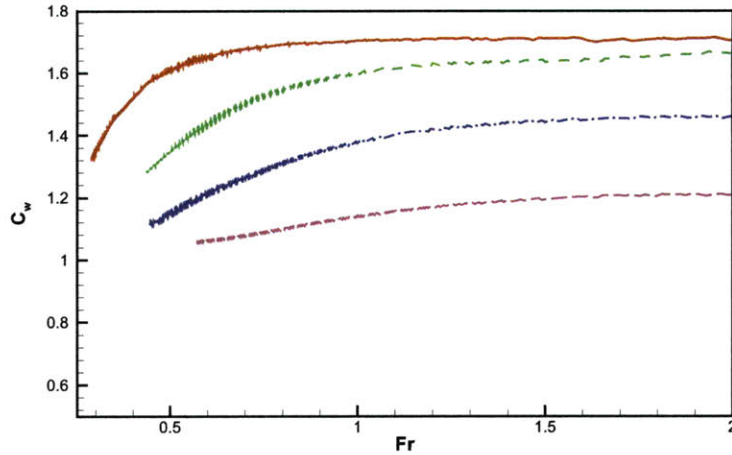
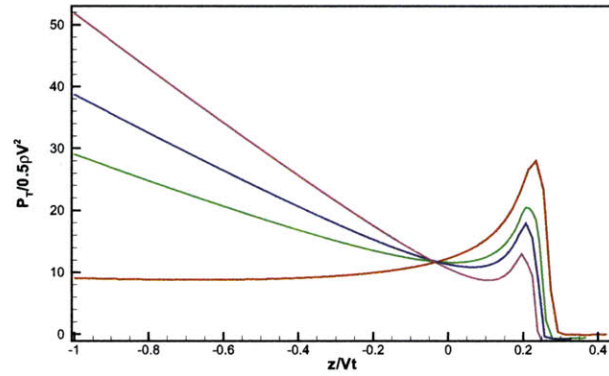


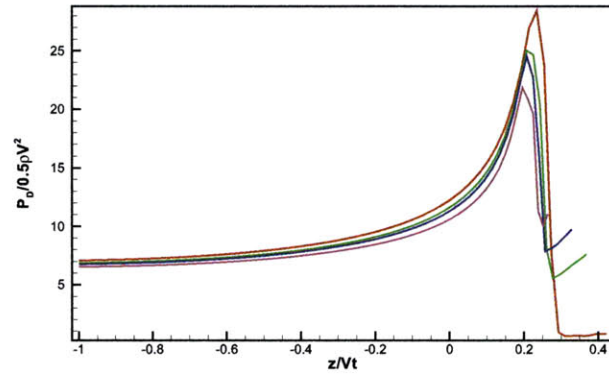
Figure 5-11: Wetting factor C_w as a function of Fr in water impact of an inverted cone with $\alpha = 30^\circ$ (—); 45° (- -); 60° (- · -); and 75° (- -).

Figures 5-12 and 5-13 show the pressure distributions on the wetted surface of the inverted cones with $\alpha = 15^\circ$ and 75° , respectively. By comparing these results as well as those in figure 5-8 for $\alpha = 45^\circ$, we observe different characteristic features of the pressure distributions as α varies. For small deadrise angles (such as $\alpha = 15^\circ$), the normalized hydrodynamic pressure has a distinct peak near the sharp turning point of the free surface (i.e. jet root). For large deadrise angles (such as $\alpha = 75^\circ$), the maximum normalized hydrodynamic pressure occurs at the cone vertex. For a fixed Fr , both the hydrodynamic and hydrostatic pressure coefficients at a fixed (normalized) wetted body position increases as α decreases. Another prevalent feature that can be observed is that the hydrodynamic pressure constitutes a relatively larger proportion in the total pressure for smaller α at any fixed Fr .

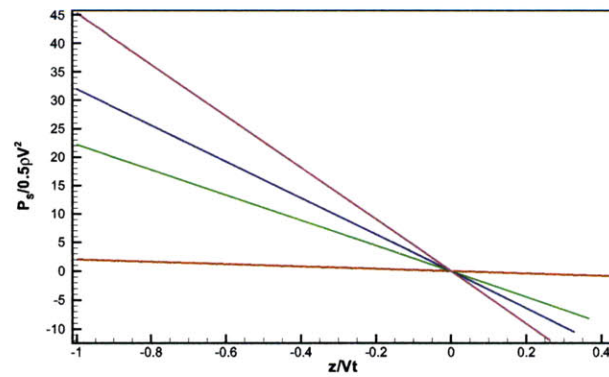
Figure 5-14 shows the total, hydrodynamic, and hydrostatic forces (normalized by $\rho V^2 \pi (Vt)^2 / (2 \tan^2 \alpha)$) on the inverted cones with various α as a function of Fr . The results of Zhao & Faltinsen (1998) and Faltinsen & Zhao (1998) without the inclusion of the gravity effect are also plotted for comparisons. For any α , the total force is seen to increase as Fr decreases, and the increase rate becomes more rapid at lower Fr . Compared to the result at $Fr = \infty$, the hydrodynamic force is somewhat



(a)

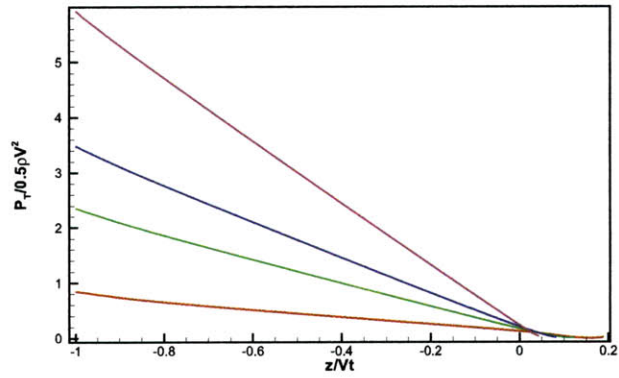


(b)

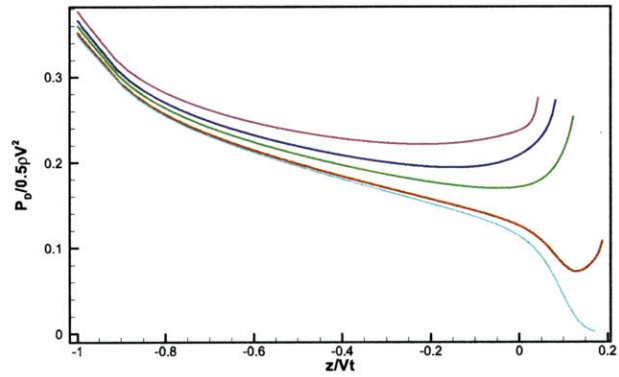


(c)

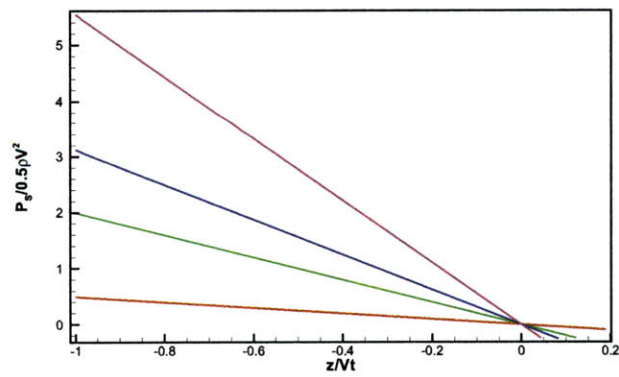
Figure 5-12: Normalized (a) total pressure, (b) hydrodynamic pressure, and (c) hydrostatic pressure on the wetted surface of an inverted cone with $\alpha = 15^\circ$ for $F_r = 1.0$ (—); 0.3 (—); 0.25 (—); and 0.21 (—).



(a)



(b)



(c)

Figure 5-13: Normalized (a) total pressure, (b) hydrodynamic pressure, and (c) hydrostatic pressure on the wetted surface of an inverted cone with $\alpha = 75^\circ$ for $F_r = \infty$ (—) (only present in figure (b)); 2.0 (—); 1.0 (—); 0.8 (—); and 0.6 (—).

underestimated by neglecting the gravity effect. For a fixed F_r , both the total and hydrodynamic forces are larger in magnitude with smaller α . The hydrodynamic force is more dominant over the hydrostatic force for smaller α except at very low F_r . Note that the relatively larger discrepancy between the present numerical results with those of Zhao & Faltinsen (1998) and Faltinsen & Zhao (1998) at smaller α is attributed to different consideration and treatment of the thin jet flow effect, as discussed in §5.4.1.

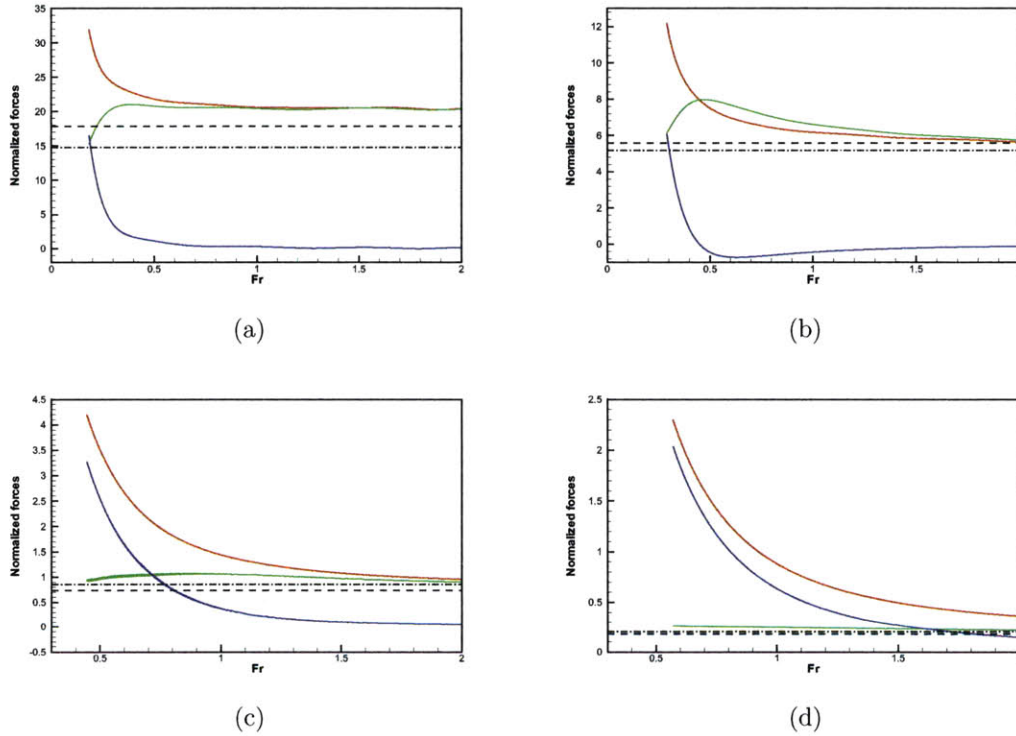


Figure 5-14: Normalized total force(—), hydrodynamic force(—), and hydrostatic force(—) on inverted cones with (a) $\alpha = 15^\circ$; (b) 30° ; (c) 60° ; and (d) 75° as a function of F_r . Also plotted are the nonlinear simulation result of Zhao & Faltinsen(1998) (- -) and the generalized Wagner solution of Faltinsen & Zhao (1998)(- · -) with the gravity effect neglected.

5.4.4 An approximate similarity solution for cone impact

From the above studies of the gravity and geometry effects in water impact of an inverted cone, it is seen that the main characteristics of the free-surface profile and

pressure distribution and impact load on the body at higher F_r (with fixed α) are similar to those with smaller α (at fixed F_r). For example, the sharp jet-flow free-surface shape can be achieved by increasing F_r or decreasing α . It is thus possible and practically useful to look for a similarity parameter at which the impact solution of different F_r and α is invariant.

Based on our numerical simulation results in a wide range of F_r with various values of α , we find that the contribution to the impact force on the body from the gravity effect is strongly correlated with the similarity parameter $\xi \equiv F_r/\alpha^{1/2}$. This relation can be expressed in a form:

$$\frac{C_f(F_r, \alpha) - C_f(F_r = \infty, \alpha)}{\tan^{\frac{1}{2}} \alpha} = 0.77\xi^{-2} \quad (5.14)$$

where $C_f \equiv F_T/[\pi\rho V^2(Vt)^2/2\tan^2\alpha]$, and $C_f(F_r = \infty, \alpha)$ represents the force coefficient obtained without the inclusion of the gravity effect. The coefficient 0.77 is obtained by fitting to the numerical data. In figure 5-15, we plot the result given by (5.14) and compare it with the numerical results with $\alpha = 15^\circ, 30^\circ, 45^\circ, 60^\circ$, and 75° . It is seen that the relation in (5.14) properly describes the impact force in water impact of an inverted cone with wide ranges of F_r and α values. With (5.14), the total impact force on the body at an arbitrary F_r including the gravity effect can be easily obtained based on the solution at $F_r = \infty$ only.

As seen in Figure 5-14, the influence of gravity on hydrodynamic forces differs from the gravity effect on total forces. In our study, we define the hydrodynamic (hydrostatic) force as the integration of hydrodynamic (hydrostatic) pressure over the instantaneous wetted body surface. Note that there exists a different (conventional) way to define the hydrostatic and hydrodynamic forces in literature. Based on the conventional definition, the hydrostatic force is equal to the integration of hydrostatic pressure ($-\rho gz$) over the body surface below $z = 0$. In consequence, the hydrodynamic force will be made up of two parts: integration of the hydrodynamic pressure ($-\rho(\frac{\partial\phi}{\partial t} + \frac{1}{2}|\nabla\phi|^2)$) over all wetted body surface and integration of the hydrostatic pressure ($-\rho gz$) on wetted body surface above $z = 0$. The so-defined hy-

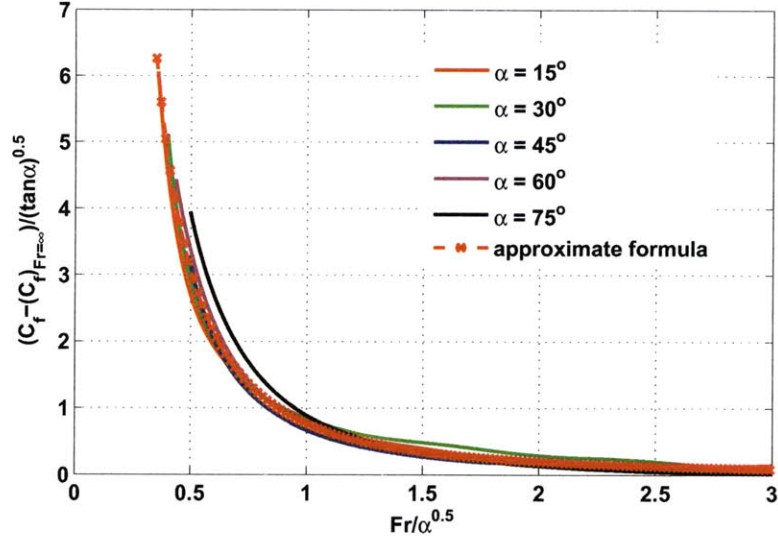


Figure 5-15: Contributions to the total force from the gravity effect as a function of the similarity parameter $Fr/\alpha^{1/2}$ in water impact of an inverted cone with $\alpha = 15^\circ$ (—), 30° (—), 45° (—), 60° (—), and 75° (—). Also plotted is the curve given by Eq. (5.14) (—x—).

drostatic force and hydrodynamic force as well as the total force are shown in Figure 5-16 for impact of cones with different deadrise angles. (Forces are all normalized by $\pi\rho V^2(Vt)^2/2\tan^2\alpha$.) From this conventional definition, we can easily estimate gravity effect on the hydrodynamic force after obtaining the total force from Eq. (5.14) and the conventional hydrostatic force (the normalized value of which is simply equal to $\frac{2}{3}Fr^{-2}$).

5.5 Numerical results for water impact of spheres

In this section, we study the characteristics of the dynamics in water impact of spheres using nonlinear simulations. As in the case of inverted cone impact, we focus on the understanding of the gravity effect in the impact process. For the sphere impact problem, there are two controlling physical parameters: Froude number $F_r = V/(gR)^{1/2}$ and dimensionless time $\tau = Vt/R$, where V is the initial impact velocity of the body and R the radius of the sphere. Clearly, F_r reflects the gravity effect while τ repre-

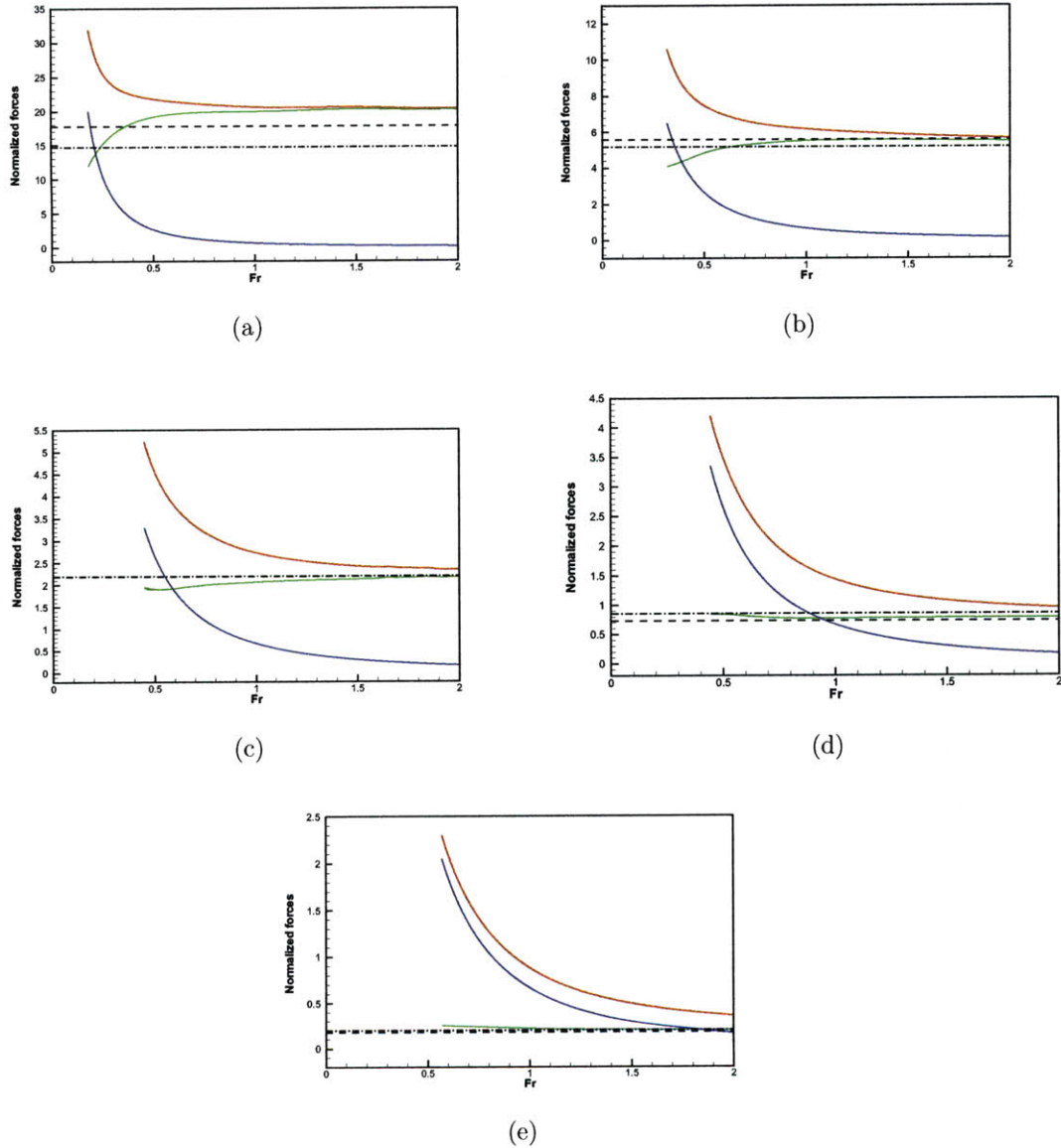


Figure 5-16: Normalized total force(—), hydrodynamic force(—), and hydrostatic force(—) (based on conventional definitions) on cones with different deadrise angles: (a) $\alpha = 15^\circ$; (b) $\alpha = 30^\circ$; (c) $\alpha = 45^\circ$; (d) $\alpha = 60^\circ$; and (e) $\alpha = 75^\circ$. Reference forces include the fully nonlinear numerical result by Zhao & Faltinsen(1998) (- -) and the generalized Wagner solution by Faltinsen & Zhao (1998)(- · -), with gravity effect neglected.

sents the geometry effect as it measures the body submergence during the impact. In the following, we validate our numerical simulations by making direct comparisons to available experimental measurements and then investigate the dependencies of the characteristics of sphere impact on F_r and τ .

5.5.1 Comparison to experimental measurements

There are a number of existing theoretical and experimental studies on water impact of spheres, most of which focus on the estimate of the hydrodynamic load on the body. For validation, we compare our numerical solution with available experimental data on slamming coefficient, $C_s \equiv F_D/(\pi\rho V^2 R^2/2)$ where F_D denotes the hydrodynamic force on the sphere. (Note that for our numerical results shown, we start the simulation with an initial small body submergence of δR with $\delta \sim 0.02$. A linear interpolation is used to approximate the solution between $\tau = 0$ and 0.02.)

Figure 5-17 shows the comparison of the slamming coefficient, as a function of the sphere submergence in the impact, between the present simulation and available experimental data (Shiffman & Spencer 1945; Nisewanger 1961; Baldwin *et al.* 1975; Moghisi & Squire 1981). The experimental data shown are obtained at relatively large Froude numbers, but the densities of the spheres used in these experiments are not known. In the numerical simulation, we thus neglect the gravity effect and assume a constant dropping velocity for convenience. The peak value of C_s from the present simulation is seen to agree well with the measurement of Moghisi & Squire (1981), but to be about 20% larger than the data of Baldwin *et al.* (1975), Nisewanger (1961), and Shiffman & Spencer (1945). The time to reach the peak C_s in the simulation is much earlier than that in Moghisi & Squire (1981), but match those in Baldwin *et al.* (1975) and Nisewanger (1961). For $\tau > 0.2$, the present numerical solution tends to agree well with the measurements of Nisewanger (1961) and Baldwin *et al.* (1975), but is significantly smaller than those of Moghisi & Squire (1981) and Shiffman & Spencer (1945). Contrasting to the constant velocity used in the simulation, the dropping velocity of the sphere may vary in these experiments. This may be the main factor causing the discrepancies among the experimental measurements and the

present simulation result.

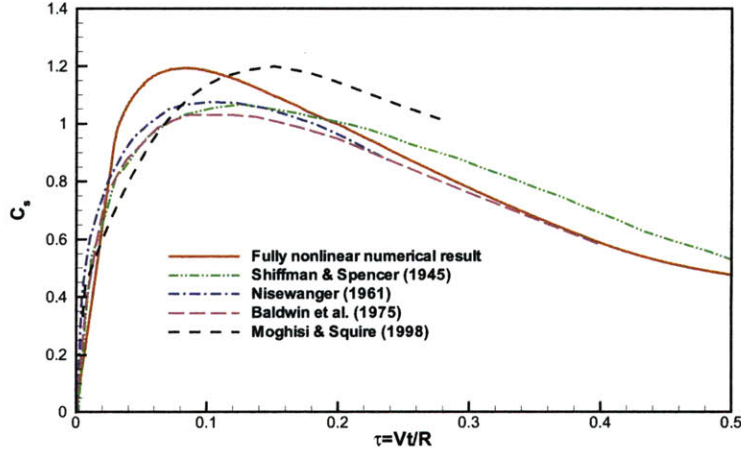
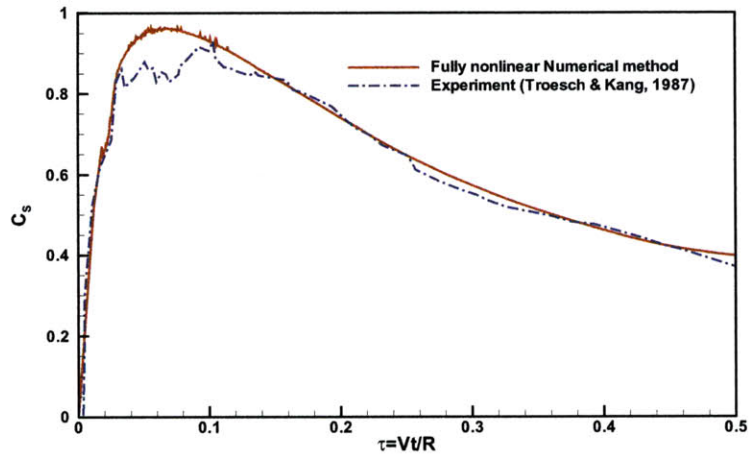


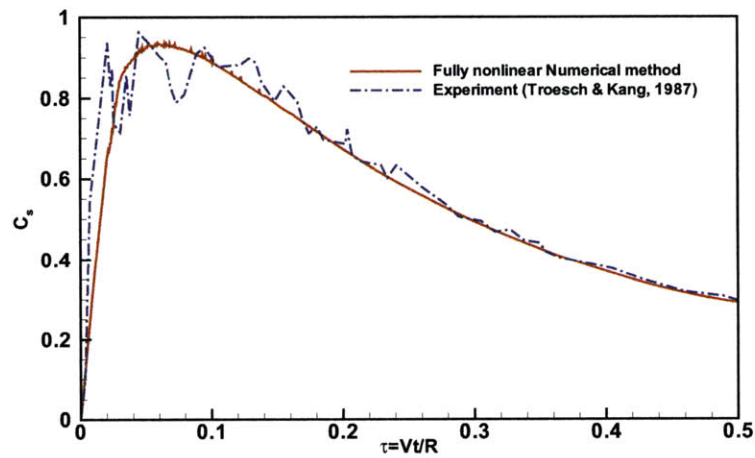
Figure 5-17: Slamming coefficient C_s as a function of the body submergence $\tau = VT/R$ in water impact of a sphere. The plotted are the present numerical result at $F_r = \infty$ (—) and experimental data of Shiffman & Spencer (1945)(- · · -), Nisewanger (1961) (- · -), Baldwin *et al.* (1975) (- -), and Moghisi & Squire (1981)(- -).

Figure 5-18 shows similar comparisons between the present simulation result and the experimental data of Troesch & Kang (1987), but at relatively low Froude numbers $F_r = 2.203$ and $F_r = 3.816$. In the experiments, the density of the sphere is a half of the water density, and the velocity of the sphere varies with time in the impact. In the simulation, the gravity effect is included and the free fall motion of the sphere is considered with the instantaneous position and velocity of the body during the impact obtained from the equation of motion. The results in figure 5-18 show that, for both cases of $F_r = 2.203$ and $F_r = 3.816$, the present simulation results compare very well with the experimental data of Troesch & Kang (1987) in both the peak value of C_s and the time to reach the peak value as well as the variation of C_s in the later stage of impact.

We note that the peak value of C_s in figure 5-17 is about 20% larger than that in figure 5-18. This is primarily due to the reduction of the dropping velocity in the impact since a light sphere is used in the experiment of Troesch & Kang (1987).



(a)



(b)

Figure 5-18: Comparisons of slamming coefficient C_s as a function of the body submergence $\tau = VT/R$ in water impact of a sphere between present numerical result (—) and experimental data of Troesch & Kang (1987) (- · -) at (a) $F_r = 2.203$ and (b) $F_r = 3.816$.

5.5.2 Impact pressure and slamming force

Nonlinear time simulations of water impact of a sphere at various Froude numbers are performed to understand the gravity effect. A constant dropping velocity during the impact is assumed in the simulations. Figure 5-19 displays the distributions of the hydrodynamic impact pressure, denoted by $C_p \equiv P_D/(\rho V^2/2)$, on the wetted body surface at various instants in water entry of the sphere with $F_r = \infty$. In the very initial stage of impact (e.g. $\tau = 0.05$), C_p shows a sharp high peak in the neighborhood of the root of jet flow as the problem is similar to the near-flat wedge impact. As τ increases, the peak value of C_p gradually decreases. In the late stage of impact (e.g. $\tau > 0.25$), the apparent peak of C_p disappears and C_p decreases smoothly from its maximum value at the bottom of the sphere to zero at the flow separation point. Similar features in the time variation of C_p are obtained for different F_r .

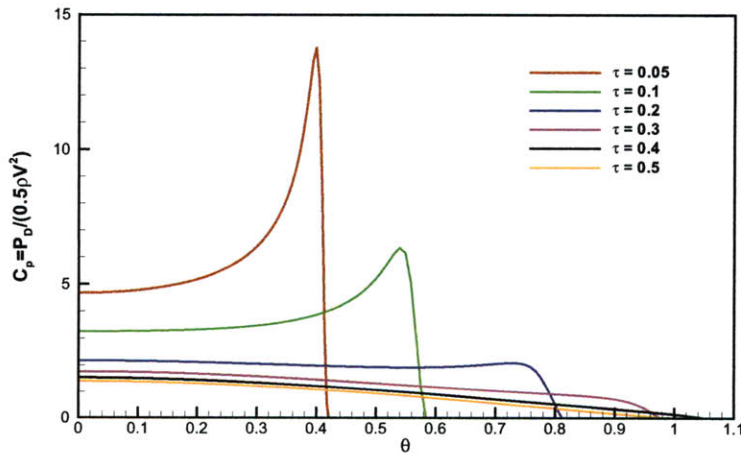


Figure 5-19: Distribution of the hydrodynamic pressure coefficient C_p in water impact of a sphere with $F_r = \infty$ at time $\tau = 0.04$ (—), 0.1 (—), 0.2 (—), 0.3 (—), 0.4 (—), and 0.5 (—).

The slamming coefficient, $C_s = F_D/(\rho V^2 \pi R^2/2)$, which measures the hydrodynamic impact force on the sphere, is plotted as a function of τ for various values of F_r in figure 5-20. For all F_r values shown ($F_r \geq 0.5$), C_s grows rapidly from zero at $\tau = 0$ to its peak value at $\tau \approx 0.085$, and then starts to decrease gradually with τ . The

differences in the results with different F_r , which are resulted from the gravity effect in the impact, can be seen only in the later stage of impact for $\tau \gtrsim 0.085$ and with $F_r \lesssim 2.0$. In particular, the results indicate that the inclusion of the gravity effect in the impact somewhat increases the value of C_s (as much as about 40% for $F_r = 0.5$ at $\tau = 0.5$). In the initial impact ($\tau \lesssim 0.085$) and with relatively large Froude number ($F_r \gtrsim 2.0$), the gravity effect plays a negligible role.

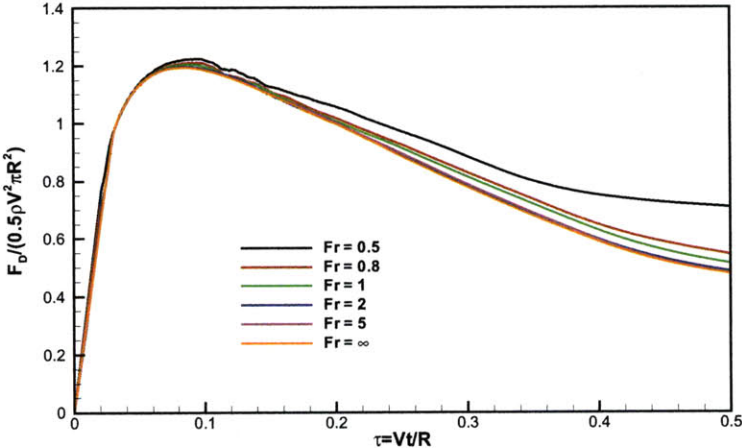


Figure 5-20: Time history of the normalized hydrodynamic force on the body during water impact of a sphere with $F_r = 0.5$ (—), 0.8 (—), 1.0 (—), 2.0 (—), 5.0 (—), and ∞ (—).

To understand the hydrostatic effect, we present the total impact force coefficient, $F_T / (\rho V^2 \pi R^2 / 2)$, for various values of F_r in figure 5-21. Similarly to the slamming coefficient, the contribution of the gravity effect to the total impact force is negligible in the initial stage of impact ($\tau \lesssim 0.085$) and for relatively large Froude numbers ($F_r \gtrsim 2.0$). The apparent gravity effect is seen only in later stage of impact ($\tau \gtrsim 0.085$) with $F_r \lesssim 2.0$). The hydrostatic contribution generally increases as F_r decreases and can be even larger than the hydrodynamic contribution to the total force at low Froude numbers such as $F_r = 0.5$.

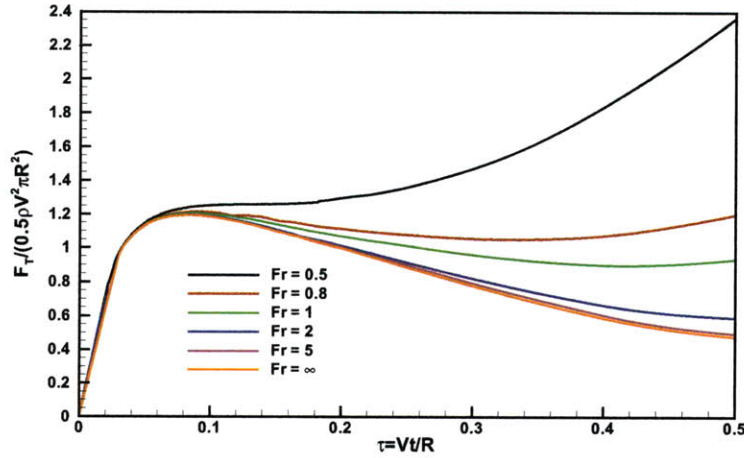


Figure 5-21: Time history of the normalized total force on the body during water impact of a sphere with $Fr = 0.5$ (—), 0.8 (—), 1.0 (—), 2.0 (—), 5.0 (—), and ∞ (—).

5.5.3 Free surface profile

In the present simulation, we are able to obtain the complete process of the development and evolution of free-surface deformation in water impact of a sphere including the gravity effect. In particular, we are able to properly determine the position at which the flow freely separates from the body and follow the evolution of the separation point in the impact. From the simulation results, we can understand the characteristics of free-surface profile evolution and as well as their dependence on Froude numbers.

Figure 5-22 shows the characteristic evolution of the free surface deformation near the body in water impact of a sphere at $Fr = \infty$ (i.e. without gravity effect). In the very initial stage of impact ($\tau \sim 0.05$), a thin jet flow attached to the body surface is developed. As the body submergence continues to increase, the jet flow moves up along the body surface, grows in size, and then freely separates from the body surface. The separation point, labeled in figure 5-22, is observed to initially move up along the body surface and remain almost fixed on the body with the separated flow pileup continuing to be developed in the late stage of impact.

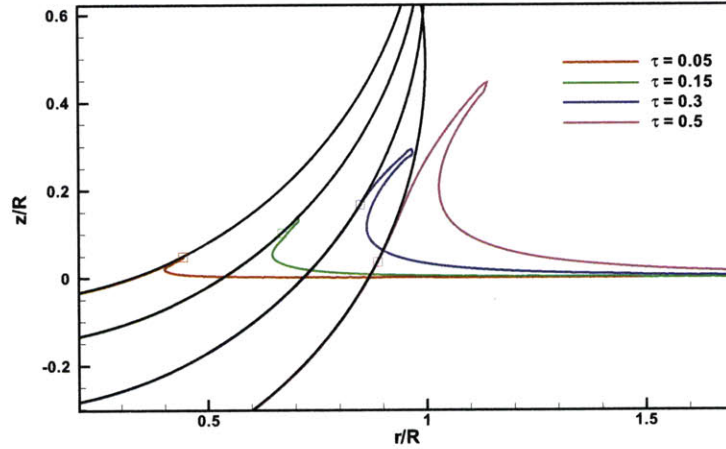


Figure 5-22: Free surface profiles near the body in water impact of a sphere with $F_r = \infty$ at different time $\tau = 0.03$ (—), 0.15 (—), 0.3 (—), and 0.5 (—). Small squares indicate the instantaneous flow separation locations.

To see the influence of gravity on the evolution of the free surface profile, in figure 5-23, we compare the results of the free-surface profile for different Froude numbers, $F_r = 0.5, 1.0,$ and ∞ , at two instants $\tau = 0.3$ and 0.5 . For smaller Froude numbers, the gravity (restoring) effect is larger. Thus, the height of water pile up near the body becomes lower and the free-surface profile looks more overturned. In addition, in the early stage of impact, the separation point is seen to move more slowly on the body surface for smaller F_r .

To further understand the behaviors of the evolution of separation point, in figure 5-24, we present the time histories of the position of flow separation on the body in water impact of a sphere at $F_r = 0.5, 0.8, 1, 2, 5,$ and ∞ . For definiteness, we use the value of the angle (θ) from the separation point to the bottom of the sphere to represent the position of separation point (cf. figure 5-3). For $F_r \gtrsim 1.0$, θ behaves almost identically. Specifically, as impact starts, θ grows with time with the growth rate gradually decreasing with time. For $\tau \gtrsim 0.385$, surprisingly, θ remains almost unchanged at a value of around 62.5° as the impact process continues. In an experimental study of water impact of a two-dimensional circular cylinder, Lin & Shieh (1997) observed a similar phenomenon that the separation point remains nearly in-

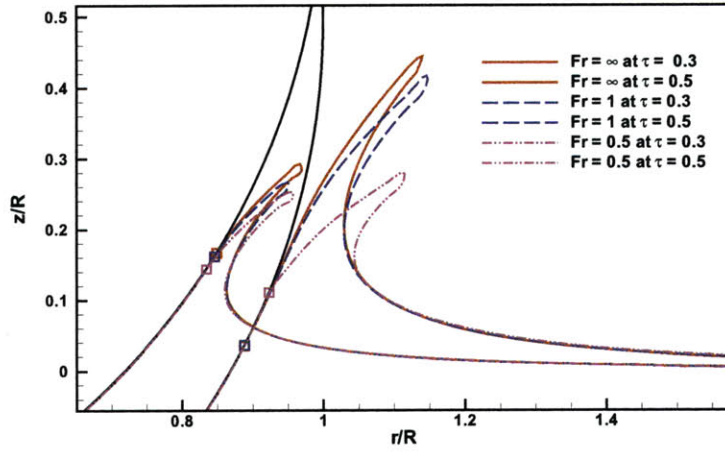


Figure 5-23: Comparison of the free surface profiles in water impact of a sphere at different Froude numbers and time: ($Fr = \infty$ (—) at $\tau = 0.3$ and 0.5 , $Fr = 1.0$ (- -) at $\tau = 0.3$ and 0.5 , and $Fr = 0.5$ (- · · -) at $\tau = 0.3$ and 0.5).

variant once the separation occurs. However, no such result in water impact of a sphere has been reported in literature. For $Fr \lesssim 1.0$, the gravity effect on the evolution of separation point becomes apparent. As shown in figure 5-24, at $Fr = 0.8$ and 0.5 , θ continues to grow with τ in the later stage of impact.

Another parameter, the wetting factor C_w , is directly related to the flow-body separation position. (Similar to that in the cone impact, C_w is defined as h_I/Vt , where h_I is the vertical distance of the flow separation point from the sphere bottom.) C_w is often evaluated in literature to study the variation of the instantaneous wetted body surface with time. Corresponding to $Fr = \infty$ and a constant sphere dropping velocity, our numerical result for C_w is compared with Shiffman & Spencer (1945)'s experimental data and empirical formula, Cooper (1950)'s experimental data, and Miloh (1991)'s asymptotic solution in Figure 5-25. Our numerical prediction for C_w is larger than others' results initially and decreases with time. If not accounting for the local rise-up of water, the asymptotic solution of C_w (based on the expanding disk approximation) has its maximum value of 1.5 at the instant of impact (Schiffman & Spencer 1951; Miloh 1981). Note that in existing experiments, body velocities vary during impact process and gravity effect plays a role as well, which may partially

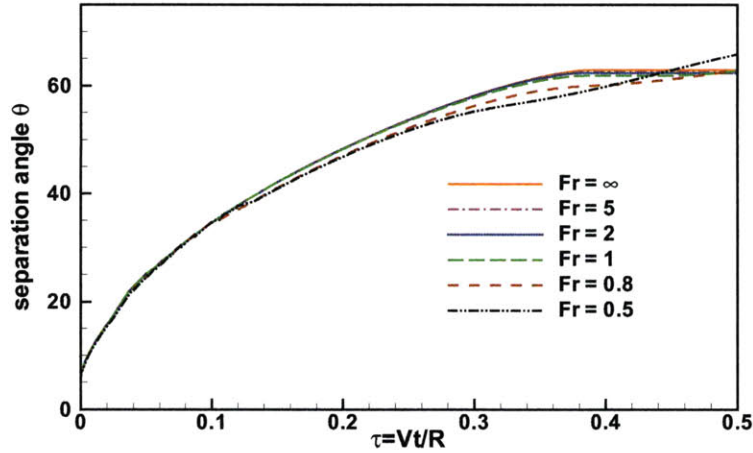


Figure 5-24: Time histories of the separation angle θ during water impact of a sphere at $Fr = 0.5$ (- · · -), 0.8 (- -), 1.0 (- -), 2.0 (—), 5.0 (- · · -), and ∞ (—).

explain the discrepancy between our result and the existing experimental data.

We finally remark that the above result is obtained for the vertical impact of a sphere. The gravity effect might play a more important role in the oblique impact of a sphere (e.g. Miloh & Shukron 1991).

5.6 Conclusions

Fully-nonlinear numerical simulations in the context of potential flow are applied to study the impact problem of axisymmetric bodies striking the horizontal water surface vertically from the air. Two representative body geometries, inverted cone and sphere, are considered with the focus on the understanding of the gravity and geometry effects upon the hydrodynamics of the impact process. In water impact of inverted cones under the gravity effect, an effective and robust technique for the treatment of thin jet flow, extended from that of Zhao & Faltinsen (1993), is developed enabling an accurate computation of impact pressure on the body and various characteristic free-surface deformations near the body. For water impact of bluff bodies such as spheres, we develop and apply a new pressure-based criterion for the determination of flow separation point on the body surface, which allows a reliable simulation of flow details

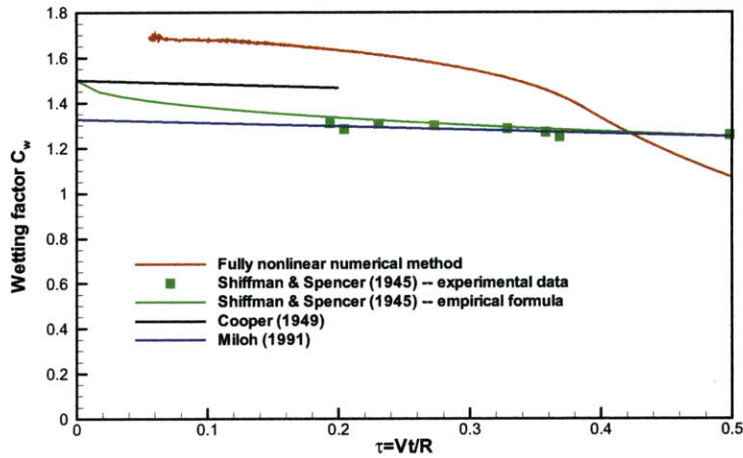


Figure 5-25: Wetting factor C_w during water impact of a sphere at $Fr = \infty$ as a function of dimensionless body submergence. Results presented include present fully nonlinear numerical solution(—), experimental data by Shiffman & Spencer(1945)(■), empirical formula by Shiffman & Spencer(1945)(—), experimental data by Cooper(1950)(—), and asymptotic solution by Miloh (1991) (—).

near the body.

For the inverted cone impact problem, we find that with the inclusion of the gravity effect, the free surface profile near the body can change from the jet-flow shape (typically obtained in the absence of the gravity effect) to the overturning wave. The hydrodynamic impact pressure and load on the body are generally underestimated if the gravity effect is neglected. Based on the numerical simulation results for a wide range of Froude number Fr and deadrise angle α values, we establish an approximate formula in terms of a single similarity parameter $Fr/\alpha^{1/2}$ for the evaluation of the contribution from the gravity effect to the total impact force on the cones. For the sphere impact problem, however, our numerical results indicate that the gravity effect is unimportant in the (very) initial stage of impact in terms of the free-surface profile and impact pressure and load on the body. The inclusion of the gravity effect is found to increase slightly the hydrodynamic impact pressure on the body in the later stage of impact only for $Fr \lesssim 2.0$. Interestingly, we also find that in the later stage of impact, flow separation remains at an almost fixed location at an angle of around

$\theta = 62.5^\circ$ measured from the bottom of the sphere for $F_r \gtrsim 1.0$.

Present study provides accurate prediction of hydrodynamic load and improved understanding of the involving violent flow feature in water impact problems which are directly related to ship slamming and big wave impact on marine structures.

5.7 References

Baldwin, L. & Steves, H.X., Vertical water entry of spheres, NSWC/WOL/TR 75-49, White Oax Laboratory, Silver Spring, MD, USA, 1975;

Battistin, D. & Iafrati, A., Hydrodynamic loads during water entry of two-dimensional and axisymmetric bodies, Journal of Fluids and Structures, Vol.17, pp.643-664, 2003;

Cointe, R., Two-Dimensional Water-Solid Impact, Journal of Offshore Mechanics and Arctic Engineering, Vol.111, pp.109-114, 1989;

Dobrovol Skaya., Z. N., On Some Problems of Similarity Flow of Fluid with a Free Surface, J. Fluid Mech., Vol.36, pp.805-829, 1969;

Dommermuth, D.G. & Yue, D.K.P., Numerical simulations of nonlinear axisymmetric flows with a free surface, J. Fluid Mech., Vol.178, pp.195-219, 1987;

Dommermuth, D.G. & Yue, D.K.P., The nonlinear three-dimensional waves generated by a moving surface disturbance, 17th Symp. on Naval Hydrodynamics, National Academy Press, Washington, DC, pp.523-539, 1989;

Faltinsen, O.M., Numerical solution of transient nonlinear free-surface motion outside or inside moving bodies, Proc. 2nd Intl Conf. on Num. ship Hydro., U.C. Berkeley, pp.347-357, 1977;

Faltinsen, O.M. & Zhao, R., Water entry of Ship Sections and Axisymmetric Bodies, AGARD FDP and Ukraine of Hydromechanics Workshop on *High Speed Body Motion in Water*, 1998;

- Greenhow, M., Wedge Entry into Initially Calm Water, *Applied Ocean Research*, Vol.9(4), pp.214-223, 1987;
- Kim, M. H., Celebi, M.S. & Kim, D.J., Fully nonlinear interactions of waves with a three-dimensional body in uniform currents, *Applied ocean research*, Vol.20, pp.309-321, 1998;
- Kim, Y., Computation of higher-order hydrodynamic forces on ships and offshore structure in waves, PhD thesis, Massachusetts Institute of Technology, 1999;
- Lin, M.-C. & Shieh, L.-D., Simultaneous Measurements of Water Impact on a Two-dimensional Body, *Fluid Dynamics Research*, Vol.19, pp.125-148, 1997;
- Lin, W.-M., Nonlinear motion of the free surface near a moving body, PhD thesis, Massachusetts Institute of Technology, 1984;
- Lin, W.-M., Newman, J.N. & Yue, D.K.P., Nonlinear forced motions of floating bodies, *Proceedings of the 15th Symposium on Naval Hydrodynamics*, Hamburg, Washington DC: National Academy Press, 1984;
- Liu, Y., Xue, M. & Yue, D.K.P., Computations of fully nonlinear three-dimensional wave-wave and wave-body interactions. Part 2. Nonlinear waves and forces on a body, *J. Fluid Mech.*, Vol.438, pp.41-66, 2001;
- Mei, X., Liu, Y. & Yue, D.K.P., On the Water Impact of General Two-dimensional Sections, *Applied Ocean Research*, Vol.21, pp.1-15, 1999;
- Miloh, T., Irregularities in solutions of the nonlinear wave diffraction problem by vertical cylinder, *Journal of the Waterway Port Coastal and Ocean Division*, Vol.106(2), pp.279-284, 1980;
- Miloh, T., Wave Slam on a Sphere Penetrating a Free Surface, *J. Eng. Math.*, Vol.15(3), pp.221-240, 1981;
- Miloh, T., On the Initial Stage Slamming of a Rigid Sphere in a Vertical Entry, *Applied Ocean Research*, Vol.13(1), pp.43-48, 1991;

- Miloh, T. & Shukron, Y., Ricochet off water of spherical projectiles, *Journal of Ship Research*, Vol. 35(2), pp. 91-100, 1991;
- Moghisi, M. & Squire, P.T., An Experimental Investigation of the Initial Force of Impact on a Sphere Striking a Liquid Surface, *J. Fluid Mech.*, Vol.198, pp.133-146, 1981;
- Newman, J.N., *Marine Hydrodynamics*, The MIT Press, Cambridge, Massachusetts, and London, England, 1977;
- Nisewanger, C.R., Experimental determination of pressure distribution on a sphere during water entry, NAVWEPS Rep. No. 7808, 1961;
- Shiffman, M. & Spencer, D.C., The force of impact on a sphere striking a water surface, AMP Rep. 42, 1R, 42. 2R. AMG-NYU No. 105, 1945;
- Shiffman, M. & Spencer, D.C., The Force of Impact on a Cone Striking a Water Surface (Vertical Entry), *Communications on Pure and Applied Mathematics*, Vol.4(4), pp.379-417, 1951;
- Sun, H. & Faltinsen, O.M., Water Impact of Horizontal Circular Cylinders and Cylindrical Shells, *Applied Ocean Research*, Vol.28, pp.299-311, 2006;
- Troesch, A.W. & Kang, C.-G., Hydrodynamic Impact Loads on Three-Dimensional Bodies, *Proceedings of the 16th Symposium on Naval Hydrodynamics*, Berkeley, pp.537-558, July 1986;
- Vinje, T. & Brevig, P., Nonlinear ship motions, *Proc. 3rd Intl Symp. Num. Ship Hydro.*, Paris, pp.257-268, 1981;
- Von Karman, Th., The Impact on Seaplane floats During Landing, NACA TN No. 321, 1929;
- Wanger, H., Landing of seaplanes, NACA TN No. 622, 1931;
- Wilson, S.K., *The Mathematics of Ship Slamming*, PhD thesis, Oxford University, 1989;

Wu, G.-X. & Eatock Taylor, R., Transient motion of a floating body in steep water waves, Proceedings of the 11th International Workshop on Water Waves and Floating Bodies, Hamburg, Germany, 1996;

Xue, M., PhD thesis, Three-dimensional fully-nonlinear simulation of waves and wave body interactions, Massachusetts Institute of Technology, Department of Ocean Engineering, 1997;

Zhao R. & Faltinsen, O.M., Water Entry of Two-dimensional Bodies, J. Fluid Mech., Vol.246, pp.593-612, 1993;

Zhao R. & Faltinsen, O.M., Water Entry of Arbitrary Axisymmetric Bodies With and Without Flow Separation, Twenty-Second Symposium on Naval Hydrodynamics, Washington, D.C., pp.652-664, 1998.

Chapter 6

Coupled Unstable Heave-Pitch Motions of a Large Floating Vessel/Structure in Waves

6.1 Introduction

In marine engineering, most floating vessels, including floating oil platforms, floating production storage and offloading (FPSO), and ships, are designed with minimum response to the excitation of wave for efficiency/safety of structures' operations. On the other hand, floating structures like wave-energy absorbers are optimized to operate at maximum motions to the action of waves for effective energy extraction. Understanding of fundamental mechanisms and basic characteristic of resonant motions and instabilities of floating bodies in waves is of critical importance for the design and operation of marine structures.

To study the global motions of a deep draft caisson vessel (DDCV), ExxonMobil conducted model tests in 1998. First, the DDCV's natural heave and pitch periods were measured from free decay tests, which are around 30s and 100s, respectively. Regular incident waves were then created by wave-makers located at the end of the wave basin and motions of the DDCV were recorded for the reaction to the incident

waves. Surprisingly, large-amplitude heave motion at natural heave frequency and pitch motion at natural pitch frequency, in addition to the wave-frequency motions, are observed when the regular incident wave has a wave period close to 22 seconds with wave amplitude $A \approx 6.4$ meters. Note that this incident wave is very long and its frequency is not close to any natural frequencies of the body motions. (This type of long waves is not rare in certain sea area, such as Celtic Sea ($H_{1/3} = 16.8\text{m}$ and $T_p = 18.7\text{s}$) and Shetland Sea ($H_{1/3} = 18\text{m}$ and $T_p = 18.2\text{s}$.) The observed resonant heave and pitch motions of the DDCV are not predicted by classical linear wave theory.

The only existing study in literature for such coupled large-amplitude motions were done by Haslum & Faltinsen (1999) and the authors tried to relate such resonant heave and pitch motions to the effect of the Mathieu instability. Mathieu instability has been well accepted as the reason for ship parametric roll motion which happens when the frequency of ship stability change is nearly twice of ship natural roll frequency (France *et al.* 2001; Francescutto 2001; Chang 2008). Mathieu instability is also responsible for a spar platform's coupled unstable heave and pitch motions under the condition that the spar experiences heave motion at natural heave frequency which happens to be about twice of the body's pitch natural frequency (Dern 1972; Koo, Kim & Randall 2004; Rho *et al.* 2005). In the above experiment conducted by ExxonMobil (1998), however, for the given incident wave frequency, the platform's natural heave frequency and natural pitch frequency, the condition of Mathieu instability is not satisfied. A new physical mechanism needs to be sought to explain the observed unstable heave and pitch motions of the DDCV.

In this study, we investigate the unstable motions of floating bodies in the context of general wave-wave and wave-body interactions. This problem is complex as it is unsteady and highly nonlinear. Dynamic couplings exist among waves (incident waves, disturbance waves, and radiation waves induced by body motions) of different frequencies, waves and body motions, and body motions of different modes. Our objectives of this study include: (1) understanding of the physical mechanism for coupled unstable heave and pitch motions of DDCV in waves; (2) systematical

investigation of the influences of related physical parameters on the unstable body motions; and (3) to predict motions of different types of floating marine structures in waves and provide insights for new structure design and system operations.

Linear stability analyses are first carried out to understand the fundamental mechanism for the occurrence of unstable coupled heave-pitch resonant motions of floating structures in waves. The dependencies of the growth rate of unstable heave and pitch motions are investigated qualitatively over related physical parameters including wave amplitude, initial disturbance, body geometry, and damping. But the linear stability analyses are valid only for the initial development stage of unstable body motions.

Fully nonlinear numerical simulations, using the PFFT-QBEM (developed in Chapter 2 and Chapter 3), are then performed to study the unstable motions of floating platforms in waves. This study fully attests the numerical scheme in terms of accuracy, efficiency, and capability in dealing with fully nonlinearity in wave-body interactions, as the large amplitude unstable body motions are developed over a long period of time. The numerical results provide a solid verification to the conclusions drawn from the theoretical analysis and at the same time, they help to understand quantitatively the influence of different physical parameters on the growth rate of unstable body motions. By comparing the fully nonlinear numerical results with those obtained from pure linear and body nonlinear numerical simulations, we understand the roles and importance of various levels of nonlinearity involved in the dynamic interactions. Especially when unstable body motions are fully developed after long time period, fully nonlinear numerical scheme is the only one that can provide accurate and reliable solutions. The fully nonlinear numerical results are then compared with the experimental measurements by ExxonMobil with good agreement.

6.2 Linear stability analysis for motions of a floating body in waves

We consider the global motion of a floating platform in response to the action of uni-directional ocean surface waves. For simplicity, we neglect the effect of wave motions in the moon-pool of the platform and model the floating body as a single truncated vertical circular cylinder with a closed bottom.

Two sets of Cartesian coordinate systems are defined for our study. The first one is an inertia (space-fixed) coordinate system, $o - xyz$, with the x -axis pointing in the direction of incident wave propagation and z -axis the vertical direction, positive upwards. The origin of the system o is placed at the undisturbed water surface. The second coordinate system, $o' - x'y'z'$, has body-fixed axes. The axes from above two sets of coordinate systems coincide when the body is at rest. Let the instantaneous position of o' , with respect of o , be denoted by the vector

$$\vec{\xi} = (\xi_1, \xi_2, \xi_3) \quad (6.1)$$

and let the position vector to a point in space be denoted by

$$\vec{x} = (x, y, z)$$

$$\vec{x}' = (x', y', z')$$

in the two coordinate systems, respectively. These position vectors are related by a linear transformation

$$\vec{x}' = D(\vec{x} - \vec{\xi}) \quad (6.2)$$

where D is the transformation matrix defined in Chapter 3.

Under the action of uni-directional surface waves, the cylinder may experience surge, heave, and pitch motions only. We denote the surge and heave displacements by ξ_1 and ξ_3 , and the angle of pitch rotation by ξ_5 , respectively. The center of gravity is located on the body centerline and at a distance H_G from the keel of the cylinder.

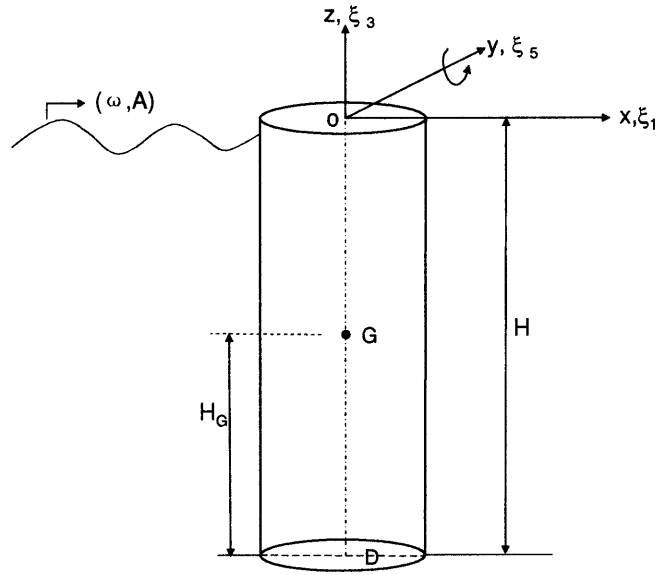


Figure 6-1: Definition sketch of a floating truncated floating circular cylinder in a regular wave.

We use (x'_G, y'_G, z'_G) to denote the location of G in the body-fixed coordinate system. For reference, the coordinate system and the translational and angular displacement conventions are shown in figure 1.

6.2.1 Mathematical formulations for general wave-body interactions

We present the initial boundary-value problem (IBVP) for the motions of a floating body in waves, in the context of an inviscid, irrotational, incompressible flow of infinite depth. The flow is described by a velocity potential $\phi(\vec{x}, t)$ which, for continuity, satisfying the Laplace equation,

$$\nabla^2 \phi(\vec{x}, t) = 0, \quad \vec{x} \in \mathcal{V}(t), \quad (6.3)$$

On the instantaneous water surface, $z = \eta(x, y, t)$, the nonlinear dynamic and kinematic boundary conditions can be written as:

$$\frac{\partial \phi}{\partial t} + \frac{1}{2} |\nabla \phi|^2 + gz = 0, \quad \bar{x} \in S_F(t), \quad (6.4)$$

and

$$\frac{\partial \phi}{\partial z} = \eta_t + \phi_x \eta_x + \phi_y \eta_y, \quad \bar{x} \in S_F(t) \quad (6.5)$$

respectively. On the impervious body boundary, $S_B(t)$, the normal velocity of the flow equals that of the boundary:

$$\frac{\partial \phi}{\partial n} = \bar{n} \cdot \bar{U}(\bar{x}, t), \quad \bar{x} \in S_B(t), \quad (6.6)$$

where \bar{n} is the unit normal pointing out of the fluid domain and \bar{U} the instantaneous velocity of the body surface. In our study, the floating body undergoes free motions in surge, heave, and pitch and \bar{U} needs to be determined from the equations of motions.

In far-field, the velocity potential satisfies the following radiation condition:

$$\nabla(\phi - \phi_I) \rightarrow 0, \quad as \bar{r} \rightarrow \infty, \quad (6.7)$$

where ϕ_I is the prescribed incident wave velocity potential, and \bar{r} the distance from the floating body.

At initial time $t = 0$, the free surface position $S_F(t = 0)$ and velocity potential on it, the body position, and the instantaneous body velocity are specified. The IBVP for general wave-body interactions is completely defined by Eq. (6.3) to Eq. (6.7) and the initial boundary conditions.

6.2.2 The solution method: linear stability analysis

We consider the motions of a floating circular cylinder under the excitation of a plane monochromatic incident wave, with frequency ω and linear amplitude $|A|$, in infinite water depth. With the assumption of weakly nonlinear waves, the total velocity

potential ϕ as well as total wave elevations can be expressed as perturbation series in the wave-slope parameter, $\epsilon \equiv kA \ll 1$ with k being the incident wave number.

The stability of the the floating cylinder's motions in waves is studied to infinitesimal disturbances. Let

$$\phi = \epsilon\phi^{(1)} + \epsilon^2\phi^{(2)} + \dots + \delta\phi' \quad (6.8)$$

where the numbered superscript represents the order in perturbation series and the prime marks disturbance. It is assumed that $\delta \ll \epsilon$ in Eq. (6.8). Correspondingly, the total free surface elevation η , body motions ξ , and the hydrodynamic forces (moments) on the body can be written as

$$\eta = \epsilon\eta^{(1)} + \epsilon^2\eta^{(2)} + \dots + \delta\eta' \quad (6.9)$$

$$\xi = \epsilon\xi^{(1)} + \epsilon^2\xi^{(2)} + \dots + \delta\xi' \quad (6.10)$$

and

$$(\mathbf{F}(t), \mathbf{M}(t)) = \epsilon(\mathbf{F}^{(1)}, \mathbf{M}^{(1)}) + \epsilon^2(\mathbf{F}^{(2)}, \mathbf{M}^{(2)}) + \dots\delta(\mathbf{F}', \mathbf{M}') \quad (6.11)$$

respectively.

Assume disturbances are applied on the body at $t = 0$ so that the body has small heave and pitch motions at their natural frequencies:

$$\xi'_3(t) = \mathbf{Re}[\xi_{3n}e^{-i\omega_{3n}t}] \quad (6.12)$$

$$\xi'_5(t) = \mathbf{Re}[\xi_{5n}e^{-i\omega_{5n}t}] \quad (6.13)$$

where ξ_{3n} and ξ_{5n} are the amplitudes of heave and pitch motions at natural heave frequency ω_{3n} and natural pitch frequency ω_{5n} , respectively. In general, ξ_{3n} and ξ_{5n} are complex numbers.

Note that the assumption for above initial disturbance forms (Eqs. (6.12) and (6.13)) has its practical basis since small natural frequency body motions could be excited under many circumstances. First of all, considering in irregular sea, waves with natural body-motion frequencies do exist and they will induce body motions at

those frequencies. Secondly, nonlinear wave-wave and wave-body interactions create waves of new frequencies which might coincide with the natural body-motion frequencies. Besides, even in a model test or in a time domain numerical simulation, start-up of the system produces transient effects which result in initial body oscillations at their natural frequencies.

If body motions induced by above initial disturbances diminish as a result of damping, the system is stable. If the disturbed body motions grow with time without external excitations applied at system natural frequencies, instability is inherent in the system. The stability of the wave-body interactions in our study will be analyzed by investigating the behavior of ξ_{3n} in Eq. (6.12) and ξ_{5n} in Eq. (6.13) with time.

For the convenience of linear stability analysis, we further assume that all quantities on $z = \eta(x, y, t)$ can be evaluated alternatively by expansions with respect to $z = 0$ so that the dynamic (Eq. (6.4)) and kinematic (Eq. (6.5)) free-surface conditions can be reformulated as:

$$\frac{\partial \phi}{\partial t} + \frac{\partial^2 \phi}{\partial z \partial t} \eta + \dots + \frac{1}{2} |\nabla \phi|^2 + \frac{1}{2} \frac{\partial}{\partial z} (|\nabla \phi|^2) \eta + \dots + g\eta = 0, \quad \text{on } z = 0 \quad (6.14)$$

and

$$\frac{\partial \phi}{\partial z} + \frac{\partial^2 \phi}{\partial z^2} \eta + \dots = \eta_t + \phi_x \eta_x + \phi_y \eta_y + \phi_{xz} \eta_x \eta + \phi_{yz} \eta_y \eta + \dots, \quad \text{on } z = 0 \quad (6.15)$$

The body boundary condition (Eq. (6.6)) needs to be expressed through expansions with respect to the mean surface S_m :

$$\begin{aligned} \bar{n}' \cdot \nabla \phi|_{S_m} = & (\bar{n}' + \bar{\alpha} \times \bar{n}' + H\bar{n}') \cdot \{ \dot{\bar{\xi}} + \dot{\bar{\alpha}} \times \bar{x}' + \dot{H}\bar{x}' - [(\bar{\xi} + \bar{\alpha} \times \bar{x}' + H\bar{x}') \cdot \nabla] \nabla \phi|_{S_m} \} \\ & - (\bar{\alpha} \times \bar{n}' + H\bar{n}') \cdot \nabla \phi|_{S_m} + \dots \end{aligned} \quad (6.16)$$

where the prime represents physical quantities in the body-fixed coordinate system, $\bar{\xi}$ and $\bar{\alpha}$ translational and rotational body motions (i.e., $\bar{\xi} = (\xi_1, \xi_2, \xi_3)$ and $\bar{\alpha} = (\xi_4, \xi_5, \xi_6)$), respectively. In Eq. (6.16), H is a matrix involving quadratic prod-

ucts of rotational quantities:

$$H = \begin{bmatrix} -\frac{1}{2}(\xi_5^2 + \xi_6^2) & 0 & 0 \\ \xi_4\xi_5 & -\frac{1}{2}(\xi_4^2 + \xi_6^2) & 0 \\ \xi_4\xi_6 & \xi_5\xi_6 & -\frac{1}{2}(\xi_4^2 + \xi_5^2) \end{bmatrix} \quad (6.17)$$

Note that $\xi_4 = \xi_6 = 0$ in our study and equation derivations will be conducted based on this condition in the following studies.

Total velocity potential as well as each components of ϕ in Eq. (6.8) satisfies the Laplace equation (Eq. (6.3)). Substituting the expansions in Eq. (6.8) ~ Eq. (6.10) into the two free-surface conditions (Eqs. (6.14) and (6.15)) and the body boundary condition (Eq. (6.16)), we can derive the governing boundary conditions for base flow and disturbance flow.

6.2.3 Base flow solution at order $O(\epsilon)$

The governing equations for the base flow of $O(\epsilon)$ can be summarized as:

$$\left. \begin{aligned} \nabla^2 \phi^{(1)}(\vec{x}, t) &= 0, & \vec{x} \in \mathcal{V}(t) \\ \left(\frac{\partial^2}{\partial t^2} + g \frac{\partial}{\partial z} \right) \phi^{(1)} &= 0, & \text{on } z = 0 \\ \eta^{(1)} &= -\frac{1}{g} \frac{\partial \phi^{(1)}}{\partial t}, & \text{on } z = 0 \\ \frac{\partial \phi^{(1)}}{\partial n} &= \frac{\partial}{\partial t} [\vec{\xi}^{(1)} + \vec{\alpha}^{(1)} \times \vec{r}] \cdot \vec{n}', & \text{on } S_m \end{aligned} \right\} \quad (6.18)$$

plus a suitable radiation condition at infinity. The $O(\epsilon)$ velocity potential can be further decomposed into the incident ($\phi_I^{(1)}$), diffraction ($\phi_D^{(1)}$), and radiation ($\phi_R^{(1)}$) potentials:

$$\phi^{(1)} = \phi_I^{(1)} + \phi_D^{(1)} + \phi_R^{(1)} \quad (6.19)$$

Except proper far-field boundary conditions, these velocity potential components need to satisfy the following equations, respectively:

$$\phi_I^{(1)} : \quad \left\{ \begin{aligned} \nabla^2 \phi_I^{(1)}(\vec{x}, t) &= 0, & \vec{x} \in \mathcal{V}(t) \\ \left(\frac{\partial^2}{\partial t^2} + g \frac{\partial}{\partial z} \right) \phi_I^{(1)} &= 0, & \text{on } z = 0 \end{aligned} \right. \quad (6.20)$$

$$\phi_D^{(1)} : \begin{cases} \nabla^2 \phi_D^{(1)}(\vec{x}, t) = 0, & \vec{x} \in \mathcal{V}(t) \\ (\frac{\partial^2}{\partial t^2} + g \frac{\partial}{\partial z}) \phi_D^{(1)} = 0, & \text{on } z = 0 \\ \frac{\partial \phi_D^{(1)}}{\partial n} = -\frac{\partial \phi_I^{(1)}}{\partial n}, & \text{on } S_m \end{cases} \quad (6.21)$$

$$\phi_R^{(1)} : \begin{cases} \nabla^2 \phi_R^{(1)}(\vec{x}, t) = 0, & \vec{x} \in \mathcal{V}(t) \\ (\frac{\partial^2}{\partial t^2} + g \frac{\partial}{\partial z}) \phi_R^{(1)} = 0, & \text{on } z = 0 \\ \frac{\partial \phi_R^{(1)}}{\partial n} = \frac{\partial}{\partial t} [\vec{\xi}^{(1)} + \vec{\alpha}^{(1)} \times \vec{r}] \cdot \vec{n}', & \text{on } S_m \end{cases} \quad (6.22)$$

Solution of $\phi_I^{(1)}$ satisfying Eq. (6.20) can be written as:

$$\phi_I^{(1)}(x, y, z) = \text{Re} \left[-\frac{iAg}{\omega} e^{kz+ikx} e^{-i\omega t} \right] \quad (6.23)$$

which represents a right-traveling wave satisfying the dispersion relation $\omega^2 = gk$. (We limit our study to a monochromatic incident wave here). The wave amplitude, A , in above equation is in general a complex number and it includes wave phase information. From now on, we introduce the expression $\phi_I^{(1)} : [AC_I^{(1)}, \omega]$ to show that the physical quantity $\phi_I^{(1)}$ has amplitude $AC_I^{(1)}$ and frequency ω , with $C_I^{(1)}$ being the transfer function for $O(\epsilon)$ incident velocity potential.

Analytical solution for $\phi_D^{(1)}$ exists only for the case of special body geometries like a vertical circular cylinder extending through the fluid of infinite depth (Mei *et al.* 2005). For general wave-body interactions, Eq. (6.21) is hard to solve theoretically and numerical $\phi_D^{(1)}$ has to be sought. But nevertheless, $\phi_D^{(1)}$ connects to the incident velocity potential through the body boundary condition. The amplitude of $\phi_D^{(1)}$ is proportion to $|A|$ and its frequency is ω , that is, $\phi_D^{(1)} : [AC_D^{(1)}, \omega]$, with the transfer function $C_D^{(1)}$.

From Eq. (6.22), we can see that the radiation velocity potential, $\phi_R^{(1)}$, is directly related to body motions which are, in turn, governed by the equations of motions. Specifically, the equation for $O(\epsilon)$ surge motion is:

$$m(\ddot{\xi}_1^{(1)} + \ddot{\xi}_5^{(1)} z'_G) + K_x \xi_1^{(1)} = F_x^{(1)} = -\rho \iint_{S_m} n_x \frac{\partial \phi^{(1)}}{\partial t} ds \quad (6.24)$$

where K_x is the external (linear) surge restoring coefficient, if any. At $O(\epsilon)$, body heave motion is determined by the following equation:

$$m\ddot{\xi}_3^{(1)} = F_z^{(1)} = -\rho \iint_{S_m} n_z \frac{\partial \phi^{(1)}}{\partial t} ds - C_{33}\xi_3^{(1)} \quad (6.25)$$

where C_{33} is the hydrostatic restoring coefficient and it equals $\rho g A_{WP}$ with A_{WP} being the area of waterplane at equilibrium. We also write down the equation for pitch motion at $O(\epsilon)$:

$$I_{22}\ddot{\xi}_5^{(1)} + m\ddot{\xi}_1^{(1)} z'_G = M_y^{(1)} = -\rho \iint_{S_m} (zn_x - xn_z) \frac{\partial \phi^{(1)}}{\partial t} ds - C_{55}\xi_5^{(1)} \quad (6.26)$$

where I_{22} is the moment of inertia (with respect to the origin of the body-fixed coordinate system o') and $C_{55} = \rho g(z_b V + L_{11})$ (z_b : z coordinate of the center of buoyancy for body in its equilibrium position; V : volume of displaced water at equilibrium; and $L_{11} = \iint x^2 ds$ with integration taken over the waterplane area).

In the right hand sides of Eq. (6.24) ~ Eq. (6.26), $\phi^{(1)}$ is the total velocity potential. A part of the total velocity potential, $\phi_I^{(1)} + \phi_D^{(1)}$, provides wave excitation forces/moment to body motions and the other part, $\phi_R^{(1)}$, is related to added mass and damping coefficients. Take the effect of $\phi_R^{(1)}$ in the equation of surge motion as an example:

$$-\rho \iint_{S_m} n_x \frac{\partial \phi_R^{(1)}}{\partial t} = -(A_{11}\ddot{\xi}_1^{(1)} + B_{11}\dot{\xi}_1^{(1)} + A_{15}\ddot{\xi}_5^{(1)} + B_{15}\dot{\xi}_5^{(1)}) \quad (6.27)$$

with A_{11} , A_{15} , B_{11} and B_{15} being the added-mass and wave damping coefficients.

With the incident wave and diffraction wave acting on body surface, the floating cylinder oscillates with motion magnitude proportion to $|A|$ and motion frequency ω . The radiation velocity potential $\phi_R^{(1)}$ relates closely to the body motion's magnitude and frequency and as a result, $\phi_R^{(1)}$ has an amplitude linear in $|A|$ and a frequency being the same as incident wave frequency ω .

From above analysis, we can conclude that the $O(\epsilon)$ base flow solutions, including velocity potentials, body motions, wave elevation, hydrodynamic pressure, hydrody-

dynamic forces/moments, have magnitudes proportional to $|A|$ and a frequency of ω :

$$S^{(1)} = \{\phi^{(1)}, \eta^{(1)}, \xi_i^{(1)}, p^{(1)}, F^{(1)}, M^{(1)}\} : [AC^{(1)}, \omega] \quad (6.28)$$

6.2.4 Disturbance flow solution

Governing equations for ϕ'

Based on Eqs. (6.8) ~ (6.10) and Eqs. (6.14) ~ (6.16), we obtain the following governing equations for the boundary value problem of disturbance flow, with order *linear* in δ :

$$\phi' : \begin{cases} \nabla^2 \phi'(\vec{x}, t) = 0, & \vec{x} \in \mathcal{V}(t) \\ \phi'_t + g\eta' = Q_{SF_1}(S^{(1)}, S') & \text{on } z = 0 \\ \phi'_z - \eta'_t = Q_{SF_2}(S^{(1)}, S') & \text{on } z = 0 \\ \frac{\partial \phi'}{\partial n} = \frac{\partial}{\partial t}[\vec{\xi}' + \vec{\alpha}' \times \vec{r}] \cdot \vec{n}' + Q_{SB}(S^{(1)}, S'), & \text{on } S_m \end{cases} \quad (6.29)$$

where $S^{(1)}$ and S' are physical quantities of base flow and disturbance flow, respectively. Note that in deriving above equations, we only keep base-flow-related physical quantities up to $O(\epsilon)$ and higher orders terms in ϵ are dropped for simplicity. In Eq. (6.29), we use $Q_{SF_1}(S^{(1)}, S')$, $Q_{SF_2}(S^{(1)}, S')$, and $Q_{SB}(S^{(1)}, S')$ to stand for the sums of a series of quadratic products of the base-flow quantities of $O(\epsilon)$ and disturbance-flow quantities of $O(\delta)$. Their detailed formulations are:

$$Q_{SF_1}(S^{(1)}, S') = -(\phi_{zt}^{(1)} \eta' + \eta^{(1)} \phi'_{zt} + \phi_x^{(1)} \phi'_x + \phi_y^{(1)} \phi'_y + \phi_z^{(1)} \phi'_z) \quad (6.30)$$

$$Q_{SF_2}(S^{(1)}, S') = -\phi_{zz}^{(1)} \eta' - \eta^{(1)} \phi'_{zz} + \phi_x^{(1)} \eta'_x + \eta_x^{(1)} \phi'_x + \phi_y^{(1)} \eta'_y + \eta_y^{(1)} \phi'_y \quad (6.31)$$

and

$$\begin{aligned} Q_{SB}(S^{(1)}, S') &= (\vec{\alpha}^{(1)} \times \vec{n}') \cdot (\dot{\vec{\xi}}' + \dot{\vec{\alpha}}' \times \vec{r} - \nabla \phi') + \\ &\quad (\vec{\alpha}' \times \vec{n}') \cdot (\dot{\vec{\xi}}^{(1)} + \dot{\vec{\alpha}}^{(1)} \times \vec{r} - \nabla \phi^{(1)}) + \\ &\quad \vec{n}' \cdot \{ \dot{\vec{H}} \vec{r} - [(\vec{\xi}^{(1)} + \vec{\alpha}^{(1)} \times \vec{r}) \cdot \nabla] \nabla \phi' - [(\vec{\xi}' + \vec{\alpha}' \times \vec{r}) \cdot \nabla] \nabla \phi^{(1)} \} \end{aligned} \quad (6.32)$$

with

$$\tilde{H} = \begin{bmatrix} -\xi_5^{(1)} \xi_5' & 0 & 0 \\ 0 & 0 & 0 \\ 0 & 0 & -\xi_5^{(1)} \xi_5' \end{bmatrix} \quad (6.33)$$

The quadratic products in $Q_{S_{F_1}}(S^{(1)}, S')$, $Q_{S_{F_2}}(S^{(1)}, S')$, and $Q_{S_B}(S^{(1)}, S')$ represent the second-order interaction between the base flow and the disturbance flow. The effect of these nonlinear interactions is that new waves of sum- and difference-frequencies will be created with amplitudes proportional to the product of base flow amplitude and disturbance flow amplitude. The sum- and difference- frequency waves will then continue to interact with base flow so that even higher- and lower- frequency waves can be induced and their amplitudes are at higher orders.

Characteristics of the ϕ' solution

The solution of Eq. (6.29) can be decomposed into two parts:

$$\phi' = \phi_1' + \phi_2' \quad (6.34)$$

The boundary value problem of ϕ_1' is governed by

$$\phi_1' : \begin{cases} \nabla^2 \phi_1'(\bar{x}, t) = 0, & \bar{x} \in \mathcal{V}(t) \\ (\phi_1')_t + g\eta_1' = 0 & \text{on } z = 0 \\ (\phi_1')_z - (\eta_1')_t = 0 & \text{on } z = 0 \\ \frac{\partial \phi_1'}{\partial n} = \frac{\partial}{\partial t} [\tilde{\xi}' + \tilde{\alpha}' \times \tilde{r}] \cdot \tilde{n}', & \text{on } S_m \end{cases} \quad (6.35)$$

which defines a typical linear radiation problem. Similar to Eq. (6.27), the solution of above equation, ϕ_1' , directly relates to the body motions caused by disturbance flow through hydrodynamic coefficients including added mass and wave damping. Specifically, the amplitude of ϕ_1' is linear in $|\tilde{\xi}'|$ and the frequencies of ϕ_1' are the same as disturbance body motion frequencies. Recalling the initial disturbances specified in Eq. (6.12) and Eq. (6.13), we can predict the amplitude and frequency of ϕ_1'

components:

$$\phi'_1 : \{[\xi_{3n}C'_{13}, \omega_{3n}]; [\xi_{5n}C'_{15}, \omega_{5n}]; \dots\} \quad (6.36)$$

with C'_{13} and C'_{15} being the corresponding transfer functions.

ϕ'_2 in Eq. (6.34) satisfies the following equations:

$$\phi'_2 : \begin{cases} \nabla^2 \phi'_2(\bar{x}, t) = 0, & \bar{x} \in \mathcal{V}(t) \\ (\phi'_2)_t + g\eta'_2 = Q_{S_{F1}}(S^{(1)}, S') & \text{on } z = 0 \\ (\phi'_2)_z - (\eta'_2)_t = Q_{S_{F2}}(S^{(1)}, S') & \text{on } z = 0 \\ \frac{\partial \phi'_2}{\partial n} = Q_{S_B}(S^{(1)}, S'), & \text{on } S_m \end{cases} \quad (6.37)$$

The interactions between base flow and disturbance flow, appearing in the form of quadratic products in $Q_{S_{F1}}(S^{(1)}, S')$, $Q_{S_{F2}}(S^{(1)}, S')$, and $Q_{S_B}(S^{(1)}, S')$, serve as the forcing terms in the boundary equations in Eq. (6.37). Based on Eq. (6.36) and the amplitude and frequency summarized for $S^{(1)}$ in Eq. (6.28), we can conclude the characteristics of ϕ'_2 as:

$$\begin{aligned} \phi'_2 : \{ & [A\xi_{3n}C'_{23}, \omega \pm \omega_{3n}]; [A\xi_{5n}C'_{25}, \omega \pm \omega_{5n}]; \\ & [A^2\xi_{3n}C'_{233}, \omega \pm (\omega \pm \omega_{3n})]; [A^2\xi_{5n}C'_{255}, \omega \pm (\omega \pm \omega_{5n})]; \dots \} \end{aligned} \quad (6.38)$$

Equations of disturbance body motions

To fully solve the solution of the disturbance flow, that is, to determine the specific values of the transfer functions, C' s, in Eqs. (6.36) and (6.38), we also need to solve the equations of disturbance motions simultaneously. By keeping terms up to $O(\epsilon\delta)$, we list here the equations governing body surge, heave, and pitch motions which are induced by the disturbance flow and interactions between base flow and the disturbance flow:

$$m(\ddot{\xi}'_1 + \ddot{\xi}'_5 z'_G) + K_x \xi'_1 = F'_x \quad (6.39)$$

$$m\ddot{\xi}'_3 = F'_z + m \frac{\partial^2}{\partial t^2} (\xi_5^{(1)} \xi'_5) z_G \quad (6.40)$$

and

$$I_{22}\ddot{\xi}'_5 + m\ddot{\xi}'_1 z'_G = M'_y - \bar{\xi}^{(1)} \times \bar{F}' - \bar{\xi}' \times \bar{F}^{(1)} + \bar{x}_G \times (\bar{\alpha}^{(1)} \times \bar{F}' + \bar{\alpha}' \times \bar{F}^{(1)}) \quad (6.41)$$

with

$$\begin{aligned} \bar{F}' &= [F'_x, 0, F'_z] = -\rho \iint_{S_m} \bar{n}' \phi'_t ds - C_{33} \xi'_3 \hat{\mathbf{k}} \\ & - \rho \iint_{S_m} \bar{n}' \{ \nabla \phi^{(1)} \cdot \nabla \phi' + (\bar{\xi}^{(1)} + \bar{\alpha}^{(1)} \times \bar{r}) \cdot \nabla \phi'_t + (\bar{\xi}' + \bar{\alpha}' \times \bar{r}) \cdot \nabla \phi_t^{(1)} \} ds \\ & - \rho \iint_{S_m} \{ [\bar{\alpha}^{(1)} \times \bar{n}'] \phi'_t + [\bar{\alpha}' \times \bar{n}'] \phi_t^{(1)} \} ds \\ & + \rho g \oint_{C_m} \bar{n}' \{ \eta^{(1)} \eta' - \eta^{(1)} (\xi'_3 - x' \xi'_5) - \eta' (\xi_3^{(1)} - x' \xi_5^{(1)}) \} dl \end{aligned} \quad (6.42)$$

and

$$\begin{aligned} M'_y &= -\rho \iint_{S_m} (z' n'_x - x' n'_z) \phi'_t ds - C_{55} \xi'_5 \\ & - \rho \iint_{S_m} (z' n'_x - x' n'_z) \{ \nabla \phi^{(1)} \cdot \nabla \phi' + (\bar{\xi}^{(1)} + \bar{\alpha}^{(1)} \times \bar{r}) \cdot \nabla \phi'_t + (\bar{\xi}' + \bar{\alpha}' \times \bar{r}) \cdot \nabla \phi_t^{(1)} \} ds \\ & - \rho \iint_{S_m} \{ [\xi_3^{(1)} n'_x - \xi_1^{(1)} n'_z] \phi'_t + [\xi'_3 n'_x - \xi'_1 n'_z] \phi_t^{(1)} \} ds \\ & + \rho g A_{WP} (\xi_1^{(1)} \xi'_3 + \xi'_1 \xi_3^{(1)}) \end{aligned} \quad (6.43)$$

C_m shown in the line-integral in Eq. (6.42) is the intersection of S_m and the plane $z = 0$.

In Eq. (6.42) and Eq. (6.43), if we make a distinction between the terms related to the disturbance body motions only and those terms involving nonlinear interactions between base flow and disturbance flow, we can reorganize Eqs. (6.39) ~ (6.41) into the following forms:

$$(m + A_{11})\ddot{\xi}'_1 + B_{11}\dot{\xi}'_1 + A_{15}\ddot{\xi}'_5 + B_{15}\dot{\xi}'_5 + K_x \xi'_1 + m\ddot{\xi}'_5 z'_G = Q_{Fx}(S^{(1)}, S') \quad (6.44)$$

$$(m + A_{33})\ddot{\xi}'_3 + B_{33}\dot{\xi}'_3 + C_{33}\xi'_3 = Q_{Fz}(S^{(1)}, S') \quad (6.45)$$

$$(I_{22} + A_{55})\ddot{\xi}'_5 + B_{55}\dot{\xi}'_5 + A_{51}\ddot{\xi}'_1 + B_{51}\dot{\xi}'_1 + C_{55}\xi'_5 + m\ddot{\xi}'_1 z'_G = Q_{My}(S^{(1)}, S') \quad (6.46)$$

Note that the hydrodynamic coefficients (i.e., added mass A_{ij} and wave damping B_{ij}) in Eqs. (6.44) and (6.45) are related to the force term $-\rho \iint_{S_m} \bar{n}' (\phi'_1)_t ds$ which origins

from the first term in the RHS of Eq. (6.42) with ϕ'_1 defined in Eq. (6.35). Similarly, A_{ij} and B_{ij} in Eq. (6.46) are related to $-\rho \iint_{S_m} (z'n'_x - x'n'_z)(\phi'_1)_t ds$ which is a part of the moment represented by the first term in the RHS of Eq. (6.43). What are kept in the RHS of Eqs. (6.44) ~ (6.46) are all the forces/moments components (including the force $-\rho \iint_{S_m} \bar{n}'(\phi'_2)_t ds$ and moment $-\rho \iint_{S_m} (z'n'_x - x'n'_z)(\phi'_2)_t ds$) induced by the nonlinear interactions between base flow and disturbance flow and they are symbolized by $Q_{Fx}(S^{(1)}, S')$, $Q_{Fz}(S^{(1)}, S')$, and $Q_{My}(S^{(1)}, S')$ for the surge, heave, and pitch motion, respectively.

The condition of instability

In above analysis, we keep the nonlinear interactions of base flow with disturbance flow up to second order which induce new waves with sum- and difference- frequencies. Initially, the disturbed body undergoes heave motion at natural heave frequency ω_{3n} with amplitude ξ_{3n} and pitch motion at natural pitch frequency ω_{5n} with amplitude ξ_{5n} . Base flow solution, $S^{(1)}$, is linearly proportion to A in amplitude and its time dependence can be represented as $e^{i\omega t}$. As a result of the interactions of base flow with disturbance flow, the RHS of Eqs. (6.44) ~ (6.46) are composed of forces/moment of sum- and difference- frequencies:

$$Q_{F/M}(S^{(1)}, S') : \{ [A\xi_{3n}C'_{03}, \omega \pm \omega_{3n}]; [A\xi_{5n}C'_{05}, \omega \pm \omega_{5n}]; [A^2\xi_{3n}C'_{003}, \omega \pm (\omega \pm \omega_{3n})]; [A^2\xi_{5n}C'_{005}, \omega \pm (\omega \pm \omega_{5n})]; \dots \} \quad (6.47)$$

These forces and moments determine the amplitudes and frequencies of disturbance body motions.

Now let's first focus our study on the disturbance heave motion at natural heave frequency and investigate how its initial disturbance amplitude ξ_{3n} defined in Eq. (6.12) evolves with time. In Eq. (6.45), if $Q_{Fz}(S^{(1)}, S')$ does not contribute force at natural heave frequency, the component of ξ'_3 at frequency ω_{3n} will die out due to damping. But if forcing of natural heave frequency exists in $Q_{Fz}(S^{(1)}, S')$, resonant heave motion will be excited and the disturbance heave motion may grow with time. By examining the frequency components of $Q_{Fz}(S^{(1)}, S')$ in Eq. (6.47), we find that

resonant heave motion happens when the following condition is satisfied

$$\omega - \omega_{5n} = \omega_{3n} \quad (6.48)$$

and the resonant excitation force comes from the second-order interaction of base flow at frequency ω with body disturbance pitch motion at natural pitch frequency ω_{5n} . Under this condition, we can isolate equation for heave motion of frequency ω_{3n} from Eq. (6.45) and write it as

$$(m + A_{33}) \frac{d^2}{dt^2} (\xi_{3n} e^{-i\omega_{3n}t}) + B_{33} \frac{d}{dt} (\xi_{3n} e^{-i\omega_{3n}t}) + C_{33} (\xi_{3n} e^{-i\omega_{3n}t}) = A \xi_{5n} C'_3 e^{-i\omega_{3n}t} \quad (6.49)$$

with ξ_{3n} and ξ_{5n} being the amplitudes of disturbance heave and pitch motions at their natural frequencies.

Similar analysis can be done for the disturbance pitch motion at natural pitch frequency and the condition to excite pitch resonance motion is

$$\omega - \omega_{3n} = \omega_{5n} \quad (6.50)$$

and under this condition, nonlinear interaction of base flow at frequency ω with body disturbance heave motion at natural heave frequency ω_{3n} excites the resonant pitch motion. The equation of disturbance pitch motion at pitch natural frequency can be derived as

$$\begin{aligned} & (I_{22} + A_{55}) \frac{d^2}{dt^2} (\xi_{5n} e^{-i\omega_{5n}t}) + B_{55} \frac{d}{dt} (\xi_{5n} e^{-i\omega_{5n}t}) + C_{55} (\xi_{5n} e^{-i\omega_{5n}t}) \\ & + A_{51} \ddot{\xi}'_1 + B_{51} \dot{\xi}'_1 + C_{55} \xi'_5 + m \ddot{\xi}'_1 z'_G = A \xi_{3n} C'_5 e^{-i\omega_{5n}t} \end{aligned} \quad (6.51)$$

Notice that condition in Eq. (6.50) is equivalent to the one in Eq. (6.48). We then summarize the condition of instability as:

$$\omega = \omega_{3n} + \omega_{5n} \quad (6.52)$$

6.2.5 Coupled equations for resonant heave-pitch motions

Combining Eq. (6.49) and Eq. (6.51), we can derive the ordinary differential equations (ODEs) governing the amplitudes of the disturbance resonant heave and pitch motions:

$$(m + A_{33})(\ddot{\xi}_{3n} - 2i\omega_{3n}\dot{\xi}_{3n}) + B_{33}(\dot{\xi}_{3n} - i\omega_{3n}\xi_{3n}) = A\xi_{5n}C'_3 \quad (6.53)$$

and

$$(I_{22} + A_{55})(\ddot{\xi}_{5n} - 2i\omega_{5n}\dot{\xi}_{5n}) + B_{55}(\dot{\xi}_{5n} - i\omega_{5n}\xi_{5n}) = A\xi_{3n}C'_5 \quad (6.54)$$

Note that the relations $C_{33} = (m + A_{33})\omega_{3n}^2$ and $C_{55} = (I_{22} + A_{55})\omega_{5n}^2$ are used in deriving above equations. Without loss of generality in illustrating the key mechanism of instability, we neglect the coupling between surge and pitch motions in Eq. (6.54).

Eq. (6.53) and Eq. (6.54) are coupled as the pitch motion amplitude affects the excitation force for heave motion and the heave motion amplitude determines the moment for pitch motion. These two equations can be combined to give the following normalized fourth-order ODE for the amplitude of resonant heave motion:

$$\begin{aligned} & \frac{d^4 \bar{\xi}_{3n}}{d\bar{t}^4} + [-2i + \bar{B}_{33} + \bar{B}_{55}] \frac{d^3 \bar{\xi}_{3n}}{d\bar{t}^3} + \\ & [(-2i\bar{\omega}_{3n} + \bar{B}_{33})(-2i\bar{\omega}_{5n} + \bar{B}_{5n}) - i\bar{\omega}_{3n}\bar{B}_{33} - i\bar{\omega}_{5n}\bar{B}_{55}] \frac{d^2 \bar{\xi}_{3n}}{d\bar{t}^2} + \\ & [i\bar{\omega}_{3n}\bar{B}_{33}(2i\bar{\omega}_{5n} - \bar{B}_{55}) + i\bar{\omega}_{5n}\bar{B}_{55}(2i\bar{\omega}_{3n} - \bar{B}_{33})] \frac{d \bar{\xi}_{3n}}{d\bar{t}} - \\ & [\bar{\omega}_{3n}\bar{B}_{33}\bar{\omega}_{5n}\bar{B}_{55} + (kA)^2 C'] \bar{\xi}_{3n} = 0 \end{aligned} \quad (6.55)$$

where $\bar{t} = \omega t$, $\bar{\xi}_{3n} = \xi_{3n}/A$, $\bar{\omega}_{3n} = \omega_{3n}/\omega$, $\bar{\omega}_{5n} = \omega_{5n}/\omega$, $\bar{B}_{33} = B_{33}/(m + A_{33})\omega$, $\bar{B}_{55} = B_{55}/(I_{22} + A_{55})\omega$, and $C' = C'_3 C'_5 / [k^2(m + A_{33})(I_{22} + A_{55})\omega^4]$. The parameter C' is related to the complex transfer functions C'_3 in Eq. (6.53) and C'_5 in Eq. (6.54). In general, C' by itself depends on many physical parameters including incident wave frequency, body motions, and the phase of the incident wave. The nonlinear free surface and body surface boundary conditions and the nonlinear couplings in forces/moment are all related to the value of C' .

General solution of the fourth-order ODE (Eq. (6.55)) can be written as

$$\bar{\xi}_{3n}(t) = \alpha_1 e^{\gamma_1 t/T} + \alpha_2 e^{\gamma_2 t/T} + \alpha_3 e^{\gamma_3 t/T} + \alpha_4 e^{\gamma_4 t/T} \quad (6.56)$$

where $T = 2\pi/\omega$, the coefficients $\alpha_i, i = 1, 2, 3, 4$ are determined by initial conditions of the problem, and $\gamma_i/2\pi, i = 1, 2, 3, 4$ are the solutions of the corresponding fourth-order polynomial equation of Eq. (6.55).

The same equation as Eq. (6.55) can be obtained for the amplitude of resonant pitch motion and the general solution for the normalized ξ_{5n} is:

$$\bar{\xi}_{5n}(t) = \beta_1 e^{\gamma_1 t/T} + \beta_2 e^{\gamma_2 t/T} + \beta_3 e^{\gamma_3 t/T} + \beta_4 e^{\gamma_4 t/T} \quad (6.57)$$

with γ_i the same as those in Eq. (6.56) and $\beta_i, i = 1, 2, 3, 4$ determined by initial conditions for pitch motion.

In view of the whole process in obtaining Eq. (6.56) or Eq. (6.57), the values of γ_i are determined by the following physical parameters:

$$\gamma_i = \mathcal{F}(\bar{\omega}_{3n}, \bar{\omega}_{5n}, \bar{B}_{33}, \bar{B}_{55}, kA, C'), \quad i = 1, 2, 3, 4 \quad (6.58)$$

where $\bar{\omega}_{3n}$ and $\bar{\omega}_{5n}$ are dependent, as seen from Eq. (6.52). Clearly, if the real part of any of $\gamma_i, \mathbf{Re}[\gamma_i], i = 1, 2, 3, 4$, is positive, the resonant heave and pitch motions are unstable with their amplitudes, ξ_{3n} and ξ_{5n} , growing with time exponentially. The value of $\mathbf{Re}[\gamma_i]$ is the growth rate of the i -th mode of resonant heave/pitch motions.

6.2.6 Surge motion effect on instability

In previous analysis, the coupling between surge and pitch motions is neglected in searching for the instability condition, for simplicity. Here we briefly discuss the effect of body surge motion on resonant pitch as well as heave motions by analyzing the complete forms of Eq. (6.44) to Eq. (6.46).

First of all, the existence of surge motion does not affect the frequency condition for instability shown in Eq. (6.55), since the values of system natural frequencies

do not vary with surge motion. Secondly, surge motion affects the values of growth rates for unstable resonant heave/pitch motions. From Eq. (6.46), we know that surge motion has a component at natural pitch frequency ω_{5n} . Under the instability condition Eq. (6.55), surge motion at natural pitch frequency interacting with base flow can provide excitation force for resonant heave motion which in turn interacts with the base flow to influence resonant pitch motion. As a result, the surge, heave, and pitch motions are all coupled. The effect of interactions between surge motion and base flow may strengthen or weaken the growth of unstable heave and pitch motions, depending on the initial conditions for any specified problem.

6.2.7 Other possible conditions of instability

Apart from physical justification, frequency combinations between base flow and disturbance flow, other than the one in Eq. (6.55), might also be able to match the natural heave and pitch frequencies so that coupled resonant heave and pitch motions could be excited. As the forcing terms shown in Eq. (6.47) are composed of many groups of sum- and difference- frequencies, we can see that resonant heave motion can be powered if the sum frequency $\omega + \omega_{5n}$, which is induced by the nonlinear interaction of base flow with initial disturbance natural-frequency pitch motion, equals ω_{3n} . At the same time, the interaction of base flow with resonant heave motion will be able to create forcing of difference frequency, $\omega_{3n} - \omega$, which excites pitch motion of frequency ω_{5n} . So, instability could happen if the following relation holds:

$$\omega = \omega_{3n} - \omega_{5n} \quad (6.59)$$

Previous discussions on the conditions of unstable body motions are limited to second-order interactions between base flow and disturbance flow. Higher-order interactions could also be the possible mechanism for instability. For example, among those frequencies involved in the third-order interactions, if

$$2\omega = \omega_{5n} + \omega_{3n} \quad (6.60)$$

that is, $\omega + (\omega - \omega_{5n}) = \omega_{3n}$, resonant heave motion happens and at the same time, the condition for resonant pitch motion, $\omega + (\omega - \omega_{3n}) = \omega_{5n}$, is automatically satisfied. But generally, less energy is involved in third-order interactions (as represented by the amplitude, $A^2 \xi'_i C'_i$) than that in second-order interactions. Damping might easily balance the excitations induced by third or higher order interactions for resonant motions.

By the end, whether a system is unstable and which mechanism is responsible for the instability have to be checked physically. Firstly, wave damping tends to stabilize the system, but the value of wave damping is determined by the design of the body configuration and the wave condition under which the floating body is operating. Secondly, incident wave with frequency satisfying the condition Eq. (6.52), (6.59) or (6.60) may or may not be popular in open seas. For example, the SPAR used in the ExxonMobil experiment has natural heave period around 30 seconds and natural pitch period around 100 seconds, respectively. Incident wave satisfying Eq. (6.52) has wave period around 22.5 seconds. But to satisfy Eq. (6.59), incident wave should have wave period around 42 seconds, which corresponds to a wavelength around 3160 meter. This type of wave may not be easily found, say, in the Gulf of Mexico ($H_{1/3} = 12.5\text{m}$ and $T_p = 14.6\text{s}$).

6.2.8 Numerical analyses on growth rates of coupled unstable heave/pitch motions

With specified values for the following parameters, $(\bar{\omega}_{3n}, \bar{\omega}_{5n}, \bar{B}_{33}, \bar{B}_{55}, kA, C')$, the growth rates $\text{Re}[\gamma_i], i = 1, 2, 3, 4$ of the amplitudes of disturbance heave (pitch) motion, based on Eq. (6.55), can be numerically obtained with little difficulty. In this section, we investigate the effects of all these related physical parameters on the instability of floating bodies in waves through numerical analyses on the behavior of growth rates.

Stability characteristics of a SPAR platform

For illustration, we first take a SPAR platform similar to the DDCV tested in the ExxonMobil experiment (1998) as an example to analyze its stability characteristics. The cylindrical body has a diameter $D = 37.2\text{m}$, a draft $H = 198\text{m}$, a meta-centric height $d_0 = 5.3\text{m}$, and a radius of pitch gyration $R_{yy} = 75.9\text{m}$. The center of gravity of the cylinder is located at a distance $h = 94.2\text{m}$ from the keel of the cylinder. This floating body's natural heave and pitch frequencies are numerically evaluated as $\omega_{3n} = 0.216 \text{ rad/s}$ (i.e., $T_{3n} \cong 29\text{s}$) and $\omega_{5n} = 0.078 \text{ rad/s}$ (i.e., $T_{5n} \cong 80\text{s}$), respectively. Based on the instability condition $\omega = \omega_{3n} + \omega_{5n}$, we consider a regular incident wave of frequency $\omega = 0.294 \text{ rad/s}$ (i.e., $T \cong 21.3\text{s}$). (The word SPAR will be used to represent above body geometry in the following studies, if not specified otherwise.)

The linear wave damping effect for this body is small in view of two reasons: (1) waves at natural heave or pitch frequencies are long waves and in principle, wave damping vanishes in the long-wave limit; and (2) the deep-draft design of the body configuration tends to restrict body motions' disturbance to water surface. We will neglect the effect of wave damping on the SPAR's instability for now and focus on investigating the dependence of growth rates on parameters kA and C' . (Note that the exact value of C' in Eq. (6.55) is hard to estimate as it represents the complicated (2nd-order) nonlinear wave-wave and wave-body interactions. To obtain C' , all the listed equations, including equations of motions, for base flow and disturbance flow need to be solved explicitly. In the following study, we will set the value of C' without much physical justification, but the effect of C' on system instability can still be illustrated.)

In figure 6-2, we show contours of the four growth rates, $\mathbf{Re}[\gamma_i], i = 1, 2, 3, 4$, for the coupled resonant heave/pitch motion of the SPAR as a function of the combined parameter $(kA)^2 C'$. For the specified range of the real and imaginary parts of $(kA)^2 C'$ ($[-0.001 : 0.001, -0.001 : 0.001]$), there are generally two positive and two negative growth rates. A positive $\mathbf{Re}[\gamma]$ value means that the SPAR's motions are unstable. The maximum value of $\mathbf{Re}[\gamma]$ dominates the growth of unstable body motions after

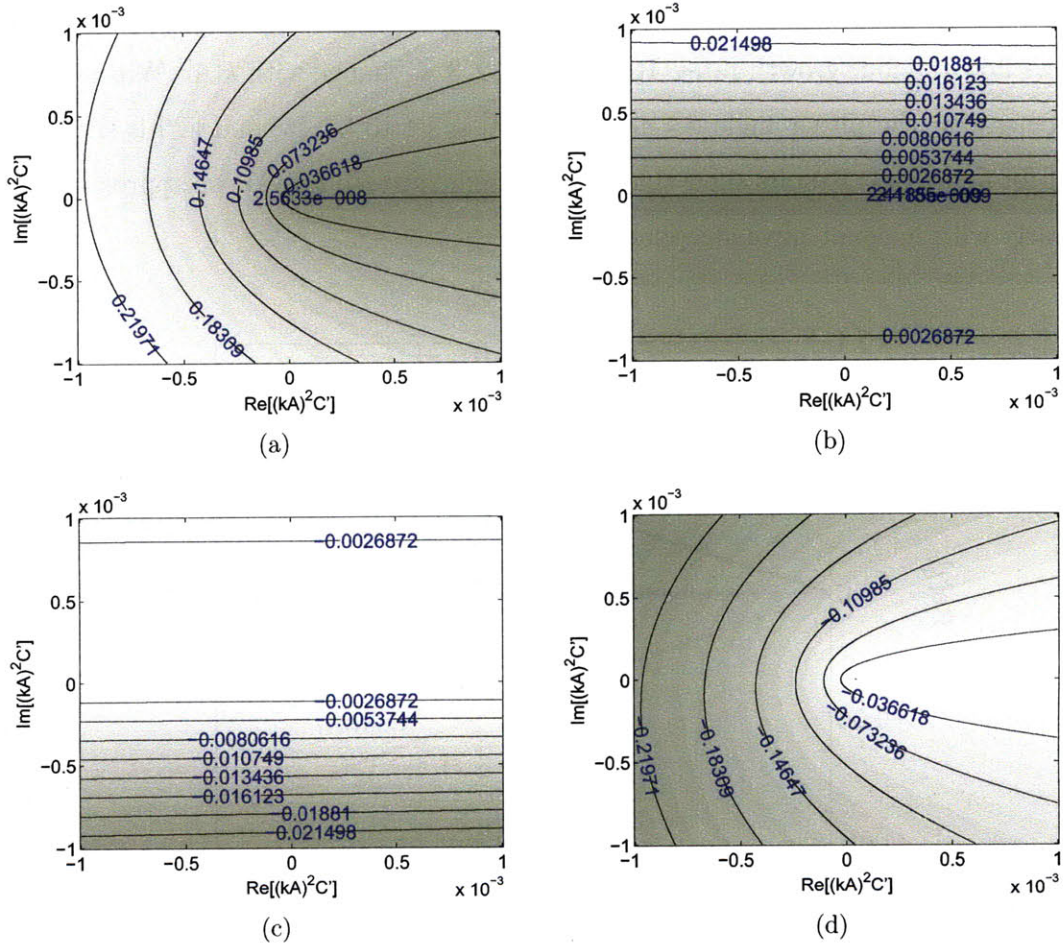


Figure 6-2: Contour of the growth rates, $\text{Re}[\gamma_i]$, $i = 1, 2, 3, 4$ (ordered from the maximum to the minimum), as a function of $(kA)^2 C'$, for the study of the SPAR's instability.

the initial development period. As shown in figure 6-2a, $\max(\mathbf{Re}[\gamma_i])$ increases with the magnitude of $(kA)^2C'$.

Effect of incident wave steepness on instability

By fixing all other physical parameters and varying the value of $|A|$, we can study the dependence of the SPAR's instability on incident wave steepness, $k|A|$. Figure 6-3 shows how the four growth rates, $\mathbf{Re}[\gamma_i], i = 1, 2, 3, 4$, change with $k|A|$. Without loss of generality, the phase angle $\theta = \arg[(kA)^2C']$ is set to be 45° and $|C'|$ is set to be 0.01 for figure 6-3. Results show that the maximum growth rate grows approximately linearly with incident wave steepness.

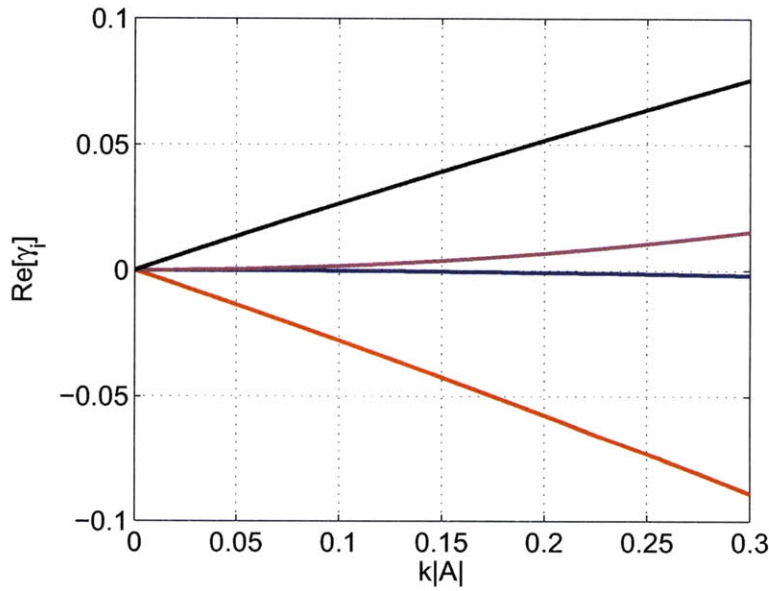


Figure 6-3: Growth rates of the SPAR's coupled resonant heave/pitch motions, $\mathbf{Re}[\gamma_i], i = 1, 2, 3, 4$, as a function of incident wave steepness $k|A|$, with $|C'| = 0.01$ and $\theta = 45^\circ$ fixed.

Dependence of growth rates on $\arg[(kA)^2C']$

Phase angle matters in stability analysis in general. We show in Figure 6-4 the effect of phase angle $\theta = \arg[(kA)^2C']$ on the SPAR's growth rates, with amplitude of $(kA)^2C'$ set to be 0.001. The maximum (minimum) value of $\mathbf{Re}[\gamma_i], i = 1, 2, 3, 4$ increases (decreases) with the absolute value of θ . Zero phase angle of $(kA)^2C'$ makes

all growth rates be zero. Physically, $\theta = 0$ means that the external forcing is exactly out of phase with the body motion under study.

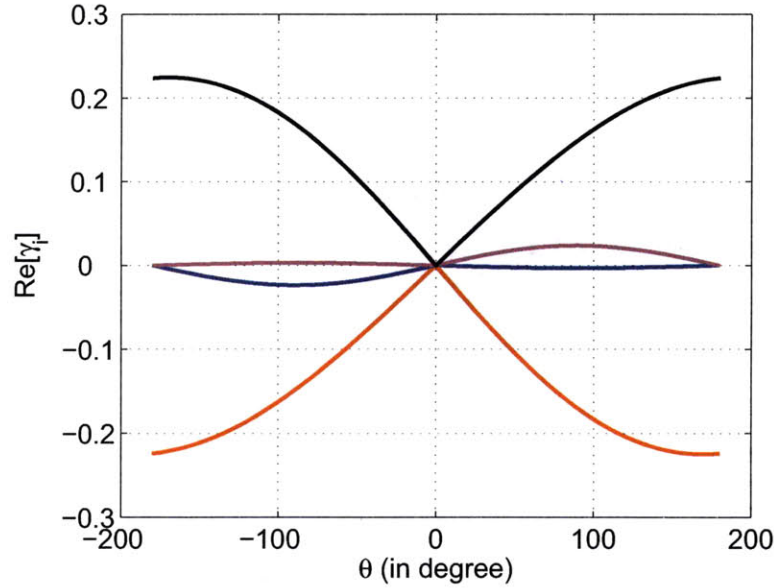


Figure 6-4: Growth rates of the SPAR's coupled resonant heave/pitch motions, $Re[\gamma_i], i = 1, 2, 3, 4$, as a function of the phase angle $\theta = \arg[(kA)^2 C']$, with $|(kA)^2 C'| = 0.001$.

For illustration, the combined effect of incident wave steepness $k|A|$ and the phase angle θ on the value of $\max(\mathbf{Re}[\gamma_i])$ is shown in figure 6-5. Large wave steepness and large (absolute) value of phase angle lead to fast growth of unstable body motions of the SPAR.

Stability characteristics of a cylindrical FPSO

The parameters $\bar{\omega}_{3n}$ and $\bar{\omega}_{5n}$ are determined by body geometry and how these frequency parameters affect the values of growth rates reflects the influence of body geometry on instability. For comparison with above results of the SPAR, we conduct stability analysis for a cylindrical FPSO in this section. The FPSO has a diameter $D = 91.6\text{m}$, a draft $H = 27\text{m}$, a meta-centric height $d_0 = 10.1\text{m}$, and a radius of pitch gyration $R_{yy} = 36\text{m}$. Its gravitational center is located at a distance $h = 22.85\text{m}$ from the cylinder bottom. This body geometry determines its natural heave frequency

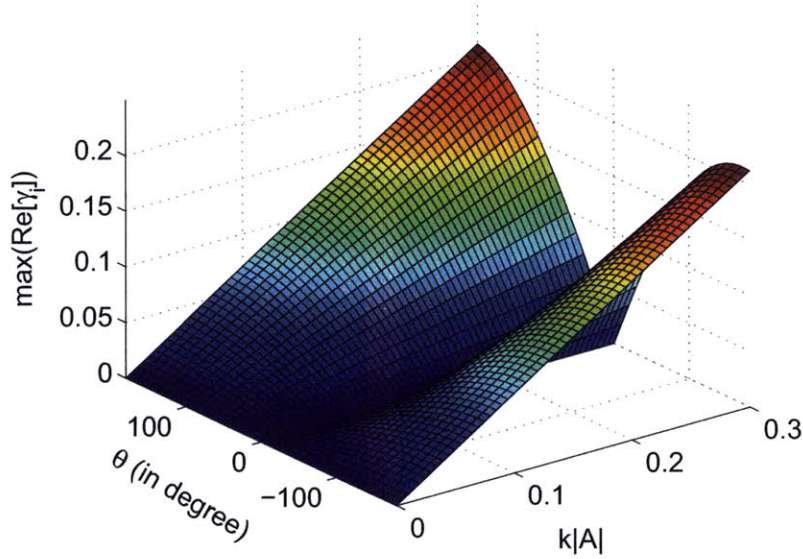


Figure 6-5: Maximum growth rate of the SPAR's coupled resonant heave/pitch motions, $\max(\mathbf{Re}[\gamma_i])$, as a function of incident wave steepness $k|A|$ and phase angle θ , with a fixed $|C'| = 10|$.

$\omega_{3n} = 0.444$ rad/s (i.e., $T_{3n} \cong 14.1s$) and natural pitch frequency $\omega_{5n} = 0.256$ rad/s (i.e., $T_{5n} \cong 24.6s$). In view of the instability condition $\omega = \omega_{3n} + \omega_{5n}$, we consider an incident wave of frequency $\omega = 0.7$ rad/s (i.e., $T \cong 9s$).

We first neglect the wave damping effect for the FPSO's instability analysis and study the growth rates' general behavior over the combined parameter $(kA)^2C'$. Figure 6-6 shows contours of the four growth rates of the FPSO's coupled resonant heave/pitch motions, $\mathbf{Re}[\gamma_i], i = 1, 2, 3, 4$, as a function of $(kA)^2C'$ for the same range $([-0.001 : 0.001, -0.001 : 0.001])$ as specified in figure 6-2 for the SPAR. Results show that motions of the cylindrical FPSO also have two positive and two negative growth rates. Difference between figure 6-2 and figure 6-6 signifies the sensitivity of body geometry effect on the instability of the system. Specifically, the cylindrical FPSO has a relatively smaller $\max(\mathbf{Re}[\gamma_i])$ (in figure 6-6a) than that of the SPAR for a specified $(kA)^2C'$ value, which means that the FPSO is more stable to initial disturbance, if wave damping effect is not taken into account.

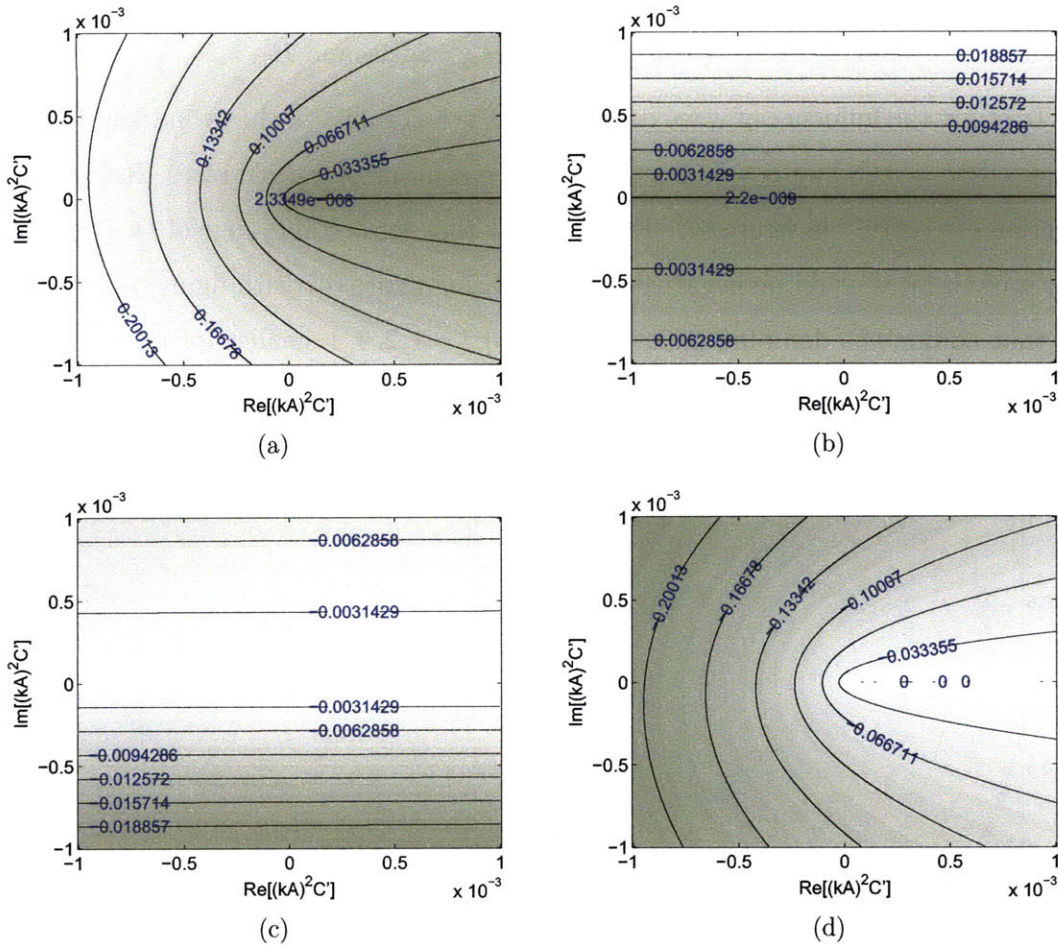


Figure 6-6: Contour of the growth rates, $\mathbf{Re}[\gamma_i], i = 1, 2, 3, 4$ (ordered from the maximum to the minimum), as a function of $(kA)^2 C'$, for the study of a cylindrical FPSO's instability.

Influence of wave damping

Body geometry effect is also reflected by the value of wave damping which is an important factor to consider in stability analysis. Contrasting to the SPAR, the cylindrical FPSO has significant wave damping due to the body's low draft and relatively large waterplane area.

Set the hydrodynamic wave damping coefficient $B_{33} = \varsigma_3 D_{3cr}$ with D_{3cr} being the critical heave damping, i.e., $D_{3cr} = 2(m + A_{33})\omega_{3n}^2$, and ς_3 being the damping ratio. Similarly, define ς_5 as the ratio of the linear wave damping of pitch motion

to the critical pitch damping ($D_{5cr} = 2(I_{22} + A_{55})\omega_{5n}^2$). Recalling the definitions for the normalized wave damping parameters \bar{B}_{33} and \bar{B}_{55} as well as the normalized frequencies $\bar{\omega}_3$ and $\bar{\omega}_5$ in Eq. (6.55), we have $\bar{B}_{33} = 2\zeta_3\bar{\omega}_3$ and $\bar{B}_{55} = 2\zeta_5\bar{\omega}_5$.

To study the influence of wave damping on the instability of the cylindrical FPSO, we specify $\zeta_3 = 0.08$ and $\zeta_5 = 0.02$ and replot the contour of growth rates, $\mathbf{Re}[\gamma_i]$ as a function of $(kA)^2C'$ in figure 6-7. Results show that for certain range of $(kA)^2C'$, all four growth rates could be negative. By comparing figure 6-7 with figure 6-6, we can see that adding the damping makes all $\mathbf{Re}[\gamma_i], i = 1, 2, 3, 4$ smaller for any specified value of $(kA)^2C'$. Damping stabilizes the system, as expected.

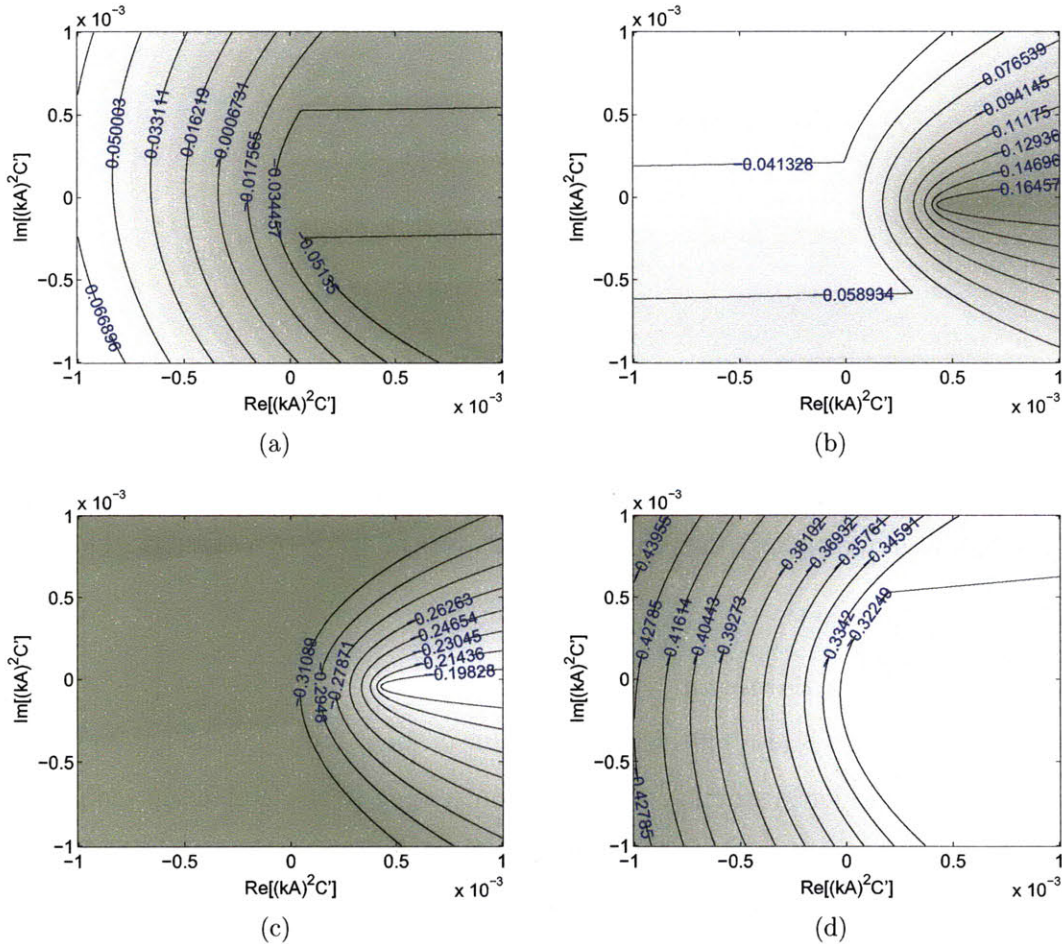


Figure 6-7: Contour of the growth rates, $\mathbf{Re}[\gamma]$ (ordered from the maximum to the minimum), as a function of $(kA)^2C'$, with damping ratios set as $\zeta_3 = 0.08$ and $\zeta_5 = 0.02$, for the study of a cylindrical FPSO's instability.

By fixing all other relevant parameters and only varying linear wave damping parameters, we show in figure 6-8 the dependence of the maximum growth rate on ζ_3 and ζ_5 . The value of $\max(\mathbf{Re}[\gamma_i])$ is visualized by the colors used in figure 6-8. It's clear that greater values of $\max(\mathbf{Re}[\gamma_i])$ happen at smaller ζ_3 and ζ_5 and increasing either damping ratio parameters can substantially reduce the value of $\max(\mathbf{Re}[\gamma_i])$. When the maximum growth rate becomes negative, the system is stable.

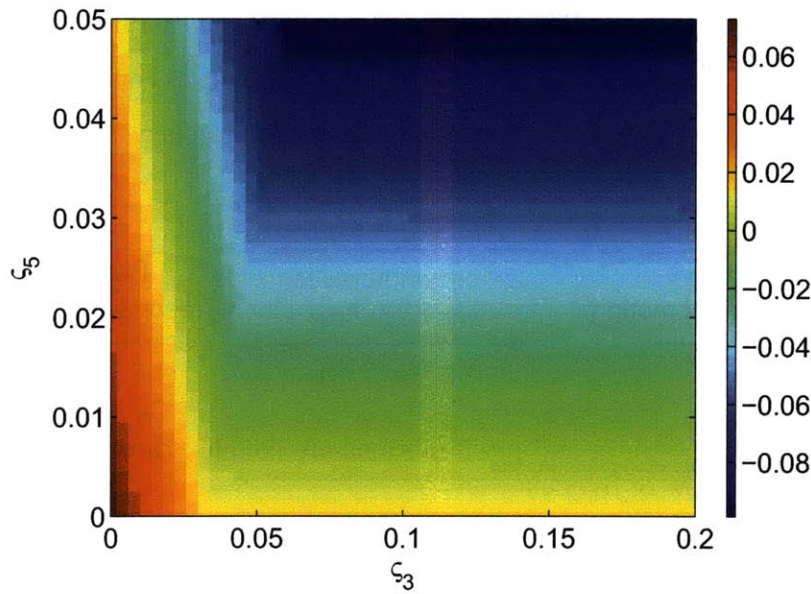


Figure 6-8: Growth rates of the FPSO's coupled resonant heave/pitch motions, $\max(\mathbf{Re}[\gamma_i])$, visualized by the colors, as a function of wave damping ratios ζ_3 and ζ_5 , with $|(kA)^2 C'| = 0.001$ and $\theta = 45^\circ$.

6.2.9 Summary of the linear stability analysis for floating bodies in waves

Through above linear stability analysis, we identify the condition for coupled unstable heave and pitch motions of floating bodies in waves. Consider initial disturbances in heave motion at natural heave frequency ω_{3n} and pitch motion at natural pitch frequency ω_{5n} and the floating body is subject to an incident wave (base flow) of frequency ω . When the incident wave frequency is about the sum of the natural heave

frequency and natural pitch frequency, unstable heave and pitch motions might be excited.

The underlying physical mechanism of instability is illustrated in figure 6-9. The 2nd-order difference-frequency interaction between base flow at ω and disturbance heave motion at ω_{3n} provides excitation forcing for resonant pitch motion as $\omega - \omega_{3n} = \omega_{5n}$. At the same time, the 2nd-order difference-frequency interaction between base flow at ω and the resonant pitch motion at ω_{5n} creates an excitation at natural heave frequency as $\omega - \omega_{5n} = \omega_{3n}$. This excitation powers the initial disturbance resonant heave motion. The combination of above interactions causes coupled resonant heave and pitch motions to grow by taking energy from the base flow.

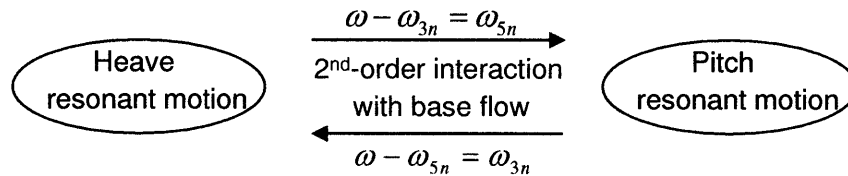


Figure 6-9: Resonant heave and pitch motions are coupled through 2nd-order interactions with base flow of frequency ω .

Recall the incident wave condition and the natural heave/pitch frequencies of the DDCV in the experiment conducted by ExxonMobil (1998). The instability mechanism discovered from our linear stability analysis can perfectly explain the observed unstable heave and pitch motions of the DDCV in the experiment.

The instability of a floating body in waves is related to many physical parameters including incident wave steepness kA , nonlinear interactions between waves and motions (represented by C' in above analysis), and body geometries which by itself relates to natural frequencies and damping (linear wave damping and viscous damping). Our linear stability analysis is capable of identifying these relevant parameters and analyzing qualitatively the effect of each parameter on the instability of the system.

However, there are complexities in applying above analysis to practical problems. First of all, above analysis is symbolic and quantitative evaluation for the influence of different parameters on instability is very challenging. Secondly, there are factors

that cannot be easily investigated through above analysis, but they are critical for the study of deterministic body motion development. One factor is the influence of initial boundary conditions on parameters like α_i in Eq. (6.56) and β_i in Eq. (6.57). Another factor is the dependence of instability on frequency detuning. Thirdly and more importantly, above linear stability analysis is valid only for the initial stage of unstable body motion evolution when body motions and disturbance waves are small.

To confirm the physical mechanism identified by the linear stability analysis and to overcome the limitations of above study, fully nonlinear numerical simulations are desirable for the study of large-amplitude motions of floating structures in waves.

6.3 Fully nonlinear numerical simulations of unstable motions of floating structures in waves

In this section, we apply direct numerical simulations to investigate the instability of floating vessels/structures' free motions in waves. Fully nonlinear numerical simulations are performed using the efficient and robust IBVP solver, PFFT-QBEM, which is described in Chapter 2. Detailed boundary-integral formulations and numerical issues in implementing PFFT-QBEM for the study of general three-dimensional nonlinear wave-body interactions are discussed in Chapter 3.

Consider the same cylindrical body geometries as those adopted in above theoretical analysis and a uni-directional regular incident wave. Only surge, heave, and pitch motions of the floating body are excited by the incident wave. To prevent free drift motion in the wave direction in nonlinear simulations, a soft artificial spring is added in the surge direction. Initial disturbances in resonant heave and pitch motions are naturally generated from the non-smooth initial start of the simulation. We perform a long-time simulation of the fully nonlinear interactions of the floating cylinder with incident wave field, including nonlinear wave-wave and wave-body interactions and interactions of different modes of body motions.

6.3.1 Confirmation of the instability condition

We first simulate the SPAR's response to the action of a regular incident wave train. The incident wave has a wave steepness of $kA = 0.02$ and a frequency of $\omega = 0.294$ rad/s. Note that the incident wave frequency is set to be exactly the sum of the SPAR's natural heave frequency $\omega_{3n} = 0.216$ rad/s and natural pitch frequency $\omega_{5n} = 0.078$ rad/s, according to the instability condition (Eq. (6.52)) identified by linear stability analysis. At $t = 0$, the SPAR sits at the crest of the incident wave and the corresponding phase angle of the incident wave is symbolized as $\theta' = 0$. We design the artificial spring in surge direction so that the natural surge period is $T_{1n} \cong 160$ s. (In practice, the natural surge period is normally large for the DDCV type of platform. The period value 160 is arbitrarily chosen here and detailed study will be carried out later for the effect of surge motion on the overall instability of the problem.)

Figure 6-10a plots the time histories of the SPAR's surge motion obtained from the fully-nonlinear simulations. The amplitudes of the surge-motion time harmonics at zero-frequency (i.e., mean value), incident wave frequency ω , natural surge frequency ω_{1n} , and all other frequencies (summed as *residue*) are evaluated from the Fourier transform of the time history of body surge motion, shown in figure 6-10b as a function of time. The results show that the surge motion is stable with the amplitude at the natural surge frequency decreasing with time. Time histories of heave motion and amplitudes of heave-motion harmonics are plotted in figures 6-10c and d, respectively. As we can see, the amplitude of heave motion at natural heave frequency grows exponentially with time. The maximum amplitude of heave motion could reach around 11 meters (as marked in the left corner of figure 6-10c) in response to the incident wave of amplitude 2.26m. Similar results for the pitch motion are shown in figures 6-10e and f. The resonant pitch motion is also unstable and the maximum pitch angle is about 11.5° after 70 ~ 80 wave periods of nonlinear wave-body interactions. Such significant heave and pitch motions would greatly affect the efficiency of the platform's operations or even lead to a failure of the marine structure.

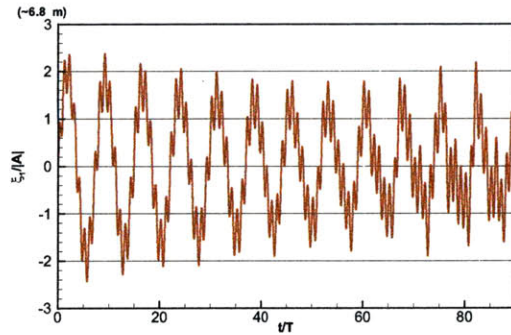
There are some common features in the time harmonics of surge, heave, and pitch

motions, shown in figures 6-10b, d and f: the amplitudes of motion harmonics at incident wave frequency ω tend to be steady while the amplitude of *residues* grow with time. As the amplitude of resonant heave motion increases with time, surge and pitch motions at natural heave frequency, excited by the heave-radiation wave, will also grow with time. Similarly, larger-amplitude resonant pitch motion induces increasing surge and heave motions at natural pitch frequency. Beside, due to the fully nonlinear couplings between waves, wave and body motions, and different modes of body motions, higher-order new frequency body motions will be created. Therefore, amplitudes of residue harmonics in every mode of body motions grow with time.

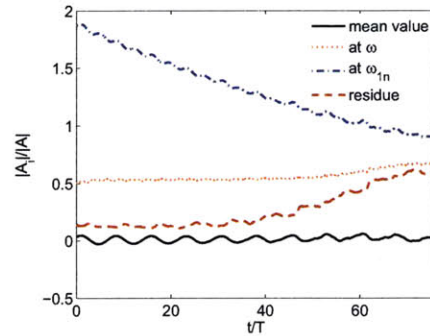
From figure 6-10, we can also see that after the unstable heave and pitch motions are developed to certain amplitudes, they stop growing as fully nonlinear interactions among incident, radiated, and diffracted wave fields and different modes of the body motions balance the instability effect. How the unstable body motions continue to evolve at later time can also be investigated by the present fully-nonlinear numerical simulations but is not the focus of current study.

6.3.2 Importance of full nonlinearity in highly-nonlinear wave-body interactions

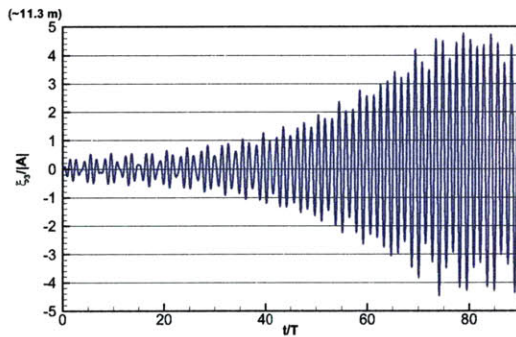
To investigate the importance of different levels of nonlinearity in the study of nonlinear wave-body interactions, here we apply three versions of PFFT-QBEM schemes (linear, body nonlinear, and fully nonlinear) to simulate the development of SPAR motions. Ideal fluid is assumed in the simulation and viscous damping effect is neglected. The incident wave has a wave steepness $kA = 0.02$, a frequency $\omega = 0.294$ rad/s, and an initial phase angle $\theta' = 0$. In the linear PFFT-QBEM scheme, the linearized free surface boundary condition is applied at undisturbed water surface $z = 0$ and the linearized body boundary condition is imposed at the mean body surface S_m . As a result, the boundary enclosing the fluid does not vary with time. The body nonlinear PFFT-QBEM approach adopts the instantaneous body surface while keeping the linearized free surface condition at $z = 0$. So, only partial nonlinear effect relating



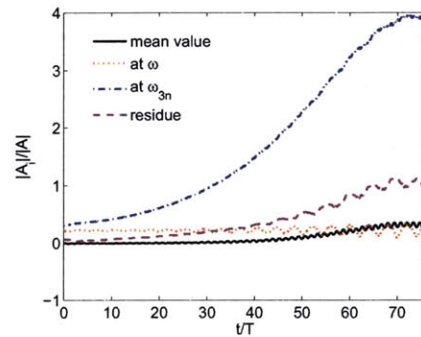
(a) Surge motion



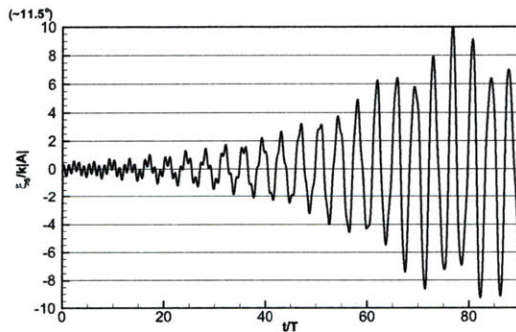
(b) Amplitudes of surge-motion harmonics



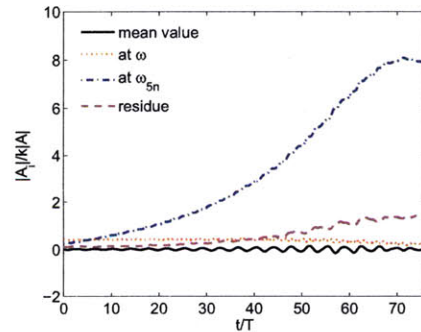
(c) Heave motion



(d) Amplitudes of heave-motion harmonics



(e) Pitch motion



(f) Amplitudes of pitch-motion harmonics

Figure 6-10: Time histories of (a) surge motion, (b) amplitudes of surge-motion harmonics, (c) heave motion, (d) amplitudes of heave-motion harmonics, (e) pitch motion, and (f) amplitudes of pitch-motion harmonics, obtained by fully-nonlinear simulations for the SPAR in a regular wave of wave steepness $k|A| = 0.02$, wave frequency $\omega = 0.294$ rad/s, and phase angle $\theta' = 0$.

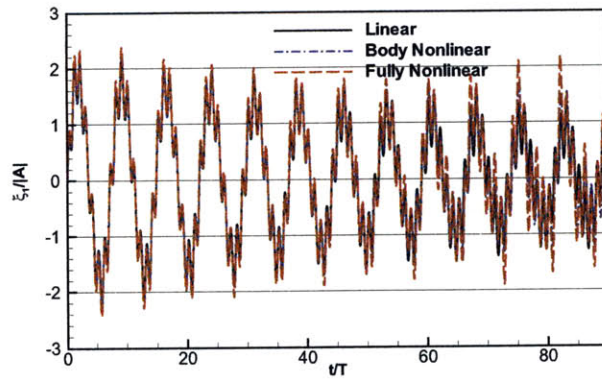
to body surface is accounted for in the body nonlinear scheme. As mentioned before, the fully nonlinear PFFT-QBEM method takes into account all the nonlinearities in the free surface and boundary conditions.

Comparison between linear, body nonlinear, and fully nonlinear numerical results for the surge, heave, and pitch motions of the SPAR is shown in figure 6-11. Solutions from three different schemes basically agree for the surge motion in figure 6-11a as surge motion is stable. But from figures 6-11b and c, it's seen that the linear solution does not predict any unstable motions while unstable heave and pitch motions are apparent when partial (in body nonlinear PFFT-QBEM) or full (in fully nonlinear PFFT-QBEM) nonlinearity is considered. However, the difference between the fully-nonlinear and body-nonlinear results grows rapidly with time, which indicates that fully nonlinear free-surface effects are of importance and need to be properly considered in order for a reliable prediction of the unstable coupled natural heave and pitch motions of a platform in large waves.

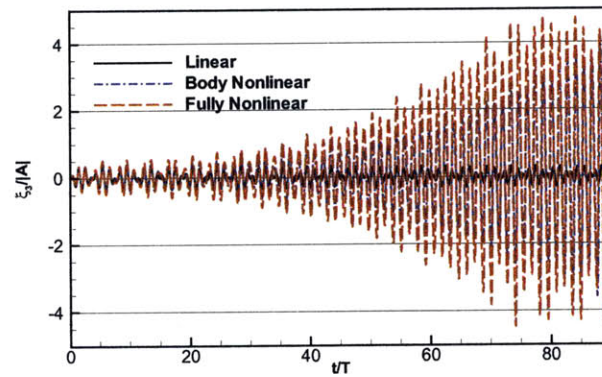
6.3.3 Effect of incident wave steepness on instability

The effect of incident wave steepness on instability is studied through fully nonlinear numerical simulations for the SPAR motions in a regular incident wave of different settings of wave steepness. The incident wave frequency is again specified as $\omega = 0.294$ rad/s and its phase angle is set as $\theta' = 0$.

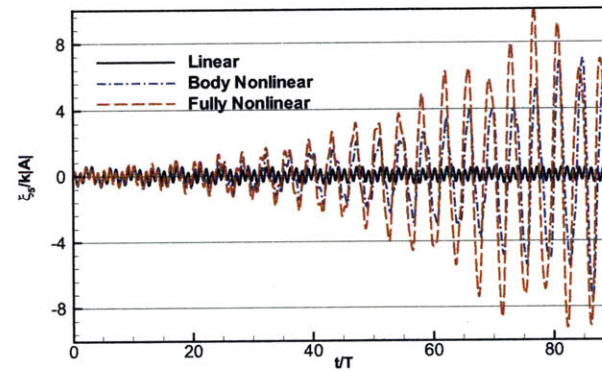
Figure 6-12a plots the time history of (normalized) amplitudes of heave motions at natural heave frequency, $|A_{3n}|$, for three groups of wave steepness ($k|A| = 0.01, 0.02$, and 0.03). Corresponding to the small wave steepness $k|A| = 0.01$, resonant heave amplitude keeps increasing with time even after 80 incident wave periods. With $k|A| = 0.02$, $|A_{3n}|$ grows with time initially and reaches its peak at about $t/T \cong 72$. For the largest wave steepness $k|A| = 0.03$, the amplitude of resonant heave motion arrives at its peak value a $t/T \cong 42$ and starts to oscillate afterwards. Comparison of the three curves in figure 6-12a shows that unstable resonant heave motion with the medium wave steepness $k|A| = 0.02$ obtains the highest peak value of $|A_{3n}|$, within the time period being tested.



(a) Surge motion

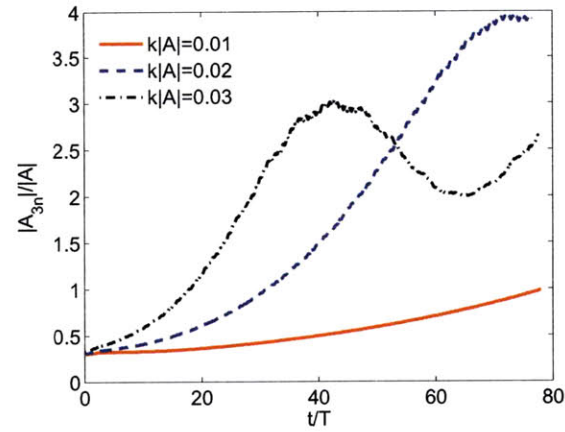


(b) Heave motion

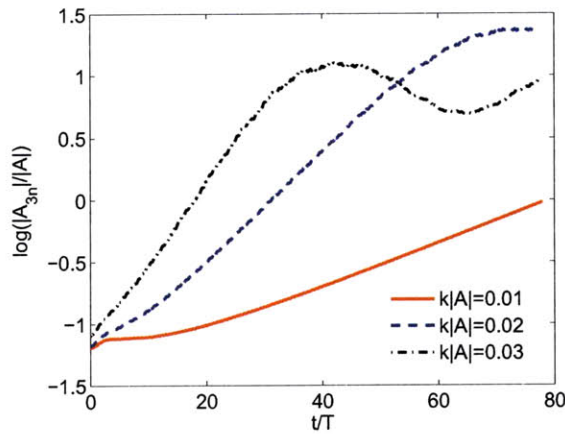


(c) Pitch motion

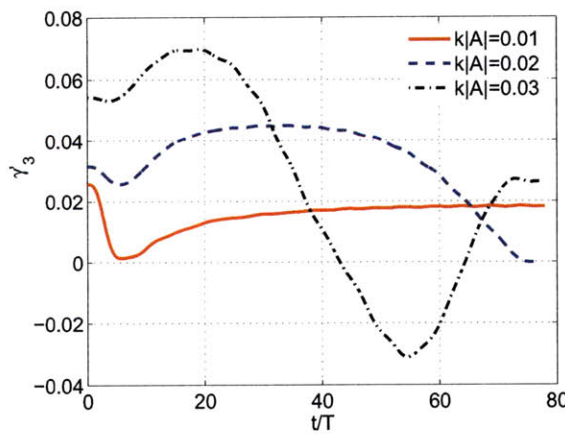
Figure 6-11: Comparison between solutions of linear(—), body nonlinear(- · -), and fully nonlinear(- -) PFFT-QBEM simulations for the time histories of (a) surge motion, (b) heave motion, and (c) pitch motion of the SPAR in waves. In the simulations, the incident wave has a wave steepness of $kA = 0.02$, a frequency of $\omega = 0.294$ rad/s and a phase angle of $\theta' = 0$.



(a)



(b)



(c)

Figure 6-12: Time histories of (a) the amplitude of resonant heave motion $|A_{3n}|$, (b) $\log(|A_{3n}|)$, and (c) the growth rate γ'_3 of resonant heave motion, with the incident wave phase angle $\theta' = 0$, frequency $\omega = 0.294$ rad/s, and wave steepness $k|A| = 0.01$ (—), 0.02 (- -), and 0.03 (- · -).

To check how the incident wave steepness affects the growth rate of the resonant heave motion, we first plot in figure 6-12b the time history of the logarithmic value of the (normalized) amplitude of resonant heave motion, $\log(|A_{3n}|/|A|)$, for the three specified $k|A|$ s. Then the slopes of $\log(|A_{3n}|/|A|)$, γ'_3 , as a function of time are compared in figure 6-12c for different incident wave steepness values. From the results, we can make the following observations: (1) in the very initial development stage of resonant heave motions, the growth rate of $|A_{3n}|$ for each given $k|A|$ varies with time. This phenomenon can be explained using Eq. (6.56) obtained from the theoretical linear stability analysis. For time small, the four growth rates $\mathbf{Re}[\gamma_i]$, $i = 1, 2, 3, 4$ all contribute to the behavior of resonant heave motion and the growth of $|A_{3n}|$ is not straightly exponential. (2) after the very initial stage, the value of $\log(|A_{3n}|/|A|)$ has approximately linear dependence on time for certain period, regardless of the exact value of incident wave steepness. This means that $|A_{3n}|$ has an exponential growth for that period of time, i.e., $|A_{3n}|/|A| \sim e^{\gamma'_3 t/T}$. Again, let's look at Eq. (6.56). If t is not small, the maximum growth rate, $\max(\mathbf{Re}[\gamma_i], i = 1, 2, 3, 4)$, dominates the growth of $|A_{3n}|$ so that we obtain a nearly steady value of γ'_3 for certain period of time, for each specified $k|A|$. Specifically, $\gamma'_3 \cong 0.019$ for $k|A| = 0.01$, $\gamma'_3 \cong 0.043$ for $k|A| = 0.02$, and $\gamma'_3 \cong 0.068$ for $k|A| = 0.03$. So, in this period of time, larger wave steepness leads to a larger growth rate and the exact (steady) values of γ'_3 have approximately linear dependence on incident wave steepness, as predicted by the linear stability analysis. (3) After the peak value of γ'_3 is reached, γ'_3 starts to oscillate. This phenomenon cannot be explained by the linear stability analysis as the theory is valid only for the initial growth period of unstable body motions.

Fully nonlinear numerical results are shown in figure 6-13 for the growth of resonant pitch motions with different incident wave steepness specified. As we can see, the influence of $k|A|$ on the growth of resonant pitch motion is very similar to that for the heave motion. Even the (steady) values of corresponding growth rates γ'_5 are close to those of γ'_3 . This is because of the fact that the resonant heave and pitch motions are coupled and the theory predicts their similar characteristics (from Eq. (6.56) and Eq. (6.57)).

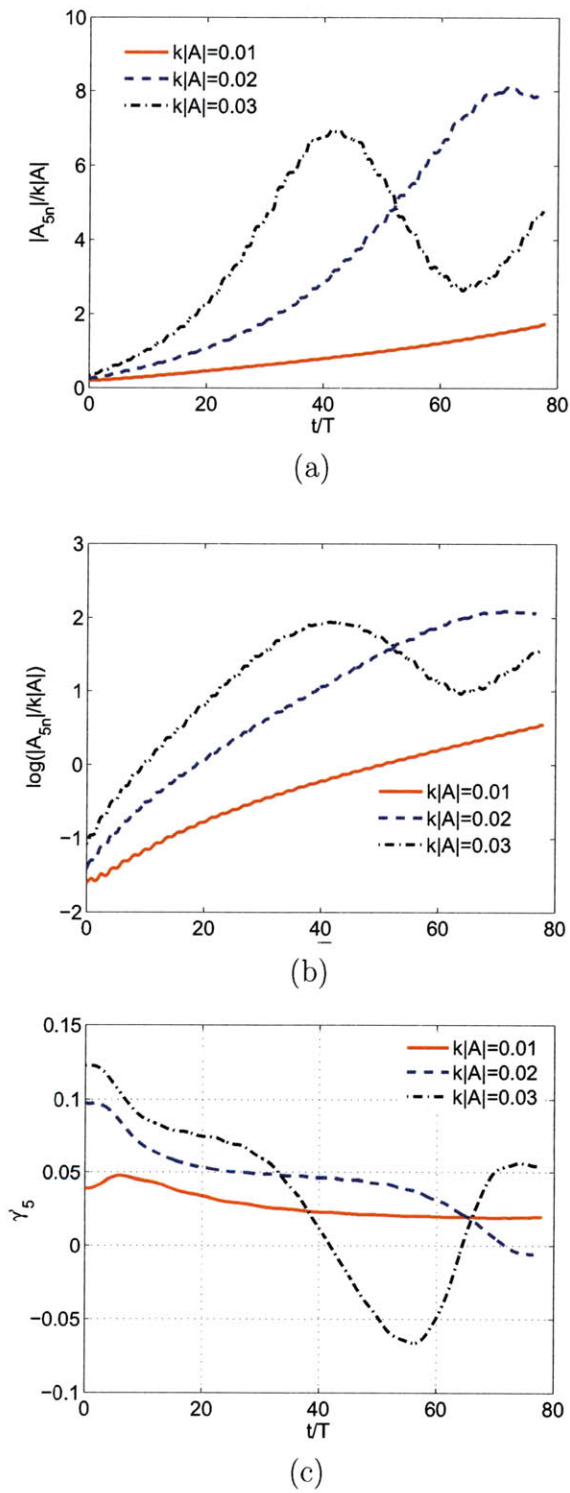


Figure 6-13: Time histories of (a) the amplitude of resonant pitch motion $|A_{5n}|$, (b) $\log(|A_{5n}|)$, and (c) the growth rate γ'_5 of resonant pitch motion with the incident wave phase angle $\theta' =$, frequency $\omega = 0.294$ rad/s, and wave steepness $k|A| =: 0.01(—), 0.02(---),$ and $0.03(- \cdot -)$.

6.3.4 Frequency detuning effect on instability

In above studies, coupled unstable heave and pitch motions occur when the incident wave frequency is set to be $\omega = 0.294$ rad/s (i.e., $T = 21.345$ s) which perfectly satisfies the instability condition (Eq. (6.52)). How does the SPAR behave if the incident wave frequency is away or in the neighborhood of $\omega = 0.294$ rad/s? This section will focus on answering this question.

With the incident wave frequency set as $\omega = 0.288$ rad/s (i.e., $T = 21.8$ s), figure 6-14 plots the time histories of SPAR's heave and pitch motions as well as their time harmonics while other incident wave parameters are specified the same as those for figure 6-10 (i.e., phase angle $\theta' = 0$ and wave steepness $k|A| = 0.02$). Results show that the heave and pitch motions are also unstable and the amplitudes of resonant motions grow with time for $t/T < 30$. But comparing figure 6-14 with figure 6-10, we can see that the slight shift in incident wave frequency makes dramatic change in the SPAR's unstable motions. At $\omega = 0.288$ rad/s, the amplitudes of resonant heave and pitch motions have much smaller peak values and growth rates than those with incident wave frequency $\omega = 0.294$ rad/s.

As another example, we show in figure 6-15 the SPAR's motions with the incident wave frequency specified at $\omega = 0.279$ rad/s (i.e., $T = 22.5$ s) further away from the 'perfect' wave frequency value $\omega = 0.294$ rad/s. In the simulation, the incident wave steepness and initial phase angle are still set as $k|A| = 0.02$ and $\theta' = 0$, respectively. For this case, the SPAR motions are generally stable and the amplitudes of resonant heave and pitch motions decay and oscillate with time.

The overall influence of incident wave frequency to the instability, namely the detuning effect, is summarized in figure 6-16. We first define γ'_3 as the exponential growth rate of the amplitude of resonant heave motion, that is, $|A_{3n}|/|A| \sim e^{\gamma'_3 t/T}$, where t is chosen to be away from the very initial development stage but smaller than the time when $|A_{3n}|$ reaches its peak value. Figure 6-16a shows the dependence of γ'_3 on the incident wave period T . At the 'perfect' incident wave period $T = 21.345$ s when the instability condition (Eq. (6.52)) is exactly satisfied, denoted by the red

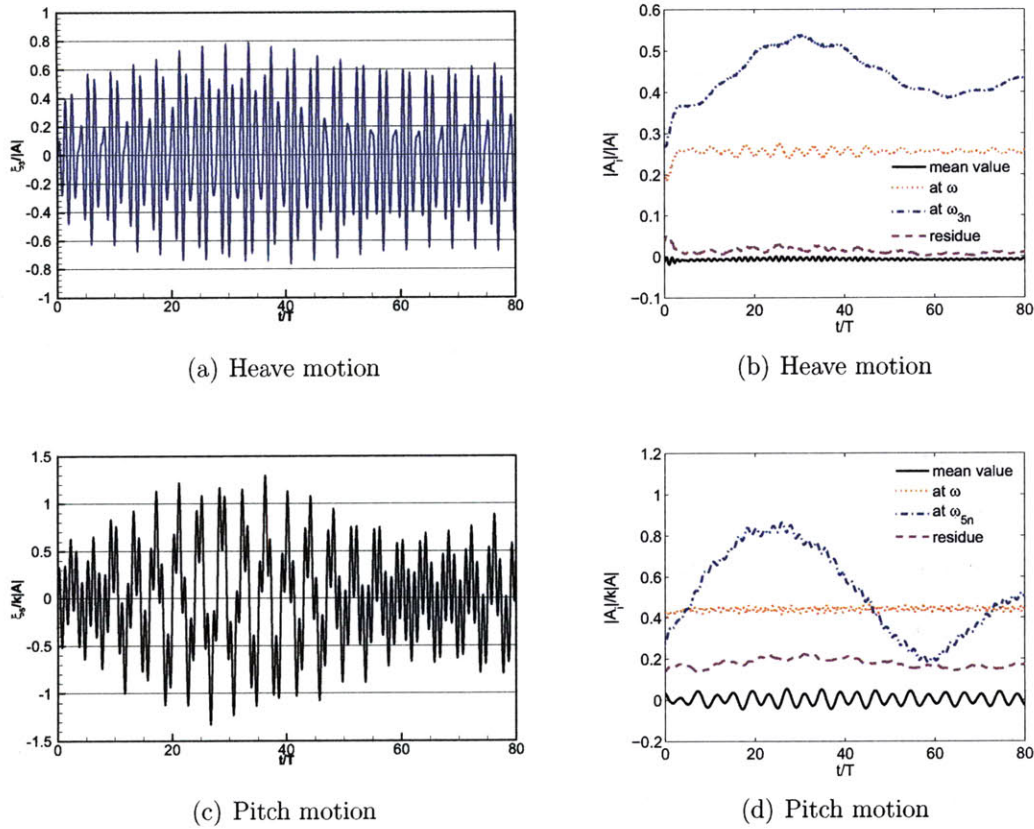


Figure 6-14: Time histories of (a) heave motion, (b) amplitudes of heave-motion harmonics, (c) pitch motion, and (d) amplitudes of pitch-motion harmonics, obtained by the fully-nonlinear simulations for the SPAR in a regular wave of wave steepness $k|A| = 0.02$, frequency $\omega = 0.288$ rad/s, and phase angle $\theta' = 0$.

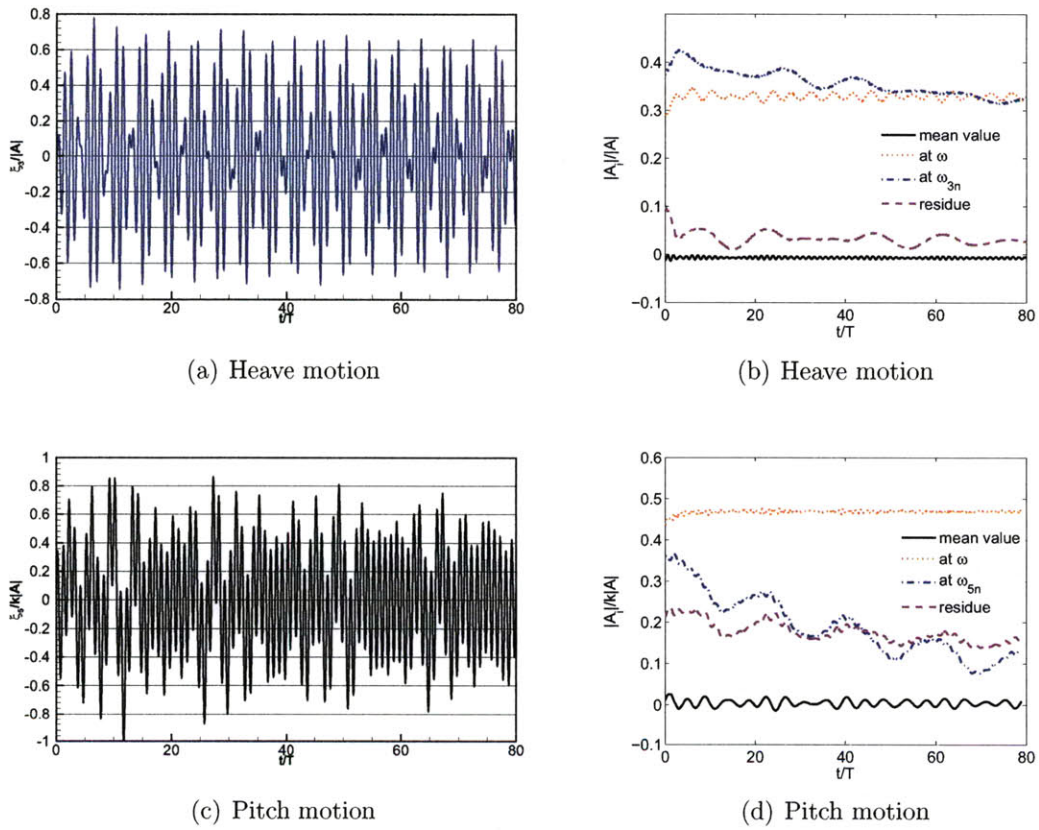


Figure 6-15: Time histories of (a) heave motion, (b) amplitudes of heave-motion harmonics, (c) pitch motion, and (d) amplitudes of pitch-motion harmonics, obtained by the fully-nonlinear simulations for the SPAR in a regular wave of wave steepness $k|A| = 0.02$, frequency $\omega = 0.279$ rad/s, and phase angle $\theta' = 0$.

dashed line in the plot, γ'_3 has approximately its peak value. Away from the ‘perfect’ incident wave period, γ'_3 diminishes. The unstable resonant heave motion of the SPAR occurs only in a narrow band of incident wave period $T \in [20.9, 21.8]s$. The corresponding maximum amplitudes of heave motion at natural heave frequency are shown in figure 6-16b as a function of T . The ‘perfect’ incident wave period does not necessarily induce the maximum value of $max(A_{3n})$ which, instead, happens near the lower bound of the unstable region. Close to the lower bound when T becomes slightly smaller than 21s, $max(A_{3n})$ decreases sharply. Near the upper bound, however, the change of $max(A_{3n})$ is relatively smoother.

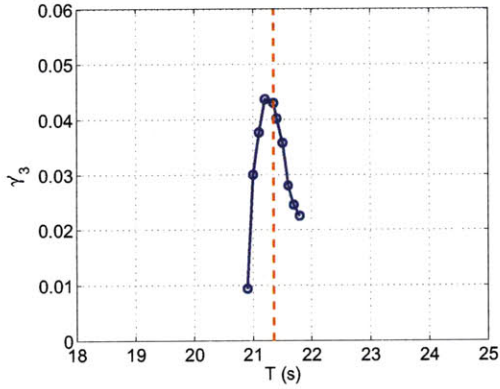
As shown in figures 6-16c and d, the SPAR’s growth rate γ'_5 and the maximum amplitudes of the resonant pitch motions have very similar dependence on the incident wave period T . (Note that the growth rate γ'_5 is defined by the following equation: $|A_{5n}|/k|A| \sim e^{\gamma'_5 t/T}$.)

Note that the detuning effect for the SPAR’s unstable motions critically depends on the incident wave steepness. Given a larger incident wave steepness, nonlinear interactions between wave-wave, wave-body, and different modes of body motions become stronger and the instability mechanism is more likely to overcome the detuning effect. As a result, a larger incident wave steepness would lead to larger resonant responses and a wider unstable frequency bandwidth.

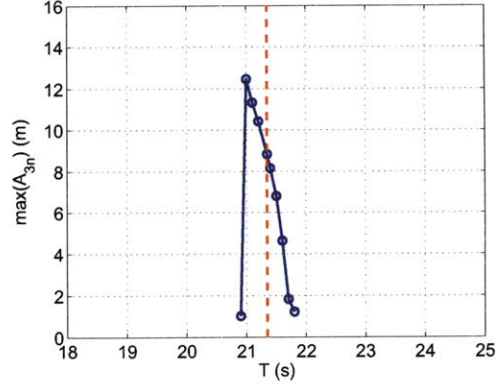
6.3.5 Influence of body geometry on instability

Fully nonlinear PFFT-QBEM scheme is also applied to study the stability of the cylindrical FPSO under the action of a specified wave field. The FPSO geometry feature has been described in the previous section and its natural heave and pitch frequencies are $\omega_{3n} = 0.444$ rad/s and $\omega_{5n} = 0.256$ rad/s, respectively. We set the incident wave frequency as $\omega = \omega_{3n} + \omega_{5n} = 0.7$ rad/s (i.e., wave period $T = 8.98s$) and wave steepness $k|A| = 0.2$. At $t = 0$, the FPSO is situated at the crest of the incident wave and we define the incident wave phase angle as $\theta' = 0$. An artificial spring is adopted in surge direction with the natural surge period being $T_{1n} \cong 60s$.

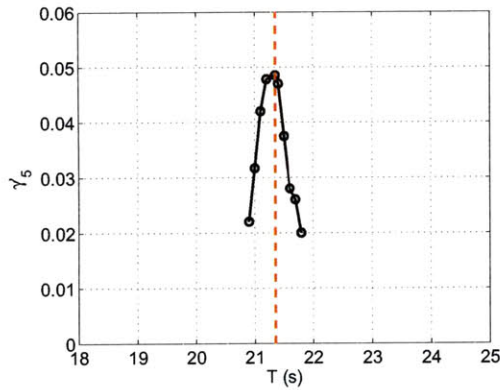
Figure 6-17 plots the time histories of FPSO’s surge, heave, and pitch motions



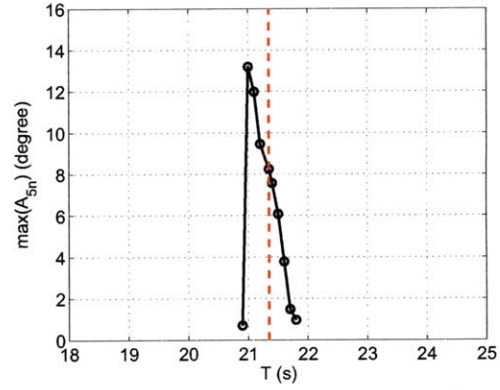
(a) Heave motion



(b) Heave motion



(c) Pitch motion



(d) Pitch motion

Figure 6-16: (a)Growth rate γ'_3 of the resonant heave motion amplitude $|A_{3n}|$, (b) maximum value of A_{3n} , (c)growth rate γ'_5 of the resonant pitch motion amplitude $|A_{5n}|$, (b) maximum value of A_{5n} in SPAR motions as a function of the incident wave period T . The plotted results are obtained using the fully nonlinear numerical simulations with incident wave of amplitude $|A| = 2.264\text{m}$ and phase angle $\theta' = 0$. The red line in each figure highlights the position where the incident wave frequency perfectly satisfies the instability condition (Eq. (6.52)) obtained from linear stability analysis.

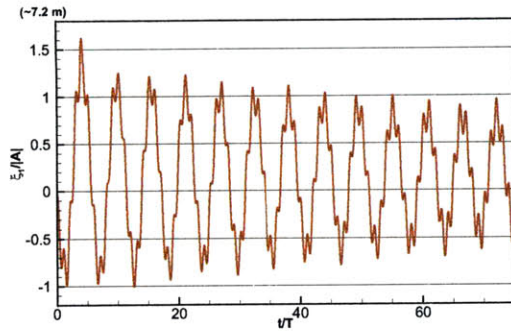
as well as the corresponding amplitudes of motion harmonics. Results show that the FPSO's surge motion is stable with the motion amplitude at natural surge frequency ω_{1n} decreasing with time monotonically. Both heave and pitch motions are unstable.

By comparing the evolutions of FPSO's motions (at $k|A| = 0.2$) with those of the SPAR (at $k|A| = 0.02$) in figure 6-10, we can see that the FPSO's resonant heave and pitch motions grow much slower with time, which unfolds the effect of body geometry on instability. Different body geometries determine different combinations of natural frequencies of body motions. More importantly, body geometry determines wave dampings which have high impact on the instability of the system. As the cylindrical FPSO's body configuration results in much bigger heave damping and pitch damping than those of the SPAR, the FPSO is stabilized by the damping so that its resonant heave and pitch motions have much slower growth rates. Also, because of the large dampings, the detuning effect for unstable FPSO motions can be more significant than that for the SPAR and a narrower unstable frequency bandwidth is expected.

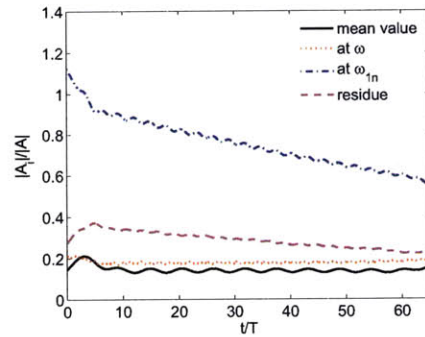
6.3.6 Effect of surge motion on instability

As discussed in the linear stability analysis, surge motion might have effects on the growth of unstable body motions due to the coupling between surge motion and pitch motion. We first use the SPAR as an example to study the influence of surge motion on instability and the results are shown in figure 6-18. By setting all other related physical parameters the same ($\omega = 0.294$ rad/s, $k|A| = 0.02$, $\theta' = 0$) and varying only the natural surge motion period ($T_{1n} = 0s$, $T_{1n} = 50s$, and $T_{1n} = 150s$), we see that the unstable heave and pitch motions are largely affected. Especially when the SPAR is restricted from surge motion (i.e., $T_{1n} = 0s$), much higher growth rates are observed in the amplitudes of heave and pitch motions. Besides, $T_{1n} = 50s$ causes a slightly faster growth of the amplitudes of SPAR's motions than that with $T_{1n} = 150s$. Overall, loose restriction in surge motion tends to stabilize the SPAR's motions under the action of a regular incident wave at the 'perfect' wave frequency.

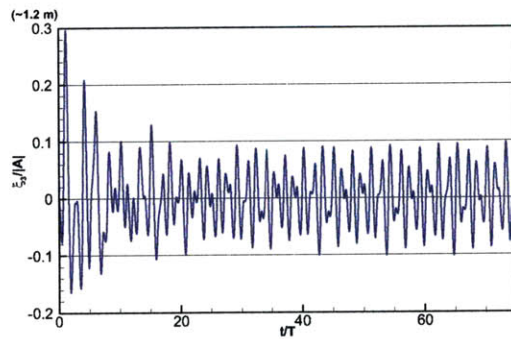
We also investigate the surge motion effect on the cylindrical FPSO's coupled unstable heave/pitch motions, for specified incident wave frequency $\omega = 0.7$ rad/s,



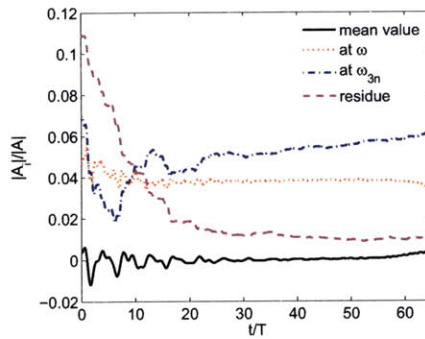
(a) Surge motion



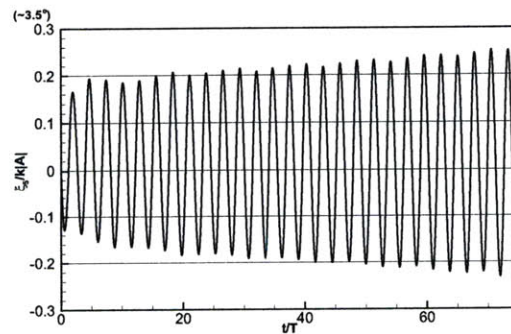
(b) Amplitude of surge motion harmonics



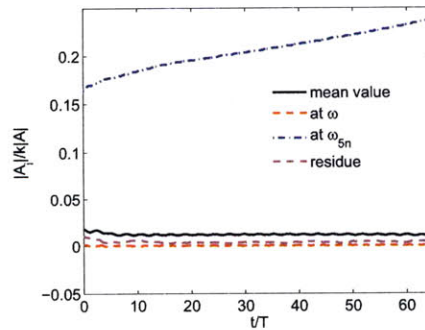
(c) Heave motion



(d) Amplitudes of heave motion harmonics

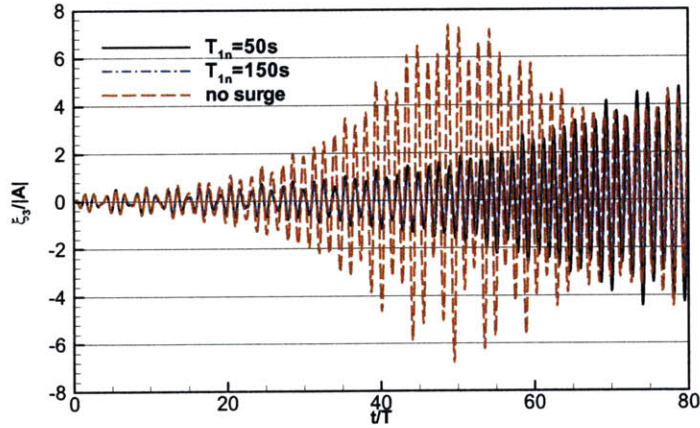


(e) Pitch motion

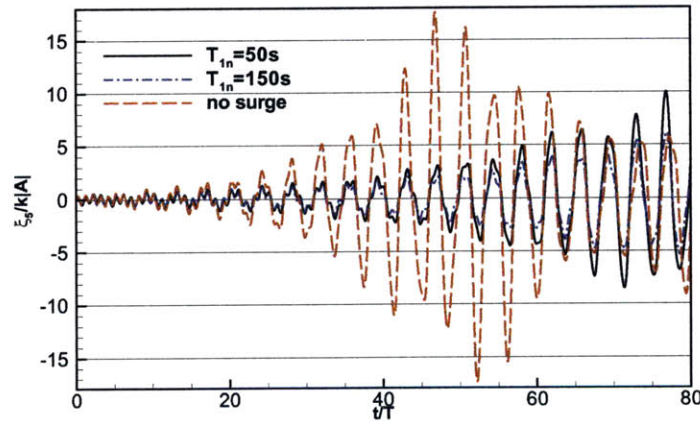


(f) Amplitudes of pitch motion harmonics

Figure 6-17: Time histories of (a) surge motion, (b) amplitudes of surge-motion harmonics, (c) heave motion, (d) amplitudes of heave-motion harmonics, (e) pitch motion, and (f) amplitudes of pitch-motion harmonics, obtained by the fully-nonlinear simulations for the cylindrical FPSO in a regular wave of wave steepness $k|A| = 0.2$, wave frequency $\omega = 0.7$ rad/s, and phase angle $\theta' = 0$.



(a) Heave motion



(b) Pitch motion

Figure 6-18: Comparison of the effects of surge motions with different natural surge periods ($T_{1n} = 0s$ (—), $T_{1n} = 50s$ (- · -), and $T_{1n} = 150s$ (- -)) on the time histories of (a) heave motion and (b) pitch motion of the SPAR from fully nonlinear numerical simulations. For this study, the following parameter settings are adopted: $\omega = 0.294$ rad/s, $k|A| = 0.02$ and $\theta' = 0$.

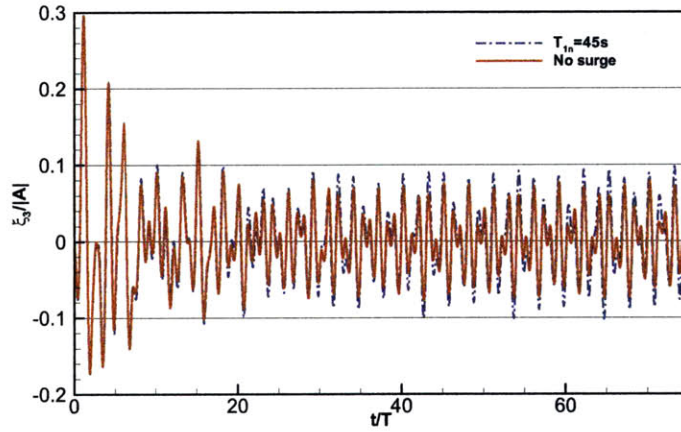
wave steepness $k|A| = 0.2$, and phase angle $\theta' = 0$. The time histories of the FPSO's heave and pitch motions are shown in figure 6-19, with different settings of natural surge motions period ($T_{1n} = 0s$ and $T_{1n} = 45s$). Results indicate that allowing surge motion makes larger growth rates of unstable heave and pitch motions than those without surge motion.

So, depending on the body geometry configurations, the existence of surge motion may increase or decrease the growth rates of unstable body motions. Studies for the effect of surge motion on instability could help the optimization of floating bodies' design.

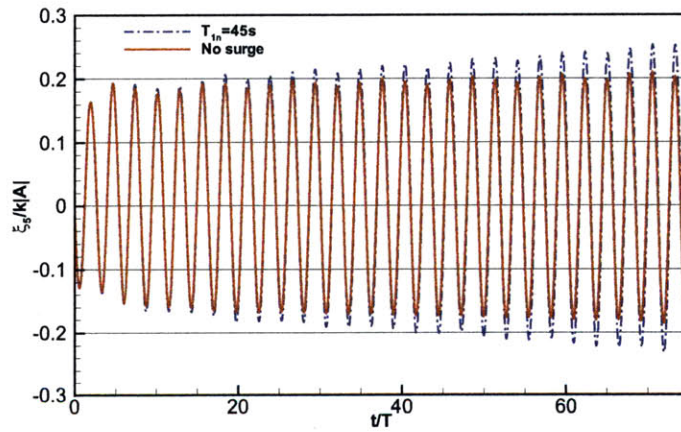
6.3.7 Effect of incident wave phase angle on instability

In above fully nonlinear numerical studies, we assume that at $t = 0$, the floating body (SPAR or FPSO) is placed on the crest of incident wave, which is reflected by the incident wave phase angle $\theta' = 0$. Different incident wave phase angles relate to different initial disturbances to the system, from the startup of the numerical simulation. In this section, we investigate the influence of the relative position (symbolled by θ') of floating body with respect to the incident wave at $t = 0$ on unstable body motions.

Given two different incident wave phase angles, $\theta' = 0$ and $\theta' = \pi/2$, we compare the time histories of the SPAR's surge motions in figure 6-20a, with other incident wave parameters set as $\omega = 0.294$ rad/s, $k|A| = 0.02$, and $T_{1n} = 160s$. Results show that the value of θ' has significant effect on the SPAR's surge motion. With $\theta' = 0$, the surge motion amplitude is much larger than that with $\theta' = \pi/2$. We evaluate the amplitude of the surge motion at natural surge frequency, $|A_{1n}|$, and plot in figure 6-20b the logarithmic value of $|A_{1n}|$ as a function of time, for three θ' values. As we can see, different incident wave phase angles result in very different initial disturbances in the resonant surge motion, but their corresponding $|A_{1n}|$ s have similar dependence on time. The effect of θ' on the SPAR's heave and surge motions are shown in figure 6-20c~f. The initial amplitudes of resonant heave/pitch motions show large discrepancy for different θ' values, but the growth rates of resonant heave/pitch motions are not affected much by the incident wave phase angle.



(a) Heave motion



(b) Pitch motion

Figure 6-19: Comparison of the effects of surge motions with different natural surge periods ($T_{1n} = 0\text{s}$ (—) and $T_{1n} = 45\text{s}$ (- · -)) on the time histories of (a) heave motion and (b) pitch motion of the cylindrical FPSO from fully nonlinear numerical simulations. For this study, the following parameter settings are adopted: $\omega = 0.7 \text{ rad/s}$, $k|A| = 0.2$ and $\theta' = 0$.

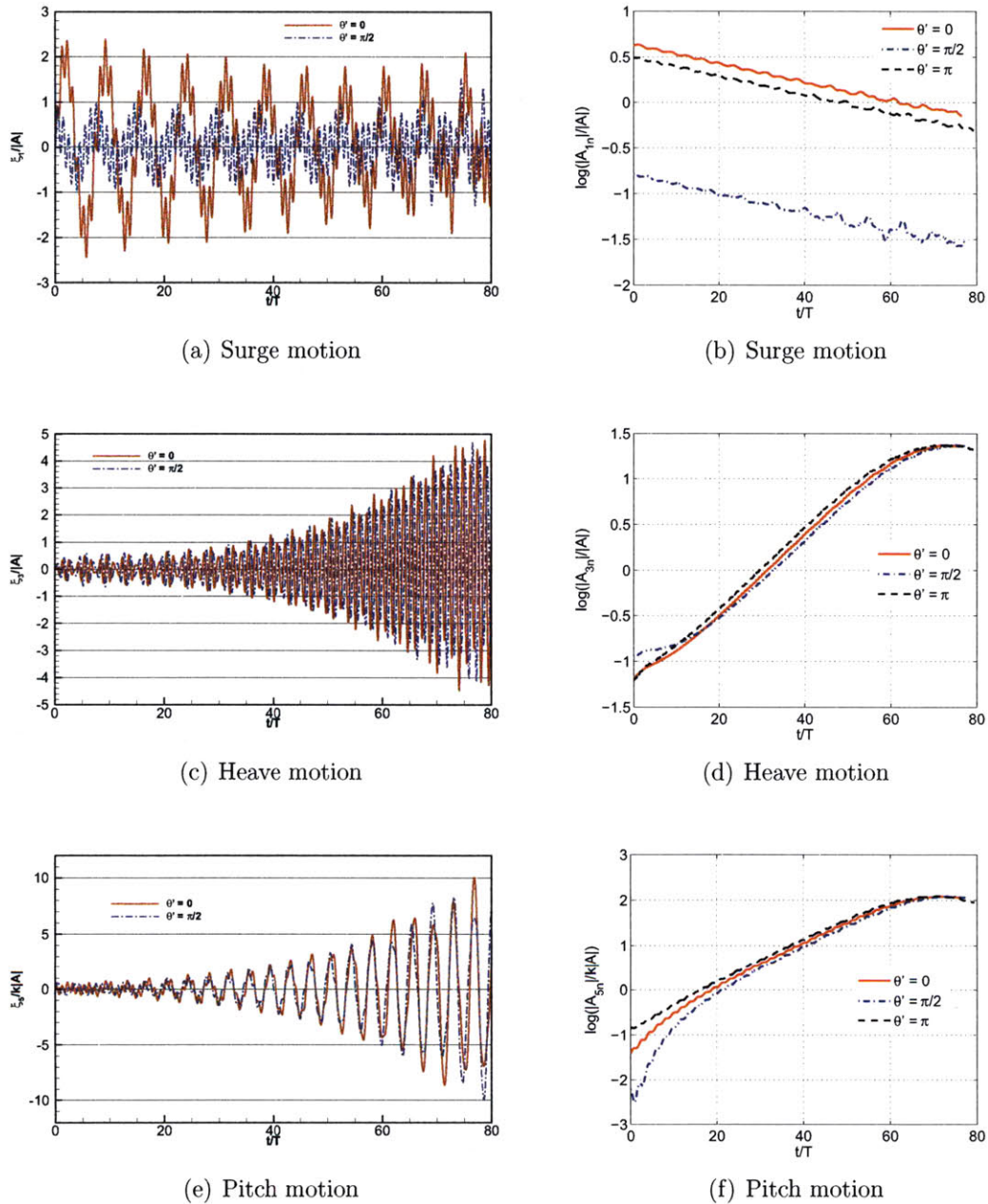


Figure 6-20: Time histories of (a) surge motion, (b) logarithmic value of the resonant surge motion amplitude, (c) heave motion, (d) logarithmic value of the resonant heave motion amplitude, (e) pitch motion, (f) logarithmic value of the resonant pitch motion amplitude, obtained by the fully-nonlinear simulations for the SPAR in a regular wave of wave steepness $k|A| = 0.02$ and wave frequency $\omega = 0.294$ rad/s. Comparisons are made for results of different incident wave phase angles: $\theta' = 0$ (—), $\theta' = \pi/2$ (- - -), and $\theta' = \pi$ (- · - ·). To avoid curve overlapping, only two groups of data are plotted in the figure (a), (c), and (e).

6.3.8 Influence of initial disturbances on instability

From last section, we know that the incident wave phase angle affects initial disturbances on resonant body motions and the initial disturbances are generated from the startup of the numerical simulations. In practical applications, disturbances are real, in view of the presence of numerous wave components in irregular seas. Here we introduce a small regular wave as an extra disturbance to the system and study how the coupled unstable body motions are affected by the existence of this disturbance.

The stability of the FPSO, subjecting to a dominant wave and a disturbance wave, is investigated here using the fully nonlinear numerical approach. The dominant wave has a wave frequency $\omega_1 = 0.7$ rad/s, a wave steepness $k|A_1| = 0.2$, and a phase angle $\theta'_1 = 0$. For the disturbance wave, we set wave frequency $\omega_2 = 0.444$ rad/s, wave steepness $k|A_2| = 0.004$, and phase angle $\theta'_2 = 0$. Notice that the disturbance wave frequency ω_2 is chosen to be the same as the FPSO's natural heave frequency ω_{3n} here. With the above parameter settings, figure 6-21 shows the time histories of the FPSO's surge, heave, and pitch motions and their time harmonics. The surge motion is stable with the amplitude of resonant surge motion decreasing with time. The FPSO's heave and pitch motions are unstable. The amplitude of resonant heave motion grows with time while the amplitude of resonant pitch motion first decreases for t small and then increases at later time. The behaviors of the resonant heave and pitch motions are related to the initial phase angles of the dominant wave and the disturbance wave. By comparing figure 6-21 with figure 6-17, we see that adding the small disturbance wave of natural heave frequency results in much larger growth rates of resonant heave and pitch motions.

6.4 Comparison to experimental data

ExxonMobil conducted model tests for a deep draft caisson vessel (DDCV) in the wave basin of the Offshore Technology Research Center in 1998. The DDCV is a vertically floating circular cylinder with a diameter $D = 37.2$ m and a draft $H = 198.2$ m. The center of gravity is located at a distance $H_G = 95.2$ m from the keel of the cylinder.

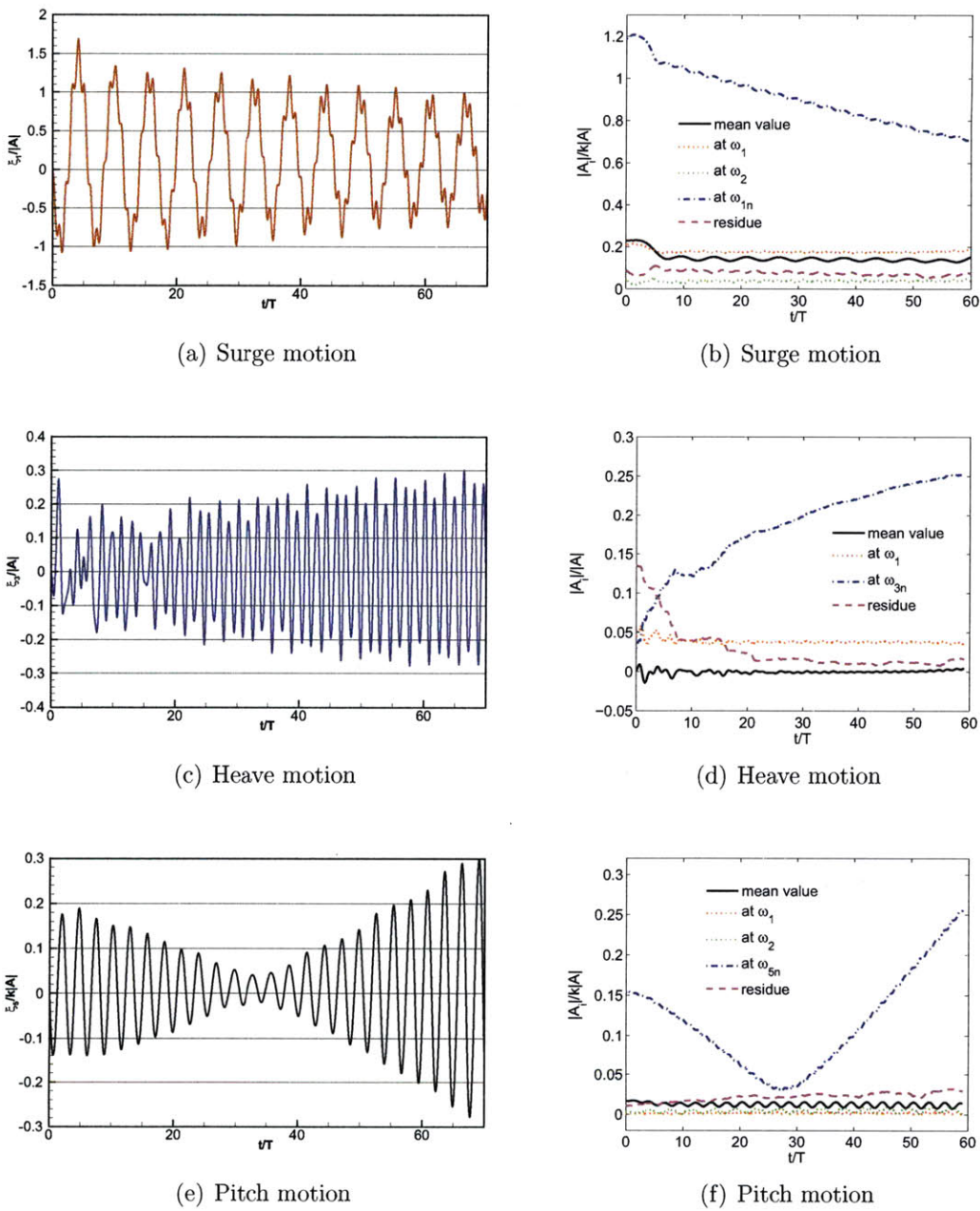


Figure 6-21: Time histories of (a) surge motion, (b) amplitudes of surge-motion harmonics, (c) heave motion, (d) amplitudes of heave-motion harmonics, (e) pitch motion, and (f) amplitudes of pitch-motion harmonics, obtained by the fully-nonlinear simulations for the cylindrical FPSO. In the study, the dominant incident wave has a frequency $\omega_1 = 0.7$ rad/s, a wave steepness $k|A_1| = 0.2$, and a phase angle $\theta'_1 = 0$ and the disturbance wave has a frequency $\omega_2 = 0.444$ rad/s, a wave steepness $k|A_2| = 0.004$, and a phase angle $\theta'_2 = 0$.

The natural surge, heave, and pitch periods of the DDCV are measured to be around 420s, 29s, and 99s, respectively. The platform was exposed to a regular incident wave train with incident wave amplitude and wave period being approximately $|A| = 6.4\text{m}$ and $T = 22\text{s}$, respectively.

Comparisons are made between the experimental measurements and numerical results obtained from the fully nonlinear simulations for heave and pitch motions of the DDCV. Note that in the experiment, the body is located at several wavelengths away from the wave maker. For comparison, we thus shift the experimental data forward by around 200s. (Specifically, the experimental records are shifted by 230s for heave motion and 195s for pitch motion to approximately match the phases, as at $t = 0$, the initial disturbances/noises in the experiment in general differs from those in numerical simulations.) Also, we only show the comparisons in the following figures up to $t = 1500\text{s}$ since it was observed that the deck of the platform touches the free surface afterwards in the experiment. Viscous dampings are always associated with body motions in the experiment because of vortices shed from body oscillations and body surface frictions. To compare fairly with experimental data, we adopt a simple model to include linear viscous damping in our potential-flow based numerical scheme.

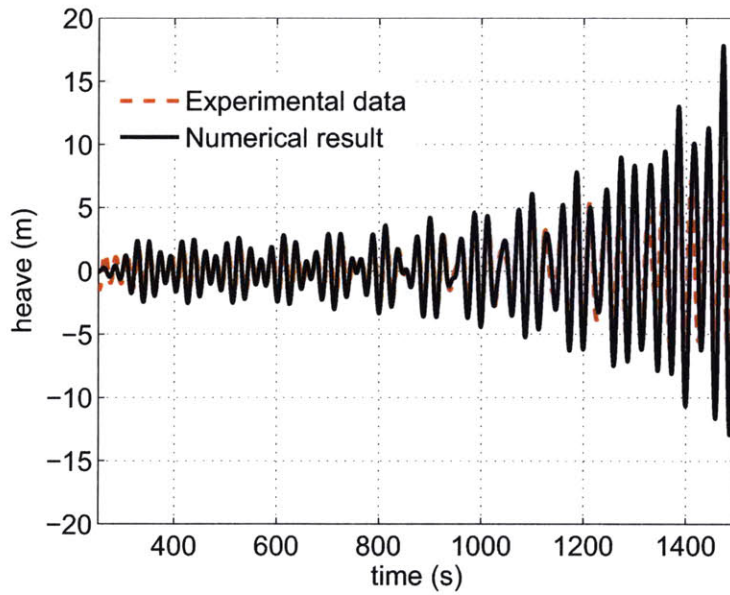
Figure 6-22 shows the direct comparison of experimental and numerical results for the time histories of the platform's heave and pitch motions. In the numerical simulations, we adopt the following parameter settings: incident wave period $T = 22\text{s}$, incident wave amplitude $|A| = 6.4\text{m}$, and the ratio of linear viscous heave (pitch) damping to the critical heave (pitch) damping $\nu_3 = 7\%$ ($\nu_5 = 10\%$). As observed from figure 6-22, the heave and pitch motions are all unstable and the numerical results match well with the experimental data in both the body motions' growing trends and their phases. But at large time, the experiment obtains higher amplitudes of heave and pitch motions than those from the numerical simulations. We think the main reason for this discrepancy is that the viscous damping inherent in the experiment is different from that being considered in numerical simulations. In the experiment, viscous damping has a component quadratically dependent in body motion amplitude, which is not taken into account by present numerical study, and this component plays

an important role when the DDCV's motions have large amplitude.

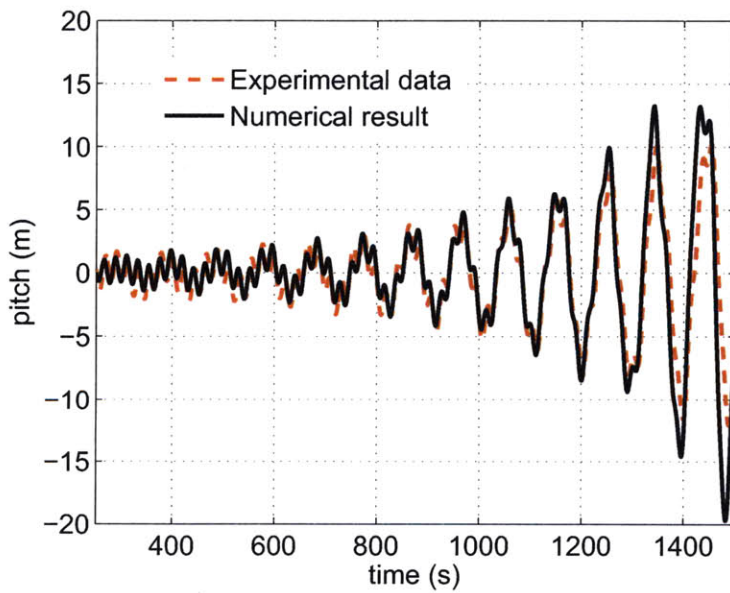
playing important role when body motions get big at large time. Our numerical simulations do not take into account the quadratic viscous damping effect.

Based on figure 6-22, we can determine the amplitudes of heave and pitch motions at their natural frequencies for the experimental and numerical results. Their logarithmic values are plotted as a function of time in figure 6-23. The slopes of those curves in figure 6-23 represent the exponential growth rates of the unstable motions of the DDCV. As we can see, the curves for experimental data have similar slopes as those of the numerical results with $\nu_3 = 7\%$ and $\nu_5 = 10\%$, for both heave and pitch motions. To show the effect of viscous damping, we also present in figure 6-23 two other groups of fully nonlinear numerical results with different linear viscous damping coefficients: ($\nu_3 = 5\%$, $\nu_5 = 8\%$) and ($\nu_3 = 3\%$, $\nu_5 = 4\%$). Results show that the viscous damping has significant influence on the growth rates of unstable body motions and smaller viscous damping results in larger growth rate values. (Note that the non-smooth starts of the curves for numerical results in figure 6-23a are caused by the smoothing startup treatment used in the numerical simulations for $t < 4T$.)

Except for the viscous damping effect, for completeness, we also study here the sensitivity of the agreement between numerical results and experimental measurements to the variations of the following two parameters: incident wave period T and incident wave amplitude A . By fixing the linear viscous damping coefficients ($\nu_3 = 3\%$, $\nu_5 = 4\%$), we obtain numerical results for several incident wave periods: $T = 22\text{s}$, $T = 21.8\text{s}$, and $T = 21.6\text{s}$, and compare the logarithmic values of resonant heave and pitch amplitudes with experimental data in figure 6-24. Among these three groups of numerical results, the one with $T = 21.6\text{s}$ agrees the best with experimental data except for large time and the one with $T = 22\text{s}$ has the highest growth rate. For the given natural heave and pitch periods of the DDCV ($T_{3n} = 29\text{s}$ and $T_{5n} = 99\text{s}$), the 'perfect' incident wave period satisfying Eq. (6.52) is $T = 22.43\text{s}$. Based on previous discussions for the frequency detuning effect on unstable body motions, we know that an incident wave period further away from the 'perfect' period corresponds to a smaller growth rate value.

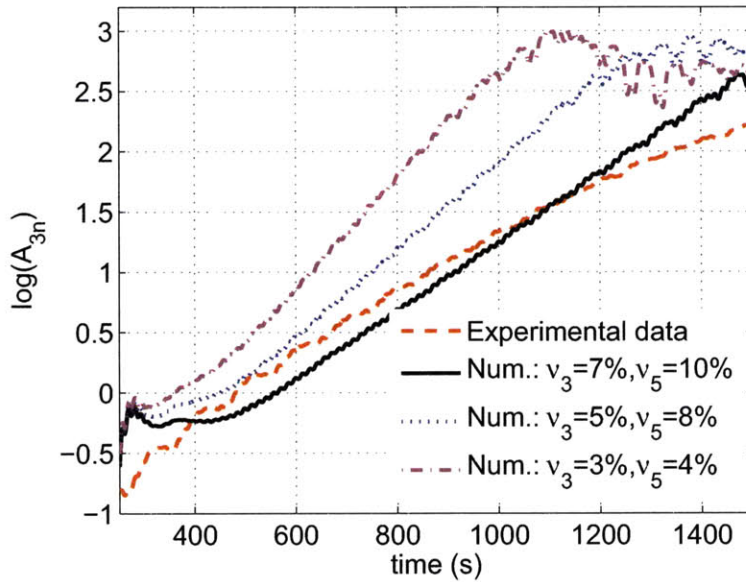


(a) Heave motion

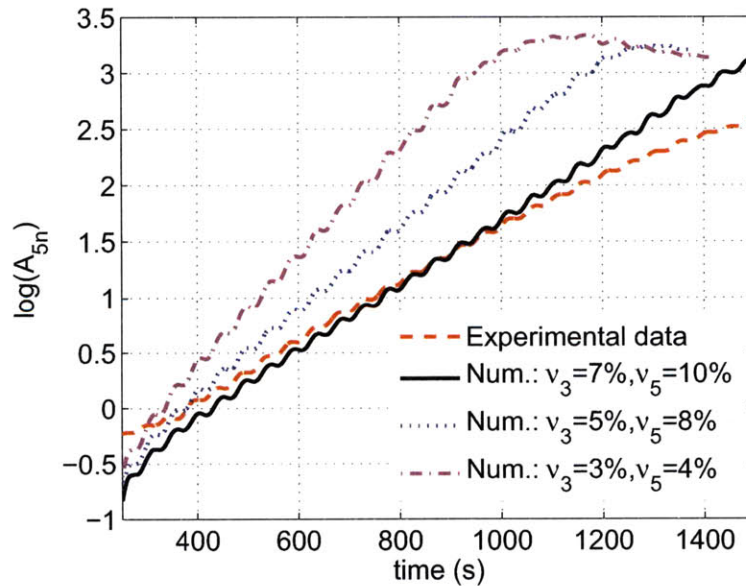


(b) Pitch motion

Figure 6-22: Comparison between experimental data (ExxonMobil, 1998)(- -) and fully-nonlinear numerical results (—) for the time histories of the (a) heave motion, and (b) pitch motion. The incident wave has a wave period $T = 22s$ and a wave amplitude $|A| = 6.4m$. In numerical simulations, we set the viscous damping coefficients as $\nu_5 = 7\%$ and $\nu_5 = 10\%$.

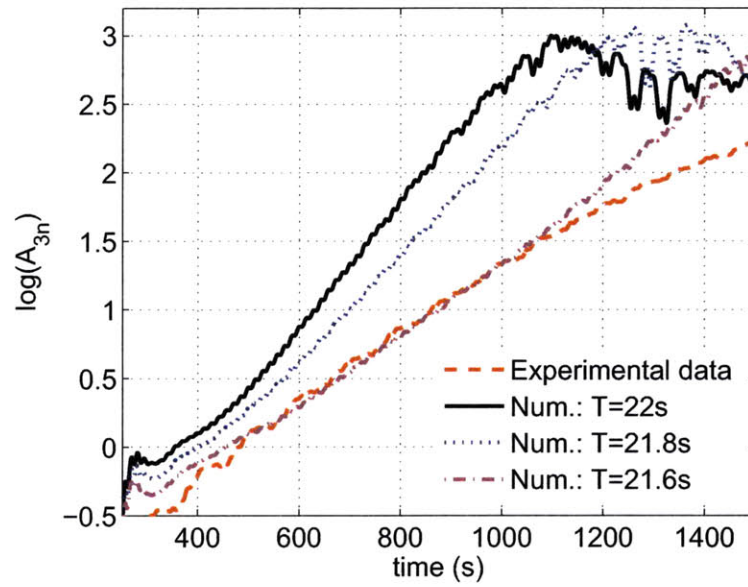


(a) Heave motion

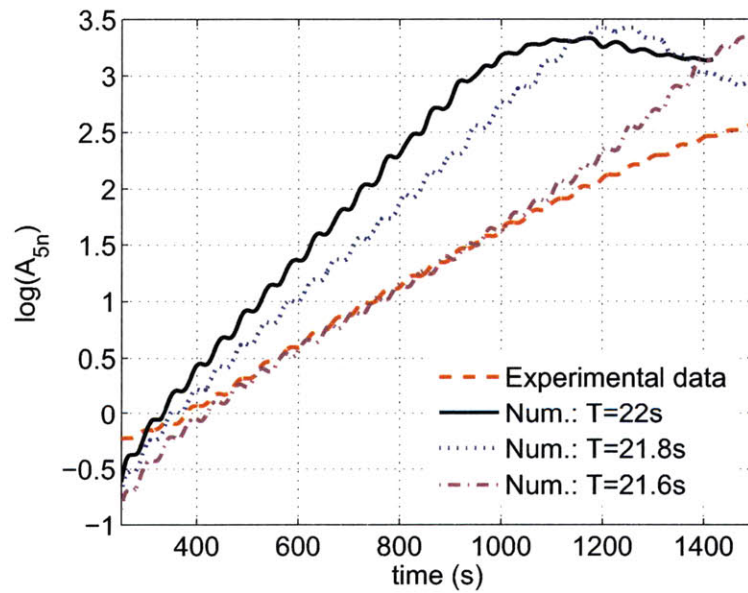


(b) Pitch motion

Figure 6-23: Time histories of the logarithmic values of the resonant (a) heave motion, and (b) pitch motion, obtained by ExxonMobil’s model tests in 1998 (---) and fully nonlinear numerical simulations with different linear viscous damping coefficients: $\nu_3 = 7\%$ and $\nu_5 = 10\%$ (—); $\nu_3 = 5\%$ and $\nu_5 = 8\%$ ($\cdot \cdot \cdot$); and $\nu_3 = 3\%$ and $\nu_5 = 4\%$ ($- \cdot -$). The incident wave has wave period $T = 22\text{s}$ and wave amplitude $A = 6.4\text{m}$ in both experiments and numerical simulations.



(a) Heave motion



(b) Pitch motion

Figure 6-24: Time histories of the logarithmic values of the resonant (a) heave motion, and (b) pitch motion, obtained by ExxonMobil's model tests in 1998 with $T = 22\text{s}$ (---) and fully nonlinear numerical simulations with $T = 22\text{s}$ (—), $T = 21.8\text{s}$ (···), and $T = 21.6\text{s}$ (- · -). The incident wave has a wave amplitude $|A| = 6.4\text{m}$ and we set the viscous damping coefficients as $\nu_3 = 3\%$ and $\nu_5 = 4\%$ in numerical simulations.

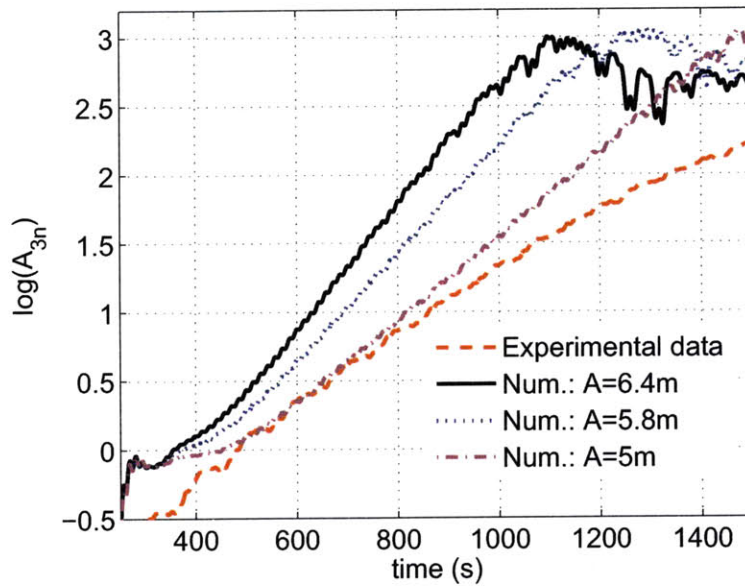
Figure 6-25 shows the effect of incident wave amplitude on the numerical growth rates for the DDCV's unstable heave and pitch motions and compares the numerical results with experimental measurements. In the numerical simulations, we adopt the following common parameter settings: $T = 22\text{s}$ and linear viscous damping $\nu_3 = 3\%$ and $\nu_5 = 4\%$. As expected, smaller incident wave amplitudes bring down the the growth of the DDCV's unstable heave and pitch motions.

At the end, we remark that direct comparisons of experimental measurements with present fully nonlinear numerical results are very challenging because of the unknown viscous dampings, unknown initial disturbances, and errors in measurements in the experiment. Being able to obtain the satisfactory comparison shown in figure 6-22 is remarkable. We further studied the sensitivity of the comparison on related parameters including viscous damping, incident wave period, and incident wave amplitude.

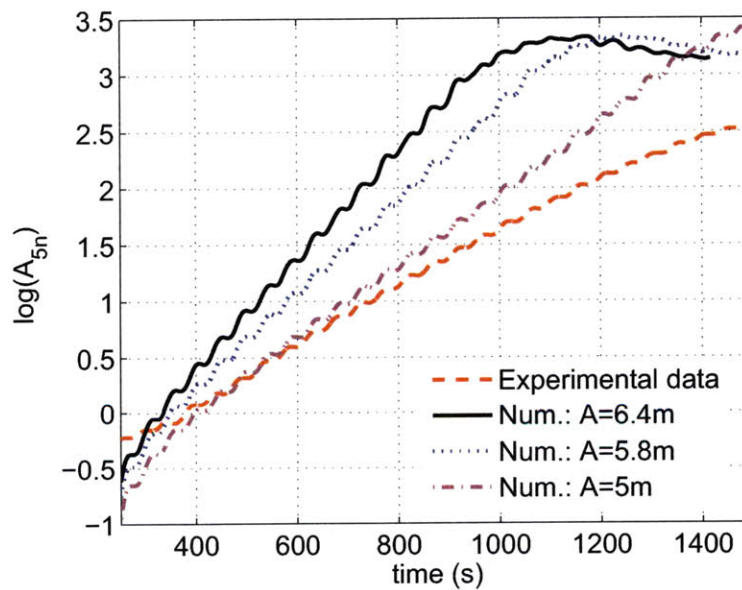
6.5 Summary and discussions

We first carry out a linear stability analysis for the stability of floating marine vessels/structures under the action of regular incident waves. The benefits of our theoretical analysis include the following several aspects:

- (1) Identify possible instability conditions (Eq. (6.52), Eq. (6.59), and Eq. (6.60)) for the coupled resonant heave-pitch motions of floating structures in waves. Given a floating body geometry and the sea condition under which the structure operates, we can determine the specific instability condition under which unstable coupled body motions could occur. As confirmed by the experiment conducted by ExxonMobil in 1998, the condition (Eq. (6.52)) is responsible for the unstable heave and pitch motions of the DDCV platform being tested.
- (2) Understand the physical mechanism for the unstable motions of the DDCV. Second-order interactions between incident wave and (disturbance) resonant heave motion provide forcing of difference frequency which coincides with the



(a) Heave motion



(b) Pitch motion

Figure 6-25: Time histories of the logarithmic values of the resonant (a) heave motion, and (b) pitch motion, obtained by ExxonMobil's model tests in 1998 with $|A| = 6.4m$ (---) and fully nonlinear numerical simulations with $|A| = 6.4m$ (—), $|A| = 5.8m$ ($\cdot \cdot \cdot$), and $|A| = 5m$ (- · -). The incident wave has wave period $T = 22s$ and we set the viscous damping coefficients as $\nu_3 = 3\%$ and $\nu_5 = 4\%$ in numerical simulations.

natural pitch frequency so that resonant pitch motion is excited. At the same time, second-order interactions between incident wave and resonant pitch motion excites body heave motion at heave natural frequency. As a result, coupled resonant heave-pitch motions might grow exponentially with time, depending on the system damping. We believe that the Mathieu instability is not the cause for the occurrence of the coupled heave-pitch resonant responses of the DDCV platform observed in experiment and numerical studies here.

- (3) Find out all possible sources contributing to the forcing of the coupled unstable heave and pitch motions. Physically, the forcing includes all the nonlinear interactions between base flow and radiation waves caused by the body motions, between base flow and body motions, and between body motions of different modes. Mathematically, appearing in the nonlinear free surface conditions, body surface condition, and the forces/moments in the equations of motions, all the nonlinear couplings between base flow and disturbance flow matter. If only capturing an incomplete combination of nonlinear couplings, a study may still deduce the instability condition but would certainly provide a wrong prediction for the growth rates of unstable body motions.
- (4) Summarize all physical parameters that are relevant to the instability of the system: incident wave steepness, body geometry, wave damping, as well as the phase angle of the forcing. How these parameters affect the growth rates of unstable body motions is investigated numerically.

The conclusions obtained from the linear stability analysis fit in the initial growth stage of unstable body motions. When large-amplitude body motions are developed, highly nonlinear interactions are involved in the system and the linear stability analysis may not be able to provide accurate predictions for the evolution of body motions. Besides, the theoretical analysis investigates only qualitatively the influence of all related physical parameters on instability. To gain the whole picture of the characteristics of unstable body motions in a large time scale, fully nonlinear numerical studies in the time domain have to be conducted, with the direct guidance provided

by the linear stability analysis.

An efficient and robust initial boundary value problem solver, based on PFFT-QBEM, is applied to numerically simulate the development of unstable body motions of floating structures in waves. The numerical scheme is able to capture all the nonlinearities involved in the wave-wave, wave-body, body motion-body motion interactions. Comparisons are made between fully nonlinear numerical results with those obtained from body-nonlinear and purely linear numerical schemes and the importance of fully-nonlinear approach for the study of unstable body motions is firmly attested. We implement the fully nonlinear PFFT-QBEM to study the motions of two types of floating bodies: SPAR and cylindrical FPSO, with the incident wave frequency exactly satisfying the instability condition Eq. (6.52). The numerical studies first confirm the instability mechanism identified by the theoretical analysis and then provide results for fully developed unstable body motions beyond the range that can be predicted by the theoretical analysis.

From the fully nonlinear numerical studies, we obtain the following quantitative understandings for the development of coupled unstable motions of cylindrical platforms in waves:

- (1) initial disturbances in resonant heave and pitch motions, originated from the startup of the simulations, vary with incident wave steepness, incident wave phase angle, and body geometry.
- (2) for time small, the evolutions of the body motions are complex, depending on the initial boundary conditions.
- (3) After the very initial development period but before peak values of body motions are reached, heave/pitch motion grows with time exponentially. The value of the grow rate has approximately linear dependence on incident wave steepness (when the wave steepness is not too large) but weak dependence on the incident wave phase angle. Body geometry, which closely relates to wave damping, has substantial effect on the growth rate of unstable heave/pitch motions. Comparatively speaking, the SPAR with small wave dampings has much faster growth

rates in the amplitudes of resonant heave and pitch motions than those of the cylindrical FPSO. Unstable heave and pitch motions happen only in a narrow band of incident wave period. For the SPAR responding to the incident wave of wave steepness 0.02, the instability range is $T \in [20.9, 21.8]s$. Larger incident wave steepness and smaller damping will lead to stronger resonant responses of the floating body and a wider instability frequency bandwidth. The ‘perfect’ incident wave frequency (satisfying Eq. (6.52)) corresponds to the maximum growth rate but not the highest value of the resonant peak amplitude. Heave and pitch motions are fully coupled as they have similar growth rates inside the instability bandwidth and similar dependence on related parameters.

- (4) Incident wave steepness and system damping determine the maximum amplitudes body motions can reach. After the first peak value, the amplitude of heave/pitch motion starts to oscillate with time as fully nonlinear interactions among the incident, radiation and diffraction wave fields, and different modes of body motions balance the instability effect.

The fully nonlinear numerical results are compared with experimental data (Exxon-Mobil, 1998) for the motions of a DDCV in response to an incident wave of 22s and amplitude of 6.4m with satisfactory agreement. Possible factors contributing to the difference between experimental measurements and numerical results are analyzed quantitatively.

The successful design and efficient operation of floating vessels/structures in waves depend critically on the accurate predictions of wave loads and body motions during transportation, installation, and operation. With the general instability mechanism identified, the study conducted in this chapter has very important practical applications.

6.6 References

- Haslum, H. A., & Faltinsen, O. M., Alternative Shape of Spar Platforms for Use in Hostile Areas, Offsh. Techn. Conf., Houston, Texas, USA, 1999;
- France, W.N., Levadou, M., Treacle, T.W., Paulling, J.R., Michel, R.K. & Moore, C., An investigation of head-sea parametric rolling and its influence on container lashing systems, SNAME Annual Meeting, 2001;
- Francescutto, A., An experimental investigation of parametric rolling in head waves, Journal of Offshore Mechanics and Arctic Engineering, Vol.123, pp.65-69, 2001;
- Chang, B.C., On the parametric rolling of ships using a numerical simulation method, Ocean Engineering, Vol.35, pp.447-457, 2008;
- Dern, J.C., Unstable motion of free spar buoys in waves, Proceedings of 9th Symposium of Naval Hydrodynamics, Paris, 1972;
- Koo, B.J., Kim M.H., & Randall R.E., Mathieu instability of a spar platform with mooring and risers, Ocean Engineering, Vol.31, pp.2175-2208, 2004;
- Rho, J.B., Choi, H.S., Shin, H.S., & Park I.K., A study on Mathieu-type instability of conventional spar platform in regular waves, International Journal of Offshore and Polar Engineering, Vol.15(2), pp.104-108, 2005;
- Mei, C.C., Stiassnie, M., & Yue, D.K.P., Theory and applications of ocean surface waves, Part 1: Linear Aspects, World Scientific Publishing Co. Pte. Ltd., 2005.

Chapter 7

Conclusions and Future Studies

This chapter summarizes the main work of this thesis and provides suggestions for future studies in the area of fully nonlinear three-dimensional wave-wave and wave-body interactions.

7.1 Conclusions

This thesis focuses on the development of an efficient and robust numerical scheme for the study of fully nonlinear three-dimensional wave-wave and wave-body interactions and the investigation of nonlinear effects in several highly nonlinear wave-body interaction problems including water initial impact, water entry, and unstable motions of a floating structure in waves.

The principal contributions of this work include, in the aspect of:

A. numerical tool

An efficient and robust initial boundary value problem solver, PFFT-QBEM, is developed for the study of three-dimensional fully nonlinear wave-wave and wave-body interaction problems.

B. theoretical analysis

- A complete asymptotic theory is developed for the air cavity development and evolution in vertical water entry of an axisymmetric body, with three-dimensional body and flow effects being taken into account;
- A linear stability analysis is carried out for the investigation of the fundamental mechanism governing the coupled unstable heave-pitch motions of a floating vessel/structure in waves;

C. understanding of nonlinear physical mechanisms

- Quantitative understanding is obtained for the effects of gravity and body geometry on the hydrodynamic loads and wave profiles in initial water impacts and cavity dynamics in later stage of water entries;
- The fundamental mechanism, basic characteristics, and parameter dependence are investigated for the coupled unstable heave-pitch motions of a floating body in waves.

In the following, each contribution mentioned above is elaborated in details.

(I) Development of an efficient and robust IBVP solver for simulations of fully-nonlinear wave-body interactions

Within the context of potential flow theorem, we develop an efficient high-order boundary element method for the solution of general boundary value problems (BVP). The pre-corrected fast Fourier transform (PFFT) algorithm is used to accelerate quadratic boundary element method (QBEM). On the one hand, PFFT-accelerated QBEM preserves QBEM's accuracy and robustness in dealing with nonlinear wave-wave and wave-body interactions with smooth/non-smooth boundaries. On the other hand, high efficiency is gained from the PFFT-accelerated QBEM scheme, as the computational cost for solving a BVP reduces from $O(N^{2-3})$ (required by traditional boundary element methods) to $O(N \ln N)$ where N is the number of boundary unknowns. To further improve the efficiency of the scheme, we introduce the mesh-neighbor-based preconditioner to the generalized minimum residual (GMRES) iterative solver to significantly improve the convergence of the iterations in solving a

boundary integral equation. Besides, with a properly designed parallel algorithm, the computational time used by PFFT-BEMs for solving a BVP decreases linearly with the number of processors on supercomputers.

We investigate the dependence of this newly developed scheme’s performance on key numerical parameters including α and d/h (where α is the order of the interpolation function used in the projection and interpolation steps, d the critical distance separating near- and far-field boundary elements in the pre-correction step, and h the uniform grid size adopted in PFFT). Combining with the mixed-Eulerian-Lagrangian (MEL) approach for nonlinear free surface tracking, PFFT-accelerated QBEM is developed into an efficient and robust initial boundary value problem (IBVP) solver for three-dimensional nonlinear wave-wave and wave-body interaction problems. Numerical issues in the implementation of PFFT-QBEM for the study of nonlinear wave-body interactions, including the stability of time-integration approaches, absorption of wave energy in the far-field damping zone, tracing of wave-body intersection line, and six degree-of-freedom body motions, are addressed systematically.

The advantageous characteristics of PFFT-QBEM make this IBVP solver an effective and practical numerical tool for the design and analysis of surface ships and marine structures.

(II) Cavity dynamics in water entry at low Froude numbers

Air cavity development and evolution in vertical water entry of an axisymmetric body are studied in the context of potential flow. We focus on a relatively low Froude number range, $F_r = V/(gD)^{1/2} \leq O(10)$, where both inertia and gravity effect are important. An asymptotic analysis is first conducted for the study of cavity dynamics. Based on the slender-body assumption and using a matched asymptotic approach, we derive a theoretical solution for the description of the dynamics and kinematics of the air cavity, with three-dimensional body and flow effects being taken into account. All existing theoretical approaches for the analysis of air cavity in water entries contain free parameters and the present asymptotic theory is the first-ever complete one. To validate and complement the asymptotic analysis, a fully nonlinear numerical

scheme, based on the axisymmetric boundary element method, is implemented for the simulation of water-entry process.

From the theoretical and numerical studies, we obtain detailed information for cavity shape, maximum radius, pinch-off position and cavity closure time. The dependence of cavity characteristics on gravity and body geometry is also investigated. Remarkably, we found that the depth of cavity closure and total cavity height increase linearly with the Froude number, independent of body geometry, for the Froude number range under study. Comparisons among the asymptotic predictions, numerical simulations, and existing experimental measurements are made with satisfactory agreement.

(III) Nonlinear computations of initial water impacts

Fully nonlinear numerical simulations, based on the axisymmetric boundary element method, are implemented for the study of initial vertical water impact of an axisymmetric body. Key numerical improvements made in this study include the accurate evaluation of pressure distribution on body surface, an effective and robust treatment for thin jet flow, and a new pressure-based criteria for the determination of the instantaneous flow-body separation point/line. The gravity and body geometry effects on the hydrodynamics of water impacts are the focuses of this study. Two representative body geometries, inverted cone and sphere, are considered.

For the inverted cone impact problem, we identify its governing (nondimensional) parameters: the deadrise angle α and the (generalized) Froude number $F_r = \sqrt{V/gt}$, which reflect the geometry and gravity effects, respectively. Hydrodynamic pressure and forces on body are evaluated and free surface profiles are captured, for a wide range of F_r and α values. We establish an approximate formula, in terms of a single similarity parameter $F_r/\alpha^{1/2}$, to evaluate the gravity effect on the total impact force on the cone.

For the sphere impact problem, the governing nondimensional parameters are $F_r = V/(gR)^{1/2}$ and $\tau = Vt/R$. From our study, we conclude that gravity effect is negligible for the very initial stage of sphere impact and for $F_r > 2$, in view of the

hydrodynamic impact pressure and free-surface profiles. One interesting finding from our study is that flow separation angle remains around 62.5° (measured from the bottom of the sphere) in the later stage of sphere impact for $F_r > 1$.

(IV) Coupled resonant heave-pitch motions of a floating body in waves

The coupled unstable heave and pitch motions of floating bodies in waves are studied through a linear stability analysis and numerical simulations. The linear stability analysis is carried out to understand the physical mechanism for the occurrence of coupled unstable body motions and investigate qualitatively the dependence of such instability on related physical parameters. The instability condition is identified, which perfectly explains the unstable heave and pitch motions of a deep draft caisson vessel (DDCV) platform observed in the experiment conducted by ExxonMobil in 1998. The stability analysis also summarizes all relevant physical parameters including incident wave steepness, body geometry, wave damping, and phase angle of external forcing, and investigate the influences of these parameters on the grow rates of unstable body motions.

To confirm the conclusions obtained from the stability analysis and to study the evolution of large-amplitude unstable body motions, we also conduct fully nonlinear numerical simulations, based on PPFT-QBEM, for the development of unstable coupled heave and pitch motions of floating bodies in waves. The efficiency and accuracy of the PPFT-QBEM scheme make it possible for accurate evaluations of all nonlinearities involved in the long-time/large-scale wave-body interactions. Through the numerical studies, we obtain quantitative understandings for the dependence of system instability on incident wave steepness, incident wave frequency, incident wave phase angle, body geometry, wave damping, viscous damping, initial disturbances and couplings between surge motion and pitch motion. The numerically obtained time histories of unstable heave and pitch motions well agree with those measured in the experiment of ExxonMobil (1998) for the DDCV in waves.

The underlying physical mechanism for the instability of floating body motions is that second-order interactions between incident wave and heave motion at natural

heave frequency provide forcing for resonant pitch motion. At the same time, second-order interactions between incident wave and pitch motion at natural pitch frequency provide forcing for resonant heave motion. Due to these nonlinear couplings involved, any initial disturbances in body heave and pitch motions at their natural frequencies might result in growing resonant heave and pitch motion. The instability mechanism identified from our study is general. Understanding of this fundamental mechanism as well as the related basic characteristics of unstable body motions is crucial for the design and operation of floating vessels/structures in surface waves.

7.2 Future studies

To extend present study, we suggest the following future research topics:

1. Application of the efficient and robust PFFT-QBEM on the study of wave-wave interactions for the understanding of kinematics of three-dimensional highly nonlinear surface waves.

PFFT-QBEM can achieve similar efficiency as the most efficient method existing in literature, the high-order spectral (HOS) method (Dommermuth & Yue 1987), for the study of nonlinear gravity waves, in the context of potential flow. Moreover, PFFT-QBEM overcomes the limitations/difficulties of HOS in applications: limited level of nonlinearity, periodic boundaries, and water bottom of simple configurations;

2. General water entries of three-dimensional bodies.

As observed in many experiments (Shlien 1994, Clane *et al.* 2004), oblique water entries give rise to many complex/interesting phenomena. Focuses of future studies could be the effects of water-entry angle (i.e. ratio of the translational velocity to the vertical velocity of the body), density ratio of the body to water, body geometry configurations, and body spinning;

3. Extensions in the study of coupled unstable motions of floating bodies in waves:

- to explicitly solve the equations, either asymptotically or numerically, listed in the linear stability analysis, for better understanding of the characteristics for the coupled resonant responses of floating structures;
- to study the unstable coupled heave-pitch motions of floating bodies in irregular waves so that the nonlinear interactions between incident waves can be taken into account;
- to examine the instability for other types of marine structures such as semi-submersible platforms, tension leg platform (TLP), small platforms in shallow water, and ships with forward speed.

7.3 References

Clane, C., Hersen F., & Bocquet, L., Secrets of successful stone-skipping, *Nature*, Vol.427, pp.29, 2004;

Dommermuth, D.G. & Yue, D.K.P., A high-order spectral method for the study of nonlinear gravity waves,, *J. Fluid Mech.*, Vol.184, pp.267-288, 1987;

Shlien, D.J., Unexpected ricochet of spheres off water, *Experiments in Fluids*, Vol.17, pp.267-271, 1994.